Drop Impact on Dry Surfaces with Phase Change

Vom Fachbereich Maschinenbau
an der Technische Universität Darmdtadt
zur
Erlangung des Grades eines Doktor-Ingenieurs (Dr. -Ing.)
genehmigte

Dissertation

vorgelegt von

M.Sc. Hai Li

aus Shanxi, China

Berichterstatter:	Prof. Dr.–Ing. C. Tropea
1. Mitberichterstatter:	Prof. Dr.–Ing. B. Weigand
2. Mitberichterstatter:	PD. Dr. habil. I. V. Roisman
Tag der Einreichung:	04.06.2013
Tag der mündlichen Prüfung:	11.07.2013

Darmstadt 2013
D17

Drop Impact on Dry Surfaces with Phase Change

Bitte zitieren Sie dieses Dokument als:
URN: urn:nbn:de:tuda-tuprints-35507
URL: http://tuprints.ulb.tu-darmstadt.de/id/eprint/3550

Hiermit versichere ich, die vorliegende Doktorarbeit unter der Betreuung von Prof. Dr.-Ing. C. Tropea und PD. Dr. habil. I. V. Roisman nur mit den angegebenen Hilfsmitteln selbständig angefertigt zu haben.

Darmstadt, den 04. Jun. 2011,

Acknowledgements

The research work at hand has been carried out at the Institute of Fluid Mechanics and Aerodynamics (SLA, Fachgebiet Strömungslehre und Aerodynamik, Technische Universität Darmstadt) from Sep. 2008 to July 2013.

I would like to thank my advisors Prof. Dr.-Ing. C. Tropea and PD Dr. Ilia Roisman for the opportunity of my doctoral study. Their invaluable guidance on experiment techniques and theoretical analyses played an indispensable role on conducting successful research. Furthermore, their lectures “Technische Strömungslehre” and “Fluid Mechanics in Emerging Technologies” were very enlightening.

I am grateful for Dr. Marschall (SLA, TU Darmstadt) for his lecture “Höhere Strömungslehre und Dimensionsanalyse” and numerous discussions on theoretical fluid mechanics, Prof. Dr.-Ing. P. Stephan (TTD, Fachgebiet Technische Thermodynamik, TU Darmstadt) for his lectures “Technische Thermodynamik I&II”, “Wärme- und Stoffübertragung”, and “Höhere Wärmeübertragung”, Prof. Dr. Bernd Jähne (HCI, Heidelberg Collaboratory for Image Processing, Universität Heidelberg) for his lectures “Modern Image Sensors” and “Computational Imaging”. These lectures improved my knowledge in these fields.

I would like to thank Prof. Sanjeev Chandra (University of Toronto, Canada), Prof. Marco Marengo (University of Bergamo, Italy), Prof. Alidad Amirfazli (York University, Canada), Prof. Dr.-Ing. B. Weigand (ITLR, Institut für Thermodynamik der Luft- und Raumfahrt, Universität Stuttgart) Dr.-Ing. Norbert Roth (ITLR, Universität Stuttgart), and Prof. Steve Garoff (Carnegie Mellon University, the U.S.A.) for fruitful discussions.

I appreciate my senior colleagues, Dr. Nils van Hinsberg, Dr. Bruno Frackowiak, Dr. Feng Xu, Dr. Belal Zeitone, M.Sc. Andreas Lembach for their friendly and patient help at the beginning of my study. My colleagues, Dr.-Ing. Klaus Hufnagel, Dr. Gisa John (Gisa Kadavelil), Dr. Walter Schäfer, Dipl.-Ing. Lars Opfer, Dipl.-Wirt.-Ing. Ilja Buchmüller, Dipl.-Wirt.-Ing. Christina Weickgenannt, Dipl.-Ing. Chi-Yao Chang, M.Sc. Haitao Yu have been helpful with inspiring discussions on experimental techniques and theoretical analyses.

Externally, Dr.phil.nat. Wolfgang Müller (TEMF, Institut Theorie Elektromagnetischer Felder, TU Darmstadt), Dr. Fei Yang (IWAR, Fachgebiet Abwassertechnik, TU Darmstadt), Dr.-Ing. Jens Bauer (SDY, Fachgebiet Strukturdynamik, TU Darmstadt), M.Sc. Ram Dayal (TTD, TU Darmstadt), Dipl.-Ing. Victor Weber (RSM, Fachgebiet Reaktive Strömungslehre und Messtechnik, TU Darmstadt), Dipl.-Ing. Stefan Bareiss (RSM, TU Darmstadt), Dipl.-Phys. Leila Nagel (Institut für Umweltphysik, Universität Heidelberg), Dipl.-Phys. Wolfgang Mischler (HCI, Universität Heidelberg), M.Eng. Jia Tian (PTW, Institut für Produktionsmanagement, Technologie und Werkzeugmaschinen, TU Darmstadt) have assisted me with equipment and valuable expertise on various topics.

A special thanks must be extended to Mrs. Ilona Kaufhold and Mr. Martin Weiß and their wonderful teams, who have been always supportive on construction and manufacture of laboratory components. Besides, Mr. Mirko Feick (PTW, TU Darmstadt), Mr. Walter Nolde (VKM, Institut für Verbrennungskraftmaschinen und Fahrzeugantriebe, TU Darmstadt) and their teams have been helpful. Mr. Horst Nothnagel (AK Busch, TU Darmstadt) helped with the liquid nitrogen. Dr.-Ing. Rolf Boelcke, Dipl.-Ing. Fred Becker and their team in EWM (Elektronikwerkstatt Maschinenbau, TU Darmstadt), and Dipl.-Ing. Christoph Halscheidt (VKM, TU Darmstadt) have been of great help on the electronics.

I would like to give a special thanks to our secretarial team: Birgit Neuthe, Petra Fuhrmann, Heike Kagerbauer, Silke Wallner, who have helped on administration issues, and especially Stephanie Lath who has helped on numerous financial issues. I appreciate our IT team: Kathleen Feustel, Denis Schinko, Micheal Kron, and Marcus Keiner, who have maintained the computer and internet system always in a perfect state.

I appreciate the assistance from my four Bachelor students: Helge Eichhorn, Katrin Heinbücher, Erik Wagenknecht, Oliver Bartella, two ADP (Advanced Design Project) teams: Jan Breitenbach, Christoph Buchenhorst, Samim Doost, and Hannah Kittel in one team, and Chris Ascher, Sebstian Gatzka, Carina Klostermann, and Patrick Stegmann in the other team, four exchange students from the U.S.A.: Jennifer Batryn (California Polytechnic State University, RISE program), Christopher Guichet (University of California, Berkeley, IREP program), Narayanon Kidambi (University of California, Berkeley, IREP program) and Mackenzie Miller (University of Colorado at Boulder, IREP program), Hiwi Students Martin Gebbers, Torben Schfäfer, Ruochen Yang, Gong Wang for their CAD work, and Jan Breitenbach for producing the CAD photos.

I thank all my colleagues for the warmhearted office atmosphere, and all my friends both in Germany and in China for their valuable support.

I appreciate the 4-year scholarship from China Scholarship Council. The experimental work was financially supported by EU project EXTICE (FP7-AAT-2007-RTD-1) and DFG project SFB - TRR 75.

Abstract

Airframe icing caused by the Supercooled Large Droplet (SLD) has been identified as a severe hazard of aviation. The impact of SLD in the in-flight icing condition remains unknown in multiple aspects. The impact velocity is very high, and most of the drop impacts are oblique. The accompanying drop splash invalidates the current engineering tools for design of the anti-icing system. Furthermore the involvement of supercooling in drop impact demands exploration. In the framework of the EU Project EXTICE and DFG project SFB - TRR 75, this thesis contributes to understanding of the impact of SLD by two experimental investigations, respectively on the effect of supercooling on drop impacts and the drop splash after high-speed impact.

In the first experiment supercooled drops were created, and the drop impact with phase change was observed by both shadowgraph imaging and infrared imaging. The dynamic spreading diameter of the drop impact on aluminum surfaces was measured. Together with an analytical approach it was found that the phase change was negligible for drop impacts in typical icing conditions. The impact of supercooled drops on superhydrophobic surfaces revealed that the duration of the first stage of solidification in the drop impact was significantly shorter than that in a sessile liquid. Ice crystals formed in the supercooled water had a similar morphology to a snowflake. The drop receding on the hydrophobic surface was influenced by the contact temperature, which was measured by the infrared imaging. At low contact temperatures, asymmetrical receding was observed.

In the second experiment high speed impacts of single drops with diameters ranging from 130 μm to 200 μm on dry surfaces of rapid motion were recorded by shadowgraph imaging up to 1 Mfps. The target velocity varied from 10m/s to 63m/s. The impact surface had an inclination ranging from 0° to 75° in order to investigate the effects of oblique impact. Six outcomes of drop impact were identified: deposition, prompt splash, corona-corona splash, corona-prompt splash, single-side splash and the aerodynamic breakup. The aerodynamic breakup on a horizontal target was an interaction between the spreading lamella and the gas boundary layer. A qualitative force analysis made on the spreading lamella pointed out that in a corona splash the stabilizing factor is surface tension, and the destabilizing factors are aerodynamic force and inertial force. The lamella thickness and critical spreading velocity correlate with each other in a complementary manner, leading

to non-monotonic threshold impact velocities at different impact angles. The velocity of the splashing jets and the asymmetric spreading radii were measured from video. The mass-loss coefficient was measured for the drop impact on horizontal targets.

Kurzfassung

Die Flugzeugvereisung, die durch das Auftreffen großer unterkühlter Tropfen (Supercooled Large Droplets, SLD) verursacht wird, ist eine große Gefahr für die Flugsicherheit. Das Erscheinungsbild nach dem Aufprall unterkühlter Tropfen hängt von vielen verschiedenen Faktoren ab, deren Einfluss jedoch noch nicht hinreichend bekannt ist. Die Tropfen treffen mit einer hohen Geschwindigkeit sowie unter einem Winkel relativ zur Oberfläche auf. Das begleitende Phänomen des Tropfensplash schränkt die gängigen numerischen Modelle zur Vorhersage des entstehenden Eisprofils stark ein. Zudem beeinflusst der Grad der Unterkühlung der autreffenden Tropfen ebenfalls die Eisbildung. In dem Rahmen des EU Projektes EXTICE und des DFG Projektes SFB - TRR 75, befasst sich diese Doktorarbeit zum einen mit der experimentellen Untersuchung des Einflusses der Unterkühlung auf dem Tropfenaufprall, zum anderen wird der schräge Tropfenaufprall mit hohen Geschwindigkeiten untersucht.

In dem ersten Experiment wurde der unterkühlte Tropfen erzeugt. Der Tropfenaufprall mit Phasenwechsel wurde mittels Schattenbild- und Infrarotaufnahme beobachtet. Der dynamische Ausbereitungsdurchmesser vom Tropfenaufprall auf eine Aluminiumoberflächen wurde gemessen. Zusammen mit einer analytischen Untersuchung wurde festgestellt, dass der Phasenwechsel beim Tropfenaufprall für die typische Flugzeugvereisung vernachlässigbar war. Der Aufprall unterkühlter Tropfen auf hydrophobe Oberflächen wies darauf hin, dass die erste Stufe der Vereisung hierbei eine wesentlich kürzere Dauer als in einer ruhrenden Flüssigkeit hatte. Die entstandenen Eiskristalle hatten eine ähnliche Form wie Schneeflocken. Der Tropfenrückprall von hydrophoben Oberflächen wurde durch die Kontakttemperatur beeinflusst. Die Kontakttemperatur wurde durch die Infrarotaufnahme gemessen. Bei niedrigen Kontakttemperaturen wurde ein asymmetrischer Tropfenrückprall beobachtet.

In dem zweiten Experiment wurde der Hochgeschwindigkeitsaufprall von einzelnen Tropfen auf ein trockenes und sich schnell bewegendes Ziel durch Schattenbildaufnahme mit einer Auflösung bis zu 1 Mfps aufgenommen. Die Tropfengröße betrug 130μm bis 200μm, die Zielgeschwindigkeit zwischen 10m/s und 63m/s. Das Ziel war zwischen 0° und 75° geneigt, um schräge Aufpralle untersuchen zu können. Sechs Verhaltensformen des Tropfens nach dem Aufprall wurden identifiziert: Ausbreitung, Prompt Splash, Corona-corona Splash, Corona-prompt

Splash, einseitiger Splash sowie der aerodynamisch bedingte Zerfall. Der aerodynamische Zerfall, der nur beim Tropfenaufprall auf ein horizontales Ziel beobachtet wurde, war das Resultat einer Interaktion zwischen der sich ausbreitenden Lamelle und der Luftgrenzschicht über dem Ziel. Eine qualitative Kraftfeldanalyse auf der sich ausbreitenden Lamelle wies darauf hin, dass in dem Corona Splash die Oberflächenspannung der stabilisierende Faktor ist und die aerodynamische Kraft sowie die Trägheitskraft sich destabilisierend auswirken. Die Lamellendicke und die kritische Ausbreitungsgeschwindigkeit korrelieren miteinander in einer ergänzenden Weise. Dies führte bei unterschiedlichen Aufprallwinkeln zu abweichenden Grenzgeschwindigkeiten, für die Splash auftrat. Die Geschwindigkeit des Splash-Flüssigkeitsstrahls und die dynamischen Ausbreitungsradien wurden den Aufnahmen entnommen. Der Massenverlust wurde für die Aufpralle auf horizontale Ziele gemessen.

Contents

Nomenclature

Latin capitals		Unit
A	area	m^2
B	local variable	—
Bi	Biot number	—
C	capacitance	F
C_{12}	coefficient in thermal radiation	$\mathrm{J\,s^{-1}\,m^{-2}\,K^{-4}}$
C_S	coefficient in thermal radiation	$\mathrm{J\,s^{-1}\,m^{-2}\,K^{-4}}$
E	electrical field	$\mathrm{V\,m^{-1}}$
F	force	N
Fo	Fourier number	—
Fr	Froude number	—
ΔG	free-energy barrier	—
H	height	m
I_e	radiant intensity	W/sr
K	a compound parameter for the splash threshold	—
L	Latent heat	J/kg
L_e	radiance	$\mathrm{W\,sr^{-1}\,m^{-2}}$
$L_{e\lambda}$	spectral radiance	$\mathrm{W\,sr^{-1}\,m^{-3}}$
La	Laplace number	—
M	relative molecular mass	—
M_e	radiant emittance	$\mathrm{W/m^2}$
N	count number	—
Nu	Nusselt number	—
P_{ec}	Peclet number	—
P_{LMK}	dimensionless parameter	—
Pr	Prandtl number	—
Q	energy	J

Q_e	charge	C
R	radius	m
R_z	surface roughness	m
Re	Reynolds number	—
R_m	reflection coefficient of unpolarized light	—
R_s	reflection coefficient of s-polarized light	—
R_p	reflection coefficient of p-polarized light	—
S	area of emitter	m^2
St	Stefan number	—
T	temperature	°C
U	voltage	V
V	volume	m^3
We	Weber number	—
X	location of the solid/liquid interface	m
$\mathscr{T}$	transmittance	—

Latin lower-case letters		**Unit**
a	speed of sound	m/s
b	Wien's displacement constant	$\mu\mathrm{m\,K}$
c	specific heat	$\mathrm{J\,kg^{-1}K^{-1}}$
c_0	speed of light	m/s
c_d	drag coefficient	—
d	diameter	m
e	thermal effusivity	$\mathrm{W\,s^{1/2}\,K^{-1}\,m^{-2}}$
f	frequency	$\mathrm{s^{-1}}$
f_{aper}	f number of aperture	—
f_d	Darcy friction factor	—
g	gravity acceleration of Earth	$\mathrm{m\,s^{-2}}$
h	Planck constant	J s
h_{conv}	heat transfer coefficient	$\mathrm{W\,m^{-2}\,K^{-1}}$
k	thermal conductivity	$\mathrm{W\,m^{-1}\,K^{-1}}$

k	angular wavenumber	$\mathrm{rad\,m^{-1}}$
$k_{Rayleigh}$	dimensionless wavenumber in Rayleigh instability	$\mathrm{rad\,m^{-1}}$
k_B	Boltzmann constant	J/K
l	characteristic length	m
m	mass	kg
mag	magnification	–
n	refractive index	–
$\tilde{n}$	complex index of refraction	–
$\vec{n}$	normal vector	–
p	pressure	Pa
q	energy density	$\mathrm{J\,m^{-2}}$
r	radial distance	m
s	length in curvilinear coordinate system	m
t	time	s
v	velocity	m/s
x	horizontal distance in 2D Cartesian coordinate system	m
y	vertical distance in 2D Cartesian coordinate system	m
z	depth	m

Greek capitals		**Unit**
Γ	capillary constant	°C
Δ	difference	–
Θ	dimensionless temperature	–
Ψ	mass-loss coefficient	–
Ω	solid angle	sr
Φ_e	radiant flux	W

Greek lower-case letters		**Unit**
α	thermal diffusivity	$\mathrm{m^2/s}$
β	attenuation coefficient	$\mathrm{m^{-1}}$

γ	adiabatic constant	–
ε	emissivity	–
ε_0	vacuum permittivity	F/m
ε_r	relative permittivity	–
ζ	penetration length	m
η	dynamic viscosity	mPa s
θ	angle	degree
κ	curvature	1/m
κ_{ex}	extinction coefficient	–
λ	wavelength	m
λ_{ms}	typical length in Mullings-Sekerka instability	m
λ_{St}	parameter in the Stefan problem	–
ν	kinematic viscosity	$\mathrm{m^2\,s}$
$\tilde{\nu}$	wave number	$\mathrm{m^{-1}}$
ξ	similarity variable	$\mathrm{m^2/s}$
ρ	density	$\mathrm{kg\,m^{-3}}$
σ	surface tension	mN/m
σ_{StB}	Stefan-Boltzmann constant	$\mathrm{W\,m^{-2}\,K^{-4}}$
τ	time constant	–
ϕ	diameter	–
χ	dimensionless distance	–

Indices

0	primary
A	initial condition
alu	aluminum
B	boundary condition
Br	Brewster
c	charging
$crit$	critical
d	drag

F	interface
G	Gas
ge	germanium
i	incident
K	contact temperature
L	liquid
lam	laminar
m	melt
max	maximum
min	minimum
n	normal component
opt	optimum
r	reflection
rec	receding
S	solid
s	secondary droplets
sp	spreading
SCL	supercooled liquid
t	transmission or tangent component
tip	ice dendrite tip
$turb$	turbulent
x	horizontal direction in 2D Cartesian coordinate system
y	vertical direction in 2D Cartesian coordinate system
∞	ambient, far field
$*$	dimensionless

Abbreviations

CoC	Circle of Confusion
CTT	Cloud Top Temperature
FOV	Field of View
LWC	Liquid Water Content
LWIR	Long-Wavelength Infrared

MCT	Mercury Cadmium Telluride
MVD	Mean Volume Diameter
MWIR	Mid-Wavelength Infrared
ODE	Ordinary Differential Equation
PCM	Phase Change Material
PDE	Partial Differential Equation
SHS	Superhydrophobic Surface
SLD	Supercooled Large Droplets
SSR	solid-state relay
WCE	Water Collection Efficiency

1 Introduction

1.1 Motivation

Aircraft icing presents a serious hazard for flight at subsonic speeds in conditions of visible moisture and temperatures below freezing. Ice accretion on wing surfaces modifies the profile of an airfoil, increasing drag while decreasing the lift. Icing on ailerons can affect the roll control, and ice accumulation on the horizontal stabilizers might cause tail stall. Ice can also cause engine stoppage by either icing up the carburetor or, in the case of a fuel-injected engine, blocking the engine's air source [141].

Many aircraft have been lost owing to ice accumulation, for example some 20 accidents where icing was a contributing factor is summarized by Valarezo in 1993 [149]. The protection of aircraft from the adverse effects of ice accretion has been a crucial design problem since the very early years of flight. The Federal Aviation Administration (FAA) requires an airplane manufacturer to demonstrate that its aircraft can fly safely in icing conditions as defined by the so-called icing envelopes in the FAA's Federal Airworthiness Regulations (FAR) Part 25, Appendix C [1].

However more recent accidents, especially the one in 1994 reported by the National Transportation Safety Board Aviation Accident Report [82, 120], have highlighted the existence of icing cloud characteristics beyond the actual certification envelope of the Appendix C, which accounts for an icing envelope characterized by water droplet diameters up to $50\,\mu$m (so called cloud droplet). Multiple meteorological investigations documented the existence of the Supercooled Large Droplets (SLD) in the range of $100\,\mu$m to $400\,\mu$m.

International airworthiness authorities, the FAA, Transport Canada (TC), and the European Aviation Safety Agency (EASA) are intending to jointly develop and issue updated regulations for certification in SLD environments based on investigations of consultative expert panels coming from research establishments, industry and national aviation regulatory bodies: the "Appendix X" [84]. If implemented, the proposed new rules will require aircraft manufacturers to demonstrate that their product can safely operate in SLD environments. To do so, they will be requested to demonstrate that specific capabilities comply with the new regulation.

Demonstration of the anti-icing capability is conducted by both experimental and numerical engineering tools. In the 1940s and 1950s, significant experimental and flight test programmes laid the foundation for protection systems, the concepts of which are still in widespread use today. Since the advent of the computer age, significant progress in theoretical, and more prominently, numerical studies of aircraft ice accretion was achieved in the late 1970s. The most influential aircraft-icing software are LEWICE from NASA John H. Glenn Research Center in the United States, TRAJICE2 from the Defence Evaluation and Research Agency (DERA) (previously the Royal Aerospace Establishment (RAE)) in the UK, CANICE from Bombardier Aeronautical Chair of Ecole Polytechnique de Montreal, FENSAP-ICE developed by Newmerical Technologies INT. in Montreal, Canada, and the icing codes developed in the French research establishment, Office National d'Etudes et de Recherches Aérospatiales (ONERA) in Paris. The numerical methods have transformed the certification of aircraft for flight in icing from an almost total reliance on rig and flight test, to design by numerical simulations for new aircraft, with verification by rig and flight test.

The conventional approach to aircraft-icing analysis begins with the determination of where and at what rate cloud water droplets impact the wing surface. This requires a droplet trajectory analysis and the evaluation of the proportion of the free stream water concentration which impacts on the structure, referred to as the water collection efficiency (WCE) distribution [42]. Once the WCE distribution is known, the analysis can proceed to determine how much and the location at which the impinging water will freeze. When this is known, the profile of the ice may be determined with thermodynamic analyses on the freezing process.

This approach implies that the cloud droplets deposit on the wing surface upon impact. However the involvement of SLD introduces new phenomena such as drop deformation, aerodynamic breakup before impact, and most influentially splash or rebound upon impact, as well as the re-impingement of secondary droplets. The drop splash, which creates a loss of total impinging mass, is identified as the most influential factor [164], because it directly alters the WCE, and further harms the prediction of the ice shape. A splash model, which accommodates the total mass, the average diameter and the velocities of the secondary droplets, is desired for incorporation into the icing software.

The current splash models are based on an idea of calibration. One model which was developed for a dense spray condition [146] was taken as the basis, and proper coefficients were found out by comparing with the experimental data of the WCE. CANICE [126], DROP3D [55, 56], a subsidiary software of FENSAP-ICE, demonstrated this possibility. However, this method restricts its application to the calibration cases. Extrapolation of these models to other conditions leads to inaccurate prediction. The splash model of LEWICE was tested with an extensive database of the WCE acquired experimentally in the Icing Research Tunnel (IRT) over the last twenty years. It was found out that both the maximum WCE and the impingement limits were inaccurately predicted [162, 163]. None of the current numerical engineering tools functions reliably in the SLD condition.

In order to improve the capability of the icing software in the SLD condition, the National Aeronautics and Space Administration (NASA) and FAA in the United States, and the Civil Aviation Authority in the UK has proposed a roadmap to develop SLD engineering tools for the design and the certification of aircraft in SLD conditions in 2003 [19, 88]. The roadmap contained quantitative characterization of the SLD icing environment (including the icing temperature, the drop size and so on), instrumentation (measurement of these microphysical characteristics of the cloud droplets), test methods (including visualization, ice shape documentation techniques, scaling techniques and spray systems), facilities (such as updated icing wind tunnel to simulate the SLD icing cloud), and ultimately the improvement of the icing codes including analytical models which physically describe the effects of the SLD. Validation exercises were expected to follow.

From Jun. 2008 to May 2012, a European project named EXTICE was conducted by 14 institutions in order to enhance the existing simulation tools in the SLD condition [91]. This project contains four technical work packages: development of new splash models by basic experiments on SLD, verification of the splash models by current icing software, icing tunnel tests involving SLD, and real-flight tests. The proposed semi-empirical splash models improved partially the ice shape simulation at low Mach numbers, but were less reliable at high Mach numbers.

The on-going DFG project SFB - TRR 75 includes two sub-projects relating to the freezing of SLD [159]. In the TP-B1 project tiny water droplets were levitated by special laser instruments. The freezing and evaporation of the drop is investigated. In the TP-C3 project, numerical investigation of nucleation of supercooled water has been conducted. The first results demonstrate that the applied numerical methods are capable of predicting the ice dendrite growth at low supercooling, where the nucleation process was purely driven by thermal diffusion. These preliminary results are not yet thorough enough for the improvement of icing software.

To sum up, the hazard created by the SLD was recognized and technical efforts on both the splash modeling and the numerical simulation were initiated in the past decade. However, no reliable splash model was developed. The SLD splash remains one of the most active subjects in the field of aircraft icing. Taking into account the expected air traffic growth in the coming decades, it is essential to reduce the rate of occurrence of ice-related incidents in order to maintain public confidence in air transport.

1.2 Structure of the Thesis

The goal of this study is to improve the understanding on drop splash in the SLD condition. The impact of supercooled drops in an aircraft icing event has several specialties. The single drop impact is a frequent occurrence in the in-flight icing condition. The drops have a particular diameter ranging from $100\,\mu$m to $400\,\mu$m, and the impact speed is very high, of the order of 100m/s. Furthermore, the droplets are supercooled, i.e. below $0\,^{\circ}$C, but still liquid.

Complete realization of all the impact conditions in the laboratory is very challenging and might not be necessary. Two experiments were conducted. The first experiment was to examine the influence of supercooling on the hydrodynamics of the drop impact process. If the influence is negligible, the high-speed impact can be conducted at room temperatures. The second experiment is single drop impact on dry surfaces of various inclinations with high impact speeds, experimentally investigating oblique drop splash.

Following this introduction, Chapter 2 delivers a literature review on the involved three topics. The first is the characteristics of the SLD condition. The findings of meteorological investigations conducted in the past 20 years was summarized in order to find out the MVD distribution, typical values of the LWC, the most frequent icing temperatures, and the distribution of icing cloud. This information defines the impact conditions which are expected to be realized in the experiments, such as the drop diameter, the impact velocity, the impact angle and the properties of the impact surface (i.e. dry or wet). The second part is related to drop impact on dry surfaces. Semi-empirical correlations on the splash threshold was summarized, and the state-of-art understanding of the physics of splash is reviewed. Current experimental results on the oblique impact, and the high-speed impact are introduced. The third part is devoted to the solidification process, including the classical Stefan problem, which are frequently used in the rest chapters for analyses, and the experimental and theoretical investigations on the nucleation and the first stage of solidification, which were specific to the supercooling. This chapter serves as a starting point of the analysis in the subsequent chapters.

The following four chapters are divided into two parts, respectively describing the two experiments. Part I, including Chapter 3 and 4, describes the experiment on the impact of supercooled water drops. Chapter 3 introduces the experimental setup. In order to acquire supercooled drops of millimeter sizes, a supercooling passage was cooled down to −196 °C with liquid nitrogen, so that a 1.5 mm drop could obtain −5 °C after a falling distance of 600 mm. A pneumatic drop generator was constructed for drop-on-demand generation of single drops. Both high-speed shadowgraph imaging at a frame rate of 20 kHz and high-speed infrared imaging at a frame rate of 718 Hz was applied for the observation. Two impact surfaces were applied: a polished aluminum surface, and a super hydrophobic surface (SHS). The experimental results are introduced in Chapter 4. The morphology of the drop impact examined the influence of solidification on the hydrodynamics of drop impact. Drop impact on SHSs documented the nucleation and ice dendrite formation during the drop impact. The infrared imaging measured the contact temperature between the deposited lamella and the substrate.

Part II, including Chapter 5 and 6, is devoted to the second experiment: the high-speed impact of single drops on dry surfaces. Chapter 5 describes the experimental setup, which was composed of a drop generator, a rotating target system, an imaging system, and a trigger system. The drop generator was the vibrating orifice drop generator. A custom made electrostatic deflector was employed to reduce the density of the drop train in order to achieve the single drop impact. The performance of the drop generator and drop deflector were systematically studied. The imaging was conducted with a frame rate up to 1 MHz, but a limited pixel resolution of 312 × 260. Greater depth of field was achieved by reducing the aperture. The illumination solution was a strong flash. The trigger system was briefly introduced, followed by an overview of the experimental setup. High impact Reynolds number (Re) and Weber number (We) were achieved. Chapter 6 delivers the experimental results on the measurement of the splash threshold, velocity of the liquid jets, the dynamic spreading radii of asymmetry, and the mass of the secondary droplets in a special case: the drop impact on a horizontally moving plate. The interaction of the drop impact with the gas boundary layer was documented in this case.

The findings of the two experimental investigations are summarized briefly in Chapter 7. An outlook on the future work of the splash modeling is given in this chapter.

2 Background

This chapter provides the background knowledge of the topics addressed in the dissertation. Section 2.1 introduces the investigation on Supercooled Large Droplets (SLD) in the field of aircraft icing, including the meteorological investigation of icing cloud characteristics, icing wind tunnel tests with the involvement of SLD, and the empirical modeling of drop splash, whose limited capability has been evidenced by various icing software. This section points out the necessity of basic research work on the single drop impact.

The second section offers a review of the experimental and theoretical investigations on the single drop impact on dry surfaces. Splash thresholds and the up-to-date understanding of the underlying mechanism is introduced. This dissertation underlines the importance of the microphysics of the drop impact process and tries to further deepen this knowledge.

The third section is devoted to phase change, because solidification is involved in SLD impact. The classical Stefan problem and its application in supercooled condition is presented; Mullins-Serkeka instability and ice dendrite formation, as well as the growth rate of the dendritic structure are briefly summarized in this section.

2.1 Supercooled Large Droplets in Aircraft Icing

Airframe icing is a topic of vital importance in aviation industry because it is mainly concerned with the safe and efficient operation of aircraft under all weather conditions. Over the last 15 years the role of SLD in aircraft icing has received increasing attention. More recent meteorological investigations on icing weather have highlighted the existence of icing cloud characteristics beyond the actual certification envelope defined by the 14 CFR Part 25 Appendix C: Atmospheric Icing Conditions for Aircraft Certification, which accounts for an icing envelope characterized by water droplet diameters up to $50\,\mu$m.

2.1.1 Definition of the SLD Icing Environment

In-situ measurements of the aircraft icing environment have been carried out in a number of meteorological projects, as summarized below. Parameters describing

SLD icing conditions have been defined from these investigations for a revision of Appendix C, and the requirement definition of basic SLD experiments.

1. Balloon-borne Soundings, undertaken by National Climatic Data Center (NCDC, USA) from 1977 to 1990 in North America [15].
2. EURICE, undertaken by European Commission from 1994 to 1998 in France, UK and Germany [5, 49].
3. First Canadian Freezing Drizzle Experiment (CFDE I), undertaken by Meteorological Service of Canada (MSC) in Mar. 1995 in North Atlantic Ocean [32,33].
4. Supercooled Large Droplet Icing Flight Research, undertaken by NASA, FAA and National Center for Atmospheric Research (NCAR, USA) in Winter 1996-1997 in Great Lakes region [87].
5. Third Canadian Freezing Drizzle Experiment (CFDE III), undertaken by MSC from Dec. 1997 to Feb. 1998 in southern Ontario, southern Quebec, Lake Ontario and Lake Erie [32, 33].
6. Freezing Rain as an In-Flight Icing Hazard, undertaken by NASA-Lewis Research Center in Winter 1997-1998 in Great Lakes region [16].
7. First ISCCP Regional Experiment Arctic Cloud Experiment (FIRE.ACE), undertaken by MSC in Apr. 1998 in Northwest Territories of Canada [30].
8. Mt. Washington Icing Sensors Project (MWISP), undertaken by NASA and FAA in Apr. 1999 in Mt. Washington [125].
9. First Alliance Icing Research Study (AIRS I), undertaken by MSC, NASA John H. Glenn Research Center, National Research Council (NRC, Canada), FAA and Transport Canada (TC) from Dec. 1999 to Feb. 2000 in Mirabel Quebec [31, 61].
10. Second Alliance Icing Research Study (AIRS II), undertaken by MSC and NASA from Nov. 2003 to Feb. 2004 in Montreal, Ontario and Quebec [31, 61].

Mean Volume Diameter (MVD)

The SLD environment is defined to be any icing environment which includes drops larger than $50\,\mu$m, a commonly used size threshold for the definition of SLD. Two typical icing weather involving SLD are freezing drizzle with droplets of $200\,\mu$m to $500\,\mu$m and freezing rain with droplets larger than $500\,\mu$m. According to the measurements during CFDE I and III [33], which were based on the average 30 second measurements and included only the cases with SLD, the largest MVD was $404\,\mu$m and the largest droplet diameter detected was $2000\,\mu$m; approximately 39% of the droplet spectra contained SLD was greater than $50\,\mu$m in diameter, and 8% had MVD $> 40\,\mu$m [32]. Table 2.1 emphasizes the freezing drizzle and freezing rain. Apparently, both freezing drizzle and freezing rain are likely to contain SLD although the MVD for freezing drizzle is often below $40\,\mu$m. It can be concluded that SLD has a wide diameter range from $50\,\mu$m to $2000\,\mu$m, and appears most frequently in freezing drizzle and freezing rain.

SLD icing environment	MVD	d_{max}	Data points
freezing drizzle (ZLE)	$<40\,\mu$m	100-500μm	1469
freezing drizzle (ZLE)	$>40\,\mu$m	100-500μm	335
freezing rain (ZRE)	$< 40\,\mu$m	$> 500\,\mu$m	193
freezing rain (ZRE)	$> 40\,\mu$m	$> 500\,\mu$m	447

Table 2.1.: MVD of Freezing Rain and Freezing Drizzle reported by Cober et al. [30].

Liquid Water Content (LWC)

The LWC is the mass of water contained per cubic meter of air. The LWC measured in CFDE I and III [32, 33], AIRS [87] and MWISP [125] campaigns shared the same bimodal distribution with a peak at $10\,\mu$m to $30\,\mu$m and a secondary peak at about $100\,\mu$m to $400\,\mu$m. During the CFDE flights [33, 60] a LWC of $0.7\,\mathrm{g\,m^{-3}}$ was detected to be the 99.9th-percentile value for small droplets, while for cases in which droplets greater than $50\,\mu$m in diameter this parameter was $0.2\,\mathrm{g\,m^{-3}}$. This observation is confirmed by AIRS [31] that, 99% LWC for small droplets was $0.45\,\mathrm{g\,m^{-3}}$, for SLD it was $0.16\,\mathrm{g\,m^{-3}}$. In MWISP [125] the bi-modal distribution had a mean LWC of $0.54\,\mathrm{g\,m^{-3}}$, with a minimum of $0.01\,\mathrm{g\,m^{-3}}$ and a maximum of $3.36\,\mathrm{g\,m^{-3}}$. Although the data from different projects did not fit each other perfectly, it can be concluded that there are two major size ranges of droplets in SLD icing environment, and the LWC of SLD is much lower than that of droplets smaller than $50\,\mu$m.

Icing Temperature

SLD icing occurs over a wide range of temperatures. Over a thirty years' period, Strapp et al. showed that all of the freezing precipitation occurred at temperatures warmer than $-10\,^{\circ}$C in St. John's, Newfoundland [143] . In CFDE I /III, the mean temperature detected was around $-3\,^{\circ}$C and the mean minimum temperature was normally higher than $-10\,^{\circ}$C [33]. SLD Flight Research Study found that the freezing rain had its average lowest temperature typically between $-4\,^{\circ}$C and

−9 °C and layers of freezing rain above −3 °C were rather common [16]. However, lower temperatures were reported for SLD as well. Freezing drizzle observed in AIRS had a relatively lower temperature, −8 °C to −10 °C [32] and icing with SLD was reported to mostly occur with Cloud Top Temperatures (CTT) between −16 °C and −8 °C [14]. Besides, in CFDE III and AIRS I there were two freezing drizzle occurrences recorded to be around −20 °C [70]. It is imaginable that SLD is more common at higher temperatures. As the temperature reduces, nucleation becomes easier especially for larger droplets. In fact the concentration of drops larger than $500\,\mu$m are substantially higher in the range 0 °C to −5 °C than at lower temperatures [32]. It can be generally concluded that higher temperatures above −10 °C favor the existence of large liquid droplets.

Distribution of Icing Cloud

Distribution of icing cloud refers mainly to icing weather forecast. Climatology of SLD was created using 14 years of coincident, 12-hourly US and Canadian surface weather reports and balloon-borne soundings in NCAR [15]. SLD found in North America appeared to occur below 3660 m in altitude, icing cloud was less than 900 m deep and was mainly formed via non-classical mechanism. These statistics are helpful to give a general concept of SLD icing clouds. However it is imaginable that in the case of fast changing weather the dimensions of icing cloud can vary significantly and these estimations are therefore not universal [70]. In all three cases of AIRS II, the horizontal and vertical scale of icing regions differed extensively [79]. In one case, while mixed phase was sampled near the cloud top, the aircraft entered into a liquid layer with a lower altitude. The vertical dimension measured varied from 500 m below the cloud top to more than 2000 m. Differences between maritime and continental conditions were also discerned [60]. It was thus suggested, the best way to avoid natural icing hazards was to have accurate forecasts, to know what conditions lead to natural icing, and to keep away from them [154].

Forecast of icing weather takes advantage of remote sensing platforms, including ground-based, airborne, and space-based systems. They are based on the sensing of electromagnetic radiation emitted or reflected from atmospheric gaseous, liquid and ice media. By knowing how the radiation interacts with these media, specifically water drops and ice particles, the sensed radiation can be correctly translated into parameters related to the icing hazard [111]. Up until now, identifying icing in mixed clouds only from the radar polarimetric measurements is rather difficult if ice crystals exist, because the ice particle’s reflectivity is dependent on the 6th power of its diameter (Rayleigh scattering) [61]. Currently, radars can only adequately measure icing clouds purely consisting of supercooled drops [79], and has a possibility of overestimation [129].

Summary

The MVD of SLD has a bimodal distribution, with two peaks of $10\,\mu$m to $30\,\mu$m and $100\,\mu$m to $400\,\mu$m. The 99% LWC of SLD icing cloud is $0.2\,\mathrm{g\,m^{-3}}$, much lower than that of small droplet, $0.7\,\mathrm{g\,m^{-3}}$. The temperature at which SLD clouds are created is most frequently higher than −10 °C. The possibility of occurrence of SLD clouds is generally lower than 2% among all icing cases, although a peak of 7% was reported. The occurrence and distribution of icing clouds is not regular, and the best way to be aware of its existence is more precise forecast. Normal relative velocity between cloud and aircraft is from 50m/s to 100m/s corresponding to ascent and descent phases, since the normal icing clouds are located at altitudes below 4000 m while the cruise height of an airliner is above 10 000 m.

2.1.2 Experimental Investigation on SLD Icing

The drop impact process in the in-flight icing is conventionally understood that a cloud droplet carried by the airflow approaches the aircraft and deposits on the solid surface upon impact. Depending on the temperature and drop size, the droplet can freeze directly upon impact or flows toward the aft surface, forming runback water, which freezes gradually along its path. Freezing upon impact induces rime ice, which has a more uniform shape and fragile structure, and is thus less dangerous. Freezing of the run back water leads to glaze ice with a complex shape, especially ice horns on the leading edge. Glaze ice severely alters the aerodynamic outline of the airfoil and is more dangerous than rime ice. The occurrence of glaze ice is significantly higher than rime ice because supercooled cloud droplets exist mostly at higher temperatures. For SLD icing condition, the glaze ice is dominant.

Significant efforts have been dedicated to the simulation of the ice shape in the past six decades. Accurate prediction of ice shape is crucial for the assessment of aerodynamic degradation of iced airfoils and consequently determines the design of anti-icing or de-icing system. In order to calculate the amount of ice that accretes on the airfoil, a thin layer of control volumes are placed adjacent to the wing (or iced) surface, as depicted in Figure 2.1. For each control volume there is impinging water, incoming water from the upstream control volume, outgoing water to the adjacent downstream control volume, evaporation and solidification. The accompanied heat fluxes include the enthalpy of the mass flows, latent heat released by evaporation and solidification, heat conduction, heat loss by the forced convection, as well as the sensible heat absorbed by supercooled water. The solution of the mass and energy balances provides the amount of accreted water for each control volume. This model is well-known as the Messinger's method, dated back to 1953 [85]. Despite some improvements, the basic principle has not changed in the past decades. It should be noted that the momentum conservation of the water transport on the solid surface is neglected, although the water motion is nominally represented by mass flow rate. The reason is that in most icing cases, the water layer is thin because of low LWC, and its velocity is rather small.

As the impinging drop increases in size, new phenomena are introduced: deformation, aerodynamic breakup before impact, splash or rebound upon impact and re-impingement of secondary droplets, as sketched in Figure 2.2. Papadakis et al. [145] visualized these phenomena in NASA Glenn Droplet Imaging Flow Tunnel (DrIFT), as illustrated in Figure 2.4. The water drop ranges between $40\,\mu$m and $370\,\mu$m and at a temperature of $-5\,^{\circ}$C. The impact velocity was up to 60.35m/s. The impact surfaces were a clean 304.8 mm-chord NACA23012 airfoil and an "iced" edition of it, with fabricated ice horns. This experiment was to access a bird's-eye view SLD impact on an airfoil, and thus the impact conditions, such as the impact speed, angle and the surface condition (wet or dry), were not precisely controlled. Although the image data were insufficient for developing models of the impact hydrodynamics, these observations point out that these phenomena do exist in SLD icing condition.

These phenomenological disparities from the conventional hypothesis of drop deposition must influence the prediction of the ice shape. One critical parameter in the ice shape prediction is the "Water Collection Efficiency" (WCE), which is defined as the ratio of impinging water flux per unit area on the wing surface and the free-stream water fluxes per unit area of the cross-section of airflow field. As depicted Figure 2.3 in a Lagrangian approach, this efficiency can be written as

$$WCE = \Delta y_0 / \Delta s. \tag{2.1}$$

The mass of local impinging water is expressed then as

$$m = LWC\, v_\infty\, WCE\, ds\, dt. \tag{2.2}$$

An accurate WCE distribution is a prerequisite of the ice shape computation. Phenomena brought by the SLD might harm the validity of WCE calculation of

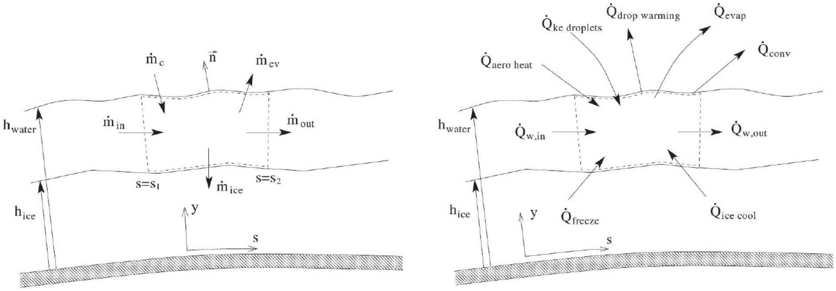

Figure 2.1.: Messinger's model: mass (left) and energy (right) balances of a control volume for ice accretion calculation [63].

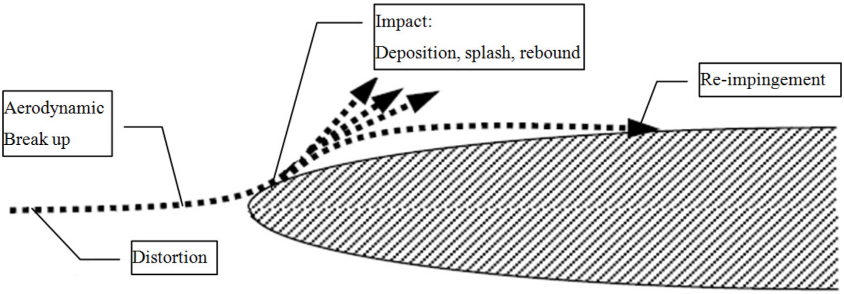

Figure 2.2.: Different behaviors of SLD.

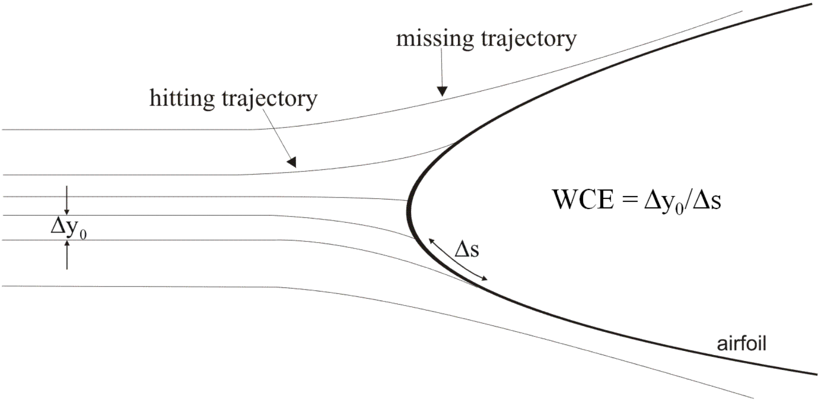

Figure 2.3.: Definition of the Water Collection Efficiency (WCE).

conventional methods. Papadakis et al. confirmed this expectation by measuring WCE experimentally in two separate investigations. The earlier one tested a water spray of 11 μm, 11.5 μm, 21 μm, 92 μm and 94 μm MVD on 8 airfoils and an s-duct engine inlet at the speed of 78m/s at 8.9 °C [104, 105]. The second one had MVD of 20 μm, 52 μm, 111 μm, 154 μm and 236 μm, tested with MS(1)-0317 airfoil, clean and iced NACA23012 airfoil of 0.91 m chord at 10 °C to 21 °C, at 78m/s [106, 107]. Results showed that LEWICE worked well with a clean airfoil and MVD of 20 μm, but for the large MVD, LEWICE produced higher WCEs and larger impingement limits than the experimental data, as presented by Figure 2.4. This discrepancy was attributed to the creation of secondary droplets upon splash. These tiny droplets sputtered away from the solid surface and were taken away by airflow.

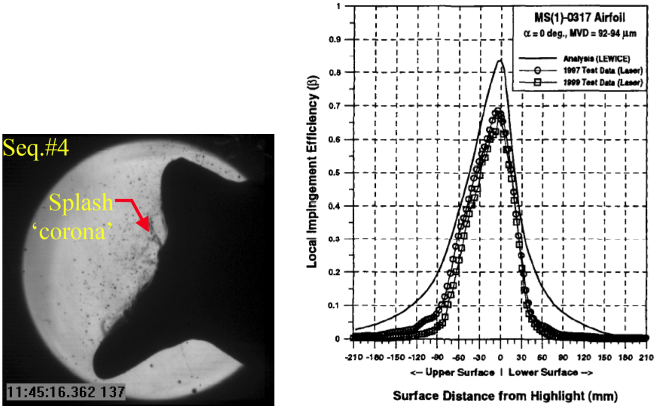

Figure 2.4.: SLD splash observed on an "iced" airfoil in an icing wind tunnel test of Papadakis et al. [145] (left), and its influence on WCE in a benchmark test of these authors [105].

This so called "mass-loss" effect was qualitatively confirmed in an icing wind tunnel test conducted by Potapczuk et al. in Icing Research Tunnel (IRT) in NASA Glenn Reseach Center [112]. NACA0012 airfoils with different chord lengths were exposed to experimentally simulated icing condition. The mass of accumulated ice was measured after icing of a certain period. The involved MVD ranged from 20 μm to 160 μm. The results indicated that as the droplet size increased, the mass of ice accumulation on the airfoil decreased.

Beside the amount of ice accretion, the ice shape was also influenced by SLD. Glaze ice has three typical ice morphologies: clear ice, horns and feathers, as pictured in Figure 2.5 and Figure 2.6. The clear ice region formed in the vicinity of the stagnation point and had a conformal surface. Horn structures formed downstream of the clear ice region. The feathers formed further downstream of the horns and extended to the impingement limit. The height of the individual feathers and the number of feathers diminished with distance from the leading edge, following the decreasing WCE. All the three features appeared in both conventional and SLD icing conditions. The difference lay in the structure of the feathers.

Figure 2.7 represents the feathers with MVD equal to $20\,\mu$m and $200\,\mu$m, respectively. The difference between them is the spacing of the feathers. Under the Appendix C conditions, the feathers were continuous, while under the SLD conditions, the feathers had bare wing surfaces between the feathers. The discrete distribution of feathers might result from rebounding of droplets at aft surfaces where the impact angle was quite small, or the re-impingement of secondary droplets generated by drop splash on the upper stream surfaces.

In conclusion, the appearance of SLD invalidates the current methodology of ice shape prediction by introducing new phenomena such as drop splash. The hydrodynamic behavior of the drop impact demands extra modeling.

2.1.3 State of Art Modeling of the SLD Impact

These various phenomena accompanied with SLD impact are not equally influential on the calculation of WCE. Numerical studies were conducted by Wright and Potapczuk to identify the most significant factors [164]. The deformation of droplets and consequent drag increase is important for the trajectory calculation of droplets. Droplet breakup before impact influences the diameter of the impacting droplets. These phenomena are notable but of a minor effect compared to drop splash. Splashing and rebounding induces the mass-loss and hence directly influences the determination of the WCE.

There are four semi-empirical models describing splash [126, 130, 131, 144, 162, 163]. The splash model is composed of five elements: the splash threshold, the mass-loss coefficient, and the number, size and velocity of the secondary droplets. The splash threshold serves as a switch. The splash model is activated only when this threshold is exceeded. The mass-loss coefficient modifies the water collection efficiency. The information on the secondary droplets provides the initial condition for the trajectory calculation of secondary droplets, which further leads to the prediction of re-impingement. The current models, although slightly different from each other, share the same concept of calibration. The splash model in DROP3D is taken as an example to elucidate the common feature [55, 56].

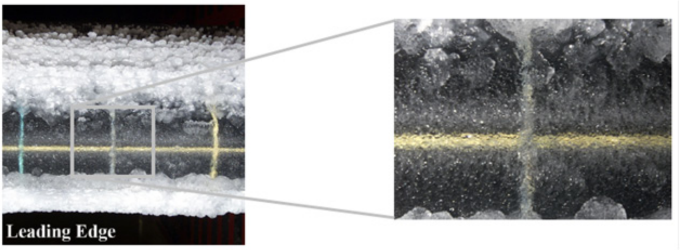

Figure 2.5.: Ice horn and clear ice formed at the leading edge in icing wind tunnel tests with SLD, imaged by Broren et al. [23].

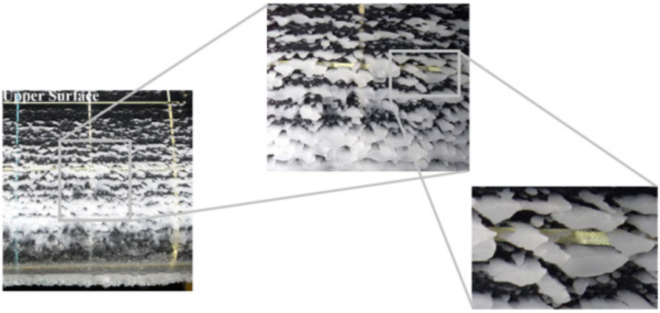

Figure 2.6.: Ice feathers formed at the impinging limit in icing wind tunnel tests with SLD, imaged by Broren et al. [23].

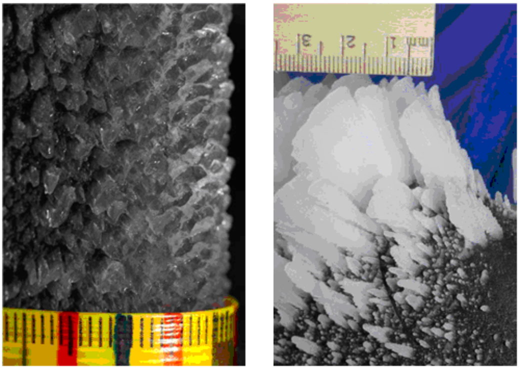

Figure 2.7.: Comparison of ice feathers created by normal cloud droplets (left) and SLD (right), imaged by Vargas et al. [150] in icing wind tunnel tests.

The deposition-rebound threshold defined by Bai and Gosman [9] and the deposition-splash threshold adopted from Trujillo [146] are

$$deposition - rebound \qquad 10 \leqq We \leqq 1320 La^{-0.18}, \tag{2.3}$$

where La is the Laplace number, and

$$deposition - splash \qquad K_{crit,spray} \geqq 540 R_z^{*-0.35}, \tag{2.4}$$

where R_z^* is the dimensionless roughness parameter, defined as the surface roughness divided by the diameter of the impinging drop. The number of secondary droplets is defined by Trujillo as [146]

$$N_s = \frac{1}{22}\left\{0.0437\left[K_{crit}\left(\frac{|\overrightarrow{v_0}|}{v_{n,0}}\right)^2 - K_{c,dry}\right] - 44.92\right\}. \tag{2.5}$$

The mass-loss coefficient, Ψ, is initially adopted from Yarin and Weiss [170] and then systematically calibrated by droplet impingement data provided by Papadakis et al. [107] and come to

$$\Psi = 3.8\left[1.0 - exp(-0.85(K_{Yarin} - 17))\right]/K_{Yarin}^{0.5}. \tag{2.6}$$

The velocity of secondary droplet is initially defined by Trujillo as [146] and then calibrated with experimental data of Papadakis et al. [107]

$$\begin{cases} \frac{u_{t,s}}{u_{t,0}} = +(0.85 + 0.0025\theta_0) \\ \frac{u_{t,s}}{u_{t,0}} = -\left[0.9930 - 0.0307(90^\circ - \theta_0) + 0.0272(90^\circ - \theta_0)^2 - 0.0086(90^\circ - \theta_0)^3\right]. \end{cases} \tag{2.7}$$

Finally the secondary droplets size is determined by the principle of mass conservation,

$$\frac{d_s}{d_0} = \left(\Psi \frac{1}{N_s}\right)^{\frac{1}{3}}. \tag{2.8}$$

This model showed good agreement under the calibration condition, however, it is not universal [162, 163]. The original models for the mass-loss coefficient and velocities of secondary droplets are derived from very different impact conditions, (e.g. significantly lower speed impact, and tremendously more dense spray) and the data calibration can not be generalized for other icing conditions. In order to find a more general model, detailed experimental study and theoretical analysis on the single drop impact is indispensable.

2.2 Drop Impact on Dry Surfaces

Taking a typical MVD of $100\,\mu$m and a typical LWC of $0.2\,\mathrm{g\,m^{-3}}$ for an estimation, the average distance between SLD is 138 times of the MVD, i.e. the temporal interval between two consecutive drop impact events is 138τ, while $\tau = d_0/v_0$ is the typical temporal unit to measure the duration of the drop impact process. The large interval indicates that the drop impact in the in-flight icing is typically single drop impact. The drop diameter is between $100\,\mu$m and $400\,\mu$m, and the impact velocity is of the order of 100m/s. Since the impact We and Re are as high as 57 000 and 40 000 respectively, drop splash is prominent.

The substrate could be dry aluminum surfaces, dry ice surfaces, thin liquid film of micrometer thicknesses, or deep pool in the millimeter range as rivulets form frequently on the wing surface [27]. Therefore the drop impact in the in-flight icing is in a very complex situation. In the scope of the dissertation, the drop impact on dry aluminum surfaces was chosen to be investigated.

This section summarizes the splash thresholds for single drop impact on solid surfaces, introduces the state of art experimental results on oblique impact, and the high-speed impact of single drops on dry surfaces.

2.2.1 Splash Threshold

The drop impact has attracted consistent attention for more than 100 years since the seminal work of Worthington in 1876 [160, 161]. Thanks to the development of high-speed cameras, six types of outcomes of the drop impact on a dry surface were revealed as shown in Figure 2.8. Splash is defined as a drop impact that results in disintegration of the primary drop, i.e. at least one secondary droplet is formed. In the case of the prompt splash, secondary droplets are ejected directly from the advancing contact line, whereas in the case of corona splash the edge of the lamella is lifted, forming a liquid sheet which further disintegrates into secondary droplets. The receding breakup and partial/total rebounding occur mostly on hydrophobic surfaces. The splash threshold concerned here is for drop impact on metal surfaces, and therefore only for the corona and prompt splash.

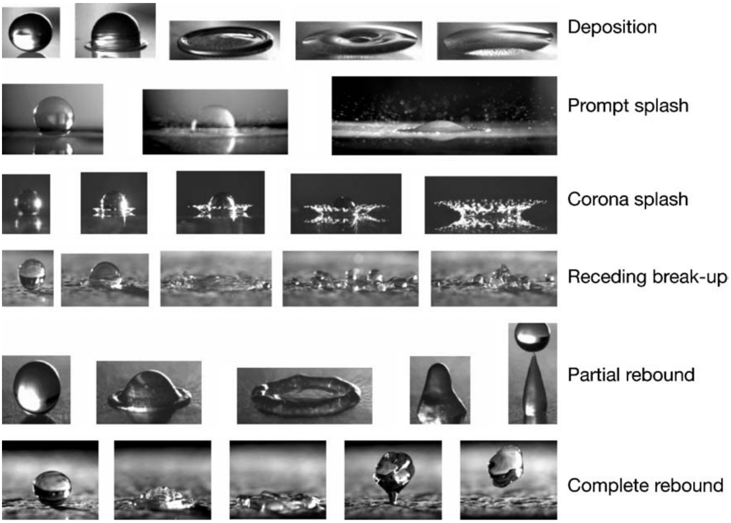

Figure 2.8.: Outcomes of the drop impact on solid surfaces, reported by Rioboo et al. [114].

The distinct morphologies of the corona splash and the prompt splash indicate different underlying mechanisms for the two types of splash. Therefore the splash threshold, which is a theoretical model that predicts the inception of the splash, should comprise two modes which are responsible for each phenomenon specifically. It is therefore of critical importance to answer the question, what creates the corona splash, and what induces the prompt splash.

Xu et al. observed the corona splash created by $\phi 3.4\,\mathrm{mm}$ ethanol drop impacting on a dry smooth surface at various surrounding gas pressures [168]. By decreasing the gas pressure, the corona splash was weakened effectively. This fact suggests that the existence of the surrounding gas plays an indispensable role on the corona splash. This finding is further supported by Mishra et al. who conducted drop impacts under gas pressures up to 12 bar [94]. Although no corona splash was observed because of the limited range of the impact velocity, it was identified that higher pressures enhanced the undulations at the periphery of the spreading lamella.

Xu et al. proposed the following scaling parameter by comparing the destabilizing stresses from the gas and the stabilizing stresses from the surface tension [168],

$$\sum\nolimits_G / \sum\nolimits_L = \sqrt{\gamma M_G}\, p \sqrt{\frac{d_0 v_0}{4k_B T}} \frac{\sqrt{\nu_L}}{\sigma}, \tag{2.9}$$

where γ is the adiabatic constant (1.4 for air), M is the relative molecular mass (29 for air), p is the pressure, d_0 and v_0 are drop diameter and impact velocity respectively, k_B is the Boltzmann constant, T is temperature in Kelvin, ν is kinematic viscosity, σ is surface tension. G denotes gas and the L denotes liquid. In this equation, the air compressibility is considered based on the assumption that a weak shock in the air presents at the early stages of drop spreading. However, the importance of the shock wave is questionable at a low impact speed of 3.74m/s applied in their experiment. This scaling method failed to provide a universal splash threshold for either their own data or the data from Mishra [94, 166, 168].

Eq. 2.9 predicts that the liquid viscosity encourages splash. This prediction was examined by the author with various liquids covering a wide range of kinematic viscosity from 0.68 cSt to 18 cSt. It was found out that at lower viscosities from 0.68 cSt to 2.60 cSt, higher viscosity promoted the splash, while the effect was reversed at higher viscosities (see Fig. 5. in [166]). This nonmonotonic influence of the viscosity explains the disparities in other experiments. Cossali et al. [34] and Rioboo et al. [114] found that the viscosity inhibited splashing, because they had only one value in the low viscosity range, while all the other test points were in the high viscosity range. Vander Wal et al. [156] found out that the viscosity promoted the splash because their range of viscosity lay exclusively in the low viscosity range. Range and Feuillebois had the same findings as Xu with a large variety of liquids (see Fig. 7. in [115]), but the nonmonotonic effect was much less prominent in the expression of We_{crit} as a function of the Oh, which led to their counterintuitive conclusion that the viscosity played a negligible role in the splash threshold. Nonetheless the encouraging effect of viscosity on the splash is surprising. Xu hypothesized that [166] for low viscosities, larger ν_L causes a thicker film which was easier to destabilize, while viscous drag became important and helped to stabilized the spreading drop at higher viscosities.

All the experiments above were conducted on smooth surfaces with negligible roughnesses. Decreasing the surrounding gas pressure to a level, where no corona splash occurred, rough surface was applied for drop impact by Xu et al. [167], in order to observe the prompt splash exclusively. It was found out that the roughness promoted the prompt splash. Interestingly, the textured surface with regular roughness elements exhibited less prompt splash than with the random roughness [166]. More interestingly, both the roughness height and width of the textured surface promoted the prompt splash at lower values and began to affect reversely at larger values. Prompt splash was completely suppressed with a dimensionless roughness height $R_z^* = 0.036$.

The finding that the random roughness enhanced the splash is in accordance with the empirical correlation from Stow and Hadfield [142]:

$$Re^{0.31}We^{0.69} = K_{crit}, \tag{2.10}$$

where K_{crit} is a roughness dependent threshold value. Mundo et al. proposed the following splash threshold for random roughness height between $R_z^* = 0.018$ and 1.3 [99],

$$OhRe^{1.25} = We^{1/2}Re^{1/4} = K_{crit} = 57.7, \tag{2.11}$$

where the K_{crit} was equal for all the roughnesses. Cossali et al. [34] suggested later that the applied roughness by Mundo et al. were in an asymptotic regime, where the K_{crit} of Stow and Hadfield achieved a nearly constant value. These models are however empirical correlations which base on an average point of view of both the prompt splash and the corona splash, because these experiments were conducted at normal atmosphere pressure, where the both types of splash occur. It should be noted that the substrate condition in the experiment of Mundo et al. could be very different from the topic of the roughness, because the roughness height was comparable with the drop size. It is arguable whether it was a rough surface, or a randomly uneven surface. Furthermore the impact surface was unlikely to be dry as we found out by repeating the same impact conditions in our experiment: a drop train impacted on a rotating cylinder, and the cylinder was cleaned by a rubber wiper.

Rein et al. [119] summarized the available splash thresholds by expressing a critical Ohnesorge number as a function of the Reynolds number, as Figure 2.9 exhibits. These semi-empirical correlations can be divided into two categories: one is for the drop impact on smooth surfaces, the other is for drop impacts on rough or slightly wetted surfaces.

The threshold from Cossali et al. [34] is for drop impacts on a thin liquid film of $80\,\mu$m, which was 2.5% of the drop diameter. Hardalupas et al. [47] conducted

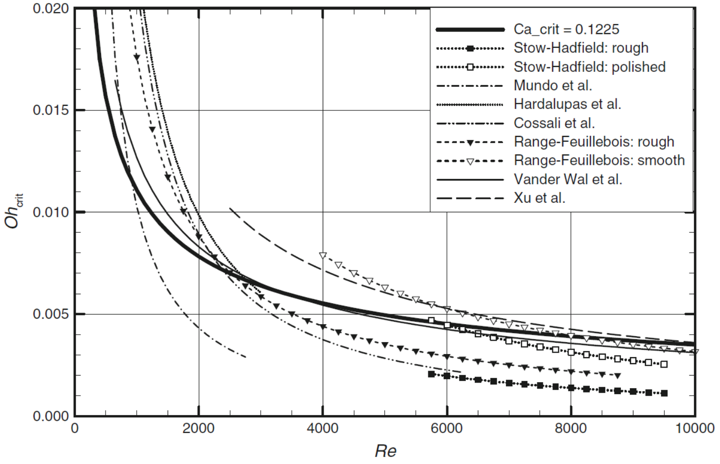

Figure 2.9.: Splash thresholds of the drop impact on solid surfaces, summarized by Rein et al. [119].

similar experiments but on curved surfaces. The plotted curve is for an impact surface of an infinitely small curvature. It is interesting to notice that the thresholds for wetted surfaces coincide with the curves for rough surfaces. This indicates that the corona splash on a wetted surface and the prompt splash on a rough surface were not clearly distinguished in these experiments. The one from Mundo et al. [99] has the lowest value because the impact surface was both wetted and manufactured with significant roughnesses.

The threshold values for drop impact on smooth surfaces were acquired mostly at larger Re, and the Oh_{crit} are in general higher than on wetted or rough surfaces. The threshold from Range and Feuillebois [115] was simplified to be a critical Weber number, $We_{crit} = B_1 log^{B_2} R_z$, where B_1 and B_2 are fitting parameters which are dependent on surface roughness R_z. Similarly, Vander Wal et al. [156] acquired a threshold as

$$Oh Re^{0.609} = K_{crit} = 0.85, \tag{2.12}$$

and further simplified it to a critical capillary number $Ca_{crit} = Oh Re^{0.5} = 0.1225$.

These thresholds are in good accordance with each other, and are simple to apply. However they are oversimplified by combining two different types of splash into one model. It will not be surprising if these thresholds become invalid while extrapolating to other conditions, for example to the interested SLD conditions.

2.2.2 Oblique Drop Impact

The oblique impact is obviously a frequent occurrence in the in-flight icing, because the normal impact takes place only at the stagnation point. The oblique impact of single drops distinguishes from the normal impact by exhibiting very different splash modes: aerodynamic breakup, partial rebounding and total rebounding. The latter two are reminiscences of the drop impact on hydrophobic surfaces.

Povarov et al. [113] conducted the drop impact on a rotating disk in order to observe the interaction between the drop and the boundary layer above the disk. The drops had diameters from 0.3 mm to 4.0 mm and a falling velocity of 0.1m/s to 10m/s. The horizontal rotating disk has an azimuthal velocity up to 60m/s at the radial position of impact. At lower rotational speed, the drop spread on the disk, and eventually broke up by the airflow. As the rotational speed increased, the drop barely touched the surface before it was blown away by the airflow. Typical observations are shown in Figure 2.10.

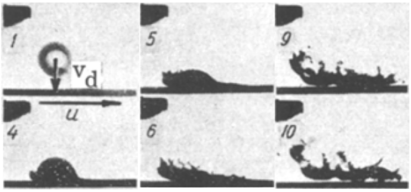

(a) Drop diameter: 2 mm, velocity of the impact surface: 30m/s.

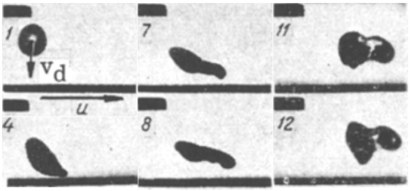

(b) Drop diameter: 2 mm, velocity of the impact surface: 60m/s.

Figure 2.10.: Interaction of a falling drop with the gas boundary layer on a rotating surface, reported by Povarov et al. [113]. The sequence of the image are indicated by the number on the upper left corner.

Chen and Wang [28] observed the drop impact on a rotating cylinder out of Teflon, on which water had a static contact angle of 103°. The drop had a velocity between 1m/s and 3m/s and a diameter between 500μm and 900μm. The rotating cylinder had a tangential velocity up to 4.5m/s. Drop deposition and partial rebounding were observed. Conditionally the drop split into two parts while spreading on the surface. Šikalo et al. [153] observed partial and total rebounding of glycerin droplets on glass surfaces of different roughnesses. The impact angle was likewise pretty small, 8°.

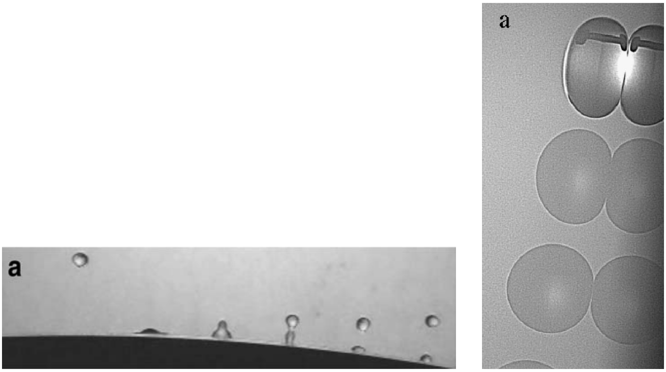

Figure 2.11.: Partial rebounding observed by Chen et al. [28] (left) and total rebounding observed by Šikalo et al. [153] (right) in oblique impacts.

At larger impact angles, asymmetric splash occurs in an oblique impact. Figure 2.12 shows the observation of Bird et al. [18] with ethanol drops impacting on a moving aluminum surface. The presence of the tangent velocity accelerated one side of the lamella, while decelerated the opposite side, leading to the asymmetric corona splash.

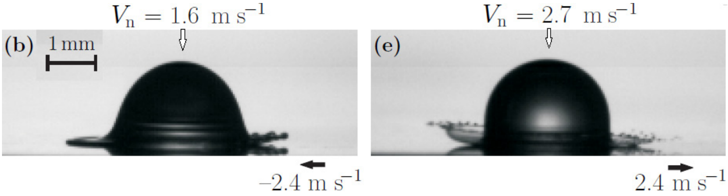

Figure 2.12.: Triggering and inhibiting a splash with the tangent velocity, reported by Bird et al. [18].

Supplementarily, Zen et al. [175] published the top view of the asymmetric splash as shown in Figure 2.13. It is interesting to notice that the uprising liquid ligament was barely connected to the spreading lamella.

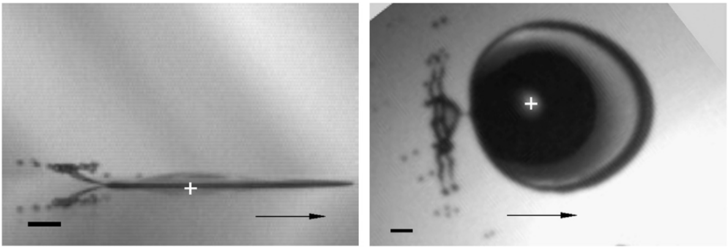

Figure 2.13.: Side view and top view of the asymmetric splash in an oblique impact, provided by Zen et al. [175].

Splash threshold for the asymmetric splash was provided by Bird et al. as [18]

$$We\,Re^{1/2}\left(1-2.5\frac{v_t}{v_n}Re^{-1/2}\right)^2 > K_{crit} = 5700, \tag{2.13}$$

where v_t and v_n are respectively tangent and normal components of the impact velocity, the coefficient 2.5 and the threshold value $K_{crit} = 5700$ were found out with the experimental data. This model is consistent with Eq. 2.11 provided by Mundo et al. although the threshold value was a lot higher because of a lower roughness. This threshold takes the tangent velocity into consideration, but the importance of the surrounding gas is missing.

It should be noted that the experiment of Mundo et al. [99] comprised exclusively oblique impact with the impingement angle between 4° and 65°. However, only the normal velocity entered the splash threshold, whereas the significance of the tangent velocity was unrecognized. The reason lies probably at the very rough surface as well as the possible liquid film on the impact surface.

2.2.3 High-speed Drop Impact

The velocity the aircraft in an in-flight icing event is of the order of 100m/s. High-speed impact of single drops is of interest. Mehdizadeh et al. [83] and Dhiman et al. [37] conducted single drop impacts on a rotating target with a high tangential velocity up to 50m/s. The drop diameter ranged between 0.5 mm and 1.33 mm. Strong prompt splash as well as rupture of the liquid film was observed as Figure

2.14 shows. On stainless steel, tiny holes appeared before the maximum spreading diameter was reached, while on glass surfaces, which was more hydrophilic, the rupture emerged during the receding phase.

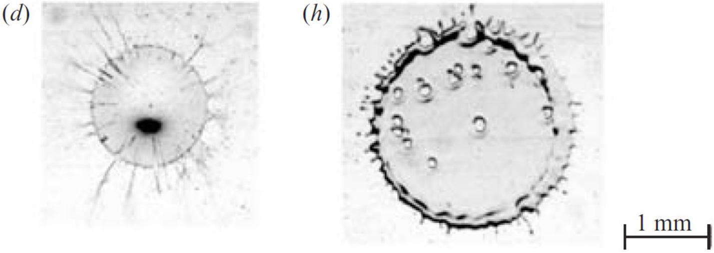

Figure 2.14.: Single shots of $\phi 0.55\,\mathrm{mm}$ drop impacting on a stainless steel surface with a velocity of $40\mathrm{m/s}$, reported by Mehdizadeh et al. [83]. Prompt splash was observed upon impact and film rupture emerged during spreading.

Pan et al. [103] realized the high-seed impact in a different regime. A drop of $0.5\,\mathrm{mm}$ was accelerated in a vertical wind tunnel to achieve a velocity as high as $42\mathrm{m/s}$ before impact on a solid surface. Both prompt splash and corona splash was observed as Figure 2.15 shows. The alcohol had similar surface tension and density to the heptane, but higher viscosity, $1.2\,\mathrm{mPa\,s}$ versus $0.72\,\mathrm{mPa\,s}$. The Oh were 0.0126 and 0.0081 respectively for the two liquids. This observation confirmed that the viscosity promoted the corona splash at low Ohnesorge numbers.

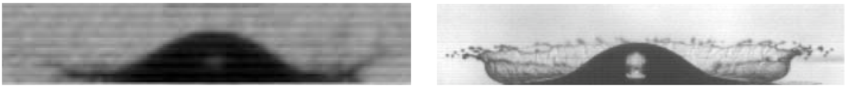

Figure 2.15.: Prompt splash (left) was documented with heptane droplet on a glass surface with an impact velocity of $9.8\mathrm{m/s}$, while corona splash (right) was observed with an alcohol drop, reported by Pan et al. [103].

Pan et al. compared their experimental data with the splash thresholds provided by Vander Wal et al. (Eq. 2.12), Mundo et al. (Eq. 2.11) and Xu et al. (Eq. 2.9), but no agreement was found. Further they pointed out that viscosity was much less influential than the surface tension in the determination of the splash mode.

The maximum spreading diameter in these experiments was found out to adequately follow the model from Pasandideh-Fard et al. [83, 103, 108],

$$d^*_{sp-max} = 0.5Re^{1/4}, \tag{2.14}$$

where $d^*_{sp-max} = d_{sp-max}/d_0$, sp denotes spreading and 0 designates the impinging drop.

Very recently, Faßmann et al. [140] characterized the secondary droplets created in the corona splash of $\phi 2.7$ mm drops impacting on a rotating glass substrate with tangential velocities of 6.25m/s, 8.31m/s and 12.99m/s. Double-frame imaging of high spatial resolution of 8μm/pixel was applied for the velocity and diameter measurement of the secondary droplets. The diameter of the secondary droplets was measured as 1.5% to 3% of the primary drop, the velocity was between 1.5 to 4 times of the impact velocity, and the total mass-loss was 2.0%, 3.9% and 5.4% of the impinging drop respectively for the three impact velocities. These data give an estimation of the mass-loss as well as the diameter and the velocity of the secondary droplets. However the precision of the measurement is questionable. Firstly, most of the secondary droplets were merely 3 × 3 pixels. The diameter measurement is hence of 33% error. Secondly, the secondary droplets had large velocities, and therefore the motion blur is of critical importance. However, the exposure time was not explicitly released. In fact it is hard to tell whether an object of 3 × 3 pixel is in focus and without motion blur.

To sum up this section, semi-empirical splash thresholds were provided for normal impacts and oblique impacts, but none of them contain all the physical factors that influence the outcome of the drop impact, and most of them do not distinguish the prompt splash and the corona splash. Two different splash thresholds for the two distinct phenomena are desirable. The experiments on oblique impact documented the rebounding and asymmetric splash, pointing out the importance of the tangent velocity. However all the experiments were all conducted for low We and Re, while high-speed impacts were all for normal impacts. For the in-flight icing, the high-speed oblique impact is desired for observation.

2.3 Solidification of Supercooled Water

Water, an ordinary substance appearing in everyday life, has attracted scientists for centuries of research on account of its more than 80 anomalous properties compared to the most other liquids [71]. Probably the best known water's anomalies is its density maximum at 4 °C, a fact recognized already more than three hundred years ago [157]. Another peculiarity is that water expands when it freezes: ice has a smaller density than liquid water, which keeps ice float on lakes. This merciful feature prevents natural bodies of water from complete freezing, and thus plays an essential role in the earth biosphere. Concerning solidification of supercooled water, the best reminiscence is the snowflake. What leads to so beautifully delicate and nearly symmetrical selection, such as shown in Figure 2.16? Kepler's monograph "on the Six-Cornered Snowflake" in 1611 [66] is often cited as the first published work in which morphology was treated as a scientific rather than a theological topic. At a time in which the existence of atoms was merely speculation, Kepler mused about the hexagonal patterns but concluded that this problem was beyond his reach. In fact, this problem is not yet completely answered four centuries later. Without submerging into tons of interesting literature on this precious material, this section selectively introduces the involved knowledge about the supercooled water in a brief way.

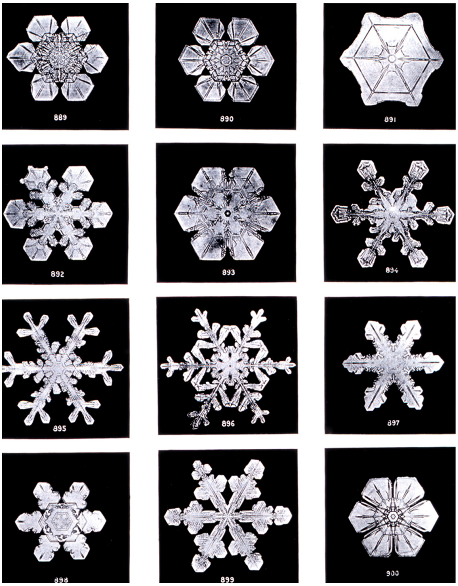

Figure 2.16: Snowflake photos by Wilson Bentley circa 1902. Bentley is one of the first known photographers of snowflakes. He perfected a process of catching flakes on black velvet in such a way that their images could be captured before they either melted or sublimated. These techniques used by Bentley to photograph snowflakes are essentially the same as used today.

2.3.1 States of Liquid Water in Cryogenic Conditions

Water does not necessarily freeze at its equilibrium melting point T_m, but can be cooled to temperatures significantly below 273.15 K. The earliest record of supercooled water is mostly likely the experiments by Daniel Fahrenheit in 1721 [41], in which he observed that water droplets in an evacuated glass bulb remained liquid to temperatures of about 264 K. The temperature T_m is defined by the thermodynamics as the temperature where the liquid and crystalline phases can coexist in equilibrium with each other. Above T_m, liquid is the stable phase, below T_m, the crystal is the stable phase. Supercooled water is in a metastable state, in which the liquid settles in a local minimum in the Gibbs free energy. The nucleation of the crystalline phase is typically initiated by a solid nucleus present in the liquid. After initiation, the supercooled melt transforms rapidly to the absolute minimum corresponding to the stable crystalline state. This process is conventionally called nucleation, while the phase change without the involvement of supercooling is named as solidification.

A liquid devoid of any nuclei can nucleate spontaneously by forming a stable germ through internal fluctuations. This process is called homogeneous nucleation, while crystallization initiated by nuclei or foreign particles is called heterogeneous nucleation [52,69]. The lowest homogeneous nucleation temperature is a genuine property of the metastable liquid itself. For water this temperature was experimentally observed as −38 °C at 1 bar as Figure 2.17 describes. Under otherwise identical conditions, heterogeneous nucleation always occurs at a higher temperature than homogeneous nucleation, because the addition of foreign nuclei to a liquid can only enhance the overall nucleation probability. In the case of SLD icing condition, the temperature is mostly over −10 °C, well above the homogeneous temperature of the supercooled water. Therefore only the heterogeneous nucleation is related.

2.3.2 The Stefan Problem

The characteristic of the phase change problem is that in addition to the temperature field, the location of the interface is unknown. This situation arises very often in applications with the result that the Stefan problem is by far the most frequently applied model of a phase change process. The Stefan problem is a mathematical model describing the phase change problem. Its solution is the transient temperature distribution in the domain of the problem and the location of the interface. Although the discussion here is focused on solidification, the principles apply to other first-order phase transitions including vapor condensation and evaporation, sublimation and so on.

Referring to a model, it is crucial to have a clear picture of exactly which phenomena are taken into account, because a model can be at best as good as its underlying physical assumptions. The phase change process involves a PCM (Phase Change Material) with constant density ρ, latent heat L, melt temperature T_m, phase-wise

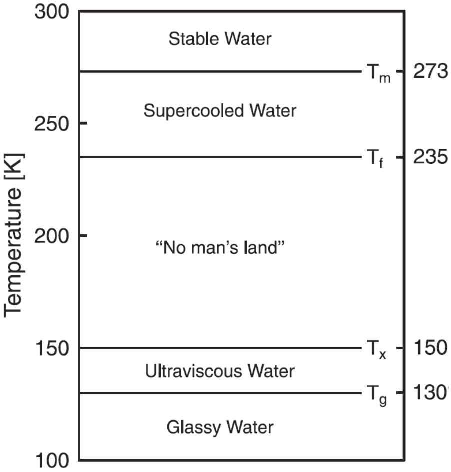

Figure 2.17.: At an ambient pressure of $1\,\mathrm{bar}$, liquid water exhibits in a number of forms. Homogeneous nucleation can be avoided by hyperquenching liquid water at extremely high cooling rates $\geqq 1 \times 10^5 \mathrm{K/s}$ to temperatures below $100\,\mathrm{K}$ [24]. This procedure results in an amorphous form of water. When glassy water is reheated, it undergoes a glass transition at about $130\,\mathrm{K}$. The region between T_f and T_x is called "no man'land" because it is not accessible on experimental time scale due to rapid crystallization of ice in this temperature range [93].

constant specific heat c_L, c_S, and thermal conductivities, k_L, k_S. Heat is transferred only isotropically by conduction, through both the solid and the liquid; the phases are separated by a sharp interface of zero thickness, and isothermal at temperature T_m, where the latent heat is absorbed or released. Simplifying assumptions for the Stefan problem are the following [4]:

1. Heat transfer is isotropically by conduction only, all other effects are assumed negligible.
2. The latent heat is constant; it is released or absorbed at the phase-change temperature.
3. The phase-change temperature is a fixed known temperature, a property of the material.
4. Thermal properties are assumed as constant in each phase.
5. Density is equal in liquid and solid phase.
6. There is neither supercooling, nor nucleation difficulties.

7. The interface is locally planar and sharp, at the phase-change temperature.
8. The surface tension and curvature of the interface is considered as insignificant.

Six assumptions are reasonably good for water/ice transition. The fourth assumption applies only to a moderate temperature range. This is acceptable for icing conditions: from 0 °C to −10 °C. The fifth assumption is to avoid movement of material, but it is invalid for most of the materials. Two types of density change are relevant in the phase change process. One is due to the dependence of density on temperature, arising in any heat transfer process. This may induce natural convection in the presence of gravity. The other is due to the difference between the solid and the liquid densities at the melt temperature. In the considered case of icing, water expands upon freezing. This effect either induces void in the bulk ice, or accommodates mechanical movement of the interface. This is probably the most unreasonable assumption in this widely used model. But for the sake of simplified analytical study, it is not considered here for small droplets of millimeters, or smaller.

If the initial temperature of the liquid phase is equal to the melt temperature T_m, the Stefan problem is called as "one-phase" Stefan problem as described in the following. A slab, $0 \leq x \leq l$, initially liquid at the melt temperature T_m, solidifies by imposing a cold temperature $T_B < T_m$ on the face $x = 0$ and keeping the back face, $x = l$, insulated. Thermodynamic properties are constant on the two phases, which are separated by a sharp interface at $x = X(t)$. To find the temperature distribution $T(x,t)$ and the location of interface $X(t)$ at $t > 0$, heat equations, initial and boundary conditions are established as below [4]:

Heat conduction equation:

$$T_t = \alpha_S T_{xx}, \quad 0 < x < X(t), \quad t > 0, \quad \text{solid region.} \tag{2.15}$$

Stefan condition at the interface:

$$T(X(t),t) = T_m, \quad t > 0. \tag{2.16}$$

Initial condition:

$$X(0) = 0. \tag{2.17}$$

Boundary condition:

$$T(0,t) = T_B < T_m, \quad t > 0. \tag{2.18}$$

The temperature needs to be found only in the liquid $0 < x < X(t)$, $t > 0$, because it is identically T_m in the solid. The term “one-phase” refers to only one of the two phases (solid) being “active”, the other phase staying at the melt temperature T_m.

The Stefan condition in a more general form is

$$\rho L X^{'}(t) = -k_L T_x(X(t)^{-}, t) + k_S T_x(X(t)^{+}, t). \tag{2.19}$$

It says that the rate of the change in latent heat $\rho L X'(t)$, equals the amount by which the heat flux jumps across the interface. In particular, the heat flux can be continuous across the interface if and only if either $L = 0$, or the interface does not move.

The Neumann solution introduce the similarity variable

$$\xi = \frac{x}{\sqrt{t}}, \tag{2.20}$$

and seek the solution in the form

$$T(x,t) = B(\xi), \tag{2.21}$$

with $B(\xi)$ an unknown function. Accordingly the interface location $X(t)$ is proportional to the $\sqrt{t}$:

$$X(t) = B_0\sqrt{t}. \tag{2.22}$$

Substituting into 2.15 and integrating we obtain

$$B(\xi) = B_1 \int_0^{\xi} e^{-\frac{s^2}{4\alpha_S}}\, ds + B_2 = B_1\sqrt{\pi\alpha_S}\, erf(\frac{\xi}{2\sqrt{\alpha_S}}) + B_2, \tag{2.23}$$

where

$$erf(z) = \frac{2}{\sqrt{\pi}} \int_0^{z} e^{-s^2} ds. \tag{2.24}$$

Constants B_1, B_2 are determined as:

$$B_1 = \frac{T_m - T_S}{\sqrt{\pi \alpha_S}\, erf(B_0/2\sqrt{\alpha_S})}, \tag{2.25}$$

and

$$B_2 = T_B. \tag{2.26}$$

Set

$$\lambda_{St} = \frac{B_0}{2\sqrt{\alpha_S}}, \quad \Delta T_S = T_m - T_B, \tag{2.27}$$

and

$$St_S = \frac{c_S T_B}{L} = \text{Stefan number}, \tag{2.28}$$

the Stefan condition Eq. 2.16 leads to an equation for λ_{St}:

$$\lambda_{St} e^{\lambda_{St}^2} erf(\lambda_{St}) = \frac{k_S}{\rho L} \frac{\Delta T_S}{\sqrt{\pi} \alpha_S} = \frac{c_S \Delta T_S}{\sqrt{\pi} L} = \frac{St_S}{\sqrt{\pi}}. \tag{2.29}$$

Hence it is more convenient to express the solution in terms of λ_{St}:

$$X(t) = 2\lambda_{St}\sqrt{\alpha_S t}, \tag{2.30}$$

and

$$T(x,t) = T_B + \Delta T_S \frac{erf(\frac{x}{2\sqrt{\alpha_S t}})}{erf(\lambda_{St})}, \tag{2.31}$$

with λ_{St} a root of the transcendental equation

$$\lambda_{St} e^{\lambda_{St}^2} erf(\lambda_{St}) = \frac{St_S}{\sqrt{\pi}}. \tag{2.32}$$

For each value of $St_S > 0$, there exists a unique root λ_{St}. Once λ_{St} is found, the solution of the problem is given by Eq. 2.30 and Eq. 2.31. This is the classical Neumann solution of the Stefan problem. The Stefan problem is a well-posed mathematical problem, which admits one unique solution.

The Stefan number St_S completely characterizes the solidification process. It represents the ratio of the sensible heat $c_S \Delta T_L$ to the latent heat L. For aircraft icing, $St_S \approx 0.06$. Phase change processes with such a small St are dominated by the latent heat.

The transcendental equation is easily solvable by the Newton-Raphson iterative method with an initial "guess" of λ_{St}. For small St an effective approximation to the root λ_{St} of Eq. 2.32 is given by the expression [4]:

$$\lambda_{St} \approx 0.706\sqrt{St}\left[1-0.21(0.5642\,St)^{0.93-0.15St}\right]. \tag{2.33}$$

This relation has less than 1% relative error for the $0 < St < 0.83$, a relative error below 5% for $0.83 < St < 4.28$.

For $St \approx 0$,

$$\lambda_{St} \approx \sqrt{\frac{St}{2}} \quad \text{for} \quad St \approx 0. \tag{2.34}$$

It also follows that for $0 \leq x \leq X(t) = 2\lambda_{St}\sqrt{\alpha_S t}$ the quantity $x/2\sqrt{\alpha t} \leq \lambda_{St} \ll 1$, and the Neumann temperature Eq. 2.31 becomes

$$T(x,t) \approx T_B + \Delta T_S \frac{x}{X(t)}, \quad 0 \leq x \leq X(t), \quad t \geq 0. \tag{2.35}$$

For each $t > 0$, this is linear in x, i.e. the temperature profile at each time is a straight line joining the point $(x = 0, T = T_B)$ with $(x = X(t), T = T_m)$.

A schematic picture of the solidification process is shown in Figure 2.18. The substrate temperature is taken as $-20\,^{\circ}\mathrm{C}$. At each time t, solid occupies $[0, X(t)]$, and liquid $[X(t), l]$. The curve $x = X(t)$ represents the interface location, schematically, demarcating the solid and liquid space-time regions.

Supercooled liquid does not necessarily require the boundary condition $T(0,t) = T_B < T_m$ to begin the solidification process, because the supercooled liquid itself has potential to start the phase change even if all the boundaries are adiabatic. For the simplest one-dimensional situation, the last three assumptions of the Stefan problem are loosed and a similar analysis is applied for the solidification of supercooled melt.

A semi-infinite slab, $x \geq 0$, is initially at a uniform temperature $T_A < T_m$ but liquid, hence supercooled. At time $t = 0$, the face $x = 0$ is brought to the melt temperature T_m (or equivalently the face $x = 0$ is insulated) and a solidification front begins propagating from $x = 0$ into the slab. Thermodynamic properties

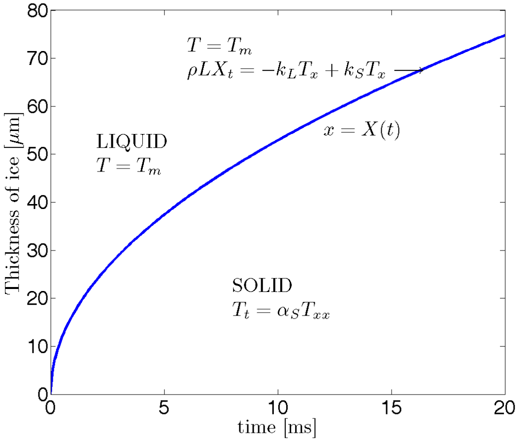

Figure 2.18.: Location of the ice /water interface calculated by the one-phase Stefan problem. The substrate temperature is taken as −20 °C.

are assumed phase-wise constant, density does not change during phase change $\rho_S = \rho_L$, and the freezing occurs at the normal melt temperature T_m. Thus the temperature at the front $x = X(t)$ is equal to T_m, ahead of it there is supercooled liquid at temperature below T_m and behind it there is solid at temperature T_m. This is one-phase Stefan problem, but the released latent heat flows from the interface to the supercooled liquid ahead of it. The mathematical description is the following [4].

Finding $T(x,t)$ and $X(t)$ satisfying

$$T(x,t) = T_m, \quad 0 < x < X(t), \quad t > 0, \tag{2.36}$$

$$T_t = \alpha_L T_{xx}, \quad X(t) < x < \infty, \quad t > 0, \tag{2.37}$$

$$T\left(X(t),t\right) = T_m, \quad t > 0, \tag{2.38}$$

$$\rho L X^{'}(t) = -k_L T_x\left(X(t)^{+},t\right), \quad t > 0, \tag{2.39}$$

$$T(x,0) = T_A < T_m, \quad 0 < x < \infty \quad \text{but liquid,} \tag{2.40}$$

$$X(0) = 0, \tag{2.41}$$

$$T(0,t) = T_m \quad \text{or} \quad -k_S T_x(0,t) = 0, \quad t > 0. \tag{2.42}$$

The problem admits a similarity solution as before. Setting $\xi = x/\sqrt{t}$, it yields $X(t) = 2\lambda_{St}\sqrt{\alpha_L t}$, $T(x,t) = B(\xi)$, further

$$X(t) = 2\lambda_{St}\sqrt{\alpha_L t}, \quad t > 0, \tag{2.43}$$

$$T(x,t) = T_m \quad 0 \le x \le X(t), \quad t > 0, \tag{2.44}$$

$$T(x,t) = T_A + (T_m - T_A)\frac{erfc\left(\frac{x}{2\sqrt{\alpha_L t}}\right)}{erfc(\lambda_{St})} \quad X(t) \le x, \quad t > 0, \tag{2.45}$$

where λ_{St} is a root of the transcendental equation

$$\lambda_{St}\sqrt{\pi}\, e^{\lambda_{St}^2} erfc(\lambda_{St}) = St_{SCL}, \quad St_{SCL} = \frac{c_L(T_m - T_A)}{L}. \tag{2.46}$$

Eq. 2.46 has a unique solution if and only if $0 \le St_{SCL} \le 1$, that is only if

$$T_m - \frac{L}{c_L} < T_A \le T_m. \tag{2.47}$$

The physical meaning is that the temperature at the interface must be raised to T_m by the only heat source, the latent heat L, for freezing to occur. When $St_{SCL} \ge 1$, the liquid is said to be hypercooled. In this case the liquid becomes glass instead of solidifying, as referred to Figure 2.17. Figure 2.19 illustrates a typical result of the one-phase Stefan problem for supercooled liquid. The initial temperature of the supercooled water is taken as −10 °C.

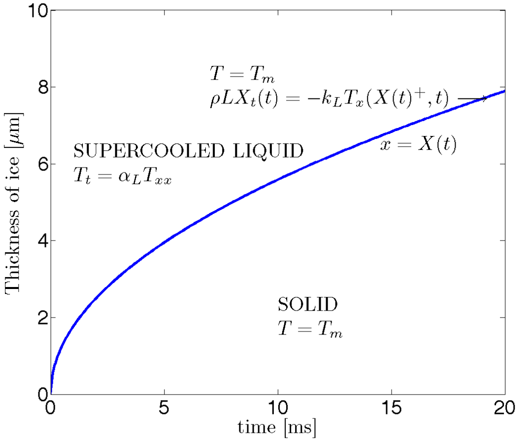

Figure 2.19.: Location of the ice/supercooled water interface calculated by the Stefan problem for the supercooled liquid. The initial temperature of the supercooled water is −10 °C.

For a one-dimensional finite slab, taking the melt temperature as reference, the initial energy is

$$Q = \rho L l + \rho c_L (T_A - T_m) l. \tag{2.48}$$

The final state has $T = T_m$ and $Q = \rho L(l - X_\infty)$ with X_∞ as the interface location. Hence it yields

$$\frac{X_\infty}{l} = St_{SCL} = \frac{c_L (T_m - T_A)}{L}. \tag{2.49}$$

The fraction of solidification depending on the supercooling is plotted in Figure 2.20. At $T_A = -10\,^\circ\mathrm{C}$, the lowest SLD icing temperature, the fraction is 12.8%.

2.3.3 Dendrite Formation in Supercooled Liquid

The one dimensional analysis of nucleation of supercooled liquid is apparently insufficient to understand the pattern of snowflakes in Figure 2.16. It is necessary to do multidimensional analysis, which unveils the instability in this problem.

Consider a deformed interface illustrated in Figure 2.21. The sketch on the left illustrates the one-phase Stefan problem for solidification of a liquid at T_m, whereas

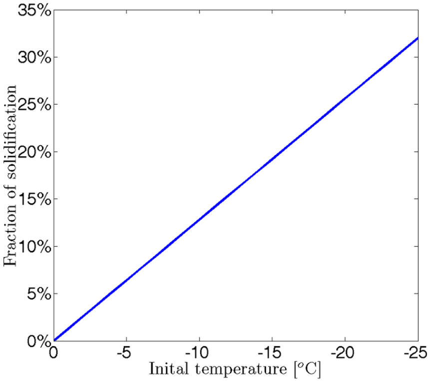

Figure 2.20: Fraction of solidification at different supercooling.

the one on the right depicts the one-phase Stefan problem for supercooled liquid. The heat sources of the two cases are the same, i.e. the latent heat released on the interface, but the heat sinks are different. In solidification without supercooling, the heat flows to the cold boundary at $T(0,t) < T_m$, while in the case with supercooling the heat sink is the supercooled melt. The temperature field is signified by the dashed isotherms. In solidification, the temperature gradient behind point A is weakened by the protruding nose. Consequently point A tends to melt and point B tends to grow. As a result the flat interface is always maintained. Therefore solidification is a stable process.

In the presence of supercooling, the situation is right on the opposite. The forward bulge of the interface at point A steepens the thermal gradient in the fluid ahead of it, leading to faster heat transfer. Therefore the bulge grows more rapidly and a depression like that at B tends to melt back. As a result, a morphological instability develops and dendritic crystals form in the supercooled liquid. On the other hand, the unstable growth of crystalline is not explosive due to the surface tension, a stabilizing factor. Gibbs-Thomson relation says that the surface tension lowers the freezing point at a curved interface to

$$T_F = T_m[1-(\sigma\kappa/\rho L)] = T_m - \Gamma_\kappa, \tag{2.50}$$

with capillary constant $\Gamma = \sigma T_m/\rho L$. σ is the surface tension and κ is the local curvature, here understood to be positive if the center of the curvature lies on the solid side of the interface, that is, the solid bulges into the liquid. In the right sketch of Figure 2.21, higher surface tension lowers the temperature at Point A and raises the temperature at Point B. As a result, heat flows from B to A, and tends to restore

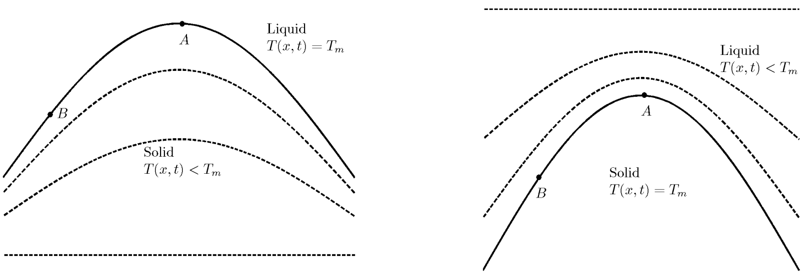

Figure 2.21.: Applying a sinuous perturbation on the ice/water interface, designated by the solid curve, the temperature field, denoted by the dashed curves, becomes uneven. The resultant temperature gradient, represented by the spacings between the isothermal curves, manifests the stable nature of solidification without supercooling, shown on the left, and the intrinsic instability of solidification in the supercooled liquid, shown on the right.

the flatness of the surface. It is the competition between these two effects that determines the instability of the interface and gives birth to the dendritic structure.

With the involvement of supercooling, the multidimensional Stefan problem becomes considerably more complicated. The interface temperature T_F now depends on the local curvature instead of being a given constant. The Stefan condition takes the form [4]:

$$\rho\left[L-(c_L-c_S)(T_m-T_F)\right]v_n=-k_L\frac{\partial T}{\partial \overrightarrow{n}}+k_S\frac{\partial T}{\partial \overrightarrow{n}}, \tag{2.51}$$

with v_n the velocity in the direction $\overrightarrow{n}$ normal to the interface. The modification of the latent heat term arises from the fact that the energy jump across the interface occurs at temperature $T_F \neq T_m$. It should be remarked here that Γ is very small typically, and therefore the freezing point depression is appreciable only for very large curvatures. For example, in the case of water/ice system $\Gamma = 18 \times 10^{-9}$ mK. For the freezing point to be depressed by 1 K, the protrusion should have a radius no larger than $2\Gamma \approx 36$ nanometers. Hence the Gibbs-Thomson effect is typically insignificant for the overall heat transfer process, and only accounts for the morphology of the interface.

The mathematical description of the morphology instability in supercooled liquid is well-known as Mullings-Sekerka Instability [97, 98, 132–134]. As in many instability problems, not every perturbation becomes unstable. The typical wavelength of Mullings-Sekerka instability is $\lambda_{ms} = 2\pi(2\alpha_L/v_n l_0)$. Note that λ_{ms} is the geometric mean of the microscopic capillary length l_0 and the macroscopic diffusion length $2\alpha_L/v_n$. It is roughly the right scale to characterize dendritic structure. A planar solidification front moving at speed v_n is linearly unstable against sinusoidal deformations whose wavelengths are larger than λ_{ms}.

The growth rate of the dendritic structure is of interest referring to the combination with drop impact hydrodynamics, because the ice dendrite would influence the impact process if its growth rate is faster than, or comparable with the impact process. It is known that the product of the growth rate, v_{tip}, of the dendrite and its tip radius R_{tip} are determined uniquely by the supercooling St_{SCL} as the Ivantsov relation [62]:

$$St_{SCL} = P_{ec}\, e^{P_{ec}} E_1(P_{ec}), \tag{2.52}$$

where $P_{ec} = R_{tip} v_{tip}/2\alpha_L$ is the Peclet number, and E_1 is the exponential integral:

$$E_1(y) = \int_{y'}^{\infty} \frac{e^{-y'}}{y'} dy'. \tag{2.53}$$

The tips of the dendrite often look very paraboloidal under small supercooling, qualitatively indicating that the Ivantsov relation is satisfied under these conditions. In order to get the tip velocity, the tip radius needs a size estimation. Langer and Müller-Krumbhaar postulated that a dendrite with a tip radius R_{tip} appreciably larger than λ_{ms} must be unstable against sharpening or splitting. In this sense, the dynamic process of dendrite formation might naturally come to rest at a state of marginal stability [72, 73, 96], for which the dimensionless group of parameters,

$$P_{LMK} = \frac{2\alpha_L l_0}{v_{tip} r_{tip}^2} = \frac{\lambda_{ms}}{2\pi r_{tip}}, \tag{2.54}$$

is a constant, independent of supercooling St_{SCL}. Setting R_{tip} equals to λ_{ms}, P_{LMK} becomes 0.025. This insightful speculation has delivered encouragingly consistent predictions with a wide range of experimental observations as Figure 2.22 shows. Comparing this graph to Figure 2.19, it is easy to find out that the real growth rate of the ice dendrite is several orders of magnitude higher than the prediction of the one-dimensional analysis with the Stefan problem. This emphasizes the dominance of the morphological instability in the growth of ice dendrite.

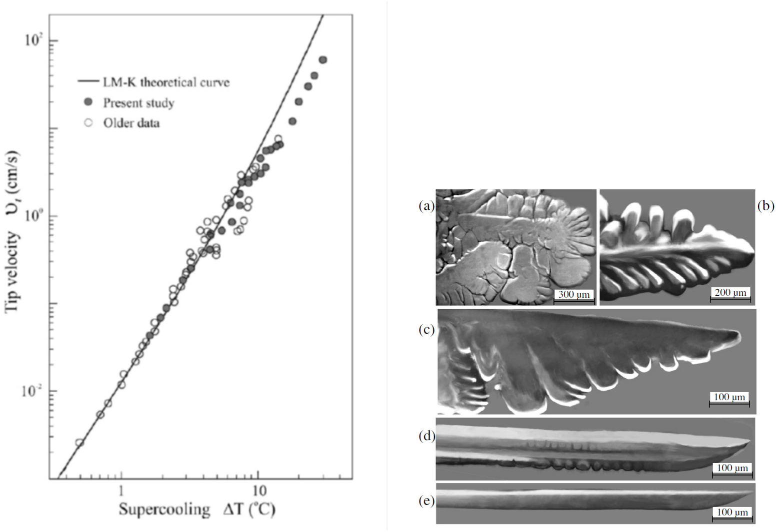

Figure 2.22.: The growth rate of the free ice dendrite, both the theoretical prediction and the experimental measurement, is shown on the left. The morphologies of the ice dendrite formed by water of various supercooling are shown on the right: (a) −0.3 °C, (b) −1 °C, (c) −2 °C, (d) −4 °C, (e) −7 °C. These data were reported by Shibkov et al. [135, 137].

Despite the apparent success, this precise agreement seems largely fortuitous [72]. This model is exclusively based on thermal diffusion and quite a number of crucial factors are omitted. Firstly, natural convection plays a notable role at the low supercooling, which makes the experimental data deviate from the theoretical prediction at low supercooling [74]. Secondly, crystalline anisotropy is not in the model. Although the model agrees well with the experimental data of υ_{tip} even at large supercooling of −10 °C, the shape of the crystal is no longer parabolic as implicated by the thermal diffusion. Thirdly, local thermodynamic equilibrium is assumed to be satisfied, which is not true for large supercooling. Two of the most striking characteristics of the snowflakes are their hexagonal symmetry and its planar shape. Ice crystals grow only very slowly in a direction perpendicular to the basal plane. Without all these factors involved, the theory of the dendritic growth is fundamentally incomplete.

Nevertheless the information about the growth rate of the ice dendrite permits the comparison between the two time scales of the hydrodynamic impact process and the ice dendrite growth. SLD exists normally above −10 °C in icing cloud, so that the ice dendrite growth has a speed of 50mm/s. This value is significantly lower than the typical impact speed of 100m/s in the in-flight icing. Therefore the ice dendrite growth from singular nucleation site should have no influence on drop impact process.

In the presence of supercooling, the solidification of the supercooled water comprises two stages as observed in multiple experiments [12, 90]. The first stage solidification is the ice dendrite formation. The ice dendrite forms rapidly in the supercooled melt, and the released latent heat warms up the supercooled water to 0 °C [53]. The second stage is the classical solidification. The second stage Solidification takes place during the first stage solidification too, but it is negligible during this short time on account of its significantly lower production rate of the latent heat than the unstable propagation of ice dendrite. Figure 2.23 is a typical scenario of the two stages of solidification.

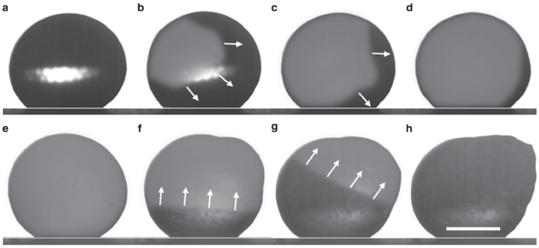

Figure 2.23.: The two-stage solidification of a sessile supercooled drop, observed by Jung et al. [64]. The upper row of photos illustrate the rapid growth of the ice dendrite. Within 18 ms, the ice dendrite covered the surface of the 5 μL drop. The lower row of photos shows the second stage solidification of the drop which took 13 seconds.

Experimental data on the growth rate of the ice dendrite in a drop or bulk water were frequently of lower values than the prediction of Langer and Müller-Krumbhaar's model of marginal instability [12, 64, 80, 90, 100]. The reason is possibly that water of large quantity was difficult to be cooled homogeneously to the indicative temperature which denoted the supercooling. Although the growth rate varied, the shape of ice dendrite should be similar to the snow flake, as Hallett showed in his experiment with bulk supercooled water [46].

The ice dendrite growth in a drop impact differs substantially from that in a sessile drop. In a stationary supercooled melt, nucleation originates from a single nucleation site. On the contrary, the dynamic motion of drop during impact offers numerous initial nucleation sites to start the crystallization volumetrically inside the drop. In fact agitation and mechanical shock have been recognized as a trigger of nucleation ever since 1911 [148, 173]. Consequently, the hydrodynamic process competes with the formation of initial nucleation sites, which could be faster than the drop impact. This open question inspired the experimental investigation described in Chapter 3 and Chapter 4.

Part I.

Impact of Supercooled Water Drops

This part reports the experimental investigation on the supercooled drop impacting on dry surfaces of various temperatures and different wettability. The aim is to evaluate the influence of nucleation and solidification on the drop impact hydrodynamics, and explore the ice dendrite growth in the case of the drop impact.

The experimental setup is sketched in Figure 2.24. A pneumatic drop generator provided water drops in a drop-on-demand mode. The drop fell through a passage which was cooled down to −196 °C by liquid nitrogen and consequently obtained supercooling. The impact surface located in an impact enclosure with controlled temperature. Both shadowgraph imaging and infrared imaging were employed to respectively observe the deformation of the liquid during impact, and to measure the transient temperature field. A labview program compiled with NI 6602 digital counter module provided synchronization of the camera, LED illumination and drop generator. Chapter 3 introduces the experimental setup in detail, and the experimental results are presented in Chapter 4.

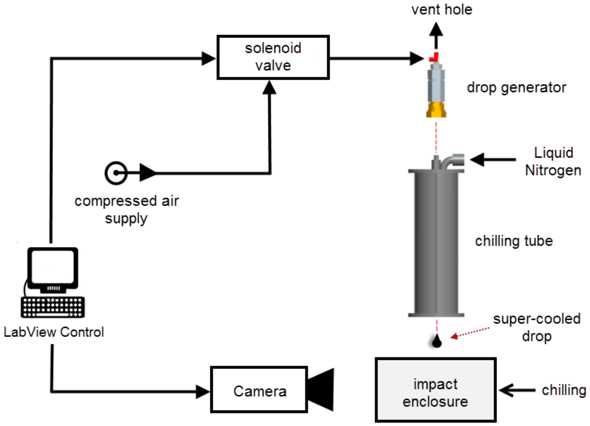

Figure 2.24.: Experiment regime of the impact of supercooled water drop.

3 Experimental Setup

This chapter introduces the experimental setup and discusses the uncertainties in the temperature measurement. Section 3.1 gives a detailed description about the supercooling method, including calculation of the drop temperature and the construction. Section 3.2 introduces the pneumatic drop generator. Section 3.3 describes the impact surface and the three imaging plans. The measurement of the static contact angle of different surfaces is also in this section. Section 3.4 is devoted to the infrared imaging, including the calibration of the camera, analysis on uncertainties, and a demonstration of measurement of the drop temperature. Section 3.5 briefly describes the synchronization and operation of the experimental setup.

3.1 Supercooling Method

Supercooling is a metastable state and tiny thermal perturbations are able to break this circumstance. Water is especially easy to nucleate. Various methods are reported to create supercooled water in experiments. These methods can be divided into two categories. The first is suspending small amount of water sample in a cold atmosphere and cooling it by free convection. The water sample can be suspended completely in the air for instance by acoustic levitation [12], or can be hung at the tip of a thermal couple [4], a needle [64] or a thin wire loop [135–137]. The second category is cooling a small sample of water in an insulated container. The container can be out of in a pyrex or fused silica [46], PMMA [90] or coated by Teflon [172]. The cooling method in this case is arbitrary, such as free convection [46], fluid refrigerant [90] or peltier element [172]. All these methods share two aspects in common: the water sample is of tiny amount, and the cooling heat flux is very low [52]. Large temperature gradient and high heat flux favors the thermal perturbation, therefore detrimental for the existence of supercooling.

The vulnerability of the supercooled water forbids its application in the most drop generators because they usually function with deformation of the liquid. Supercooled water drop is conventionally created in the icing wind tunnel for aircraft icing test. Tiny water drops (below $50\,\mu$m for conventional icing condition and below $500\,\mu$m for SLD condition) are fed into cold airflow at icing temperatures between $0\,°$C and $-20\,°$C. After a long traveling distance (several meters at least), water drops achieve thermal equilibrium with the air flow. This operation is in general extremely expensive because the expensive construction of cooling system and the power-hungry operation of the entire icing wind tunnel.

In order to achieve a solution of low cost and work with larger water drops for the convenience of optical observation, liquid nitrogen was employed to create a cold passage at −196 °C. The water droplet with an initial temperature of 0 °C fell through a short but cold passage within a short time (approximately 0.4 s for a falling distance of 0.6 m), and was expected to have an appreciable supercooling, such as −10 °C.

3.1.1 Temperature of the Water Drop in Free Fall

Assuming a drop keeps spherical all through the free fall and neglecting the inner convection, the velocity of the drop in free fall is governed by

$$m\ddot{y} = mg - \frac{1}{2}\rho_{air}\, c_d A \dot{y}^2, \tag{3.1}$$

where m is the mass of the drop, A is the reference area $A = \pi\left(\frac{d}{2}\right)^2$, c_d is the drag coefficient for a sphere given by [95]

$$c_d = \frac{24}{Re} + \frac{2.6\left(\frac{Re}{5.0}\right)}{1+\left(\frac{Re}{5.0}\right)^{1.52}} + \frac{0.411\left(\frac{Re}{263000}\right)^{-7.94}}{1+\left(\frac{Re}{263000}\right)^{-8.00}} + \left(\frac{Re^{0.80}}{46100}\right). \tag{3.2}$$

This formula is valid for Re from 0.1 to 1×10^6. The initial conditions are

$$y = 0, \quad t = 0, \tag{3.3}$$

and

$$\dot{y} = 0, \quad t = 0. \tag{3.4}$$

The heat transfer between the drop and the cold environment is accomplished by free convection, forced convection and thermal radiation. The free convection contributes little because the velocity of the drop increased rapidly. The contribution of the thermal radiation is negligible as estimated in the following. The tube was anticipated to have a length of 600 mm, at least 200 times larger than the drop diameter. Therefore it is reasonable to model the thermal radiation between the drop and the tube as between such two surfaces that one is completely enclosed by the other. This case is equivalent to thermal radiation between two parallel flat surfaces. Assuming both the water surface and the copper surface are not transparent for the thermal radiation, and thus only emission and reflection exist, the heat flux density (in $\mathrm{W\,m^{-2}}$) results in

$$\dot{q} = C_{12}\left[\left(\frac{T_1}{100}\right)^4 - \left(\frac{T_2}{100}\right)^4\right], \tag{3.5}$$

where T_1 and T_2 are taken at $273\,\mathrm{K}$ and $77\,\mathrm{K}$ respectively for water and copper surfaces. The coefficient C_{12} is defined as

$$C_{12} = \frac{C_S}{\frac{1}{\varepsilon_1} + \frac{1}{\varepsilon_2} - 1}, \tag{3.6}$$

where C_S is $5.67\,\mathrm{J\,s^{-1}\,m^{-2}\,K^{-4}}$, a scaled coefficient derived from Stefan-Boltzmann constant for the convenience of arithmetic. ε_1 and ε_2 are emissivity of water and copper, taken as 0.96 and 0.049 respectively [139]. The emissivity of metal is in general very low because of the high reflectivity.

Substituting these values into Eq. 3.5 and Eq. 3.6, the heat flux density of radiation is $15.3\,\mathrm{W\,m^{-2}}$. This value is negligible compared to heat transfer by forced convection: $6\,\mathrm{W\,m^{-2}\,K^{-1}}$ to $260\,\mathrm{W\,m^{-2}\,K^{-1}}$ at temperature differences of over $150\,\mathrm{K}$ as computed below. Therefore only the forced convection is considered in the temperature calculation.

The heat transfer by forced convection is governed by

$$\dot{Q} = h_{conv}A(T - T_\infty) = \frac{cm\Delta T}{\Delta t}, \tag{3.7}$$

where h_{conv} is the heat transfer coefficient, A is the surface area, $A = \pi d^2$, m is the mass of the drop, c is the specific heat of water at the temperature T. The initial condition is:

$$T(t = 0) = 0. \tag{3.8}$$

The heat transfer coefficient h_{conv} is calculated by the Nusselt number:

$$Nu = \frac{h_{conv}d}{k_{air}}. \tag{3.9}$$

The Nusselt number of a sphere in an airflow is given by [139]

$$Nu = 2 + \sqrt{Nu_{lam}^2 + Nu_{turb}^2}, \tag{3.10}$$

with

$$Nu_{lam} = 0.644Re^{\frac{1}{2}}Pr^{\frac{1}{3}}, \tag{3.11}$$

and

$$Nu_{turb} = \frac{0.037Re^{0.8}Pr}{1 + 2.443Re^{-0.1}(Pr^{\frac{2}{3}} - 1)}. \tag{3.12}$$

The chilling passage was planed to be a copper pipe with inner diameter of 10 mm and wall thickness of 0.5 mm. All around this pipe was liquid nitrogen at −196 °C. The air temperature at the inlet and outlet of the chilling passage was higher because both of the positions were imperfectly insulated. In the calculation the air temperature was taken as 100 K as an average, thus $T_\infty = 100\,\mathrm{K}$. The temperature of the drop was not homogeneous on account of the low thermal conductivity of the water substance. But the temperature difference inside the drop should be significantly smaller than the difference between the drop and the cold environment. Hence the driven temperature difference was taken as between the average temperature of the drop and the air temperature.

The thermal properties of air was taken at 100 K: air density $\rho_{air} = 3.552\,\mathrm{kg\,m^3}$, kinematic viscosity $\nu = 1.257 \times 10^{-6}\,\mathrm{m^2\,s^{-1}}$, Prandtl number $Pr = 0.75$, thermal conductivity $k_{air} = 9.32 \times 10^{-3}\,\mathrm{W\,m^{-1}\,K^{-1}}$. The density [48], the specific heat [7], the viscosity [45] and the thermal conductivity [57] of supercooled water were taken as Table 3.1.

Eq. 3.1 is a second order Ordinary Differential Equation (ODE) and Eq. 3.7 is a first order ODE. They were numerically solved by the forward Euler method with time step of 0.001 s. More details on the numerical computation can be found in the ADP report of P. Stegmann et al. [8]. The results are shown in the diagrams in Figure 3.1. This computation suggested that this supercooling method was able to create supercooled water drops effectively.

It should be noted that the initial temperature of the water must be kept a couple of Celsius above the freezing point to avoid freezing in the drop generator. Furthermore, Figure 2.20 shows that at the deepest achievable supercooling of 10 K, merely 12.8% water could be frozen. In order to observe a stronger influence of nucleation ice dendrite growth, smaller drops should be used, as long as the resolution of imaging allows.

Temperature °C	Density $\mathrm{kg\,m^{-3}}$	Specific Heat $\mathrm{J\,kg^{-1}\,K^{1}}$	Dynamic Viscosity $\mathrm{kg\,m^{-1}\,s^{-1}}$	Conductivity $\mathrm{W\,m^{-1}\,K^{-1}}$
0	999.99	4.2136	1.79	0.5611
−1	999.98	4.2164	1.86	0.5592
−2	999.97	4.2192	1.93	0.5573
−3	999.96	4.2220	2.01	0.5554
−4	999.94	4.2274	2.08	0.5535
−5	999.93	4.2328	2.16	0.5516
−6	999.91	4.2382	2.25	0.5498
−7	999.89	4.2436	2.35	0.5479
−8	999.87	4.2490	2.45	0.5460
−9	999.84	4.2546	2.55	0.5442
−10	999.82	4.2602	2.66	0.5423

Table 3.1.: Properties of supercooled water.

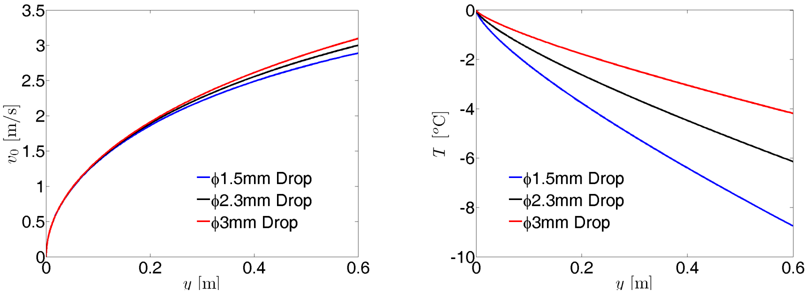

Figure 3.1.: The analytically predicted velocity and temperature profiles of water drops in free fall.

3.1.2 Heterogeneous Temperature Field inside the Water Drop

The Biot number, $Bi = (h_{conv}d)/\lambda_{water}$, is an indicator of the temperature gradient in a transient heat conduction problem. The Bi increases rapidly in the free fall as the drop velocity rises. At the exit of the cooling passage, the Biot numbers are 0.86, 1.01 and 1.21 for the 1.5 mm, 2.3 mm, and 3 mm drops according to the analytical computation in the last subsection. Such high Bi indicates large temperature gradient inside the drop.

The one dimensional heat transfer in the sphere coordinate system is governed by

$$\frac{\partial T}{\partial t} = \frac{\alpha}{r^2}\frac{\partial}{\partial r}\left(r^2\frac{\partial T}{\partial r}\right). \tag{3.13}$$

The initial condition is

$$T(r, t=0) = T_A. \tag{3.14}$$

The boundary condition is

$$\left(\frac{\lambda}{h_{conv}}\frac{\partial T}{\partial r} + T\right)_{r=R} = T_\infty, \quad t > 0, \tag{3.15}$$

where R is the radius of the drop.

Introducing the dimensionless temperature Θ

$$\Theta \equiv \frac{T - T_\infty}{T_A - T_\infty}, \tag{3.16}$$

the dimensionless distance from the center of the sphere

$$\chi \equiv \frac{r}{R}, \tag{3.17}$$

and the Fourier number as the dimensionless time

$$Fo = \frac{\alpha t}{R^2}, \tag{3.18}$$

Eq. 3.13 is transformed to

$$\frac{\partial \Theta}{\partial Fo} = \frac{1}{\chi^2}\frac{\partial}{\partial \chi}\left(\chi^2\frac{\partial \Theta}{\partial \chi}\right). \tag{3.19}$$

The initial condition becomes

$$\Theta(\chi, 0) = 1. \tag{3.20}$$

The boundary condition is then

$$\left(\frac{1}{Bi}\frac{\partial\Theta}{\chi}+\Theta\right)_{|\chi|=1}=0, \quad Fo>0. \tag{3.21}$$

An exact solution of this Partial Differential Equation (PDE) is of impractical form. However a simplified solution exists when the time is so short that the sphere can be regarded as a semi-infinite plate.

Defining the dimensionless distance from the surface χ^* as

$$\chi^* \equiv \frac{|x|}{2\sqrt{\alpha t}}, \tag{3.22}$$

where $|x|$ is the distance from the surface, and a different form of the Biot number Bi^* as

$$Bi^* \equiv \frac{h_{conv}\sqrt{\alpha t}}{\lambda}\left(Bi\sqrt{Fo}\right), \tag{3.23}$$

Eq. 3.13 has the solution [26]:

$$\Theta = erf\,\chi^* + e^{-\chi^{*2}}e^{(\chi^*+Bi^*)^2}\left[1-erf(\chi^*+Bi^*)\right]. \tag{3.24}$$

A precise calculation of this equation requires numerical methods, because the Bi^* varies with the transient heat transfer coefficient. A rigorous mathematical treatment is excessive for the purpose of qualitative evaluation of the temperature inhomogeneity. Therefore the h_{conv} is taken as a constant, which is the average of the instantaneous heat transfer coefficients calculated in the last subsection. The temperature field of the $\phi 1.5$ mm and the $\phi 3$ mm drop at four times are shown in Figure 3.2.

Heterogeneity of the temperature is significant in both cases. The supercooling exists only near the surface of the drop. Although unfavored by the existence of the supercooled liquid, the large temperature gradient did not fail the supercooling method.

Since the empirical correlations for the drag coefficient and the convective heat transfer coefficient are well validated in the past decades, the error of this analytical analysis results from the assumptions as summarized in the following. Firstly, the initial condition and the boundary condition are idealized as uniform and constant, while such ideal conditions can not be fulfilled in experiments. The initial

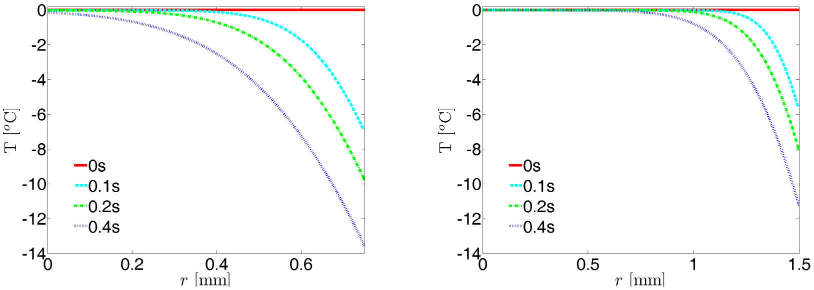

Figure 3.2.: The analytically predicted transient temperature fields inside the drop of $\phi 1.5\,\mathrm{mm}$ (left) and $\phi 3\,\mathrm{mm}$ (right).

temperature of the water must be above 0 °C to avoid freezing, and the temperature in the supercooling passage was nonuniform. Secondly, the convective heat transfer is taken as homogeneous and temporally invariant. In fact the convection is dependent on the local velocity of the gas flow, which is neither spatially nor temporally constant. Finally, the simplification of the semi-infinite plate is actually violated in the case of the $\phi 1.5\,\mathrm{mm}$ drop, because the temperature at the center of the drop reduces. Therefore this computation serves as a qualitative justification of the supercooling method, instead of precise prediction of the temperature of the drop. In-situ measurement of the drop temperature is necessary.

3.1.3 Construction of the Supercooling Method

Two technical problems accompanied this supercooling method. One was the condensation at −196 °C, the other was the temperature control of the drop generator.

At such a low temperature no desiccants could eliminate the condensation in and around the cooling passage, since these substances achieve the lowest dew point of −80 °C. The solution was to create a dry nitrogen atmosphere as Figure 3.3 illustrates. On the right side of the photo there is a 0.6 m long chilling tube, which was a container for the liquid nitrogen. A copper pipe with 10 mm inner diameter and 0.5 mm wall thickness was fixed along the center line of the chilling tube, providing the cold passage for supercooling. The drop generator was right above the chilling tube, shown in brown. All these components were enclosed by walls around the frames. Two walls of the enclosure are made transparent in the CAD picture for the convenience of exhibition. All the walls as well as the chilling tube were insulated by 19 mm thick Armaflex LTD material (thermal conductivity

0.021 W m^{-1} K^{-1} at −165 °C) except the yellow bottom plate, which was made of a rigid material, Polystyrene (Styrodur 2800 C, 50 mm thick, thermal conductivity 0.033 W m^{-1} K^{-1}).

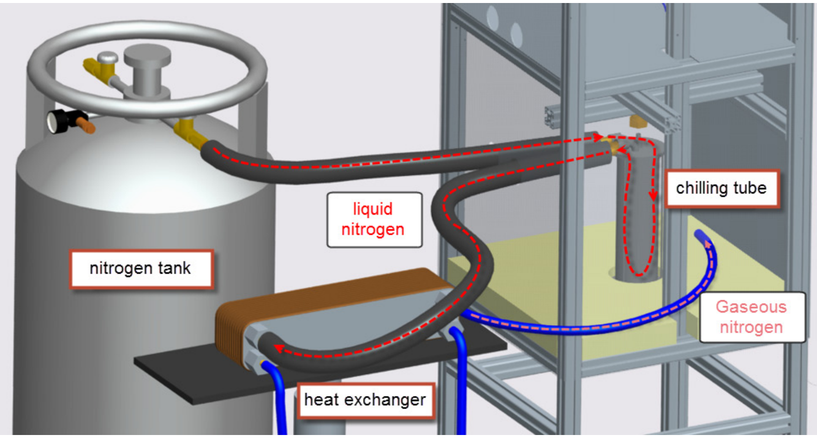

Figure 3.3.: Construction of the supercooling passage, and creation of the dry nitrogen atmosphere.

The liquid nitrogen flew firstly to the chilling tube to create the cooling passage. Then it entered a compact heat exchanger in the liquid state. The liquid nitrogen was transformed to the gas phase by tap water flowing on the warm side of the exchanger. The cold nitrogen gas was then fed into the enclosure to form a dry nitrogen atmosphere. The flow of nitrogen gas must be continuous, because the enclosure was so dry that once the nitrogen gas flow stopped, humidity entered the enclosure and condensed on the inlet of the cold passage. Meanwhile, the gas flow was kept at such a weak level that the the drop generation was undisturbed by the gas flow. Sufficient amount of liquid nitrogen was stored in the vacuum insulated container on the left side of Figure 3.3 to facilitate the continuous feed of the dry gas.

The drop generator was cooled down to 0 °C by forced convection induced by the cold nitrogen gas flow. In order to avoid freezing, a surface temperature sensor (Self Adhesive Patch Thermocouple, NiCr-Ni (K), −100 °C to 200 °C, response time 70 ms, Conatex, St. Wendel, Germany) and a Peltier-Element (5.4 mm×10 mm×10 mm, rated voltage 0.8 V, power 1.6 W maximum, Conrad, Germany) was stick to the brass outlet of the drop generator. The temperature of the gas could be varied between −20 °C and −50 °C by changing the flow rates of the tap water and the nitrogen. In operation, it was ensured that the read temperature from the temperature sensor was always at 0 °C. On account of the thermal resistance of the brass cap and the thermal contact resistance, the initial temperature of the drop was not very precisely controlled, which resulted in variation of the initial temperature for around 3 K. This construction was supported by P. Stegmann et al. in their ADP work [8] and K. Heinbücher in her Bachelor thesis [51].

3.2 Pneumatic Drop Generator

Smaller drops were preferred by supercooling, while larger drops were advantageous for visualization. 1 mm to 2 mm would be the optimal diameter range. An additional requirement was that the drop must have zero horizontal velocity, or else it probably impacted on the inner wall of the cold passage and blocked it by freezing.

The most simple way to generate a drop is to allow liquid to flow slowly out of a needle. When the gravity of the suspending liquid exceeds the surface tension and the adhesive force between the liquid and the needle surface, the drop detaches itself. The thinnest needle found on the market was the "FS 0.17" from Hamilton. This silica needle had 170 μm outer diameter and 80 μm inner diameter. According to $mg = \pi d \sigma \sin(\theta)$, the detaching drop should be 1.94 mm in diameter, taking $\theta = 90°$. In fact the drop had a larger diameter, roughly 3 mm, implying that the adhesive force on the liquid/solid interface is considerable.

A logic idea to create smaller droplets with a needle is to increase the "gravity", for example by an additional upward acceleration created by a spring which jumps upwards. Another option is the electrostatic force, by placing an electrode with a high voltage underneath the needle tip. In order to generate drops between $\phi 1$ mm and $\phi 2$ mm by a $\phi 0.3$ mm needle which produces normally $\phi 3$ mm drop, the auxiliary acceleration must be between $3.4g$ and $27g$. The method with the electrostatic field was experimentally tried out. A $\phi 4$ cm circular plate with a hole of $\phi 5$ mm in the center was put 5 mm beneath the needle and connected with 2.8 kV. Drop of $\phi 1$ mm detached successfully and rushed through the center hole. However, as soon as the needle tip had any offset from the center of the plate, the drop flew inclined along the electric field, impacting on the cold passage. The horizontal velocity was significant, because the electrical field was multiple times greater than the gravity field. Imaginably, a spring would have the same problem. Therefore this method was abandon.

Another kind of drop-on-demand drop generator exerts a pulse of pressure on water of a small amount in a chamber, which has a tiny hole on the bottom as the outlet of the liquid. There are two methods to provide the pressure pulse. The first is the piezoelectric effect such as the drop generator in an inkjet printer cartridge. On account of minimal movement of the piezoelectric element, this method generates small droplets typically below $\phi 20\,\mu\mathrm{m}$ [169]. The other is pneumatic as depicted in Figure 3.4. Thanks to discussion with the inventors, Prof. S. Chandra and his group, we acquired the design of the prototype and amended the drop generator according to our specific demands.

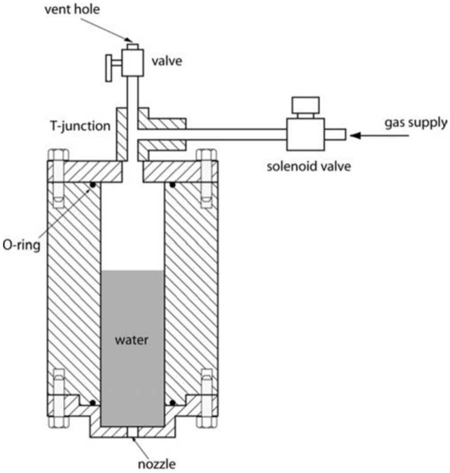

Figure 3.4.: The body of the drop generator consisted of a cylinder container with water and a T-junction. The diameter of the nozzle was too small for liquid to flow through it by gravity alone. A pressure pulse was delivered by fash switch of the solenoid valve. The vent hole was open to the atmosphere. A gas pulse applied sufficient pressure to force out a single drop. Then the gas escaped to the atmosphere through the vent, preventing further drops from escaping. Water drops of $\phi 230\,\mu\mathrm{m}$ was generated with a $\phi 102\,\mu\mathrm{m}$ nozzle [29].

3.2.1 Construction

Figure 3.5 and Figure 3.6 depict the construction of the pneumatic drop generator. The drop generator was composed of one T-conjunction at the top with the exit tube, several thread adapters from Pipe thread EN G 1/4 (or G 1/8 for the one with small T-conjunction) to G 1, a Pipe thread EN G 1 end cap, a Teflon sealing ring and a pinhole. The hydraulic components were purchased from Landefeld. The sealing ring was manufactured. The precision pinhole was from EdmundOptics with the hole diameter of 800 μm or 500 μm. The end cap was made of brass and the pinhole was made of stainless steel, so that the contained water sample could be cooled down to 0 °C by forced convection of the nitrogen gas at the outer surface of these metal components. The other components were made of less conductive materials (thread adapters out of Polypropylene and PVC, T-conjunction out of Polyamide 66), for the sake of better temperature control. The Peltier element and the temperature sensor mentioned in the last section was stuck to the brass cap.

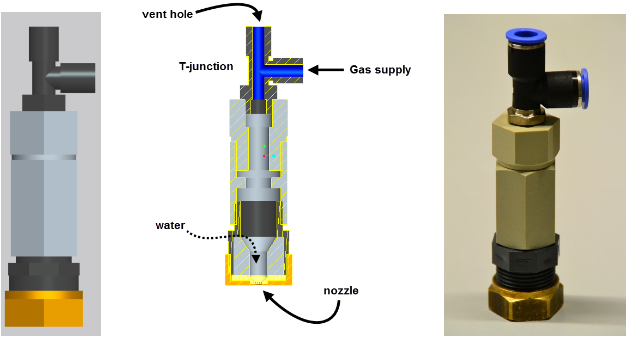

Figure 3.5.: Construction of the pneumatic drop generator with big T-conjunction.

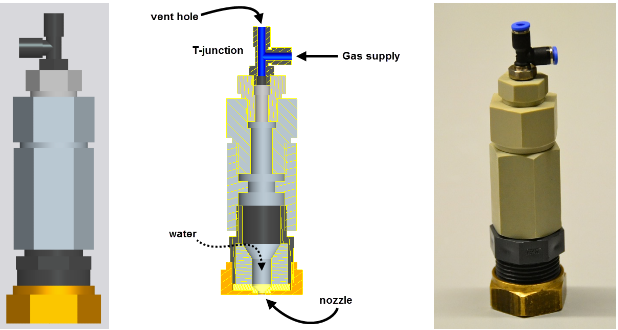

Figure 3.6.: Construction of the pneumatic drop generator with small T-conjunction.

The maximum depth of water in the container is determined by the diameter of the pinhole as

$$H = \frac{2\sigma cos\theta}{\rho g R}, \tag{3.25}$$

where σ is the liquid-air surface tension, θ is the contact angle of water on stainless steel (roughly 45° [20]), R is the radius of the pinhole. Therefore the maximum height is 24 mm for $\phi 800\,\mu$m pinhole and 38 mm for $\phi 500\,\mu$m pinhole. In practice 10 mm deep water was fed to the drop generator. The air pressure was provided by the compressed air (maximum 6 bar in the lab) and a miniature pressure regulator (R308-P0, 0 bar to 0.25 bar, AirCom Pneumatic GmbH, Ratingen, Germany). The pulse was provided by a solenoid valve (Model: M 218 24 V=, Landefeld, Germany) which was controlled by NI 6602 digital counter module. The solenoid valve was not manufactured for the fast operation and the response time was not indicated in the product information. Therefore the valve was probably not fully opened while responding to the controlling 24 V pulses of milliseconds duration.

Typical performance of the pneumatic drop generator is demonstrated by image sequences from Figure 3.7 to Figure 3.11 with the specific construction and parameter settings noted in the caption. Drops of desired diameter were acquired. Figure 3.12 from the inventors of the original prototype provides a qualitative description of the function mechanism. Another advantage of the drop generator was that the drop has zero initial velocity, so that it would not impact on the chilling passage as long as the positioning was ensured. The construction was supported by E. Wagenknecht with his Bachelor thesis [155], where the performance demonstration of this device was firstly introduced. Further analysis is conducted here in this section.

3.2.2 Operation

The performance of the pneumatic drop generator was determined by both the mechanical construction and the two controlling parameters, the pressure level and the pulse duration. The simple construction and operation lead to easy custom reconstruction for particular applications. This subsection offers guidelines on the product design by inspecting the function principle of the drop generator further.

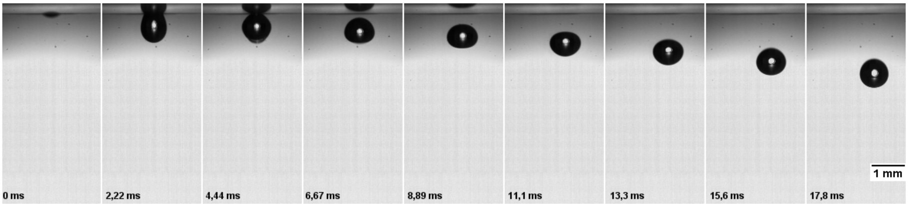

Figure 3.7.: Pneumatic drop generator with big T-conjunction, $7.5\,\mathrm{cm}$ exit tube, $500\,\mu\mathrm{m}$ pinhole, $0.1\,\mathrm{bar}$ pressure, $4\,\mathrm{ms}$ pulse width.

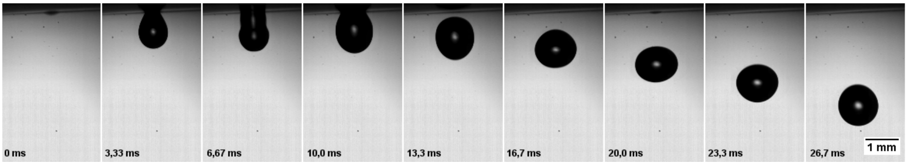

Figure 3.8.: Pneumatic drop generator with big T-conjunction, $7.5\,\mathrm{cm}$ exit tube, $800\,\mu\mathrm{m}$ pinhole, $0.1\,\mathrm{bar}$ pressure, $3\,\mathrm{ms}$ pulse width.

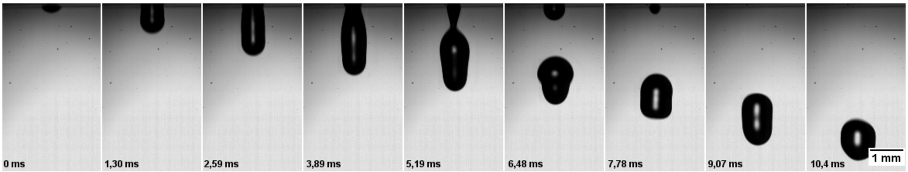

Figure 3.9.: Pneumatic drop generator with small T-conjunction, $10\,\mathrm{cm}$ exit tube, $500\,\mu\mathrm{m}$ pinhole, $0.1\,\mathrm{bar}$ pressure, $3\,\mathrm{ms}$ pulse width.

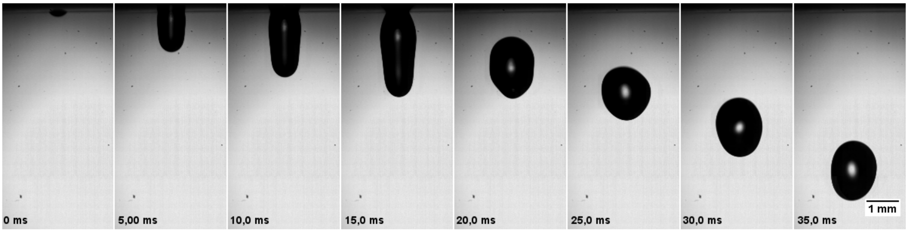

Figure 3.10.: Pneumatic drop generator with small T-conjunction, $4.5\,\mathrm{cm}$ exit tube, $500\,\mu\mathrm{m}$ pinhole, $0.1\,\mathrm{bar}$ pressure, $4\,\mathrm{ms}$ pulse width.

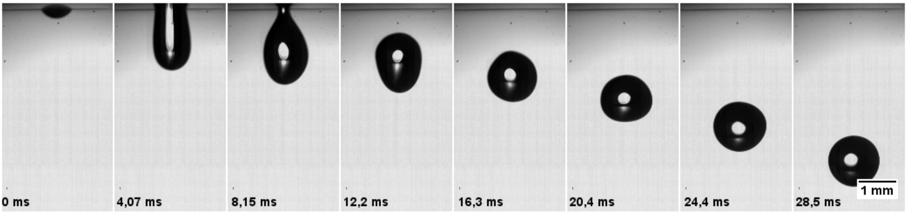

Figure 3.11.: Pneumatic drop generator with small T-conjunction, $6\,\mathrm{cm}$ exit tube, $800\,\mu\mathrm{m}$ pinhole, $0.1\,\mathrm{bar}$ pressure, $3\,\mathrm{ms}$ pulse width.

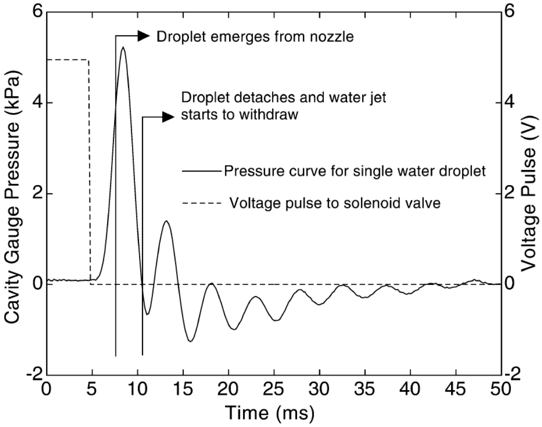

Figure 3.12.: Time $t = 0$ corresponds to the start of the electrical pulse. The pressure in the cavity oscillated at a constant frequency while its amplitude gradually decreased. The gauge pressure was initially positive, but then became negative for a short time as it oscillated. Water emerged when the pressure exceeded a level, and detached while the remaining liquid started to withdraw at the negative pressure. This pressure oscillation inside the chamber can be modeled as a Helmholtz resonator with a damping frequency as $f = \frac{a}{2\pi}\frac{A}{lV}$, where A is the cross-sectional area of the neck and l is the effective length (defined as $l = l_n + 0.8\sqrt{A}$, with l_n the neck length, V the volume of the cavity and a the speed of sound in air [29].

Flexible Construction

The intake tube (between the solenoid valve and the T-conjunction) as well as exit tube (between the T-conjunction and the outer atmosphere) can be amended for different lengths. Both of the tubes influence the pressure peak inside the chamber.

A longer intake tube leads to lower pressure peak inside the chamber due to friction in the tube. The pressure drop is described by Darcy-Weisbach equation as

$$\Delta p = f_d \frac{l}{d} \frac{\rho v^2}{2}, \tag{3.26}$$

where l is the length of the tube, d is the hydraulic diameter of the tube, ρ is density of the compressed air, v is velocity of the air flow, f_d is the Darcy friction factor. This friction was economically beneficial. The minimum pressure required to force the liquid out of the pinhole is given by Eq. 3.26 as $\Delta p = 2\sigma cos(\theta)/R_{jet}$. This yields 396 Pa and 247 Pa for $\phi 500\,\mu$m and $\phi 800\,\mu$m pinhole respectively. Operation at such low gauge pressures demand very expensive low pressure regulators. Friction in the intake tube helps to increase the pressure level, making an ordinary regulator applicable. The finally applied pressure were significantly higher than the minimum value, as indicated in the caption of Figure 3.7 to Figure 3.11.

The exit tube raises the pressure peak as the length increased [43], likewise according to Darcy-Weisbach equation. The exit tube provided another possibility of pressure control by simply changing the tube length. This was helpful on precise regulation at low pressures.

The intake and exit tubes helped to avoid condensation. Since the atmosphere around the drop generator and the chilling tube was dry nitrogen gas, the compressed air with humidity was not allowed to enter this region. The compressed air was fed into the drop generator with the intake tube and exhausted outside the enclosure with the exit tube. The two tubes isolated the compressed air from the dry nitrogen atmosphere.

Adjusting the Pressure Level

The pressure is to be optimized by two conflicting factors. On the one hand, the pressure peak must be sufficient, or else the liquid is retracted back to the chamber without detachment, as shown in Figure 3.13.

On the other hand, the pressure should not be too high. An excessive pressure peak pushes out a long liquid jet, which dissembles into multiple drops, as shown

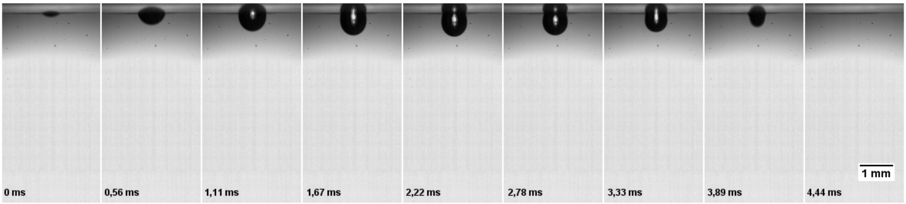

Figure 3.13.: Pneumatic drop generator with big T-conjunction, 4.5cm exit tube, 500μm pinhole, 0.1bar pressure, 3ms pulse width

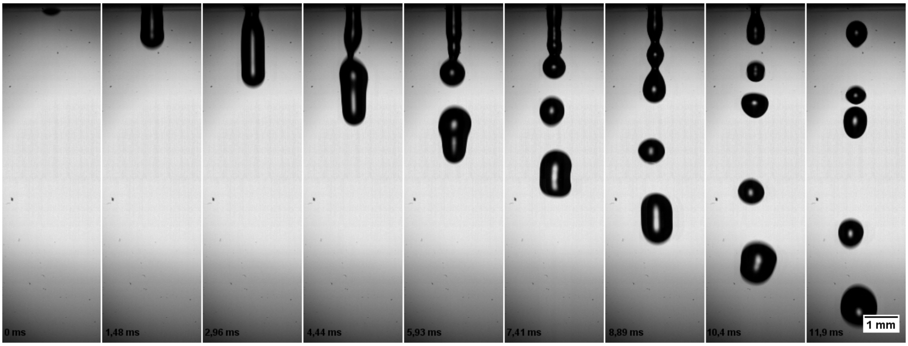

Figure 3.14.: Pneumatic drop generator with small T-conjunction, $10\,\mathrm{cm}$ exit tube, $500\,\mu\mathrm{m}$ pinhole, $0.2\,\mathrm{bar}$ pressure, $3\,\mathrm{ms}$ pulse width.

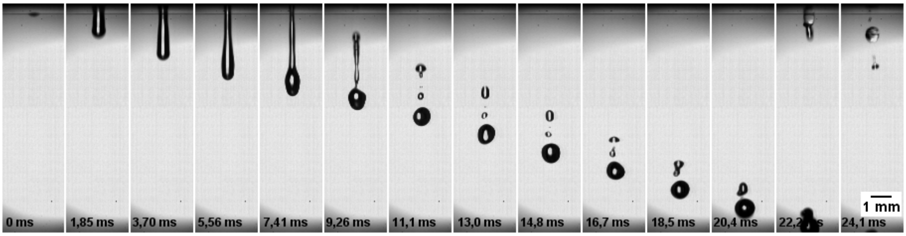

Figure 3.15.: Pneumatic drop generator with big T-conjunction, $26\,\mathrm{cm}$ exit tube, $500\,\mu\mathrm{m}$ pinhole, $0.2\,\mathrm{bar}$ pressure, $3\,\mathrm{ms}$ pulse width.

in Figure 3.14. Moreover the pressure can be insufficiently damped after the first pressure peak, which consequently leads to continual drop generation by the subsequent pressure peaks, as shown in Figure 3.15. It is advisable to set pressure slightly higher than the sufficient level to facilitate single drop generation.

Necessity of the Negative Pressure

The presence of the negative pressure after the first pressure peak plays an indispensable role on a successful operation of the drop generator. In Figure 3.16, the water was not completely retracted back into the chamber. Upon the second trigger, water dripped out of the outlet.

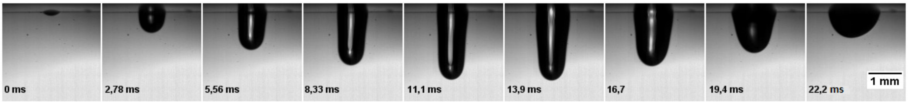

Figure 3.16.: Pneumatic drop generator with small T-conjunction, no exit tube, 500 μm pinhole, 0.3 bar pressure, 4 ms pulse width.

Figure 3.17 illustrates a successful operation of the first drop. Although unseen, the outlet was wet, and water dripped out upon the second trigger. It was therefore necessary to make several tests before ran it in the experiment.

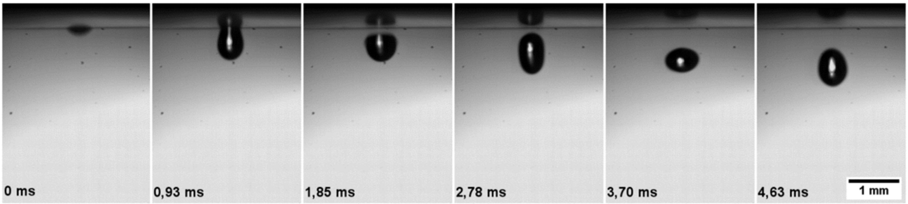

Figure 3.17.: Pneumatic drop generator with big T-conjunction, no exit tube 500 μm pinhole, 0.5 bar pressure, 4 ms pulse width.

It was experimentally found out that a certain length of the exit tube is necessary to maintain the negative pressure of sufficient level. Figure 3.12 shows that the first negative pressure peak is typically pretty low. The presence of the exit tube helps to reduces the resonate frequency and consequently increases the duration of the negative pressure. The final effect is stronger retraction of the liquid.

Adjusting the Pulse Width

Longer electrical pulse width, in other words longer opening time of the solenoid valve, could raise the pressure peak inside the chamber slightly [43], but for application it was of little influence, as the comparison between Figure 3.7 and Figure 3.18, as well as the comparison between Figure 3.10 and Figure 3.19 demonstrates.

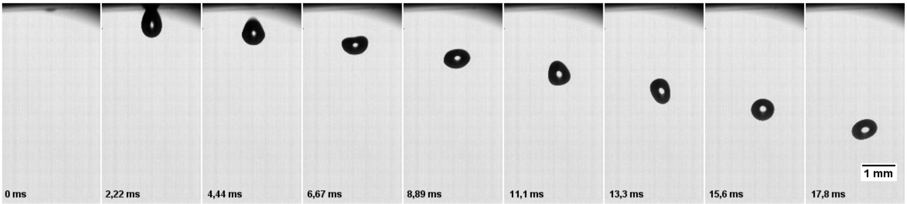

Figure 3.18.: Pneumatic drop generator with big T-conjunction, 7.5 cm exit tube, 500 μm pinhole, 0.1 bar pressure, 20 ms pulse width.

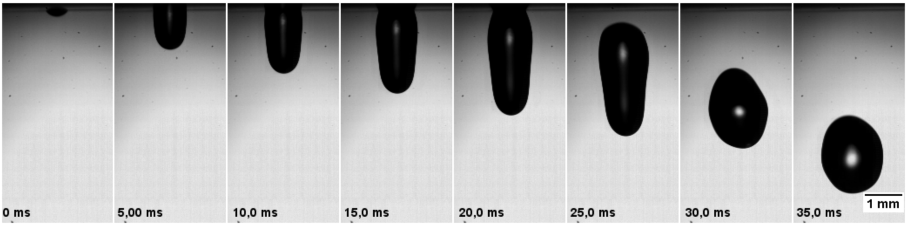

Figure 3.19.: Pneumatic drop generator with small T-conjunction, 4.5 cm exit tube, 500 mm pinhole, 0.1 bar pressure, 10 ms pulse width.

The opening time of solenoid valve exhibited notable effects only when the net force on the coming drop existed, but it then created a longer water jet which separated into multiple drops, spoiling the requirement of the drop-on-demand generation mode. Therefore it was advisable to apply short pulse. Only the minimum values were applied in the experiments: 3 ms to 4 ms, since the solenoid vale did not respond on pulses shorter than 3 ms.

The Range of the Drop Diameter

The drop diameter was influenced by both the diameter of the pinhole and pressure profile of inside the chamber. Table 3.2 summarizes the diameters of the drop acquired in the tests and the corresponding constructions. The pressure setting is not listed, because it is dependent on the construction, and is therefore not meaningful for comparison. Both the pressure and the duration of the pulse were set to be slightly above the sufficient level, as suggested by the test results above.

T-Conjunction	Exit tube	Pinhole	Drop diameter
Big	75 mm	500 μm	0.80 mm
Big	75 mm	800 μm	1.15 mm
Small	45 mm	500 μm	1.67 mm
Small	60 mm	800 μm	1.36 mm

Table 3.2.: Achieved drop diameter by the pneumatic drop generator of different constructions.

The T-conjunction influences the pressure peak and the damping frequency on account of difference sizes of the cross section, according to the Helmholtz resonator. Smaller cross section led to a higher level and a longer duration of the first pressure peak, which consequently squeezed more liquid out of the pinhole, forming bigger drops. It was observed that the small T-conjunction was accompanied with larger drops than the big T-conjunction.

Bigger pinholes tended to produce bigger droplets, as the results with the big T-conjunction indicate. The results acquired with the small T-conjunction exhibit the opposite direction, because the 500 μm pinhole required a longer pulse than the 800 μm pinhole, therefore more liquid was squeezed out, forming a larger drop. It is expectable that if the pulse widths are equal and the pressure for the 500 μm is increased, the drop diameter should be smaller.

Drops of ϕ 1.5 mm was the most favorite compromise for both cooling and the observation. Therefore the construction with small T-conjunction and 800 μm pinhole was chosen for the application in the experiment.

3.3 Observation Plans

Three type of imaging were planned for the observation of the supercooled drop impact, as Figure 3.20 depicts. The first was shadowgraph imaging, in order to observe the dynamic motion of the drop during impact. The second was of similar construction but with the infrared camera, in order to measure temperature of the drop both before impact and during rebounding on hydrophobic surfaces. This plan is named as the side-view infrared imaging. The third was to measure the contact temperature between the substrate and the residual lamella. It is named as the bottom-view infrared imaging.

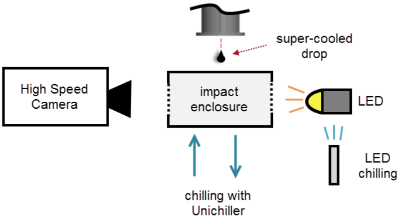

(a) Shadowgraph imaging

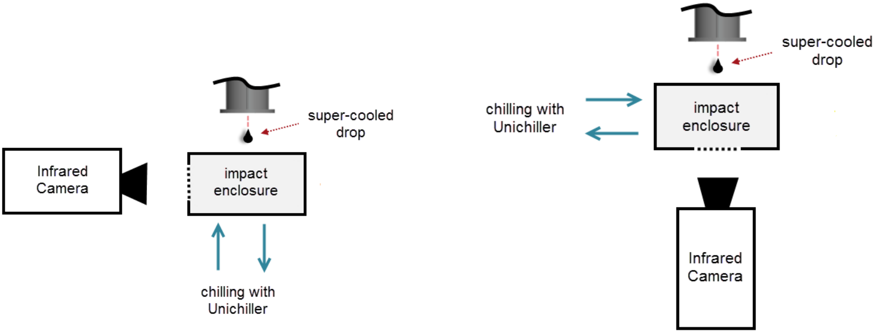

(b) The side-view (left) and bottom-view (right) infrared imaging.

Figure 3.20.: Observation plans

The impact surface must have the typical in-flight icing temperatures, from 0 °C to −20 °C, and keep dry throughout the operation. The temperature control was provided by a cold plate with internal circulating refrigerant, as Figure 3.21 shows. The cold plate was contained in a box out of Polystyrene, which was named as the impact enclosure. The enclosure on the left is for the bottom-view imaging. Its interior dimension was 145 mm×220 mm×45 mm. The enclosure on the right was for the side-view imaging. It had 330 mm×90 mm×50 mm interior space. The coolant was further cooled by a chilling machine (Unichiller UC020Tw, temperature range −20 °C and 40 °C, refrigerant is Ethylene glycol, Peter Huber Kältemaschinenbau GmbH, Offenburg, Germany).

Likewise condensation was a serious issue as it happened to the supercooling passage. The enclosure must have an opening on account of the entrance for the impinging drop. The desiccant can not avoid condensation because of this opening.

As soon as the air inside the enclosure is cooled down below the dew point, water condenses on the cold surface. Moisture of the outer atmosphere was consequently transported by diffusion into the box where the concentration of water vapor is lower. The colder the impact surface is, the faster the diffusion becomes. The slow adsorption of humidity by desiccants is unable to guaranty a dry impact surface. Therefore cooling was undertaken as the drying method. A Peltier-element (40 mm×40 mm×4 mm, rated voltage 15.4 V, maximum power 41 W, maximum temperature difference ≥60 °C, Conrad, Germany) was glued onto the cold plate by thermal paste. This created a significantly colder surface to attract the humidity. This method has been evidently effective.

The impact surface in the shadowgraph imaging was located on a 3 mm thick aluminum/wood slider, which slid in a slot in the cold plate, as Figure 3.22 depicts. After each drop impact, the slider was drawn out for a certain length, so that the impact surface was renewed. The 170 mm length allowed roughly 10 impacts before consumption. The rest part of the slider was made of less conductive material in order to avoid warming by free convection outside the enclosure. The optical access was provided by two pieces of insulating glass with thermal conductivity of $3\,\mathrm{W\,m^{-2}\,K^{-1}}$. Because of the relatively high thermal conductivity, the outer surface of the insulating glass was lower than dew point at low operating temperatures. It was necessary to clean the glass before each video recording. At −20 °C the condensation happened so fast that the glasses were rarely dry. As a result the illumination was weakened, but this did not affect the image quality significantly.

The high-speed camera was Photron FASTCAM SA 1.1. The frame rate was taken at 20 kHz, and the pixel resolution was 768 × 368 with $13\,\mu$m /pixel. The illumination was a custom assembled LED lamp. A high power LED (Edison EdiPower II EPSW-VF55 24 W 2050 Lm) with illumination area of 10 mm×10 mm was glued to a heat sink with thermal paste. The heat sink was cooled down by continuous flow of compressed air during operation in order to prevent overheating. A convex lens with focal length of 20 mm and diameter of 20 mm was fixed in front of the LED, in order to converge the light beam to the optical axis, as Figure 3.23 shows. As a result, the illumination intensity was significantly increased.

In the side-view infrared imaging shown by Figure 3.24, the front insulating glass was replaced by an infrared window embedded in a 20 mm thick polystyrene wall. The infrared window comprised two pieces of 4 mm thick infrared glass (NT63-215, 40 mm Diameter Germanium Window, $8\,\mu$m to $12\,\mu$m, AR Coating, EdmundOptics, the transmittance spectrum is shown in Figure 3.25), so that the window functioned as an insulating glass, in order to minimize the condensation on the outer surface of the infrared glass. The infrared glass has high transmittance for a wide

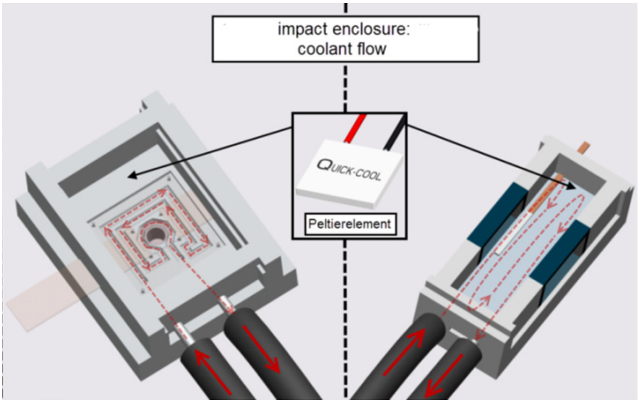

Figure 3.21.: The cold plate was cooled by circulating refrigerant in the internal channel. The Peltier element created a cold surface to absorb the humidity in the air, effectively eliminating the condensation on the impact surface.

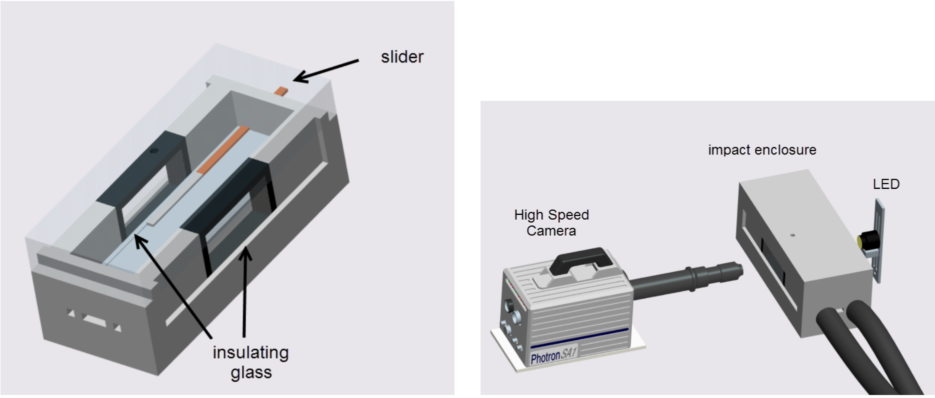

Figure 3.22.: The aluminum impact surface was provided by the slider. The impact surface was renewed after each impact by pulling out the slider for around $10\,\mathrm{mm}$. The insulating glasses provided the optical access. The configuration of the shadowgraph imaging is shown on the right.

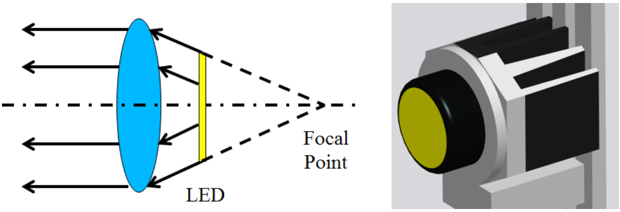

Figure 3.23.: A lens with 20 mm focal length was fixed in front of the LED in order to concentrate the light beam on the optical axis. The focal length was chosen as such a value that the light beams were as if from the focal point of the lens, as shown on the left. A heat sink was stuck to the LED on the backside to dissipate the heat more efficiently, as shown on the right.

range of thermal radiation as shown in Figure 3.25. The back insulating glass was displaced by a polystyrene plate, in order to provide a uniform temperature background.

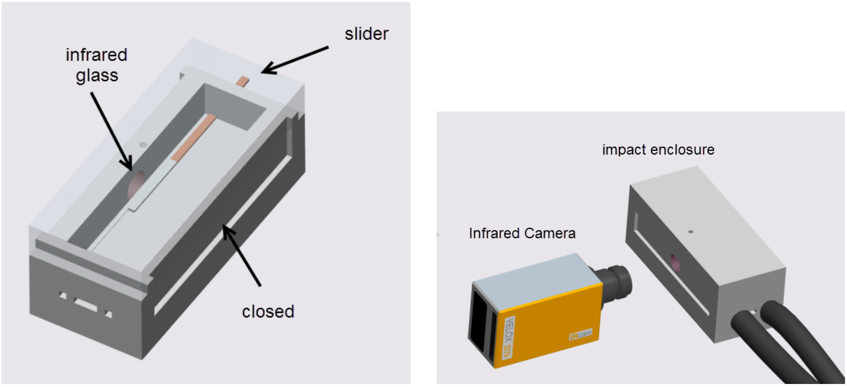

Figure 3.24.: Configuration of the side-view infrared imaging. The infrared optical access was provided by the infrared glasses, and the background of a uniform temperature was provided by a polystyrene plate.

The impact enclosure and the impact surface for the bottom-view of infrared imaging are shown in Figure 3.26. The drop impact took place on a 12 μm thick aluminium film, which was laid on top of an infrared glass. The aluminum provided a uniform background and avoided direct contact of the infrared glass with the freezing drop. The bottom side of the aluminium film had black body coat-

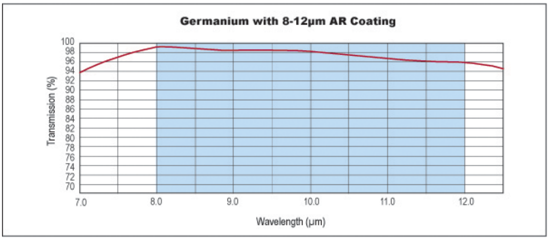

Figure 3.25.: The transmittance of the infrared glass for radiation of different wavelengths, provided by EdmundOptics.

ing in order to avoid reflection of the surrounding infrared radiation. Likewise, the double-glass infrared window was employed for the same purpose of thermal insulation. This construction was supported by N. Kidambi in his IREP summer exchange program [67].

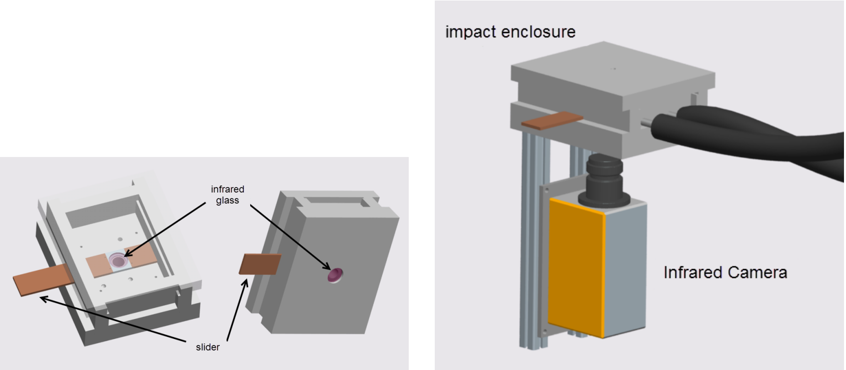

Figure 3.26.: Configuration of the bottom-view infrared imaging. The drop impact took place on the infrared glass, on top of which a $12\,\mu\text{m}$ thick aluminium film was laid. After each impact, the slider was pulled out, warmed above the dew point, and the aluminum film was cleaned before the next drop impact. The infrared camera measured the temperature of the aluminum film, which was expected to be the temperature of the bottom of the lamella.

Superhydrophobic surfaces (SHS) offer strong drop receding and even total rebounding [6]. Supercooled drop impact was conducted on such surfaces because solidification might have a noticeable influence on the receding or rebounding.

The wettability of a surface is measured by the contact angle. The contact angles of water on both the aluminum surface and the SHS were measured. The angle measurement could be easily done by a protractor on an image, but the precision is limited and the measurement is a little bit subjective. Therefore a curve fitting method was chosen.

The outline of a sessile drop on a surface was recognized and extracted from the raw image by transforming it to a binary image. One portion of the outline adjacent to the contact point was selected for the curve fitting. The contact point was defined as the point projection of the three phase contact line on the 2D image. This part outline was fitted by a polynomial curve by the "Polyfit" function provided by Matlab. After comparison, the best fit came out to be a two degree polynomial function. The first order gradient of this parabolic function at the contact point gave the value of the contact angle. Figure 3.27 shows the results of this method. More detailed information on the Matlab programming can be found in the Bachelor thesis of H. Eichhorn [40].

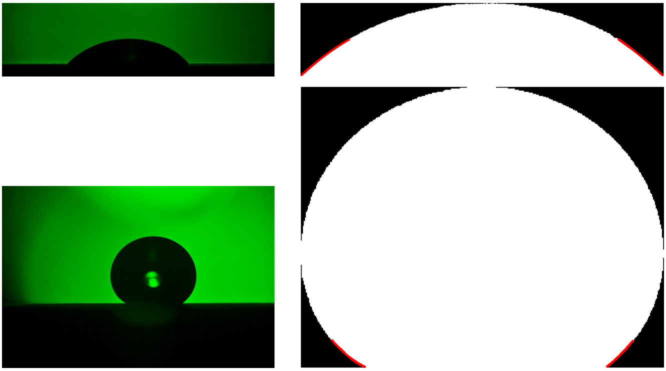

Figure 3.27.: Measurement of the contact angle on an aluminum surface (up) and a SHS (down). The red line at the feet of the drop are the fitted curve. The first order gradient of the curve at the contact point is the contact angle. The contact angle on the aluminum surface was measured as 40°, while the angles were respectively 151° and 137° for the left and right sides of the drop on the SHS.

The static contact angle on the aluminum surface was measured as 40°. On the SHS the drop had an asymmetrical shape. 151° and 137° were obtained for the left and right contact angle respectively. An average value of 144° was chosen as a descriptive value. It must be admitted that the hydrophobicity was not perfectly reproducible. The SHS was created by the TEGOTOP coating (Evonik Degussa GmbH, Hanau, Germany) on aluminum surfaces.

The applied SHS is of significant roughnesses. Figure 3.28 pictures the surface texture of the SHS by microscopy, and the roughness of a 4 mm sample is shown in Figure 3.29. The average surface roughness was measured as $R_z = 4.48\,\mu\text{m}$.

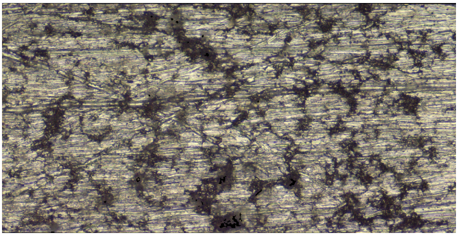

Figure 3.28.: The surface texture of the applied SHS, measured by INFINITEFOCUS (Alicona GmbH, Munich, Germany). The sample had a size of $0.63\,\text{mm} \times 1.26\,\text{mm}$.

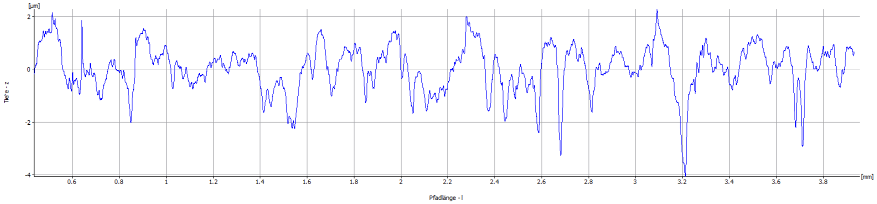

Figure 3.29.: The surface roughness of the applied SHS, measured by INFINITEFOCUS (Alicona GmbH, Munich, Germany). The sample was 4 mm long, $0.32\,\mu\text{m}$ wide. The measured average roughness was $R_z = 4.48\,\mu\text{m}$.

3.4 Measurement of the Water Drop Temperature

This section explains the challenges of infrared imaging in the low temperature range, introduces the calibration of the camera, discusses different factors that influence the precision of the temperature measurement, and finally demonstrates the result of the drop temperature measurement. The results verified the effectiveness and reproducibility of the supercooling method.

3.4.1 Challenges Accompanying the Low Temperature

The employed infrared camera, “IRCAM Velox 327k M” (IRCAM GmbH, Erlangen, Germany), is a mid-wavelength infrared camera (MWIR) with the wavelength spectrum from 3.4 μm and 5 μm. The detector is out of mercury cadmium telluride (MCT), cooled down by a Stirling engine cryocooler. The dot pitch is 24 μm. The full frame pixel resolution is 640 × 512. The maximum frame rate is 207 Hz at full frame and 820 Hz at the minimum pixel resolution of 256 × 256. This resolution was excessive for the measurement. The integration time is variable from 50 μs to 12.75 ms. The noise-equivalent temperature difference (NETD) is 20 mK. The infrared objective is “IR M 50” with focal length 50 mm, aperture F/2, wavelength spectrum 3 μm to 5 μm.

Planck’s law describes the electromagnetic radiation emitted by a black body in thermal equilibrium at a definite temperature as

$$L_{e\lambda}(T) = \frac{hc_0^2}{\lambda^5} \cdot \frac{2}{\exp\left(\frac{hc_0}{k_B \lambda T}\right) - 1}, \tag{3.27}$$

where $L_{e\lambda}$ is the spectral radiance in W sr^{-1} m^{-3}, c_0 is the speed of light 2.9978×10^8m/s, k_B is the Boltzmann constant $1.380\,34 \times 10^{-23}$ J/K, h is the Planck constant 6.6252×10^{-34} J s, λ is the wavelength and the T is temperature in K. In the interested temperature range, Planck’s law gives values as depicted in Figure 3.30.

The radiant emittance M_e in W/m^2, the power emitted per unit area of the emitting body, is thus

$$M_e = \int_0^\infty L_{e\lambda}(\lambda, T) d\lambda \int d\Omega, \tag{3.28}$$

where Ω is the solid angle in sr. Integrating Ω over half-sphere of a Lambertian surface results in Stefan-Boltzmann law as Eq. 3.29.

$$M_e = \sigma_{StB} \cdot T^4, \tag{3.29}$$

where σ_{StB} is the Stefan-Boltzmann constant 5.67×10^{-8} W m^{-2} K^{-4}. The radiant emittance is proportional to the fourth power of the temperature of the black body emitter. As the temperature drops, the radiation diminishes rapidly.

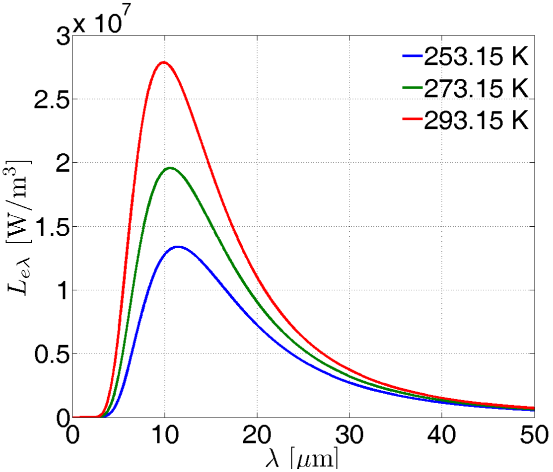

Figure 3.30.: Planck's law

The other fact the Planck's law states is that, the wavelength of the maximum radiation becomes larger as the temperature decreases. The quantitative description of this nature is given by Wien's displacement law as

$$\lambda_{max} = \frac{b}{T}, \tag{3.30}$$

where b is the Wien's displacement constant $2900\,\mu$m K. The effective wavelength of the interested temperature range is from $4\,\mu$m and $40\,\mu$m, and the emission peak lies between $8\,\mu$m and $12\,\mu$m. Therefore the long-wavelength of infrared light (LWIR) dominates the radiation. This range of the wavelength deviates significantly from the spectrum of the infrared camera, from $3\,\mu$m to $5\,\mu$m. The is another limiting factor of the frame rate beside the weak radiation at the low temperatures.

The third limitation was created by large magnification. The object, namely the water drop, has a dimension of 1.5 mm. It was desired to have roughly 20 pixels along the diameter, so that an accurate measurement of the temperature field of a drop in the dynamic deformation could be achieved. The spatial resolution was chosen to be 78μm/pixel and consequently the field of view was 20 mm×20 mm. This setting was invariant for all the infrared imaging.

The standard infrared objective "IR M 50" could not achieve such high magnification because its distance to the infrared detector was limited. To increase the distance, an extension ring was manufactured out of PMMA as shown in Figure

3.31. The dot pitch of the chip is 24 μm, thus the magnification is 0.308. Larger magnification does not reduce the radiance emitted from the object, but reduces the irradiance, the radiation energy per unit area landing on the chip, and hence weakens the contrast.

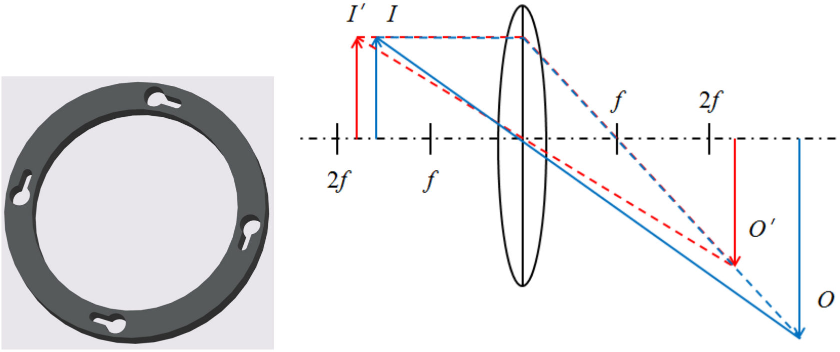

Figure 3.31.: The extension ring (left) between the infrared camera and the objective enhanced the magnification. O designates the object, and I is the image. The blue line is the original optical path of the 50 mm objective. The red line designates the light path after the extension ring is installed. Closer working distance (between the object and the lens) requires larger distance between the lens and the detector, resulting in smaller field of view. The extension ring was coated by black body spray.

The low radiant emittance, the long wave length and the large magnification limited the frame rate to 718 Hz with an integration time of 0.2 ms. No significant motion blur occurred for this optical arrangement. The frame rate was fixed for all the infrared imaging.

3.4.2 Calibration of the Infrared Camera

One benchmark image was taken at 0 °C as shown in Figure 3.32. The chip does not have a homogeneous sensitivity. Pixel-wise calibration was therefore required.

The calibration was taken with the same construction as in the real experiment, as Figure 3.24 and Figure 3.26 illustrate. The infrared window was also mounted. For the bottom-view, the uniform temperature field was provided by the aluminum film. For the side-view, the temperature field was provided by a

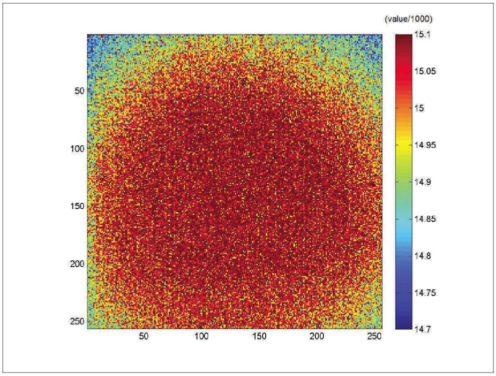

Figure 3.32.: Heterogeneity of the infrared detector. The center of the chip was obviously brighter than the periphery. This is vignetting due to the large magnification.

40 mm×40 mm×10 mm aluminum plate which lay in the 10 mm wide slot in the cold plate. Both of the objects were coated with black body spray. The temperature was measured with the “Self Adhesive Patch Thermocouple” at the backside of the aluminum film, or the aluminum plate. Uniform temperature distribution was adequately achieved in both cases, because the free convection inside the enclosure was low compared to heat conduction in the metal.

The calibration data was taken from −20 °C to 20 °C. For each temperature 100 images were recorded for an average. The gray value of each pixel was related to the real temperature by a two degree polynomial curve fitting:

$$B_3 = B_0 + B_1 T + B_2 T^2, \tag{3.31}$$

where B_3 is the raw gray value of the image, and T is the preset temperature. The three coefficients of the parabolic function were saved in a three-layer TIF image. The inverse function was taken to calculate the temperature after the imaging was done in the experiment. In Eq. 3.31 T was taken as the indeterminate, instead of B_3. The only reason was to allowed a polynomial curve fitting. The other way around resulted in a square root function. The quality of curve fitting was examined by the standard derivation as shown in Figure 3.33. The values were reasonably low, 0.2 °C, implying that the calibration was valid. More detailed description of the calibration can be found in the ADP report of Buchenhorst et al. [25].

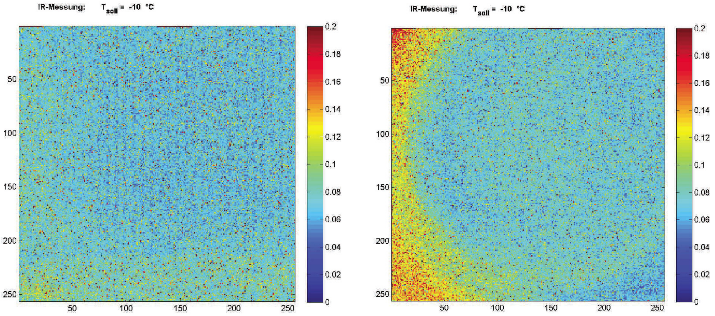

Figure 3.33.: The standard derivation of the calibration at −10 °C, the side-view imaging (left) and the bottom-view imaging (right). The values were reasonably small.

Probably due to the imprecise positioning during installation of the camera and the impact enclosure, the valid region was only a portion of the image as shown in Figure 3.34 and Figure 3.35. The horizontal green line in Figure 3.34 shows the position of the impact surface. The bright line below was due to high reflectivity of the aluminium slider. The slider was not well coated by the black body spray, because the coating was easily damaged by the movement of the slider.

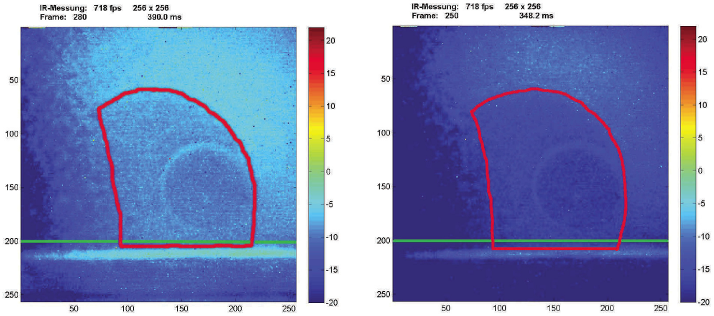

Figure 3.34.: The valid region after calibration for the side-view imaging at −10 °C and −20 °C.

3.4.3 Uncertainties in Temperature Measurement

The measurement of the temperature of a spherical water drop differs considerably from the calibration case. Firstly, the drop surface is not flat. Secondly,

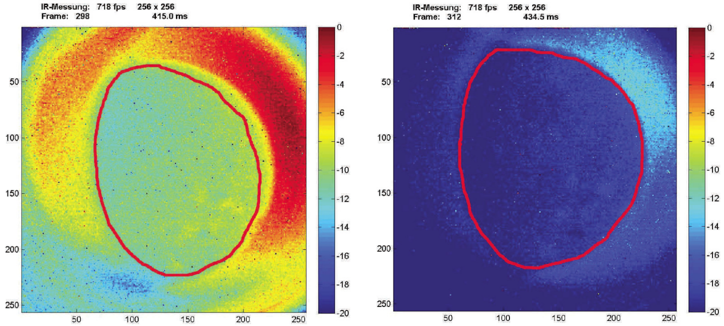

Figure 3.35.: The valid region after calibration for the bottom-view imaging at −10 °C and −20 °C.

the emissivity of real material is wavelength dependent. Finally, transmission and reflection of the thermal radiation from the surrounding environment are detrimental. This subsection evaluates the influence of these factors and justifies the reliability of the temperature measurement.

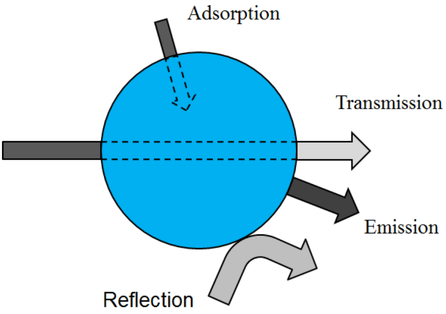

Figure 3.36.: Emission, adsorption, transmission and reflection on a spherical water drop.

Curved Surface

If a surface is an ideal diffuse radiator, Lambert's cosine law says that the radiant intensity observed is directly proportional to the cosine of the angle θ between the observer's line of sight and the surface normal, as Eq. 3.32 quantifies.

$$I_e(\theta) = I_e(\theta = 0)\, cos\theta, \tag{3.32}$$

where I_e is the radiant intensity in $\mathrm{W\,sr^{-1}}$.

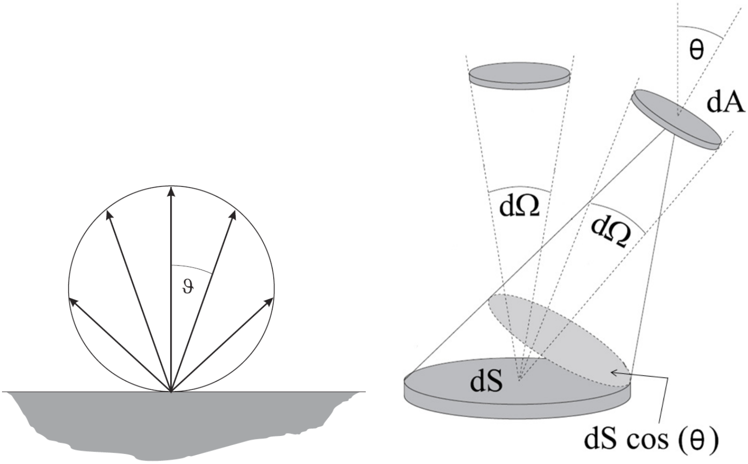

Figure 3.37.: Lambert's cosine law [50].

In Figure 3.37 on the right, dA denotes an area element of the detector surface, dS is an area element of the radiator surface. The radiant flux Φ_e in W, which dA receives from dS, is proportional to the angle θ, the area dS, dA, and inversely proportional to r^2. r is the distance between the two elements dA and dS. This leads to

$$d\Phi_e = L_e \frac{dA\, dS}{r^2} \cos\theta = L_e\, d\Omega\, dS\, \cos\theta, \tag{3.33}$$

where $d\Omega = dA/r^2$ is the solid angle in sr. The radiance, L_e, measures the radiant flux that is emitted from a unit surface and falls within a unit solid angle, in $\mathrm{W\,sr^{-1}\,m^{-2}}$.

Divided by $d\Omega$, Eq. 3.33 is related to Eq. 3.32 as

$$dI_e \equiv \frac{d\Phi_e}{d\Omega} = L_e\, dS\, \cos\theta. \tag{3.34}$$

Comparing Eq. 3.32 and Eq. 3.34, it results in

$$I_e(\theta = 0) = L_e\, dS. \tag{3.35}$$

Therefore L_e is constant for an ideal diffuse surface.

When the sensor element dA deviates from the normal direction of dS, the radiant flux that dA receives from dS reduces according to Lambert's law. On the other hand, dA is able to "see" a larger area than dS. We fix the position of dA and vary the orientation of dS relative to dA. For a certain combination of camera and objective, the angular aperture is a fixed property of the imaging system. In the right sketch of Figure 3.37, the two solid lines originating from dA element designate the angular aperture. Any surfaces lying between the two solid lines share the same projected area, $dS\cos\theta$, in the normal direction of element dA. The projected area $dS\cos\theta$ is the area that dA perceives. If the radiance L_e is not orientation dependent as a Lambertian surface, all of these surfaces send equal radiant flux to dA. In other words, the reduction of radiant flux according to the Lambert's law is exactly compensated by the enlargement of the visible area of the detector. This answers why a Lambertian surface appears equally bright in any direction.

Water does not have a Lambertian surface, however. The emissivity is orientation dependent, as Figure 3.38 shows. From the normal direction to 55°, the emissivity keeps constant and hence the drop surface could be regarded as Lambertian. As the angular deviation increases further, the emissivity reduces rapidly to zero. Therefore the curvature does not influence the precision of the measurement in the center part of the drop.

Emissivity

Water does not have a "gray" surface, as Figure 3.39 manifests. It is necessary to take an averaged value of the wavelength dependent emissivity, in order to evaluate the error of the measurement quantitatively. According to the Planck's law, the effective wavelength lies between $4\,\mu$m and $40\,\mu$m with a peak at $10\,\mu$m for the interested temperature range from $0\,^{\circ}$C to $-20\,^{\circ}$C. The emissivity was finally chosen to be 0.97 for a rough but adequately good estimation.

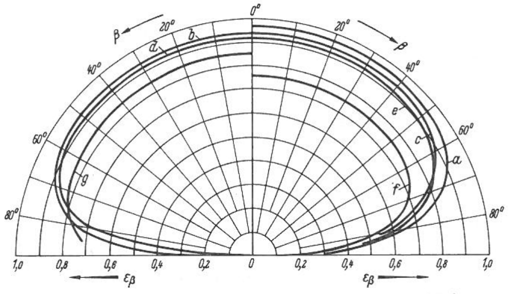

Figure 3.38.: The orientation dependency of emissivity of water, data from VDI Wärmeatlas [58].

It should be noted that the thermal radiation is filtered by the glass window, and further selected by the infrared objective. The infrared objective has a spectrum of $3\,\mu$m to $5\,\mu$m. These bias on wavelength however does not influence the estimation of the emissivity, because it is taken into account in the calibration.

Reflection

The incident light ray on the air/water interface is partially reflected by the water surface and partially transmitted into water and eventually absorbed, providing that the water layer has an infinite depth.

The law of reflection states that the angle of incidence equals the angle of reflection.

$$\theta_i = \theta_f, \tag{3.36}$$

where i denotes incidence and r denotes reflection.

Snell's law states that for a given pair of media and a light ray with a single wavelength, the ratio of the sines of the angle of incidence θ_i and angle of refraction θ_t is equivalent to the ratio of phase velocities (v_i/v_t) in the two media, or equivalently, to the opposite ratio of the indices of refraction (n_t/n_i):

$$\frac{sin\theta_i}{sin\theta_t} = \frac{n_t}{n_i}, \tag{3.37}$$

where t denotes transmission. Since the refraction index of air is nearly 1, n is used here to designate the refractive index of water.

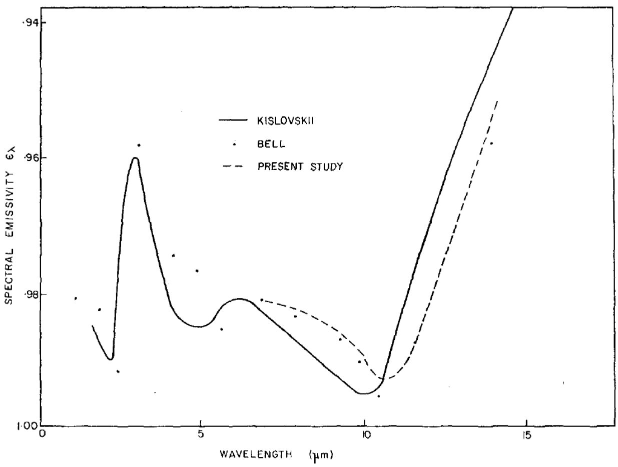

Figure 3.39.: The wavelength dependency of the emissivity of water reported by Robinson et al. [122].

It is critically important to know what fraction of the light is reflected and what fraction is transmitted. The reflection coefficient describes the intensity of a reflected light ray relative to an incident light ray. It is calculated with the angle of incidence and the refractive index as Fresnel equations, Eq. 3.38 and Eq. 3.39, represent.

The reflection coefficient depends also on the polarization of the incident light ray. The s-polarized light has its electric field in the plane of the interface (perpendicular to the direction of the light propagation). The p-polarized light has its electric field in a perpendicular direction to the s-polarized light (parallel to the direction of light propagation). The reflection coefficient for s-polarized light R_s is given by:

$$R_{\mathrm{s}} = \left|\frac{\cos\theta_{\mathrm{i}} - n\cos\theta_{\mathrm{t}}}{\cos\theta_{\mathrm{i}} + n\cos\theta_{\mathrm{t}}}\right|^2 = \left|\frac{\cos\theta_{\mathrm{i}} - n\sqrt{1-\left(\frac{1}{n}\sin\theta_{\mathrm{i}}\right)^2}}{\cos\theta_{\mathrm{i}} + n\sqrt{1-\left(\frac{1}{n}\sin\theta_{\mathrm{i}}\right)^2}}\right|^2, \tag{3.38}$$

where the second form is derived from the first one by eliminating θ_t using Snell's law and trigonometric identities.

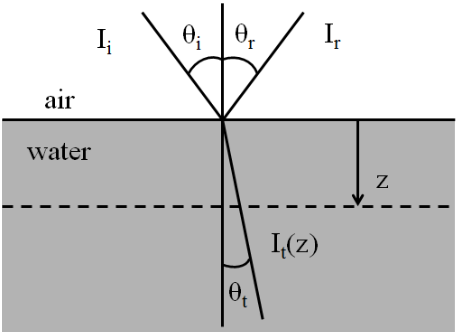

Figure 3.40.: Refraction, reflection, transmission and absorption of radiation on a surface of a partially transparent material.

For the p-polarized light, the reflection coefficient R_p is given by

$$R_\mathrm{p} = \left| \frac{\cos\theta_\mathrm{t} - n\cos\theta_\mathrm{i}}{\cos\theta_\mathrm{t} + n\cos\theta_\mathrm{i}} \right|^2 = \left| \frac{\sqrt{1-\left(\frac{1}{n}\sin\theta_\mathrm{i}\right)^2} - n\cos\theta_\mathrm{i}}{\sqrt{1-\left(\frac{1}{n}\sin\theta_\mathrm{i}\right)^2} + n\cos\theta_\mathrm{i}} \right|^2 . \tag{3.39}$$

If the light is unpolarized, the reflection coefficient is

$$R_\mathrm{m} = \frac{R_s + R_p}{2} \tag{3.40}$$

Taking n=1.2 as an example, the angular dependence of the reflection coefficients R_s, R_p and R_m is shown in Figure 3.41 and Figure 3.42.

It is obvious to identify that, the reflection coefficient is pretty low and keeps constant until 50°, which is the Brewster angle θ_{Br} for the given refractive index. At the Brewster angle, the p-polarized light is not reflected, $R_p = 0$. The Brewster angle is given by Eq. 3.41.

$$\theta_{Br} = \arctan n. \tag{3.41}$$

Below the Brewster angle, the reflection coefficient can be simplified as Eq. 3.42

$$R_\mathrm{m}(\theta = 0) = \left(\frac{n-1}{n+1}\right)^2 . \tag{3.42}$$

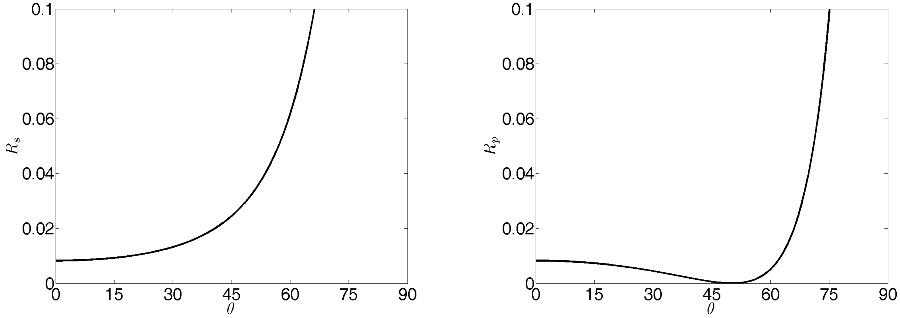

Figure 3.41.: Orientation dependence of Reflection coefficients R_s and R_p, $n = 1.2$.

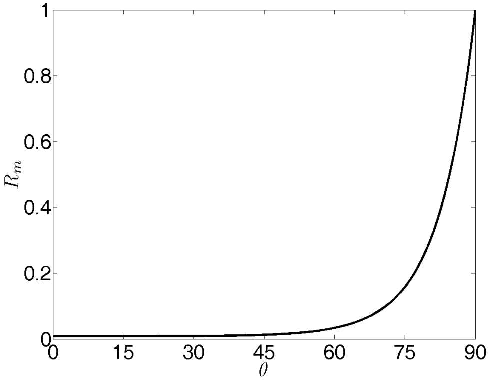

Figure 3.42.: Orientation dependence of Reflection coefficient, $n = 1.2$.

For angle of incidence smaller than the Brewster angle, the reflection coefficient is roughly 0.8% which induces error of 0.5 K, assuming the surrounding has the same temperature as the water drop. A surrounding of a lower temperature helps on further suppressing the error.

The reflection coefficient is wavelength and temperature dependent, because of the refractive index. The wavelength dependency of refractive index of water at room temperature is given by Downing and Williams in 1975 [38]. The data for water at different temperatures, including the supercooled water, are given by Zasetsky et al. [174] in 2005, as the diagrams in Figure 3.43 show.

The covered wavelength ranges from $2.5\,\mu$m to $25\,\mu$m as the spectroscopic wavenumber $\tilde{\nu} = 1/\lambda$ indicates. The refractive index has an irregular dependency

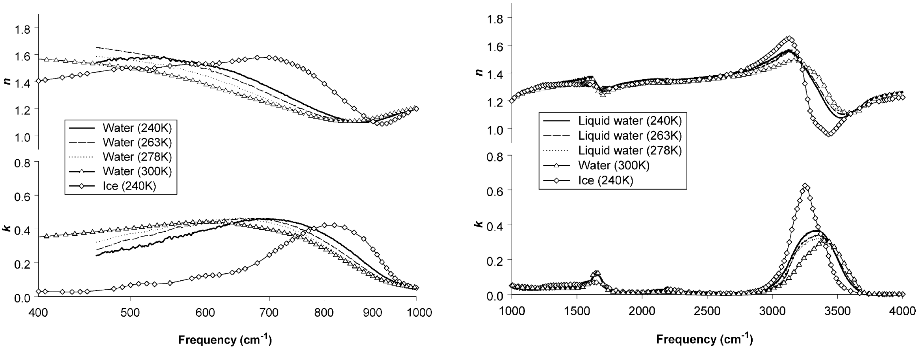

Figure 3.43.: The complex index of refraction and absorption of water and ice at different temperatures [174].

on wavelength, and the variation in the interested wavelength between 4 μm and 40 μm is as large as from 1.2 to 1.65. Taken the 25 °C water as an example, the wavelength dependency of the reflection coefficient is shown in Figure 3.44.

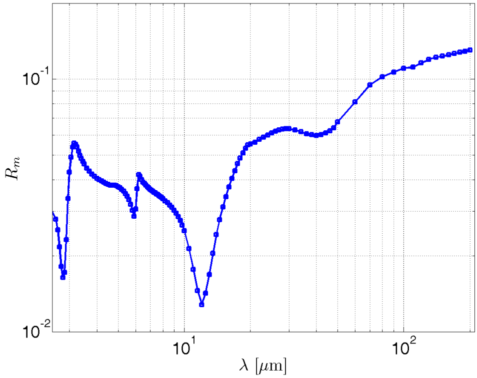

Figure 3.44.: Reflection coefficient of the normal incidence. Water at 25 °C. Data of the refractive indices are from Downing and Williams in 1975 [38].

Radiation of the long wavelength has strong temperature dependence and high reflection coefficient, which would create large error in the measurement. However, the effective wavelength in our experiment is limited to 4 μm to 5 μm, which is shared by both the emitter and the infrared detector. Therefore the final error should be insignificant. The temperature is negligibly influential in this range of wavelength, so that the value for room temperature can be taken for the supercooled water.

Comparing Figure 3.44 and Figure 3.39, it is easy to recognize that the emissivity of water is defined as $\varepsilon = 1 - R_m$. This indicates that the reported emissivity in Figure 3.39 was measured for water of a sufficient depth, and the transmission is therefore neglected. Likewise, the emissivity has similar orientation dependence as the reflection coefficient. It should be noted that the emissivity in Figure 3.39 was measured for the entire spectrum instead of a single wavelength.

Transmission

The transmitted light ray is absorbed by water exponentially according to Beer-Lambert law as

$$\Phi_e(z) = \Phi_e(0)\exp(-\beta\, z) = \Phi_e(0)\exp\left(-\frac{z}{\zeta}\right), \tag{3.43}$$

where $\Phi_e(z)$ is the radiant flux of transmitted light at the depth of z, $\Phi_e(0)$ is the initial intensity of the transmitted light ray, β is the attenuation coefficient and ζ is the penetration length defined as$1/\beta$. In the discussion of transmission, only normal incidence of light ray is considered and thus the minimal reflection is neglected.

It is essential to know how far the light ray reaches before it is completely absorbed by the water substance. This information is incorporated in the complex index of refraction as

$$\tilde{n} = n + i\kappa_{ex}, \tag{3.44}$$

where κ_{ex} in the imaginary part is the extinction coefficient. β is related to the extinction coefficient by Beer-Lambert's law as

$$\beta(\lambda) = \frac{4\pi\kappa_{ex}}{\lambda}. \tag{3.45}$$

The attenuation coefficient β and penetration depth ζ for room temperature water is calculated as in Figure 3.45.

The ambient temperature of the drop is the inner temperature of the impact enclosure, between −20 °C and 5 °C, where LWIR is dominating. Taking the $10\,\mu$m wavelength for an estimation, the penetration length is $20\,\mu$m.

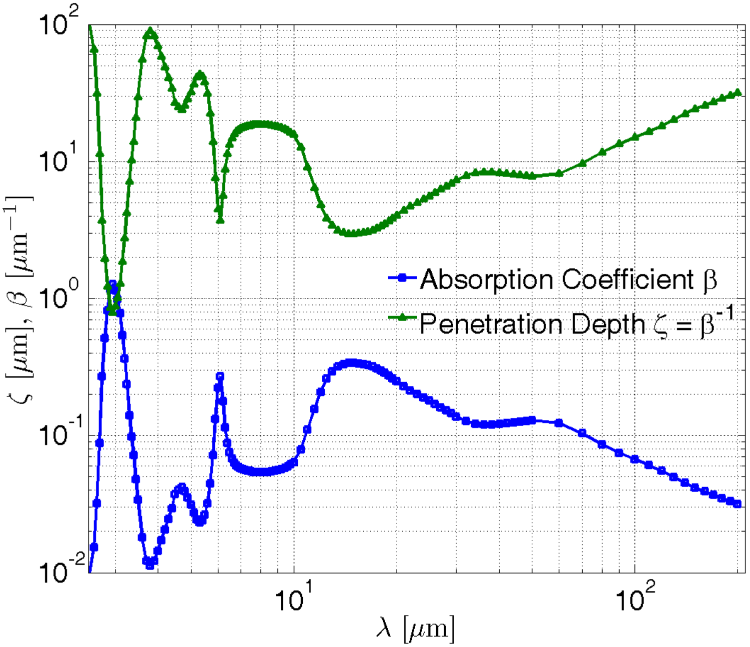

Figure 3.45.: The penetration depth of 25 °C water, according to the data of Downing and Williams in 1975 [38].

The transmittance is defined as

$$\mathcal{T}_\lambda = \frac{\Phi_e(z)}{\Phi_e(0)} = exp(-\beta\, z). \tag{3.46}$$

At the depth of z, $exp(-\beta z)$ fraction of incident radiant flux is absorbed, and the rest is transmitted further. Taking β =0.05 μm^{-1}, it is easy to prove that at the depth of 100 μm, the transmittance is almost 0. This means that except at the marginal edge of the water drop, transmission of background radiation through the water drop can be ignored.

Temperature Gradient

In light of the discussion above, a depth dependent emissivity $\varepsilon(z)$ is defined as [50]

$$\varepsilon(z) = 1 - \mathscr{T}(z) = 1 - exp(-\beta\, z). \tag{3.47}$$

The emissivity is therefore not a material property, but a depth dependent parameter. For infinitely thin water layer (z =0), the emissivity is 0 and transmittance is 1. For water of an infinite depth, the emissivity is as in Figure 3.39.

Each layer has its contribution for the total emissivity as

$$\frac{d\varepsilon(z)}{dz} = \beta \exp(-\beta\, z). \tag{3.48}$$

Thereby the differential emissivity $d\varepsilon(z)$ for the water layer at z with the thickness dz is defined as

$$d\varepsilon(z) = \beta \exp(-\beta\, z)\, dz. \tag{3.49}$$

The emitted radiant flux by this layer is then

$$d\Phi_e\,(\lambda, T(z)) = d\varepsilon\, \Phi_e\,(\lambda, T(z))\,, \tag{3.50}$$

where $\Phi_e\,(\lambda, T(z))$ is the radiant flux from a black body at temperature $T(z)$. The total radiant flux is the superposition of different layers as

$$\Phi_e(\lambda) = \int\limits_0^\infty \Phi_e\,(\lambda, T(z))\; d\varepsilon = \beta \int\limits_0^\infty \Phi_e\,(\lambda T(z)) \exp(-\beta\, z)\, dz. \tag{3.51}$$

If the temperature of water is constant, $T(z) = T_0$, and taking $\Phi_e(\lambda, z = 0)$ as $\Phi_{e,0}$ for abbreviation, Eq. 3.51 gives,

$$\Phi_e(\lambda) = \Phi_{e,0}\, \beta \int\limits_0^\infty \exp(-\beta\, z)\, dz = \Phi_{e,0}. \tag{3.52}$$

This states that a semi-transparent material of uniform temperature is equivalent to a black body material at the same temperature.

In the presence of considerable temperature gradient, for instance a linear temperature profile, the black body radiant flux $\Phi_e(\lambda, T(z))$ becomes $\Phi_{e,0} + Bz$. This leads to [50]

$$\Phi_e(\lambda) = \beta \int_0^\infty (Bz + \Phi_{e,0}) \exp(-\beta z)\, dz = \frac{B}{\beta} + \Phi_{e,0} = B\zeta + \Phi_{e,0} = \Phi_e\left(\lambda, T(z = \zeta)\right). \tag{3.53}$$

Such a emitter is equivalent to a black body with the temperature at $z = \zeta(\lambda)$. Therefore the temperature that detector measures is not the surface temperature but an interior temperature at this depth. This could be particularly important for the supercooled drop, because of the strong temperature inhomogeneity inside the drop. However, the discrepancy should be insignificant, because the penetration depth is estimated to be merely 20 μm.

3.4.4 Demonstration of the Temperature Measurement

A water drop was generated by the pneumatic drop generator at the room temperature. It fell and impacted on a surface at 0 °C in the impact enclosure. This process was recorded by the infrared camera as the image sequence in Figure 3.46 shows. The image is 8.19 mm×10.84 mm and 105 × 139 in pixel resolution. This is a cropped image from the original 256 × 256 format, because not the entire image had valid calibration. The measured drop diameter was 1.34 mm. The periphery of the drop appeared colder than in the center because of the non-Lambertian property of water surface. The drop temperature was at the room temperature of 16.5 °C, while the measured value was 14.5±0.5 °C. The 2 °C difference corresponds to the emissivity of water, 0.97. The measurement uncertainty came from the heterogeneous temperature field of the drop surface, instead of the precision of the camera, which is 20 mK. This benchmark test provides a demonstration of the validity of the temperature measurement.

Figure 3.47 illustrates a typical impact of a supercooled drop. The drop temperature measured from the image was −7±0.25 °C, hence the real temperature was −5 °C. This measurement demonstrates that the supercooling method was effective and the supercooled drop was reproducible. Recalling the theoretical calculation, the supercooling was weaker. The reason lay mainly at the difference in the boundary condition and the initial condition as discussed in Section 3.1.2.

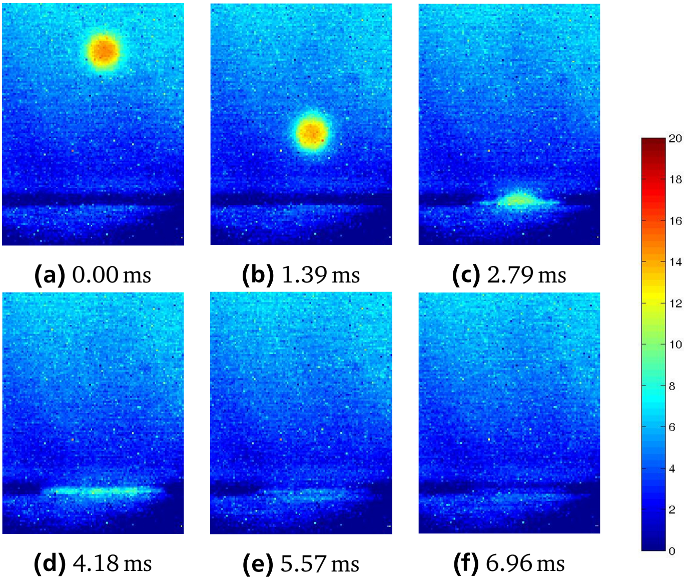

(a) 0.00 ms **(b)** 1.39 ms **(c)** 2.79 ms

(d) 4.18 ms **(e)** 5.57 ms **(f)** 6.96 ms

Figure 3.46.: Infrared imaging of a falling water drop with an initial temperature 14 °C. The background temperature was 0 °C, and the measured temperature of the drop was 14.5±0.5 °C.

The deformation of the drop during impact was not time resolved because of the limited frame rate of recording. The residual film thickness was only 2 to 3 pixels in image. The limited spatial resolution as well as the non-Lambertian ice/water surface made the temperature measurement in this case an impossible mission. As a result, the side-view infrared imaging was only taken for drop impact on SHSs, where total rebounding appeared.

It is noticeable that the residual lamella disappeared faster in Figure 3.46 than in Figure 3.47. The reason is that in Figure 3.46 only the sensible heat was dissipated as the drop temperature reduced from 15 °C to 0 °C. In Figure 3.47, the dissipation of the latent heat had taken a significantly longer time.

The ice dendrite growth should finish quickly after impact. The observed temperature change should be solidification. This inference is supported by a simple analysis with the Stefan problem. The substrate was at −20 °C and the initial temperature of the liquid was taken as 0 °C. Taking the time as 100 ms as in Figure 3.47, the one-phase Stefan problem yields 170 μm ice, which is a typical thickness of the residual lamella. Therefore solidification was observed. It should be noted

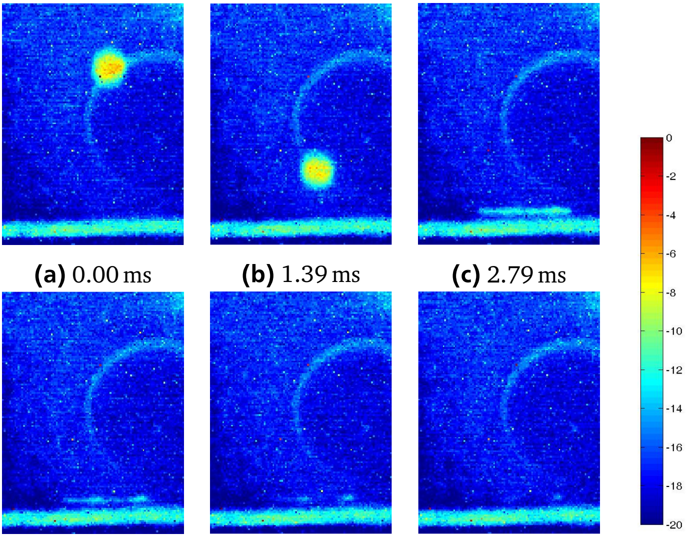

(a) 0.00 ms **(b)** 1.39 ms **(c)** 2.79 ms

(d) 40.39 ms **(e)** 77.99 ms **(f)** 114.21 ms

Figure 3.47.: Infrared imaging of a supercooled water drop. The background was −20 °C, and the measured drop temperature was −7±0.25 °C.

that the fraction of solidified water after ice dendrite growth is merely 6.4% with the initial temperature at −5 °C. Therefore it is reasonable to take the lamella as pure liquid instead of a mixture of water and ice.

3.5 Operation of the Experimental Setup

Figure 3.48 shows the synchronization system of the experimental setup of the shadowgraph and the infrared imaging, respectively. The trigger system was provided by NI 6602 counter module and two Labview codes. Figure 3.49 shows the front panel of the two labview programs.

In the shadowgraph imaging, the NI 6602 module provided three trigger signals respectively to the camera, the LED and the drop generator. The drop generator was the first to act. The camera was started before the drop fell in to the field of view. The LED was turned on slightly before the recording. The delay times were tested out easily by trial and error. The switch of the drop generator, the “Valve On” button in the labview code, enabled the independent test of the drop generator and the imaging system.

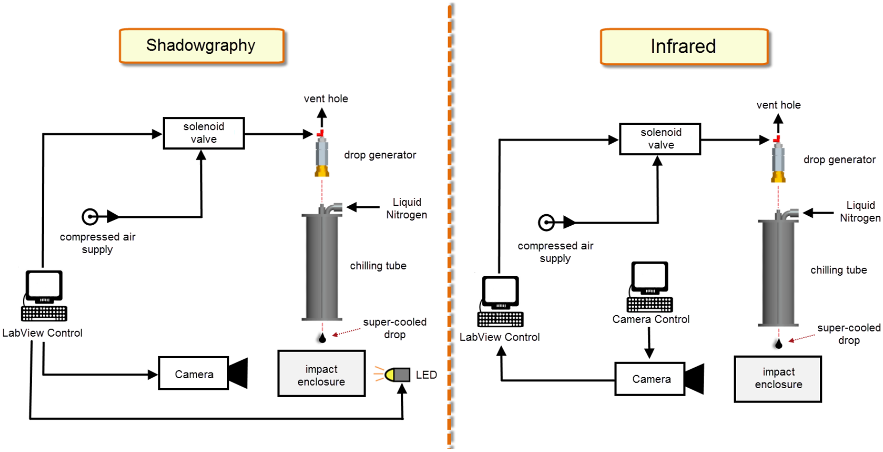

Figure 3.48.: Synchronization system of experimental setup for the shadowgraph imaging (left) and infrared imaging (right).

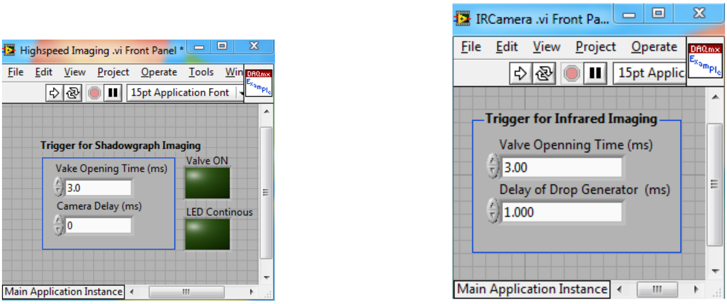

Trigger for Shadowgraph Imaging

Vake Opening Time (ms) 3.0

Camera Delay (ms) 0

Valve ON

LED Continous

Trigger for Infrared Imaging

Valve Openning Time (ms) 3.00

Delay of Drop Generator (ms) 1.000

Figure 3.49.: Labview program for shadowgraph imaging (left) and infrared imaging (right)

In order to acquire sufficient illumination, the LED was overdriven by a voltage higher than the rated value, which increased the probability of breakdown. Two methods were undertaken to protect the LED. The first method was effective cooling. High power operation is accompanied with massive heat generation. In order to control the operating temperature, the LED was stuck to a heat sink of large surface, which was further cooled by continuous air flow. The second method was to operate the LED in “flash” mode while overdriven for recording, while the “continuous” mode was used with the rated voltage for general illumination.

The trigger for the infrared imaging was differently designed, because the infrared camera does not accept a trigger signal as input. On the contrary it provides a sequence of square wave pulses for each frame of recording. This signal was used to trigger the drop generator. Although the free fall took roughly 500 frames, the recording time of 1000 frames was sufficient for observation.

The entire experimental setup is shown in Figure 3.50. Taking the shadowgraph imaging as an example, the operation procedure is as the following. After adjustment of the drop generator and the chilling tube, the supercooling enclosure was closed and sealed with tape. The liquid nitrogen was the first to start. It took roughly 30 minutes to fill the the supercooling tube and cool the drop generator down to 0 °C. Then the Huber chiller was started to cooled down the substrate. A stable temperature of the substrate could be achieved usually within 10 minutes. The slider with impact surface was then inserted into the impact box. After 5 minutes the impact surface was cooled down to a stable temperature, and recording started. After consumption, the impact surface was always warmed over the dew point before the next insertion, in order to avoid condensation on top of the impact surface.

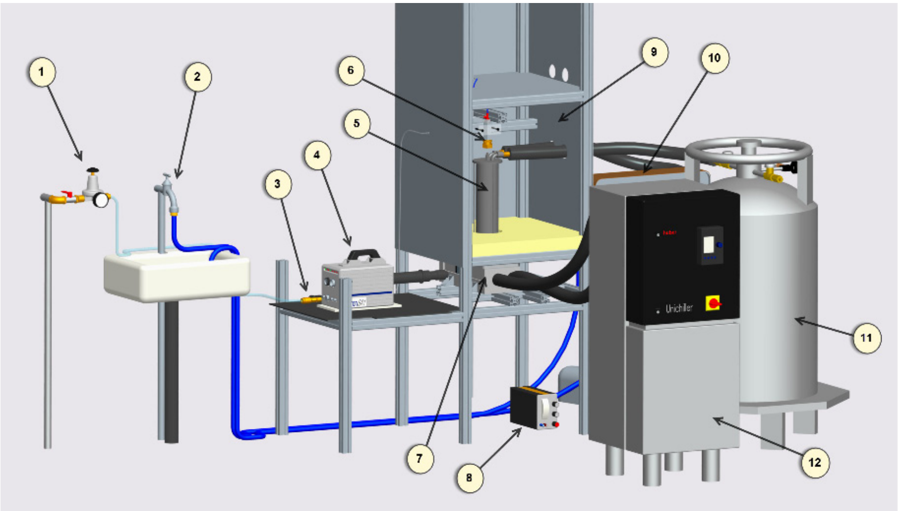

Figure 3.50.: Experimental setup for the impact of supercooled water drops (shadowgraph imaging)

1	Pressure regulator	7	Impact enclosure
2	Tap water supply	8	DC power supply
3	Solenoid valve	9	Supercooling enclosure
4	High-speed camera	10	Heat exchanger
5	Chilling tube	11	Liquid Nitrogen container
6	Pneumatic drop generator	12	UniChiller

4 Results and Discussion

This chapter is dedicated to the experimental results on the impact of supercooled drops. Beside graphic demonstration of the observed phenomenon, quantitative data were obtained from the raw images to facilitate a parametric study. Theoretical analysis was also applied to extrapolate the findings to a wider range of the drop impact condition. This chapter emphasizes on the analysis, and more supporting graphic data can be found in Appendix C and the ADP report of C. Buchenhorst et al. [25], where the raw image data were firstly reported.

The influence of phase change on the drop spreading is evaluated by drop impact on aluminum surfaces of different temperatures. Both experimental results and an analytical approach were introduced in Section 4.1. Drop impact on superhydrophobic surfaces leads to strong receding and rebounding, which allow better observation of the differences brought by the nucleation and ice dendrite formation. Section 4.2 introduces the impact of supercooled drop on the SHS. Both shadowgraph and infrared imaging were applied. The measurement of the contact temperature is also introduced in this section. The findings of the experimental investigations are summarized in the Section 4.3.

4.1 Influence of Phase Change on Drop Spreading

This section examines the influence of phase change on the drop impact on aluminum surfaces by examining the dynamic spreading diameter. An analytical study is taken to extrapolate the findings to wider drop impact conditions.

4.1.1 The Dynamic Spreading Diameter

Single drops were generated with a typical diameter of 1.5 mm. The impact velocity was typically 3.4 m/s. The drop had three indicative temperatures: 20 °C, 0 °C and −5 °C. The drop temperature was imprecisely controlled, varying from −2 °C to −5 °C, but did not affect the purpose of measurements. The substrate had three temperatures optionally: 0 °C, −10 °C, and −18 °C.

The drop diameter and the impact velocity were almost invariable on account of the construction. Consequently the We and Re varied only with the properties of the liquid. The viscosity of water increases from 1.00 Pa s at 20 °C to 2.16 Pa s at

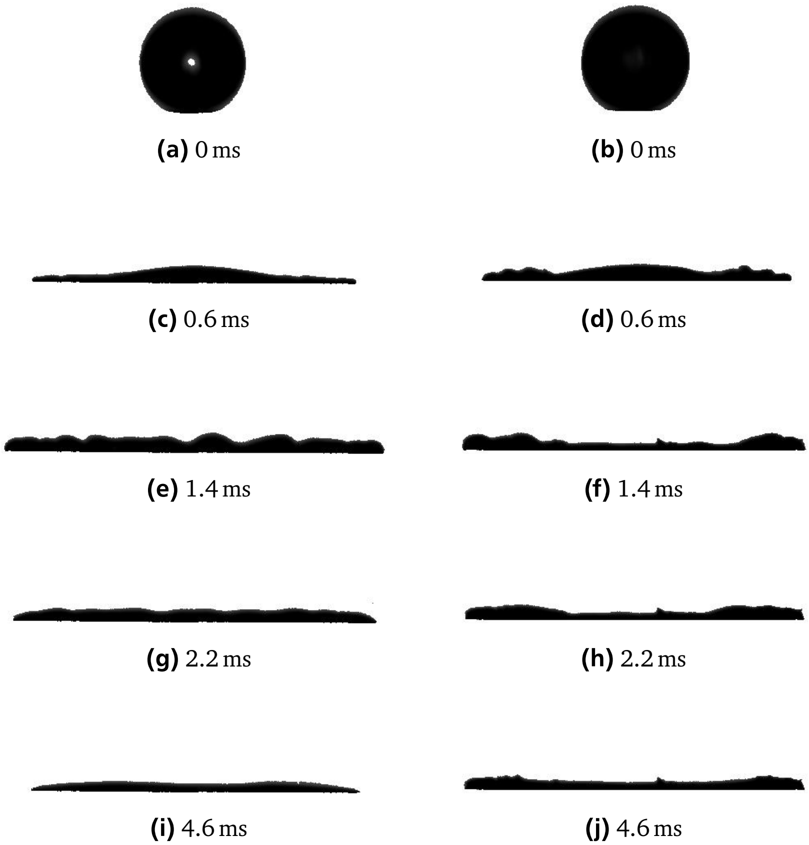

(a) 0 ms
(b) 0 ms
(c) 0.6 ms
(d) 0.6 ms
(e) 1.4 ms
(f) 1.4 ms
(g) 2.2 ms
(h) 2.2 ms
(i) 4.6 ms
(j) 4.6 ms

Figure 4.1.: Impact of a supercooled drop on aluminum surfaces at 0 °C (left) and at −10 °C (right). The supercooled drop was approximately −5 °C. The drop diameters were 1.70 mm (left) and 1.73 mm (right), and the impact velocities were 3.48 m/s (left) and 3.56 m/s (right).

−5 °C, more than doubled. The surface tension increases from 72.5mN/m at 20 °C to 76mN/m at −5 °C [54].

Figure 4.1 illustrates the typical scenarios of drop impact on aluminum surfaces at different temperatures. Independent of the drop temperature and the substrate temperature, the spreading phase exhibited essentially the same morphology.

Noticeably, on the right side of Figure 4.1, the residual lamella had sharp edges, indicating the rapid growth of the ice dendrite. The emergence of the sharp edges exhibited clear dependence on the substrate temperature. At higher substrate temperatures the sharp edges were absent, and became more frequent when the substrate temperature dropped below −10 °C. The emergence of the sharp edges was random. Despite the emergence of the rapid ice dendrite, the morphology of drop spreading remained uninfluenced, because only tiny portion of water (6.4% of water for the 5 K supercooling) solidified by the nucleation. The fragile structure seems to be easily broken by the deformation of the liquid drop.

Assuming that the drop was initially at 0 °C and the substrate was at −10 °C, the Stefan problem calculates that merely 21 μm thick ice layer builds up on the impact surface during the 1.4 ms spreading time. Comparatively, the thickness of the spreading lamella was 247 μm at the same time instant. Therefore the residual lamella should be a mixture of ice and water, instead of being completely frozen.

Figure 4.2 exhibited the dynamic spreading diameter from the impact to the maximum spreading. The difference brought by the supercooling is invisible. The maximum spreading diameter is reported by Figure 4.3 with more impact incidents. Except the data for the 25 °C drops, all the data clustered tightly together. The theoretical model [123], which was originally developed for isothermal drop impact at the room temperature, was applicable in the test cases, in which phase change was involved. The only notable difference was brought by the viscosity. The 25 °C drop had larger spreading diameter because of the lower viscosity. The measured values lay slightly below the curve, probably due to the imprecise determination of the liquid properties, which was caused by the variation of the drop temperature for 2 K.

4.1.2 Influence of Phase Change at Wider Impact Conditions

The weakness of the experimental setup was that the Re and We of the drop impact were basically invariable. The test range might lie coincidentally in a particular tiny range of the two parameters, where the phase change has no significant influence. An analytical study was conducted to evaluate the influence of the two stages of solidification in a wider range of the impact Re and We.

Concerning the second stage of solidification, the physical problem is considered to be that a water drop at 0 °C impacts on a substrate at −20 °C, which is the lowest in-flight icing temperature. It is assumed that if the ice layer grows to the thickness of the liquid film in the center part of the spreading lamella when the maximum spreading diameter is reached, solidification influences the drop spreading considerably. The spreading time is taken as three times of the time constant τ, as found out in our experiment. The film thickness in the center of the lamella

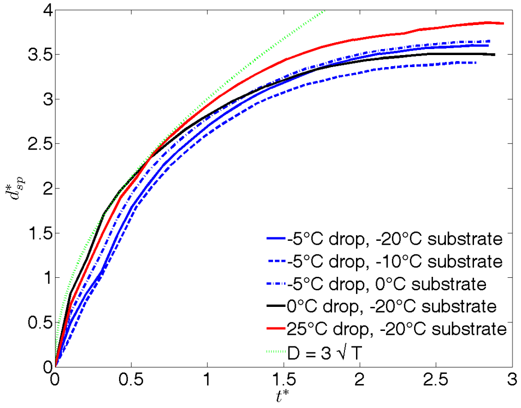

Figure 4.2.: The dynamic spreading diameter of drop impact on an aluminum surface. The dimensionless spreading diameter is defined as $d^*_{sp} = d_{sp}/d_0$, where d_{sp} is the diameter of the spreading lamella, d_0 is the diameter of the impinging drop. The dimensionless time is defined as $t^* = t/\tau$, where $\tau = d_0/v_0$ is the time constant, and v_0 designates the impact velocity. The density [48], the viscosity [45] and the surface tension [54] were taken for both water and supercooled water at 20 °C, 0 °C and −5 °C.

was inaccessible by the shadowgraph imaging, because it is thinner than the rim at the periphery. Therefore a validated model was taken from [123] and [10] as

$$H^* = 0.79 Re^{-2/5}. \tag{4.1}$$

The thickness of the ice layer was calculated according to the classical Stefan problem (Eq. 2.30 in Chapter 2) as $H = 2\lambda_{St}\sqrt{\alpha_S \cdot 3\tau}$, where λ_{St} is calculated as 0.007 846 for the given boundary condition and material properties of ice at 0 °C. These analysis leads to

$$d_0 v_0 < \left[\frac{2\lambda_{St}\sqrt{3\alpha_S}}{0.79\left(\frac{\rho}{\eta}\right)^{-2/5}}\right]^{10} \equiv constant. \tag{4.2}$$

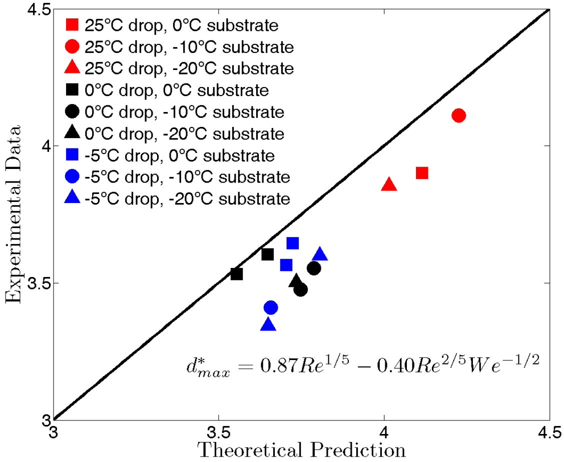

Figure 4.3.: The maximum dimensionless spreading diameter of drop impact on the aluminum surface. The theoretical model is taken from Roisman [123].

If the product $d_0 v_0$ is smaller than this value, ice layer has sufficient time to grow, and is consequently influential on the drop spreading. This simple relation is plotted in Figure 4.4 to disclose the range of the impact velocity and the drop diameter. Apparently the envelope of impact velocity is incomparable with the speed of flight. This result suggests that solidification can be neglected for drop impact in typical SLD icing conditions.

Applying the same approach to the ice dendrite growth, i.e. the first stage of solidification, the physical problem is simplified to be that nucleation was triggered right upon impact, and the nucleation sites locate exclusively on the substrate. Consequently, the ice dendrite grows from the substrate upwards. If the ice dendrite grows to the thickness of the center part of the lamella at the instant of maximum spreading, nucleation influences the drop spreading. The growth rates of the dendrite tip, v_{tip}, were taken as 8mm/s for 5 K supercooling, which is the greatest supercooling realized in our experiment, and 50mm/s for 10 K supercooling, which

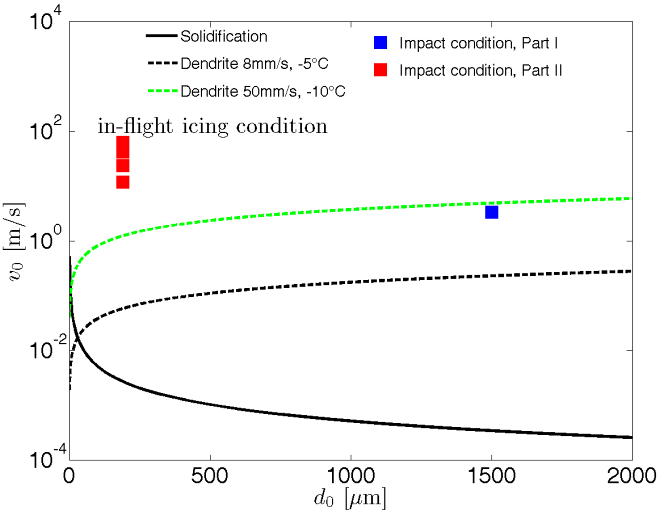

Figure 4.4.: Influence envelope of solidification and ice dendrite growth. The ice dendrite growth rates are taken from the data of Shibkov et al. [135, 137]. For drop impacts above the curve, the drop spreading is uninfluenced.

corresponds to the lower border of the SLD temperature envelope. The height of the ice dendrite is then $H = v_{tip} \cdot 3\tau$. This analysis yields

$$d_0^{-2} v_0^3 < \left[\frac{3 v_{tip}}{0.79 \left(\frac{\rho}{\eta} \right)^{-2/5}} \right]^5 \equiv constant. \tag{4.3}$$

Likewise, if the product $d_0^{-2} v_0^3$ is smaller than this value, ice dendrite has sufficient time to grow, or else the drop spreading is uninfluenced by the free ice dendrite. This simple relation is also plotted in Figure 4.4. The impact conditions of the supercooled drop is represented by an average value on the plot in blue, and the impact conditions achieved in the experiment on drop splash (described in Part II) are represented in red by four typical data points.

In the presence of low supercooling, the drop spreading is uninfluenced. As the supercooling deepens, the effect of nucleation could eventually emerge. The supercooling in our experiment is limited to −5 °C at the maximum. Deeper supercooling would be interesting for further exploration of the influence of nucleation on the drop spreading. For typical icing conditions with small droplets of around 200 μm and high impact speeds such as up to 63m/s achieved in the drop splash experiment, the influence of ice dendrite should be negligible.

4.2 Impact of Supercooled Drop on Superhydrophobic Surfaces

Drop impact on the SHS is accompanied with strong receding and even total rebounding, which offers an opportunity to observe the heterogeneous nucleation and ice dendrite formation clearly. Figure 4.5 demonstrates the hydrophobicity of the employed superhydrophobic coating, providing a benchmark case without supercooling for the purpose of comparison. With an initial temperature above 0 °C, the water drop always rebounded completely from the SHS, independent of the substrate temperature from 5 °C to −20 °C. Considerably, splash was observed unanimously.

4.2.1 The First Stage of Solidification during Drop Impact on SHSs

Figure 4.6 documented the first stage of solidification during impact of a supercooled drop on a SHS at 0 °C. The ice dendrite growth was identified as the transition of the liquid surface from transparent with glare points to translucent. The splash, the spreading stage and early stages of the receding were of the similar morphology to Figure 4.5, i.e. uninfluenced by the presence of supercooling. The liquid surface started to turn translucent when the receding reached the end at the 4.75 ms. At the 9.75 ms when the upper part of the liquid separated from the lower part, a sharp edge formed at the tip of the remaining lamella. At the 56.25 ms the rebounding drop fell back to the field of view. It had a different shape from a spherical drop. After re-impingement at the 64.75 ms the drop ceased motion in a roughly cubic shape. These non-spherical shapes indicate ice structures inside the liquid. The Stefan problem [4] calculates that 3.8% to 6.4% of water solidifies in nucleation with an initial temperature from −3 °C to −5 °C, simplifying the boundary condition as adiabatic within the short time. Therefore the ice structure was a mixture of water and ice. The ice must have a volumetric structure to hold the liquid by capillary forces in such a particular shape.

It is expectable that the temperature of the drop increased from its initial temperature to 0 °C during the first stage of solidification. Figure 4.7 confirms the expectation by documenting the temperature variation of a supercooled drop during the impact on a SHS. The substrate temperature was kept at 5 °C in order to

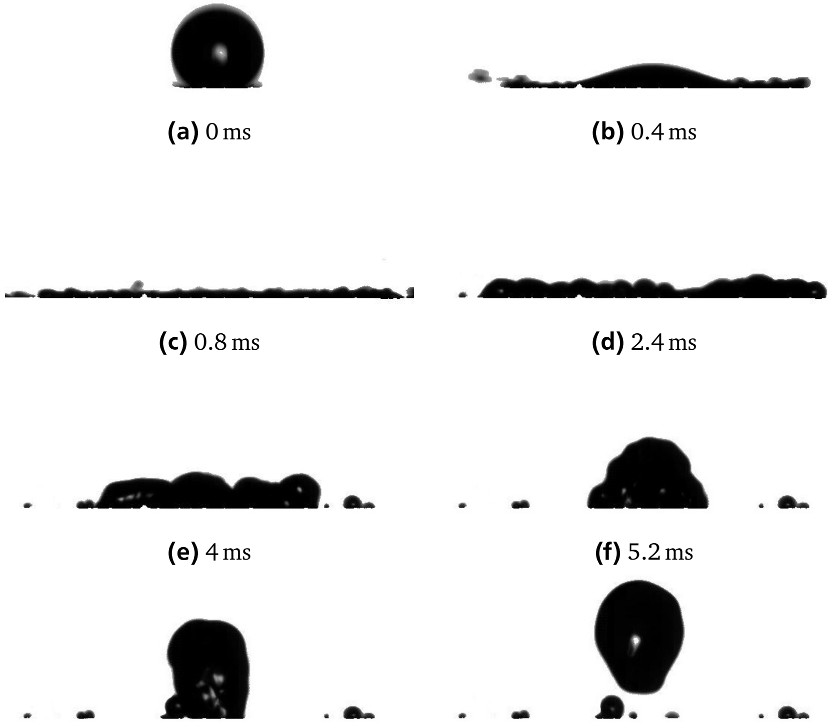

(a) 0 ms **(b)** 0.4 ms

(c) 0.8 ms **(d)** 2.4 ms

(e) 4 ms **(f)** 5.2 ms

(g) 6.4 ms **(h)** 9.2 ms

Figure 4.5.: 20 °C water drop impacted on a SHS at −10 °C. Drop diameter: 1.59 mm, impact velocity: 3.3m/s.

ensure successful total rebounding, and to build contrast between the 0 °C drop after nucleation and the ambient by the 5 °C difference. The temperature of the impinging drop reads as −5 °C, therefore the drop had a weak supercooling of 3 K on account of the 2 K error. The image is cropped with a field of view of 8.98 mm×5.99 mm, and 115 × 110 in pixels. Interestingly, nucleation did not occur right upon impact, rather, the drop retained the initial temperature until the 5.57 ms. The temperature of the rebounding drop took 9.75 ms to rise to 0 °C.

The first stage of solidification in the case of drop impact differs from that in a sessile drop in two aspects: absence of the ice dendrite front and shorter duration.

(a) 0 ms **(b)** 0.5 ms

(c) 1.75 ms **(d)** 2.75 ms

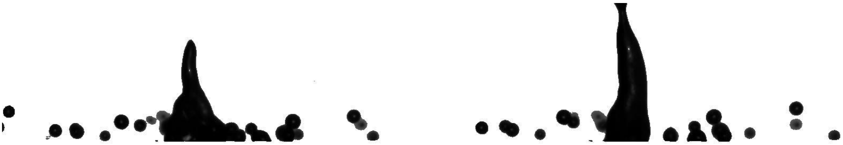

(e) 3.75 ms **(f)** 4.75 ms

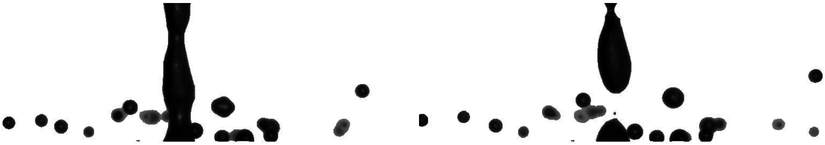

(g) 7.25 ms **(h)** 9.75 ms

(i) 19.25 ms **(j)** 56.25 ms

(k) 61.25 ms **(l)** 64.75 ms

Figure 4.6.: A supercooled drop impacted on a SHS at 0 °C. Drop diameter: 1.57 mm, impact velocity: 3.38m/s.

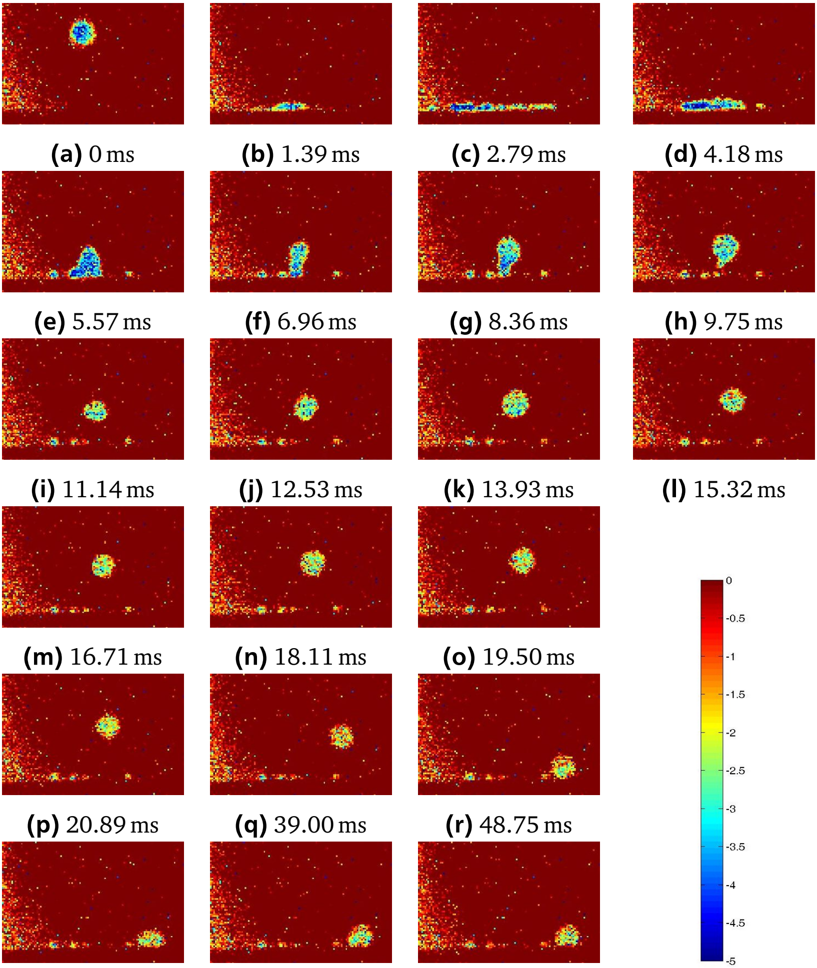

(a) 0 ms **(b)** 1.39 ms **(c)** 2.79 ms **(d)** 4.18 ms

(e) 5.57 ms **(f)** 6.96 ms **(g)** 8.36 ms **(h)** 9.75 ms

(i) 11.14 ms **(j)** 12.53 ms **(k)** 13.93 ms **(l)** 15.32 ms

(m) 16.71 ms **(n)** 18.11 ms **(o)** 19.50 ms

(p) 20.89 ms **(q)** 39.00 ms **(r)** 48.75 ms

(s) 51.53 ms **(t)** 52.92 ms **(u)** 568.25 ms

Figure 4.7.: Infrared imaging: total rebounding of a supercooled drop on a 5 °C SHS. The diameter of the rebounding drop was measured as 1.3 mm, and the drop temperature was −3 °C. The heterogeneous nucleation lasted from the 5.57 ms to the 15.32 ms. The drop in image (u) had the same temperature as in image (t), indicating negligible influence of the substrate on the overall heat transfer and phase change within this short time.

In the experiments with sessile liquid film (Shibkov et al. [135, 137]), or sessile supercooled drop (Bauerecker et al. [12] and Jung et al. [64]), the the nucleation site was singular, and a clear propagating front of the ice dendrite was identified, as shown in Figure 2.23 in Chapter 2. In the case of a drop impact, the ice dendrite was unrecognizable, and the nucleation took place uniformly across the entire drop surface. At the measured 3 K supercooling, the ice dendrite growth has a speed of 2mm/s (read from Figure 2.22 in Chapter 2). The first stage of solidification would take 650 ms to finish the $\phi 1.5$ mm drop. However in the case of drop impact, the duration was significantly shorter. At the achieved low supercooling of 3 K to 5 K, the nucleation process is known to be primarily governed by thermal diffusion [72, 73], and the growth rate of the ice dendrite must be the same for the both cases of with and without liquid flow. The difference between the two cases is the initial nucleation site, i.e. when, where and how much they formed. In the presence of strong liquid flow, numerous initial nucleation sites formed simultaneously. The ice dendrite initiated from each singular nucleation site met each other and stopped their growth, forming an overall uniform nucleation process inside the drop. Furthermore, the liquid flow promoted the contact of the individual ice dendrites, as well as the contact of the nucleation sites with the supercooled liquid. Consequently, the duration of the first stage of solidification was much shorter than that in a sessile liquid.

Multiple recordings as Figure 4.7 were acquired. The duration of the nucleation varied greatly, from 4.17 ms to 18.07 ms. Since the measured temperature of the impinging drop varied merely from −2 °C to −3 °C, corresponding to 1mm/s to 2mm/s growth rate of the ice dendrite, this variation was caused by the random formation of the initial nucleation sites. This randomness in the experiment might be attributed to the spatial heterogeneity of wettability of the SHS, which influenced the dynamic motion of the drop, and further influenced the formation of the nucleation sites. The wettability of the SHS was not perfectly reproducible.

Occasionally, nucleation occurred right upon impact. Figure 4.8 illustrates a typical total rebounding of the supercooled drop on a SHS at 5 °C, and the non-spherical shape of the drop head emerged in the first image after impact. The drop head recovered the spherical shape at the 0.45 ms, suggesting that the ice structure was so fragile that the deformation of the liquid could easily break it. The same effect can be recognized in Figure 4.6, where drop easily deformed despite the formation of the ice/water structure. This is not surprising because only a tiny fraction of the drop solidified during the heterogeneous nucleation at the achieved low supercooling.

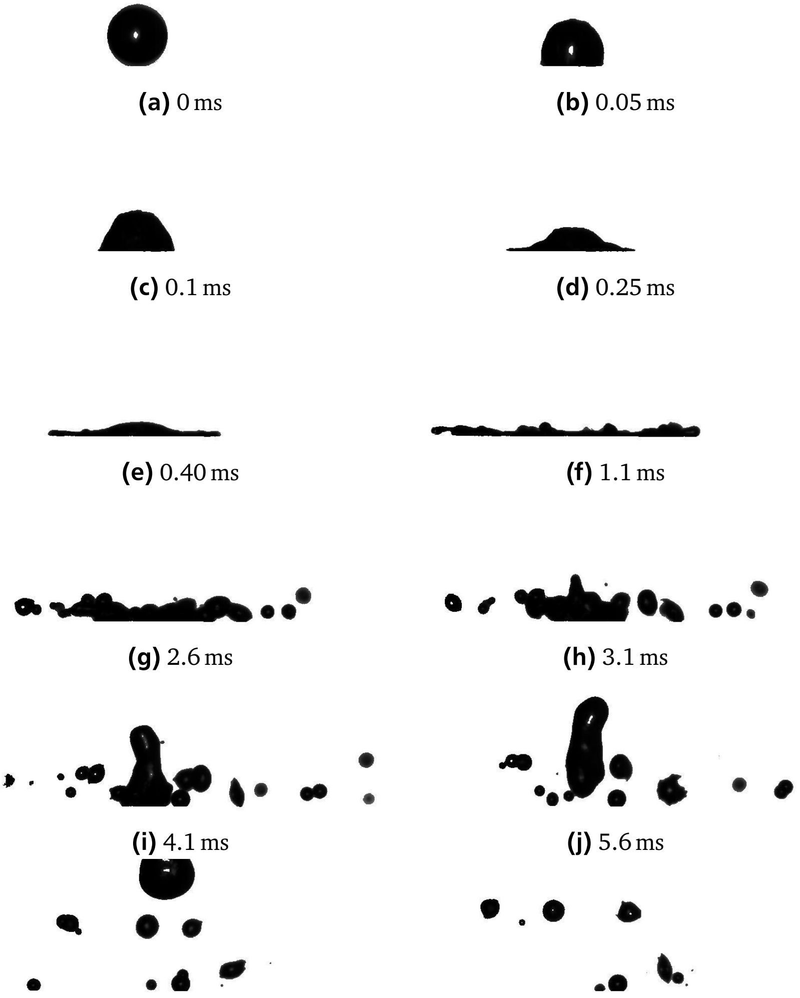

(a) 0 ms

(b) 0.05 ms

(c) 0.1 ms

(d) 0.25 ms

(e) 0.40 ms

(f) 1.1 ms

(g) 2.6 ms

(h) 3.1 ms

(i) 4.1 ms

(j) 5.6 ms

(k) 9.1 ms

(l) 11.85 ms

Figure 4.8.: A supercooled drop impacted on a SHS at 5 °C. Drop diameter: 1.46 mm, impact velocity: 3.32m/s. The non-spherical drop head appeared in the first image after impact, i.e. at the 0.05 ms.

At the 3.1 ms, one secondary "drop" with both smooth profile and sharp tips appeared on the right side of the spreading lamella. At the 5.6 ms it turned right opposite to the camera, exhibiting its unique structure: a piece of ice flake inlaid in a liquid drop. The shape of the ice structure was successfully captured. The ice crystal had a structure similar to a snowflake in Figure 2.16.

The observed ice crystal was in a planar shape. The ice crystal grows mainly parallel to the basal plane, which is defined as (1, 0, 0) plane according to the Miller index in crystallography [73, 80]. The planar shape of the ice crystal was recognized and documented by Macklin and Ryan (1966) [80] as Table 4.1 summarizes. Growth in the direction perpendicular to the basal plane is significantly weaker, although three dimensional structure exists [80]. The reason for this peculiar shape could be the non-isotropy of surface tension and/or interface kinetics, as discussed by Langer in 1980 [72].

Supercooling K	Type of Crystal
0 to 0.9	Disc crystals, plane stellar dendrites; surface needles
0.9 to 2.9	Plane stellar dendrites or dendrite sheets
2.7 to 5.5	Simple double pyramids (pyramidal caps)
5.5	Complex double pyramids showing secondary and higher order non-rational growth

Table 4.1.: Habits of ice crystals grown in pure water as a function of supercooling summarized by Macklin and Ryan [80].

4.2.2 Influence of Phase Change on Drop Receding

The impact of supercooled drop was conducted on a SHS of decreasing temperatures from 0 °C to −20 °C. On this SHS of slightly higher hydrophobicity, total drop rebounding took place until the substrate cooled down to −2 °C. As the substrate temperature further dropped, partial rebounding and receding eventually emerged. Figure 4.9 pictures the partial rebounding and the receding of supercooled drops on the SHS at three typical temperatures. The decreasing temperature weakened the receding effectively. Similar effect was observed by Mishchenko et al. [92], who observed the same effect in drop impact on SHS with water above 0 °C.

The time instant when the liquid surface started to turn translucent became earlier as the substrate became colder, from at the end of receding on substrates above −10 °C to during the receding on the −15 °C and −20 °C substrates. The spreading was mostly uninfluenced.

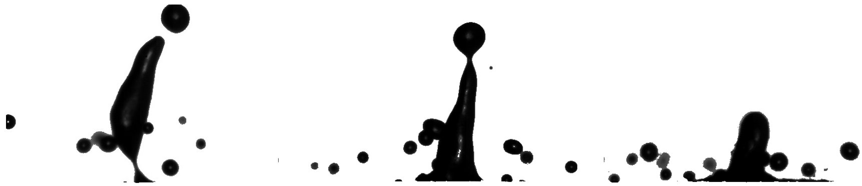

(a) −4 °C, at 6.8 ms. **(b)** −10 °C, at 6.7 ms. **(c)** −20 °C, at 6.05 ms.

Figure 4.9.: Receding of the supercooled drop after impact on a SHS at various temperatures. The drop diameters were approximately 1.50 mm and the impact velocities were approximately 3.4m/s. The complete recordings are listed in Appendix C.

Occasionally nucleation took place during spreading as represented by Figure 4.10. The occurrence of this type of early nucleation was random, absent at high substrate temperatures above −10 °C, and became more frequent at lower substrate temperatures.

(a) 0 ms **(b)** 0.65 ms **(c)** 3 ms

Figure 4.10.: A supercooled drop impacted on SHS at −20 °C. Drop diameter: 1.57 mm, impact velocity: 3.41m/s. Nucleation happened during spreading as shown by the sharp tip at 0.65 ms. Receding was hindered significantly by the ice structure.

These observations demonstrate that the receding was influenced by the substrate temperature, more precisely speaking, the contact temperature between the solidifying water and the solid substrate. It is hence of interest to measure the contact temperature during drop impact. The bottom-view of the infrared imaging offered this opportunity. Meanwhile this imaging provided a “top” view of the drop spreading.

Before the involvement of the supercooling, it is necessary to clarify the ice accretion resulting from a 0 °C drop impact, in order to highlight the difference caused by nucleation. Assuming a 0 °C drop impacted on a 12 μm thin aluminum film, which was laid on top of a 4 mm thick germanium infrared glass as Figure 4.11 depicts, the measured temperature is the temperature of the aluminum film at the bottom side, instead of the temperature of the spreading lamella. It is therefore necessary to evaluate the response time of the aluminum film before the measurement, namely how long it takes for the bottom side of the aluminum film to have the same temperature as its top side. Neglecting the contact thermal resistance, the temperature at the top side of the aluminum film is equal to the temperature of the bottom of the freezing lamella.

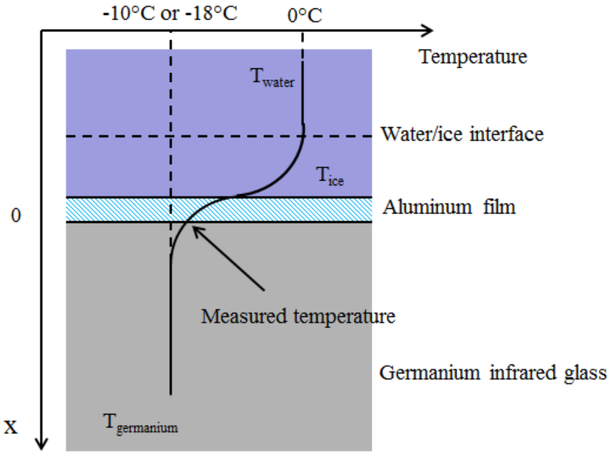

Figure 4.11.: Composition of the mechanical system in the measurement of the contact temperature.

A quick estimation is taken with the assumption that, during the short time the heat is conducted at a constant heat flux density $\dot{q} = \Delta T/(H_{alu}/k_{alu})$ in $\mathrm{W\,m^{-2}}$, where H_{alu} is the thickness of the aluminum film, k_{alu} is the thermal conductivity of aluminum. The total heat consumption per unit area is $q = \rho c_{alu} \Delta T H_{alu}$ in $\mathrm{J\,m^{-2}}$. This leads to the response time $t_{response} = q/\dot{q} = c_p \rho H_{alu}^2/k_{alu} = 1.48 \mu s$. Since the estimated value was nearly three orders of magnitude smaller than the recording period of the infrared camera, 1.39 ms, the bottom side of the aluminum film should faithfully follow the temperature of the ice/aluminum interface.

The temperature at the interface is neither the temperature of the lamella nor the temperature of the germanium substrate. Rather, it is an intermediate value determined by both the initial temperatures of the mediums and their thermal properties, more precisely speaking, the ratio of the two thermal effusivities. The thermal effusivity of a material is defined as

$$e = \sqrt{k \rho c_p}. \tag{4.4}$$

The contact temperature is closer to the medium with higher effusivity. This answers why it feels colder while touching a cold medal surface than a wood one of the same temperature. Table 4.2 lists the properties of ice, aluminum and germanium. These values yield thermal effusivities of $5.74 \times 10^8\,\mathrm{W\,s^{1/2}\,K^{-1}\,m^{-2}}$ for aluminum, $1.02 \times 10^8\,\mathrm{W\,s^{1/2}\,K^{-1}\,m^{-2}}$ for germanium and $4.17 \times 10^6\,\mathrm{W\,s^{1/2}\,K^{-1}\,m^{-2}}$ for ice. It is therefore anticipated that the contact temperature does not rise much when the drop impacts on the cold surface. Since the response time of the aluminum film is sufficiently short and its thermal effusivity is 5 times higher than germanium, this thin film is neglected in the calculation.

	Ice	Aluminum	Germanium
Thermal conductivity ($\mathrm{W\,m^{-1}\,K^{-1}}$)	2.22	237	60.2
Density ($\mathrm{kg\,m^{-3}}$)	916	2700	5323
Specific heat ($\mathrm{kJ\,kg^{-1}\,K^{-1}}$)	2.05	0.897	0.3197

Table 4.2.: Properties of aluminum, germanium and ice.

Taking one of the two sides for an example, it is a one-dimensional transient heat conduction problem. This process is governed by Eq. 2.15 in Chapter 2. For the convenience of reference, this equation is rewritten in a different form here as

$$\frac{\partial T}{\partial t} = \alpha \frac{\partial^2 T}{\partial x^2}. \tag{4.5}$$

The initial condition is

$$T(x, t = 0) = T_A, \tag{4.6}$$

where the initial temperature of ice is T_{A-ice} =0 °C, and the other T_{A-ge} =−10 °C and −18 °C, dependent on the temperature setting.

The boundary condition for each side is an imposed heat flux, although the value is unknown before the solution is found,

$$-k\left(\frac{\partial T}{\partial x}\right) = \dot{q}, \tag{4.7}$$

with $x = 0$ is at the interface of ice/germanium.

On the water/ice side, the phase change keeps the water/ice interface at 0 °C. Consequently this side appears as a semi-infinite slab, before the water is completely frozen. The germanium infrared glass on the other side has a thickness

4 mm thick, several orders of magnitude thicker than the 200 μm lamella. Therefore it is reasonable to simplify the contact temperature as between two semi-infinite plates. Eq. 3.24 in Chapter 3 provides the analytical solution for each side as

$$\Theta = erf\,\chi^* + e^{-\chi^{*2}} e^{(\chi^* + Bi^*)^2} \left[1 - erf(\chi^* + Bi^*)\right],$$

where Θ is the dimensionless temperature, and χ^* is the dimensionless distance from the interface.

Since the contact resistance is neglected, the temperatures of the two materials change infinitely fast from the initial temperature to the contact temperature at the interface. This assumption implicates infinitely large Bi for the transient heat conduction of each side. In case of $Bi \rightarrow \infty$, Eq. 3.24 is further simplified as

$$\Theta = erf\,\chi^*. \tag{4.8}$$

At the interface between ice and germanium, the contact temperature is a singular value and the heat fluxes must be of equal magnitudes for both sides:

$$T_{ice}(x = 0^-) = T_{ge}(x = 0^+) \equiv T_K, \tag{4.9}$$

and

$$\dot{q}_{ice}(x = 0^-) = k_{ice}\frac{\partial T}{\partial x} = k_{ge}\frac{\partial T}{\partial x} = \dot{q}_{ge}(x = 0^+). \tag{4.10}$$

For each medium, the solution is provided by Eq. 4.8:

$$\Theta_{ice} \equiv \frac{T - T_K}{T_{A-ice} - T_K} = -erf\,\frac{x}{2\alpha_{ice} t}, \quad (x < 0), \tag{4.11}$$

and

$$\Theta_{ge} \equiv \frac{T - T_K}{T_{A-ge} - T_K} = erf\,\frac{x}{2\alpha_{ge} t}, \quad (x > 0). \tag{4.12}$$

With Eq. 4.10, it yields [59]

$$T_K = \frac{T_{A-ice} + \frac{e_{ge}}{e_{ice}} T_{A-ge}}{1 + \frac{e_{ge}}{e_{ice}}}. \tag{4.13}$$

Obviously, the contact temperature T_K is time invariant.

The image sequences in Figure 4.12 represent typical results of the contact temperature measurement. The drop was supercooled, and the substrates were at $-10\,^{\circ}\mathrm{C}$ and $-18\,^{\circ}\mathrm{C}$ respectively. The original image was $20\,\mathrm{mm} \times 20\,\mathrm{mm}$ wide with the pixel resolution of 256×256. Since not the entire region had valid calibration, only a portion was cropped for illustration. The field of view in the image sequence is $9.55\,\mathrm{mm} \times 12.27\,\mathrm{mm}$, 122×157 in pixels.

One image was successfully captured during the spreading phase in the bottom-view, the same effect as in the side-view infrared imaging shown in Figure 3.46 and Figure 3.47 in Chapter 3. This confirms that the response time of the aluminum film was sufficiently short.

The temperature of the bottom of the lamella kept constant for a certain time after the drop impact, as the theoretical prediction Eq. 4.13 states. The contact temperatures are calculated by Eq. 4.13 as $-8\,^{\circ}\mathrm{C}$ and $-15\,^{\circ}\mathrm{C}$ for the $-10\,^{\circ}\mathrm{C}$ and $-18\,^{\circ}\mathrm{C}$ germanium substrates respectively, while the infrared imaging measured them as $-7.5\pm0.5^{\circ}\mathrm{C}$ and $-14.5\pm0.5^{\circ}\mathrm{C}$ accordingly. The experimental data and the theoretical prediction met an almost exact agreement. Eventually the periphery of the lamella cooled down, and the substrate warmed up as elucidated by the weakening sharpness of the border, indicating that the simplification of semi-infinite slab began to be violated.

This bottom-view infrared imaging provided a “top” view of drop spreading. Above $-10\,^{\circ}\mathrm{C}$, which is the lowest SLD icing temperature, the drop spreading was mostly symmetrical, thus the spreading was uninfluenced by the nucleation with the realized low supercooling of $5\,\mathrm{K}$ at the maximum. On the colder substrate at $-18\,^{\circ}\mathrm{C}$, the maximum spreading diameter was still unaffected. However the subsequent cooling effect reveals the uneven thickness of the residual lamella, indicating that the ice/water mixture formed during the first stage of solidification hindered the motion of the liquid.

The drop receding on the SHS is parameterized by the minimum receding diameter $d_{rec-min}$, which is defined as the diameter of the residual lamella when receding reached the maximum as illustrated in Figure 4.13 on the left. The $d_{rec-min}$ is scaled by the maximum spreading diameter d_{sp-max}. The contact temperature is calculated by Eq. 4.13, and further nondimensionalized by the Stefan number. Since the drop diameter and the impact velocity was limited to a narrow range, the contact temperature was the only independent variable in these tests. The $d_{rec-min}$ increased quasilinearly as the contact temperature decreased. Larger data randomness at low contact temperatures was caused by the nucleation during spreading as pictured in Figure 4.10.

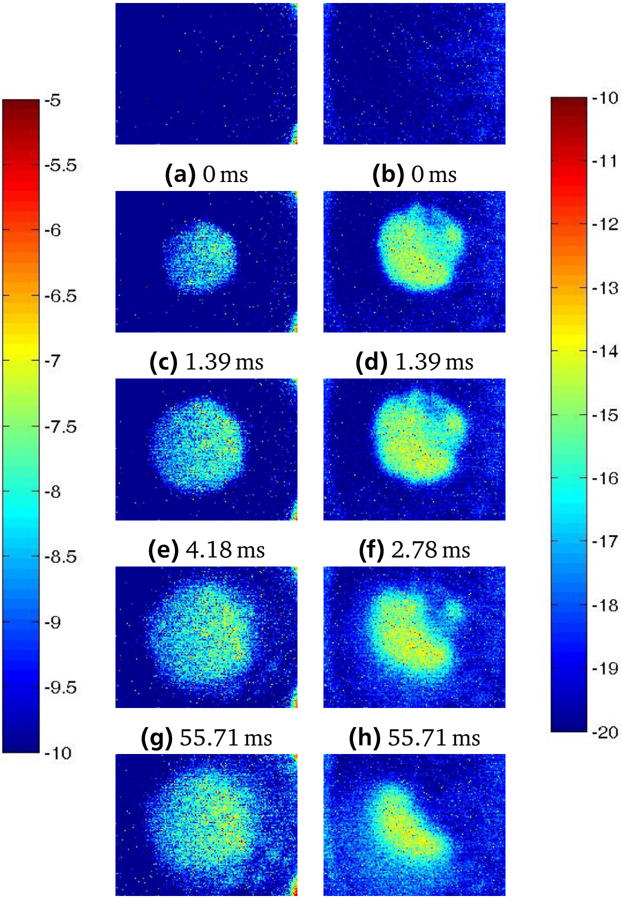

(a) 0 ms **(b)** 0 ms

(c) 1.39 ms **(d)** 1.39 ms

(e) 4.18 ms **(f)** 2.78 ms

(g) 55.71 ms **(h)** 55.71 ms

(i) 267.41 ms **(j)** 257.15 ms

Figure 4.12.: Measurement of the contact temperature. T_K on substrates at $-10\,^{\circ}\mathrm{C}$ (left) and at $-18\,^{\circ}\mathrm{C}$ (right) were measured as $-7.5 \pm 0.5^{\circ}\mathrm{C}$ and $-14.5 \pm 0.5^{\circ}\mathrm{C}$ respectively, corresponding to the theoretical prediction of $-8\,^{\circ}\mathrm{C}$ and $-15\,^{\circ}\mathrm{C}$.

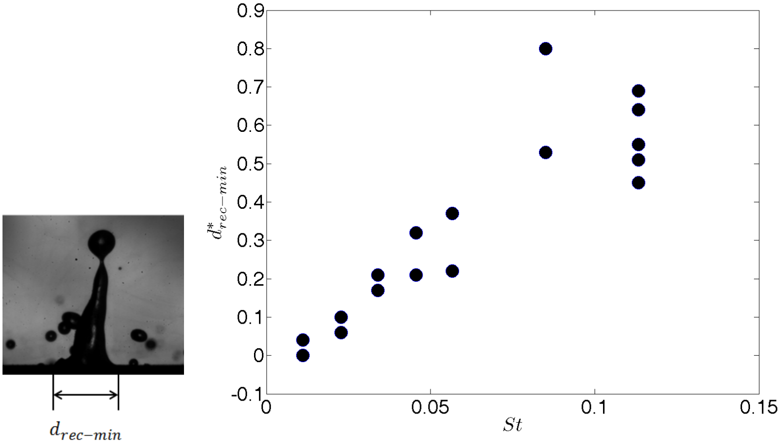

Figure 4.13.: The dimensionless minimum receding diameter $d^*_{rec-min} = d_{rec-min}/d_{sp-max}$ on SHSs of different temperatures. The Stefan number is defined as $St = c_{ice}(T_m - T_B)/L$, where T_K is contact temperature, T_m is the melting temperature, and L is the latent heat.

4.2.3 Physics of the Rime Ice

The rime ice forms at very low temperatures approaching −20 °C. This type of ice has a regular shape as shown in Figure 4.14 and its structure is fragile, easy to be removed from the wing surface. The conventional hypothesis of its formation is that cloud droplets freeze completely upon impact. In the Messinger Model as depicted in Figure 2.1, only the impinging mass is considered in the mass balance, whereas the energy balance is completely ignored. This method leads to accurate prediction of ice shape, for example by LEWICE [165]. However our experimental results prove that complete freezing upon impact is impossible because of the slow second stage of solidification. It is the first stage of nucleation and the resultant formation of the ice/water mixture which hinders, or prohibits, the motion of the liquid, leading to such an “apparent” complete freezing. Without supercooling, the rime ice is an impossible phenomenon.

Another oversimplification of the conventional assumption with the Messinger’s model is that the drop impacts on dry ice surface. In the icing wind tunnel test of Tsao et al. [147], rime ice was observed with the MVD of 15 μm MVD, the LWC of 0.5 $\mathrm{g\,m^{-3}}$, the impact velocity of 77m/s, and at the temperature of −21 °C. Assum-

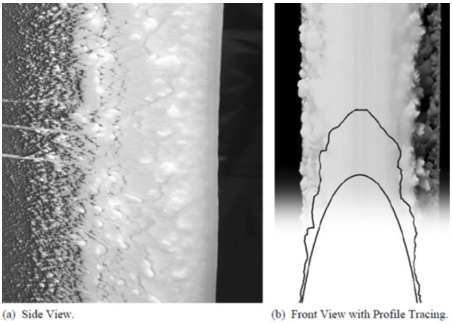
(a) Side View.

(b) Front View with Profile Tracing.

Figure 4.14.: Rime ice observed in icing wind tunnel tests of Tsao et al. [147].

ing the droplet had a uniform spatial distribution, the spatial interval between two drops was then 1.5 mm, and the temporal interval was 0.02 ms. In such a short time, 0.25 μm thick ice was formed according to the one-phase Stefan problem, while the residual film thickness was 0.89 μm according to Eq. 4.1. Therefore the drops impacted on a mushy layer of ice/water mixture instead of a dry surface. Further it can be inferred that the spontaneous nucleation on this mushy layer should be a frequent event, leading to the motion cease of the impinging drop.

4.3 Conclusion

Supercooled drop was created by a 1.5 mm drop falling through a cold passage at −196 °C. Such a low temperature was provided by circulating liquid nitrogen. The drop acquired approximately −5 °C after a falling distance of 600 mm. The impact surfaces included aluminum surfaces and superhydrophobic surfaces. The substrate was dry and its temperature from 5 °C to −20 °C was well controlled.

The measurement of the dynamic spreading diameter of drop impact on aluminum surfaces revealed the invisible difference brought by the two stages of solidification. An analytical approach was applied to examine the influence of solidification and ice dendrite growth at wider impact conditions. It was found out that the phase change was negligible for typical in-flight icing conditions.

The drop receding and rebounding on the SHS delivered better observation of the first stage solidification during the drop impact. The drop impact was identified as a trigger of the heterogeneous nucleation. Nucleation could occur right upon impact, during spreading, or during receding. The time of nucleation had a clear dependence on the contact temperature between the solidifying water and the solid substrate. At a contact temperatures higher than −10 °C, the nucleation occurred always after the receding reached the maximum. At lower contact temperatures, the nucleation occurred earlier, but still mostly after the maximum spreading was achieved. Occasionally, nucleation during drop spreading was observed on the −15 °C and −20 °C substrates.

The temperature rise during nucleation was recorded by the infrared imaging, and first stage of solidification was recognized in the shadowgraph imaging as the transition of the liquid surface from transparent to translucent. It was found out that the duration of the first stage solidification was much shorter during drop impact than in a sessile liquid. The surface temperature changed uniformly, indicating that nucleation took place uniformly inside the drop. The observations indicate that multiple initial nucleation sites formed simultaneously during drop impact. After nucleation, the drop, as well as the secondary droplets, became mixtures of ice and water. The ice crystals created in the supercooled water was had a similar morphology as snowflakes. Both the nucleation and the duration of the first stage of solidification were in a random manner because the location and amount of the initial nucleation sites were uncontrollable.

The receding of the liquid lamella on the SHS was influenced by the contact temperature, which was measured by the bottom-view infrared imaging. The measured value and the theoretical prediction met an exact agreement. The contact temperature exhibited no difference between the impact of 0 °C drop and a supercooled liquid drop.

These results unveil that the presence of supercooling is a prerequisite of the formation of rime ice. It is the ice/water mixture which hinders the motion of the impinging water on the wing surface, instead of complete freezing as conventionally assumed.

Since the phase change was uninfluential at low supercooling of −5 °C, the drop splash experiment with high impact velocities was conducted at the room temperatures, as described in the next two chapters.

Part II.

High Speed Impact of Single Drops on Dry Surfaces

Part II reports the experimental investigation on the high-speed oblique drop impact on dry surfaces. The drop impact incident in an in-flight icing event imposes four requirements on the experimental investigation: supercooling, high impact velocities in the order of 100m/s, various impact angles, and single drops from $100\,\mu$m to $400\,\mu$m in diameter. The supercooling has little effect on the hydrodynamics of the high speed drop impact at low supercooling, therefore it was neglected, and the experiment was conducted at room temperature. The other two requirements were fulfilled in the experiment. Chapter 5 describes the experimental setup and the results are introduced Chapter 6. The observations provide a close-up view of the drop impact in the in-flight condition.

5 Experimental Setup

This chapter introduces the experimental setup. Section 5.1 discusses different methods to realize the high-speed drop impact, and points out the most practical solution. Section 5.2 and 5.3 introduce the drop generation. The drop generator comprised two parts: a vibrating orifice drop generator which produced drops in the required diameter range, and an electrostatic deflector which selected individual drops for the single drop impact. Section 5.4 is devoted to imaging system, including the choice of temporal and spatial resolution, the enhancement of the depth of field, and the illumination solution. Section 5.5 describes the synchronization system, which was a crucial part for both the trigger of imaging system, and the operation of the drop generator. The performance of the experimental setup is presented in Section 5.6 quantitatively with the impact Re and We.

5.1 High-speed Impact Method

In order to achieve high impact velocities, either the drop or the impact surface needs to be accelerated. In an icing wind tunnel, droplets are accelerated by the airflow. Despite the expensive construction, this experimental regime is not suitable for observation of the single drop impact on account of two disadvantages. Firstly the location of the drop impact can not be precisely controlled, because the trajectory of the drop is strongly influenced by the airflow in the long journey before impact. Secondly, the acceleration of a long duration harms the sphericity of large drops.

The alternative, low-speed drops impacting on a high-speed substrate, is of much lower cost. The drop is generated shortly ahead of the coming substrate, so its trajectory and shape is less influenced by the airflow as in a wind tunnel test.

The most convenient way to accelerate the solid substrate is to rotate it by an AC motor. The tangential speed is determined by the radius of the target and the angular frequency as $v = 2\pi f R$, where f is the frequency of the motor rotation, and R is the radius. Large radius was preferred for high tangential speeds. In order to reduce the aerodynamic drag which demands the power of the motor, a 700C road bicycle wheel was employed as Figure 5.1 illustrates. The wheel was completely covered by carbon fiber without any spokes. Therefore the form drag is much lower than with an ordinary bicycle wheel with 28 to 36 spokes. In order to realize a high-speed rotation of 3000 rpm, the hub of the wheel was removed, and a new shaft out of stainless steel was mounted. The ball bearing was changed by a stronger type (SKF Pendelkugellager, Kistenpfennig, Mainz, Germany). The bead seat diameter of the wheel was 622 mm. The targets, on which the impact surface located, were mounted on the rim of the wheel. Two targets in the opposite direction were simultaneously mounted, in order to keep the dynamic balance. The target had a height of 24 mm. The final radius of rotation was 343.75 mm. A tangential velocity of 100m/s required the angular speed at 290.91 rad/s, which corresponded to 2780 rpm.

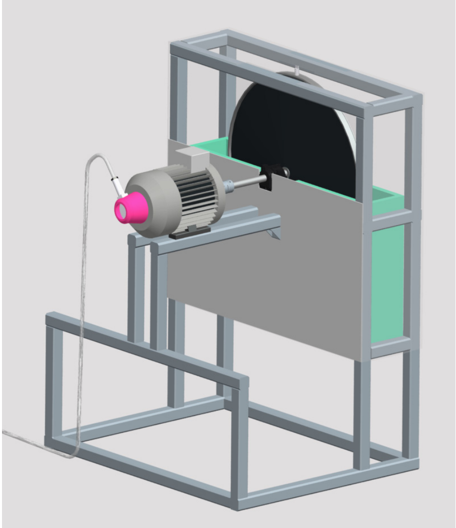

Figure 5.1.: The target is mounted on the wheel at the apex of the rotation. The wheel and the target was encapsulated with 2 mm thick aluminum plate for the sake of safety. Only one plate is displayed in grey while the others are made transparent for the purpose of exhibition. The green parts are extra Polystyrene plates also for the purpose of security. The pink part at the backside of the motor is the encoder which provides signals for the motor control.

The majority of the drag was created by the targets. Simplifying the target as a ϕ14 mm cylinder with a height of 24 mm, the Reynolds number at the tangential speed of 100m/s was 1.59×10^5. Reading from [35], the drag coefficient was approximately 1.0. The aerodynamic drag was thus estimated as $F_d = \rho v^2 dl/2 =$

2.17 N, and the torque as 0.75 Nm. The total torque for the two targets was then as 1.5 Nm. Since the skin friction on the wheel and the friction at the bearing contributed to the load requirement as well, the design factor of safety was taken as 2. Finally 3 Nm was decided as the minimum rated torque of the motor.

A Siemens AC motor (1LA7090-2AA10-Z), which has an operating speed of 2860 rpm at the full rated torque of 5 Nm, was chosen for application. The speed control is provided by the frequency converter SINAMICS G120, which operates between 5 Hz to 50 Hz, corresponding to 10m/s to 100m/s of the tangential speed. The torque at the maximum rotational frequency of 50 Hz was 2.80 Nm, and the power consumption was 0.88 kW, lower than the capacity of the motor, 1.5 kW. Additionally an EMC (Electromagnetic compatibility) filter was incorporated in the control unit in order to minimize the electromagnetic interference created by the frequency converter.

The horizontal translation of the impact surface was advantageous at the image processing. In order to achieve a horizontal motion of the target, the location of the drop impact was chosen to be at the highest point of the rotation. Since the target rotated instead of translated linearly, it is necessary to examine the difference. The radius of rotation was 343.75 mm, while the greatest field of view applied in the experiment was 2.6 mm in width. A simple plane geometry calculation shows that the sagitta of the chord composed by the width of the field of view was merely 2.5 μm. Therefore the velocity of the target was practically horizontal.

The velocity of the target was measured from the video in order to examine the precision of the motor controller. The difference between the measured value and the motor setting was at the maximum 1%. This is probably due to the error in the radius measurement. Therefore the velocity of the target was taken as the setting of the motor.

The aluminum targets were manufactured with different inclinations to allow oblique impact, as Figure 5.2 shows. The targets are named by their angles, such as the 75° target in Figure 5.2. The surface was polished with a roughness of R_z =1±0.25μm as measured by Mahr Perthometer (resolution: 12 nm, Mahr GmbH, Göttingen, Germany).

Security is of critical importance in the operation with high speeds. The most dangerous aspect was the imbalance. At high speed rotation asymmetries of the mass distribution cause vibration, which further induces failure of the bearing, the wheel, even the frame structure. The dynamic balance was accomplished with the technical support from Fachgebiet Strukturdynamik in TU Darmstadt. Two acceleration sensors were stuck to the bearing to measure the vibration. Two resonance frequencies of the rotating system were detected as 22 Hz and 36 Hz. The radial

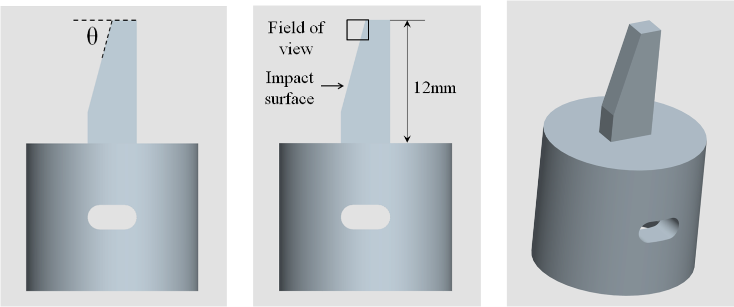

Figure 5.2.: Impact surface with different inclinations. The target is named according to the inclination θ as marked in the left photo. The impact surface was 2 mm wide. The field of view of the imaging system was close to the top edge of the target.

acceleration was reduced from $80g$ to less than $1g$ at the rotational frequency of 20 Hz, which was close to the resonance frequency. In practice, the vibration was minimal. The balance test was done without the targets. In order to keep the dynamic balance the weight difference between each pair of targets were limited to 0.01 g. Besides the weight of the target was around 3.4 g, minimal compared to total weight of the entire rotator, approximately 1 kg.

The second risk was the fatigue of material. The rotating targets exerted centrifugal force on the rim of the bicycle wheel. The force was unsteady because of continual on and off operation of the motor and the adjustment of the rotational frequency. Therefore the rim was subjected to a cyclic loading which in general creates progressive and localized structural damage of a material. It was tested that the wheel with targets was able to sustain the maximum rotational frequency of 50 Hz, but the nominal maximum stress for fatigue is less than the ultimate tensile stress limit, and may be below the yield stress limit. It was unknown when the rim would break. Therefore 2 mm thick aluminum plates were mounted on the frame in order to contain the risk in a limited space. After operation of three years, the problem with the material fatigue did not emerge.

It is unavoidable that strong wind was caused by the fast rotating target. The small drops were blown away from the region of observation. Because of this limitation, the maximum rotational frequency applied was set as 30 Hz, corresponding to a tangential speed of 63m/s. The wind was recognized as one of the two major factors which led to low probability of successful capturing of the impact process.

In summary the high-speed impact was realized by fast rotating targets and low-speed drops. The target angle was variable from 0° to 75°, and the target speed ranged from 10m/s to 63m/s.

5.2 Vibrating Orifice Drop Generator

The vibrating orifice drop generator was chosen for the drop generation on account of two advantages. Firstly, it produces drops in the required diameter range from $60\,\mu$m to $260\,\mu$m. Secondly, the drop has a velocity of the order of 10m/s, so that the drop can penetrate the strong wind induced by the rotating target. On the other hand, this drop generator has two disadvantages. Firstly, the drops are generated in a train instead of in a drop-on-demand mode. Consequently drops interact with each other during the impact process, undesired for our application. Secondly, the target is continuously wetted by the drop train, violating the condition of a dry impact surface. This section introduces the performance of this drop generator, and the next section introduces the solution to prevent the two disadvantages.

5.2.1 Construction and Typical Performance

The disintegration of the liquid jet into drops as well as the involved instability has been a subject of interest since the nineteenth century. Pioneer works are for instance from Bidone (1829) [17], Savart (1883) [127], Magnus (1855) [81], Boussinesq (1877) [21], Plateau (1873) [110] and Rayleigh (1878) [118]. The Plateau-Rayleigh instability [118] predicts that perturbation wave should have a nondimensional wavenumber $k_{Rayleigh} = \pi d/\lambda$ smaller than 1 in order to make the drop disintegrate from an inviscid liquid jet. The most rapid growth of the perturbation wave resides at $k_{Rayleigh} = 0.697$. Weber (1931) [158] included the effect of viscosity in his analysis of the jet breakup, and found out that the most unstable perturbation has longer wavelength for viscous liquid, but the condition of $k_{Rayleigh} < 1$ does not alter. These theoretical works promoted the invention of the vibrating orifice drop generator.

In the presence of a controlled auxiliary disturbance, a liquid jet disintegrates uniformly into small drops, forming a monodisperse drop train. The drops have equal diameters, and the intervals between drops are also uniform. The external disturbance is the most widely realized by piezoceramics which is connected to an excitation voltage signal. Although the vibration of the peizoceramics is as tiny as in nanometers, the disturbance is amplified effectively as the Rayleigh instability predicts. The drop size is approximately twice the diameter of the liquid jet.

Various such devices were developed since 1960s, for instance by Schneider [76, 128], Dabora [36] and Liu [13]. There are also commercial products such as SBG-2000 (PALAS GmbH, Karlsruhe, Germany), MTG-01-G1 (FMP Technology GmbH, Erlangen, Germany) and Model 3450 Vibrating Orifice Aerosol Generator (TSI, Shoreview, U.S.A.). In our experiment the TSI nozzle was applied, as shown in Figure 5.3.

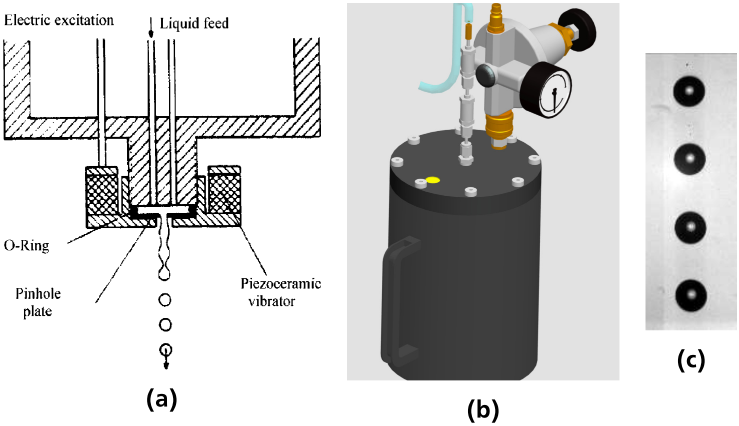

Figure 5.3.: A sketch of the TSI nozzle is shown in (a) [22]. The pinhole plate was the "Precision Pinhole" from EdmundOptics. The pinhole was cleaned by an ultrasonic water bath each time before operation. Any contamination of the pinhole made the monodisperse drop train fail to appear. The $24\,\mathrm{V}$ square wave excitation signal was provided by NI 6602 module together with a solid-state relay. The liquid feed was provided by the pressure chamber shown in (b). The flow rate was controlled by the pressure regulator (DRF 31 GS, $0\,\mathrm{bar}$ to $1\,\mathrm{bar}$, Landefeld, Germany) with an appropriate manometer. Two filters (SS-2F-2 and SS-2F-7, Swagelok) with nominal pore size of $7\,\mu\mathrm{m}$ and $2\,\mu\mathrm{m}$ were mounted in a sequence downstream of the liquid flow in order to avoid foreign particles in the liquid. It was experimentally found out that impurity considerably harms the generation of the monodisperse drop train. A typical monodisperse drop train generated with the $100\,\mu\mathrm{m}$ pinhole is shown in (c). The drops had a diameter of $175\,\mu\mathrm{m}$ and a velocity of $11.4\mathrm{m/s}$.

High-speed videos such as Figure 5.3 (c) were taken to examine the applicable range of the drop diameter and the liquid jet velocity. Three pinholes were applied:

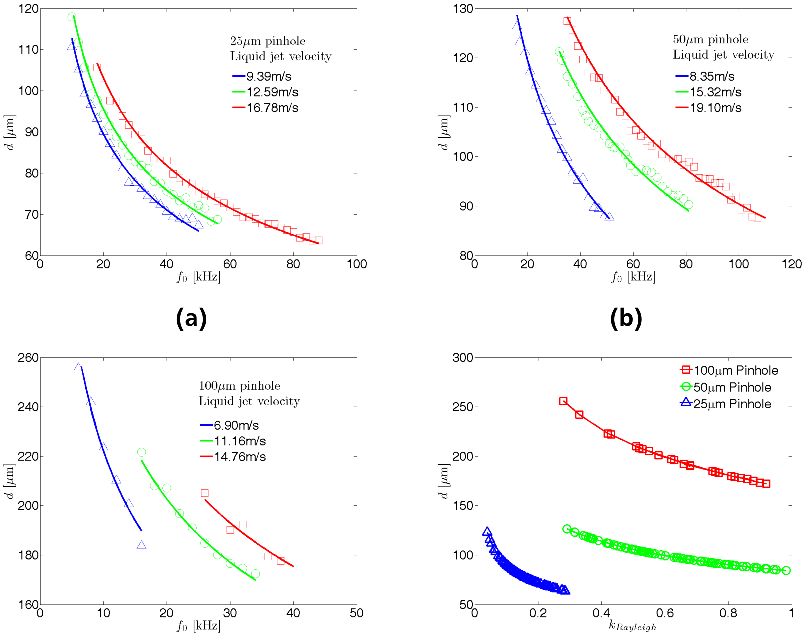

(a)

(b)

(c)

(d)

Figure 5.4.: The "frequency - diameter" charts ((a) to (c)) provide practical data for the operation of the vibrating orifice drop generator. f_0 denotes the excitation frequency. The dimensionless wavenumber was calculated as $k_{Rayleigh} = \pi d_{jet} f_0 / v_{jet}$, where d_{jet} is equal to the pinhole diameter. For each jet velocity there was a applicable range of excitation frequency, which changed the size of the drop appreciably. The marked jet velocity was an average value for the test points on one curve. The measured data scattered a little bit along the average curve on account of the fluctuation of the flow rate. Larger jet diameters tended to have narrower effective range of excitation frequency. It must be noted that the applicable frequency for a certain jet velocity could vary slightly at each start. Diagram (d) shows the agreement with the Rayleigh instability.

25 μm, 50 μm and 100 μm, and the results are plotted in Figure 5.4. The effective dimensionless wavenumber was calculated as $k_{Rayleigh} = \pi d f / v_{jet}$, resulting in a wide range of 0.040 to 0.951. The lower end of $k_{Rayleigh}$ was significantly lower

than the values reported in literature, such as 0.35 in [22], 0.29 in [151] and 0.44 in [128]. The higher end of the applicable $k_{Rayleigh}$ agrees well with the data in these literatures. The 100 μm pinhole was chosen for application because larger drops are better for imaging, and they have greater inertia against the wind induced by the rotating target.

The operation of the drop generator was not always trouble free because of the strict requirements on the cleanness of the pinhole and the purity of the liquid. The basic idea to control drop disintegration with auxiliary perturbations is on the contrary very simple. Inspired by the simple design nearly 50 years ago [76, 128] and the prohibiting price of the TSI drop generator of 17 000 Euros, a revised version of the drop generator was given to birth as shown in Figure 5.5. The main body was manufactured by the 3D printing with Teflon, and the piezoceramics was a 0.4 Euro buzzer which appears for instance in toys. This apparently cheaper version functioned the same as the TSI nozzle. Furthermore, the 3D printing technique allows an arbitrary shape of the drop generator. This invention was supported by M. Miller in her IREP summer exchange program [89].

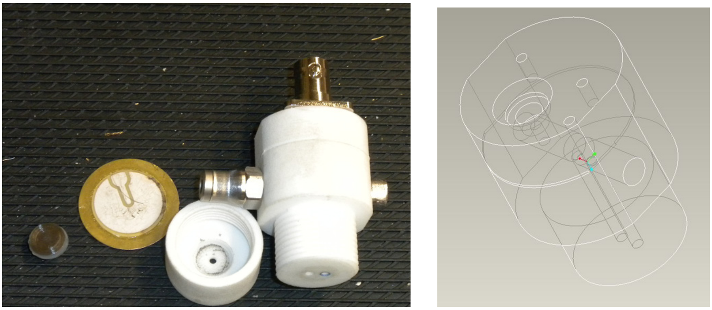

Figure 5.5.: The custom made vibrating orifice drop generator. The main body had a hydraulic plug-connector (RiB 01 04 10 CV, Landefeld, Germany) for the liquid feed, a BNC connector for the excitation signal, and a thin slot for the piezoceramics buzzer. The cap contained the pinhole and sealing ring out of rubber. The CAD image shows the interior liquid passage for water jet and purging. The buzzer accepts 5 V TTL signal, and thus can be directly controlled by the NI 6602 module.

5.2.2 Satellite Drop Formation and Merging

The Rayleigh instability does not reveal all the secrets of the drop generation. It is well-known that satellite drops appear upon jet breakup. In other words one perturbation wave disintegrates into multiple drops. The satellite drops eventually merge with the major drops, forming monodisperse drop chain. The life cycle of satellite droplets was observed by the high-speed shadowgraph imaging, as Figure 5.6 and Figure 5.7 represent.

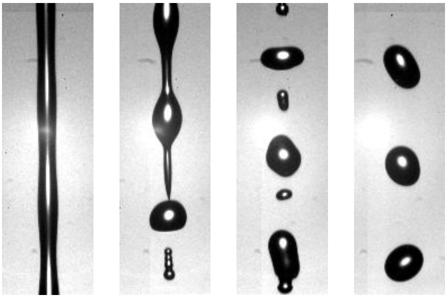

Figure 5.6.: The monodisperse drop train was created with a $100\mu\mathrm{m}$ pinhole and a $20\,\mathrm{kHz}$ excitation signal. The drop had an equivalent diameter of $199\mu\mathrm{m}$ and a downward velocity of $10.4\mathrm{m/s}$. The four images were taken at $6\,\mathrm{mm}$, $9\,\mathrm{mm}$, $10.5\,\mathrm{mm}$ and $18\,\mathrm{mm}$ downstream from the outlet of the drop generator. The disturbance wave had a roughly sinusoidal shape at early stages. Approaching the disintegration point, the perturbation wave became composed of a thin strip and a plump bulge, which resulted in periodical generation of a major drop and a satellite drop one after another. Both the major drop and the satellite oscillated along the vertical path, and generally merged with each other regularly, forming a stable drop train.

Two Domains of Drop Train Formation

Small perturbations brought by the piezoceramics grow according to the Rayleigh instability. As the amplitude of the perturbation wave increases to the magnitude order of the jet radius, the surface shape starts to deviate from sinusoidal shape. In the presence of such finite amplitude perturbation waves, the linear instability analysis of Rayleigh and Weber is no longer applicable, because the linear approx-

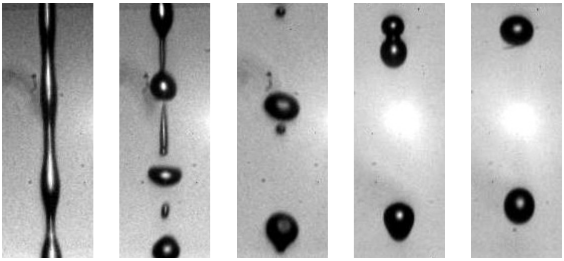

Figure 5.7.: The monodisperse drop train was created with a $25\,\mu\text{m}$ pinhole and a $30\,\text{kHz}$ excitation signal. The drop had an average diameter of $87\,\mu\text{m}$ and a downward velocity of 9.3m/s. The five images were taken at $1\,\text{mm}$, $1.5\,\text{mm}$, $4\,\text{mm}$, $9\,\text{mm}$ and $11.4\,\text{mm}$ downstream from the outlet of the drop generator. The deformation of the liquid jet, the formation of two drops by one perturbation wave, and the first merging of the drops was the same as with $100\,\mu\text{m}$ pinhole. The peculiarity with $25\,\mu\text{m}$ pinhole was the secondary merging: the major drops collided with each other regularly, and formed a stable drop train of larger drops.

imation is only valid for infinitesimal disturbances. Despite more than 100 years development, the nonlinear physics associated with the growth of large perturbations close to the breakup point, and details of satellite formation are not yet completely understood [39].

Upon jet breakup, the major drop and the satellite drop must acquire a velocity difference, so that one catches up with the other, and finally the both collide. Orme and coworkers' experiments [101, 102] in vacuum suggest that the velocity difference is induced by different capillary forces upstream and downstream at the instant of jet breakup. Regular merging plays an indispensable role in a successful generation of the monodisperse drop train.

Figure 5.8 and Figure 5.9 quantify the formation and merging of the satellite droplets. In the most cases of $50\,\mu\text{m}$ and $100\,\mu\text{m}$ pinholes, the perturbation wave had the same frequency as the excitation frequency. In such cases one wave broke into two droplets, which finally formed a stable drop by merging with each other, as Figure 5.6 represents. The frequency of the jet breakup was therefore twice of the frequency of the perturbation wave, which was equal to the frequency of the stable drops.

In the case of $25\,\mu\text{m}$ pinhole, the perturbation waves had unanimously higher frequencies than the excitation frequency. This implies that the jet breakup was primarily controlled by ambient disturbances, as the diagram on the right in Fig-

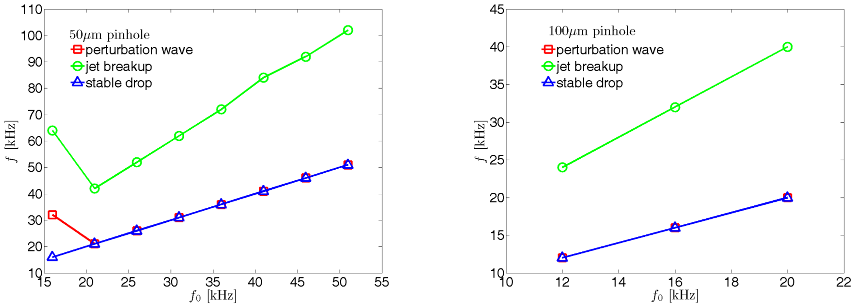

Figure 5.8.: Frequencies of the perturbation wave, the jet breakup and stable drops of the drop train generated with the 50 μm and 100 μm pinholes. The liquid jet speeds were between 7.3m/s and 8.3m/s. The speed of stable drop was approximately 1m/s slower than the jet speed.

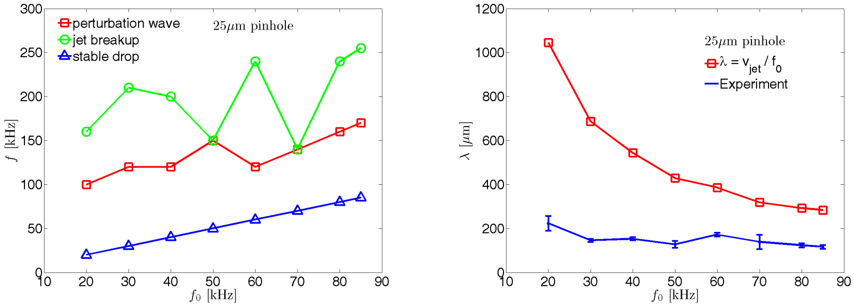

Figure 5.9.: Frequencies of the perturbation wave, jet breakup and stable drops of the drop train formed with the 25 μm pinhole (left). The liquid jet speeds was between 18.5 and 20m/s. The speeds of the stable drop were approximately 4m/s lower than the jet speeds. The measured wavelength of the perturbation wave is compared with the theoretical calculation on the right.

ure 5.9 manifests. Furthermore, nonlinear effects made the perturbation wave disintegrate irregularly into 1 to 1.75 drops on average. However, despite these complexities monodispersed drop train was formed and its frequency was exactly the same as the frequency of the excitation signal. The drop train with the 50 μm pinhole at 16 Hz was in this case.

This performance is a reminiscence of the amplitude modulation by Orme et al. [101, 102] and frequency modulation of Brenn et al. [22] of this type of drop generator. In these two operation modes, two signals are provided for excitation. The first signal is called as carrier signal, which is responsible for the active control of the jet breakup. The second signal is called as modulation signal, which creates a velocity difference between major drops by influencing the capillary force at the instant of the jet breakup [22]. Consequently it determines how many major drops merge with each other to form a monodisperse train, which is called modulation drops. The carrier signal is an integral multiple of the modulation signal. In our experiment, the excitation signal functioned as the modulation signal while the disturbance from the ambience functioned as the carrier signal. All the drops formed in one period of the modulation signal merged with each other and formed a bigger drop. Although it was unintentional, the drop generator with only one excitation signal functioned as if two signals were present.

Depending on whether the excitation signal governs the jet breakup, two domains can be defined according to $k_{Rayleigh}$. Figure 5.10 manifests this differentiation by reporting the jet breakup length of the three drop trains. The threshold value of the two domains was identified as $k_{Rayleigh} = 0.4$. If $k_{Rayleigh}$ is beyond this threshold, the jet breakup was controlled by the excitation signal. When $k_{Rayleigh}$ dropped below 0.4, the ambient disturbance dominated.

The Rayleigh instability explains the existence of this threshold by the optimum wavenumber $k_{Rayleigh-opt} = 0.697$. The liquid jets of $50\,\mu$m and $100\,\mu$m agreed qualitative well with the prediction by the shortest breakup length locating nearly at the $k_{Rayleigh-opt}$. When the set $k_{Rayleigh}$ deviates too far away from the $k_{Rayleigh-opt}$, the ambient disturbances surpassed the imposed perturbation and began to take charge of the breakup process. The real $k_{Rayleigh}$ calculated by the wave frequency was closer to the $k_{Rayleigh-opt}$ than the apparent one, which was merely nominal.

The threshold value varied slightly as the flow condition changed. In Figure 5.4 (d) the threshold was identified as 0.36. Ashgriz et al. reported this value as 0.29 [151], although no monodiserpse drop train was acquired in their experiment when $k_{Rayleigh}$ was below this threshold.

Length of the Stable Drop Train

Another two properties of the drop train were of interest: the merging distance, which was defined as the distance from the outlet of the drop generator to where the stable drop train formed, and the length of the stable drop train, which was

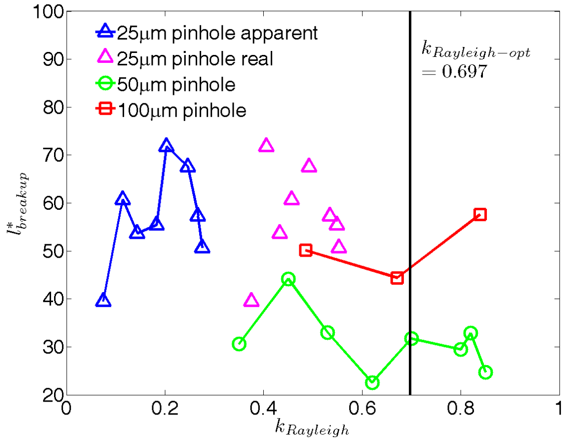

Figure 5.10.: Dimensionless jet breakup length. The jet breakup length was defined as the distance from the outlet of the drop generator to the jet breakup point. This length was nondimensionalized by the jet diameter as $l^*_{breakup} = l_{breakup}/d_{jet}$. The dimensionless wavenumber was calculated as $k_{Rayleigh} = \pi d_{jet} f_0 / v_{jet}$ except for the magenta triangles, for which the measured wave frequency f_{wave} replaced the excitation frequency f_0. These data points represent the ambient disturbances, which governed the jet breakup with the 25 μm pinhole. The same data used for Figure 5.8 and Figure 5.9 were applied in this graph.

defined as the distance from the first appearance of the stable drop to where the monodisperse condition was violated. Figure 5.11 reports on these two aspects.

The merging distance of the 25 μm jet was very long at low excitation frequencies because 3 to 5 major drops merged to form the final drop train. Similar situation happened to the 50 μm jet but with a smaller discrepancy. For most of the other cases, 5 mm was a good estimation of the merging distance.

The monodisperse drop train had a constant velocity. However eventually the drops were decelerated and the major drops began to collide with each other irregularly. Both bigger drops and reasonably high velocities helped to resist the external disturbances. The comparison between the 100 μm jet and the 50 μm jet evidenced the effect of the drop diameter. The former jet generated ϕ177 μm to ϕ213 μm drops, while the latter had ϕ88 μm to ϕ119 μm drops. The velocities of the two drop trains were similar, between 7.3m/s and 8.3m/s. Out of the same ef-

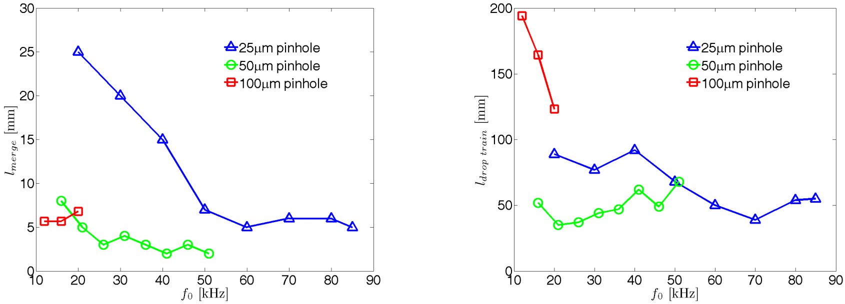

Figure 5.11.: The merging distance (left) and the length of the stable drop train (right) with the 25 μm, 50 μm and 100 μm pinholes.

fect, the $l_{droptrain}$ of the 100 μm jet experienced a sharp decrease as the excitation frequency increased. The 25 μm jet proved the effect of the velocity as compared to the 50 μm jet. The 25 μm jet created smaller drops, from 64 μm to 99 μm in diameter, but the lengths of the stable drop train were similar to the 50 μm jet, because the speed of the stable drop was twice higher, 19m/s.

In summary the vibrating orifice drop generator could operate with pinholes from 25 μm to 100 μm. The applicable jet velocity covered 6m/s to 20m/s. For each jet velocity there existed a wide range of effective excitation frequencies from 16 kHz to 100 kHz, which led to drop sizes from 50 μm to 200 μm. The breakup length rose with increasing jet diameter and jet speed, but mostly below 1.5 mm for the 25 μm and the 50 μm jet, and around 5 mm for the 100 μm. The merging distance was below 8 mm for most cases. The length of stable drop train was approximately 50 mm for the 25 μm and the 50 μm jets and increased significantly to over 120 mm with the 100 μm jet. These information are useful for the operation of the drop deflection.

5.3 Electrostatic Deflection of Charged Drops

The intervals between drops in a drop train must be enlarged in order to avoid interaction of multiple drops upon impact. Meanwhile, the drop train must be switched off periodically in order to retrieve the dry impact surface. The centrifugal force removed the deposited water effectively from the impact surface within 20 s, as experimentally found out. An ideal solution would be a fast “switch”, which could arbitrarily control each individual drop.

The method was a well-known technique, the electrostatic deflection of charged drops. Dated back to 1867, Lord Kelvin documented by his invention, the Kelvin water dropper [65], that a stream of dripping water passing through an electrically connected ring acquires net charges which is the opposite of the ring charge. Such charged drops can be directed in another electrostatic field by the Coulomb force. This technology was extensively developed in the early 1950s in the contemporary inkjet printers.

Figure 5.12 depicts the function principle of the electrostatic deflector on the left and the construction on the right.

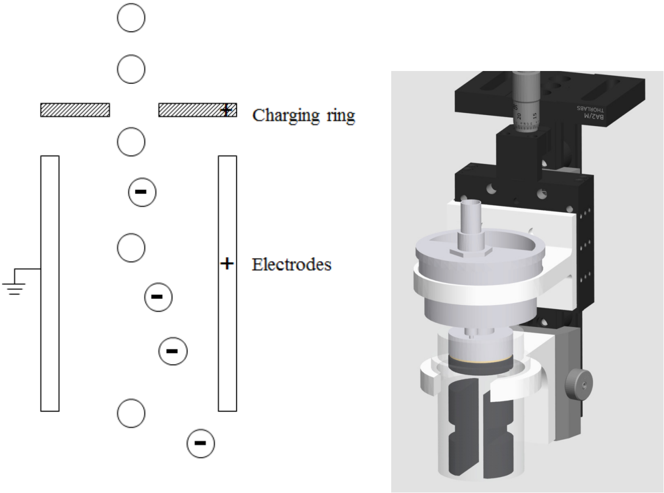

Figure 5.12.: Function principle and construction of the electrostatic deflector of the charged drops. The electrodes are the two black plates at the bottom. The drop generator and electrostatic deflector are mounted on a rail to ensure the alignment. The distance between the charging ring and the drop generator can be varied by the vertical translation stage.

A charging ring with a positive voltage of 100 V to 300 V was fixed several millimeters underneath the outlet of the drop generator, so that the drop acquired negative charge when it pinched off from the water jet. The electrical field for deflection was established by applying a potential difference of 1 kV to 5 kV between two parallel plates, which are called electrodes. Applying a pulse sequence to the charging ring, the drop could be selectively charged and deflected. The charging signal and the excitation signal of the vibrating orifice drop generator were synchronized to facilitate the selection. In practice 75% to 90% of the drop were charged and deflected, and the rest drops without charge were expected to impact on the target.

The circular charging ring was made of a bare PCB (printed circuit board) with a $\phi 3\,\mathrm{mm}$ hole at the center. The laminated copper film had a thickness of $170\,\mu\mathrm{m}$ and the non-conductive plate was of 2 mm thickness. The ground of the charging voltage was connected to the body of the vibrating orifice drop generator, hence also the water. The copper film on the PCB shielded the electrostatic field between the charging ring and the drop generator from the stronger field created by the electrodes. The electrodes were made of stainless steel, and were coated with insulating varnish in order to avoid short circuit caused by water during operation. The distance between the electrodes was 8 mm, which allows empirically 8 kV voltage on the electrodes. In practice, less than 6 kV was allowed because the moisture reduced the breakdown limit. The length of the electrodes was chosen as 40 mm.

The position of the charging ring and the length of the electrodes were restricted by the existence of monodisperse drop train. The gap width between outlet of the drop generator must be greater than the breakup length of the liquid jet, or else no net charge was to be obtained. Merging of satellite drops must be completed before the drops rush through the charging ring, or else regular merging was not guaranteed since smaller drops were easier to be deflected. The drop generator was mounted on a manual translation stage so that the gap width could be varied for application of liquid jets of different diameters. The length of the electrodes must be shorter than the length of the stable drop train, or else spray formed, and consequently the trajectory of drops were out of control.

5.3.1 Quantity of Charge

The quantity of charge is of interest since it directly relates to the distance of deflection. It was desired to have sufficient charge so that the drop could achieve 3 mm horizontal deflection after traveling along the electrodes for 40 mm. In the opposite, the quantity of charge was restricted by three factors. Firstly, the charge should not be so high that the internal repulsive force exceeds the surface tension, resulting in catastrophical disintegration of the drop. The maximum charge is predicted by Lord Rayleigh as [117]

$$Q_{e-max} = \sqrt{8\pi^2 \varepsilon_0 d^3 \sigma}, \tag{5.1}$$

where $\varepsilon_0 = 8.854\,187\,817 \times 10^{-12}$F/m is vacuum permittivity, d is diameter of the drop and σ is the surface tension. This yields a maximum charge of 2×10^{-11} C for a $100\,\mu$m drop. The realized charge quantity was far from this value.

The second factor was the repulsive force between the drops. Since most of the drops possessed the same charge for deflection, they act repel each other. The repulsive force should not be large enough to squeeze the drops laterally out of the main stream as in experiment of Orme et al. with molten metal droplets [77]. Observation by high-speed imaging manifested that no difference on the drop train was created by a constant charging voltage of 300 V.

The last restriction was related to the operation with sequential charging pulses. The charged drop was accelerated by the Coulomb force while the other uncharged drops kept their original speed. Eventually the charged drop would collide with the downstream drop. With the electrodes deactivated, this collision was observed several centimeters away from the drop generator. Once the electrodes was active, the collision was effectively prohibited because of the additional horizontal movement of the charged drops.

The configuration of the charging ring together with the drop generator is analogous to a capacitor with the two components as the conductors on each side. The dielectric medium between the two conductors is air. Distilled water has an electrical conductivity of 2×10^{-4} S/m [78]. This is very low compared to metal (e.g. aluminum has an electrical conductivity of 3.5×10^{7} S/m), but it is sufficiently conductive to comprise one side of the capacitor. In fact, 50 picosiemens per meter is the border between conductive and dielectric material [2]. Methanol with a lower electrical conductivity of 7×10^{-6} S/m and aqueous solution of sodium sulfate with a higher conductivity were also tested. Both of them exhibited equal effectiveness as water in deflection.

The electrical conductivity influences the characteristic time for the drop to get a charge of equilibration [75]. Materials of higher electrical resistivity needs longer time. For example silicone oil requires hours of charging time at the presence of thousands of volts per centimeter, while for water the value is on the order of microseconds or less. For the vibrating orifice drop generator, the charging time is the breakup time of the liquid jet, namely from the water coming out from the drop generator to one drop pinches off from the water jet. If the charging time is longer than the characteristic time, the quantity of charge could be calculated by an analogy with a capacitor as

$$Q_e = C U_c, \tag{5.2}$$

where C is the capacitance and the U_c is the charging voltage.

The analogy with a capacitor led to an accurate model for the quantity of charge as developed by Schneider et al. [78]. In their experiment, the charger was a tube instead of a ring. Liquid jet flew and broke inside the charging tube. This geometrical configuration is analogous to a coaxial cable with the capacitance calculated as

$$C_{tube} = \frac{2\pi\varepsilon l}{\ln\left(R_2/R_1\right)}, \tag{5.3}$$

where $\varepsilon = \varepsilon_r \varepsilon_0$ is the absolute permittivity. The relative permittivity ε_r is taken as 1 because the medium is air, and the vacuum permittivity is $\varepsilon_0 = 8.854\,187\,817 \times 10^{-12}\,\mathrm{F/m}$. R_2 is the radius of the outer cable, and the R_1 is the radius of the inner tube. The model for the quantity of charge was derived as

$$Q_e = \frac{2\pi\varepsilon_0\lambda}{ln(R_{charger}/R_{jet})}U = C_{tube}U_c \tag{5.4}$$

where U_c was the applied voltage on the charging tube, $\lambda = v_{jet}/f$ was the wavelength of the perturbation wave, $R_{charger}$ and R_{jet} were the radii of the charging tube and the liquid jet, respectively. This model assumed that the charging time was sufficient, and the nonlinear perturbation on the liquid jet had a negligible effect on the charging. This model was verified by measuring the current with a microammeter. The stream of the charged drop was directed into an insulated container, and the current from the container to ground was measured. The model fitted the measurement perfectly with tubes of different lengths. The breakup length was reported as 1.5 mm and the jet speed was 6m/s. This experiment implies that the characteristic time for distilled water is below 0.25 ms with a charging voltage of 20 V. In our experiment the applied charging voltage was between 100 V and 300 V, so the characteristic time should be much shorter.

A similar analogy was attempted with our construction. Overall the drop generator and the charging ring comprised a parallel-plate capacitor. This is inaccurate, because the ground side was not a plate but had a complex shape, which was composed of a plate and the liquid jet. Simplifying the gap as much larger than the breakup length, the liquid jet becomes negligible. The capacitance of a parallel-plate capacitor is

$$C_{plate} = \varepsilon_0 A/H_y, \tag{5.5}$$

where A is the area of the plate, H_y is the gap between the two plates, and likewise air is the dielectric medium. The area was taken as the surface of the cylindrical liquid jet $A = \pi d_{jet} \lambda = \pi d_{jet} v_{jet}/f$. The corresponding charge is

$$Q_e = C_{plate} U = \frac{\varepsilon_0 \pi d_{jet} v_{jet}}{H_y f} U_c. \tag{5.6}$$

The quantity of charge was measured by the horizontal deflection. It was ensured that the observation point was within the monodisperse drop train, so that the drops had a constant vertical velocity. Therefore the drop was a projectile exposed to an electrical potential field. The time of motion was determined by $t = l_y / v_y$, where l_y was the vertical distance from the top of the electrode to the observation point, v_y was the vertical translation speed. The aerodynamic drag was neglected because the horizontal speed was relatively low. The quantity of charge was measured by

$$\frac{EQ_e}{m} = \frac{2l_x}{(\frac{l_y}{v_y})^2}, \tag{5.7}$$

where $E = U_x/H_x$ is the electrical field, U_x is voltage on the electrodes, from 1.5 kV to 3 kV, the $H_x = 8$ mm is the distance between the electrodes, m is the mass of the drop, l_x is the horizontal deflection. The monodisperse drop train was created by the vibrating orifice drop generator with a 100 μm pinhole. The drops had a uniform diameter of 209 μm, the vertical speed v_y was 6.66m/s, and l_y was 34.86 mm. It is known that the quantity of charge is proportional to the charging voltage, therefore a singular voltage was applied to the charging ring as U_C =200 V.

Figure 5.13 demonstrates the inaccuracy of Eq. 5.6. The predicted value was more than one order of magnitude lower than experimental results. The reason is explained in Figure 5.14 by numerical simulation of the E field. The protrusion on one side of the capacitor is to simulate the liquid jet. A strong concentration of E field exists around the tip of the liquid jet. The quantity of surface charge is the integration of the local E field as

$$Q_e = \varepsilon \oint E \, dA, \tag{5.8}$$

where dA is the infinitesimal area element. Two special form of this equation are Eq. 5.3 and Eq. 5.5, where the area of the ideal capacitor is analytically integrable.

The real situation in the application is not in this case. Figure 5.14 shows that the effective E field around the tip of the protrusion is 10 times higher than the average value.

Further development of the model was of little importance, because the major difficulty was geometrical. On the other hand, it can be inferred that large surface deformation around the jet tip might conditionally play a notable role on the charge quantity, because the local E field determines the charge quantity.

Figure 5.15 pictures the electrical field between the electrodes. The measured charge quantity by Eq. 5.8 should be higher than the real value because of the undesired electrical field between the charging ring and the electrodes. This error should be nevertheless insignificant because of the strong concentration of the E field between the electrodes. The CST field was calculated with the guidance of Dr. W. Müller from TEMF (Institut Theorie Elektromagnetischer Felder, TU Darmstadt).

For the purpose of practical application, the diameter dependence of the charge quantity was tested as Figure 5.16 shows. The quantity of charge was nearly linearly proportional to the drop diameter.

5.3.2 Selective Deflection with Pulse Sequence

A sequence of voltage pulses was applied to the charging ring in order to selectively deflect a portion of the drops while keep the rest drops uncharged and fall straight into the observation region. Synchronization of the charging signal with the excitation signal of the drop generation, as Figure 5.17 represents, was compulsory for a periodic deflection.

The excitation signal served as a clock for the charging signal. The charging signal had an idle state of “high” in order to deflect all the droplets by default. The falling edge of the charging signal was triggered by 1 out of N pulses of the excitation signal. The duration of the low voltage, specified as “low time”, was at the maximum one period of the excitation signal. Longer “low time” led to charge of multiple drops, while shorter in general led to less quantity of charge, as Figure 5.18 shows. The duration of the high voltage, specified as “high time”, is the rest of the N periods of the excitation signal.

Essentially the charging signal was to be synchronized with the drop generation, instead of the excitation pulses. Each pulse of the excitation signal corresponded to one drop breakup from the liquid jet, but it was unknown at which phase of the excitation signal the drop pinched off from the liquid jet. To examine the relation between the jet breakup and the excitation signal, the charging signal was shifted with a phase offset relative to the excitation signal as shown in Figure 5.19. The

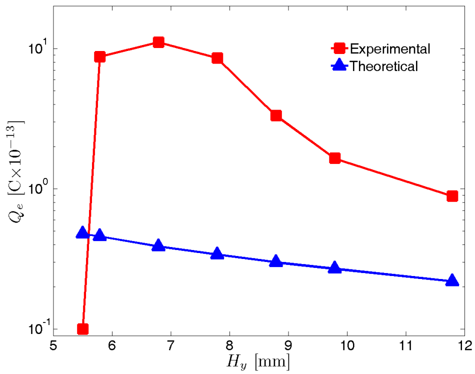

Figure 5.13.: Quantity of charge measured in experiment as Eq. 5.8 and predicted by the capacitor model as Eq. 5.6. The charge quantity was measured for different H_y, thus different E fields. The quantity of charge increased as the H_y narrowed since the E field intensified. When $H_y < 7\,\mathrm{mm}$, the quantity of charge began to reduce, probably because the breakup time became shorter than the characteristic time of charging. As soon as the tip went beyond the copper film of the charging ring, the charge reduced immediately to 0. The breakup length of the liquid jet determined the minimum gap width H_y.

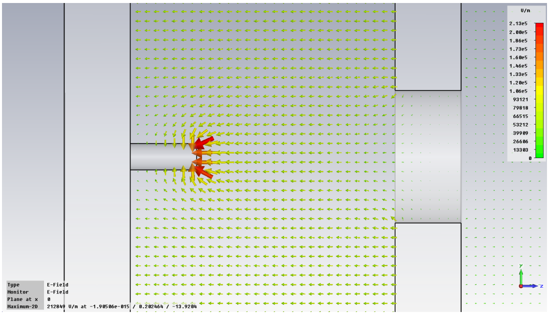

Figure 5.14.: Static electric field between the drop generator and the charging ring simulated by CST (Computer Simulation Technology). The bottom of the drop generator is on the left. The liquid jet is $200\,\mu\mathrm{m}$ in diameter and $1\,\mathrm{mm}$ in length. The charging ring was simulated by a $\phi 40\,\mathrm{mm}$ circular plate with a $\phi 2\,\mathrm{mm}$ hole in the center. The gap width is $H_y = 4\,\mathrm{mm}$. $300\,\mathrm{V}$ constant voltage is applied to the charging ring.

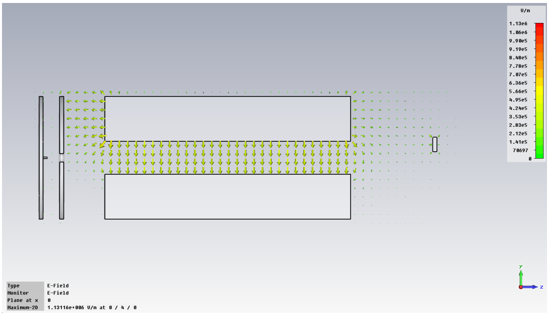

Figure 5.15.: Static electric field between the electrodes simulated by CST. The charging ring is 40 mm in diameter, the gap between the charging ring and the electrodes is 15 mm, the electrodes are 80 mm long and the gap between them is 8 mm. 5 kV voltage difference is applied between the electrodes.

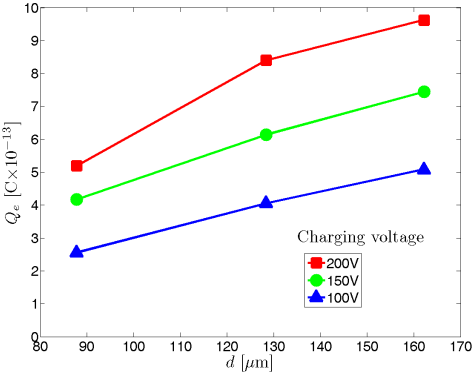

Figure 5.16.: The approximately linear dependence of the charge quantity on the drop diameter.

phase offset was quantified in percentage of one period of the excitation signal. The effect of the deflection was tested by high-speed imaging as shown in Figure 5.20.

It appeared that the jet breakup was at the rising edge of the excitation signal, since only one drop was deflected. As the phase offset increased, the charged was more evenly distributed in two drops until the offset exceeded 50%, when the effect reversed. This correlation between the jet breakup and excitation signal varied slightly in each experiment. Consequently the correct value was to be found

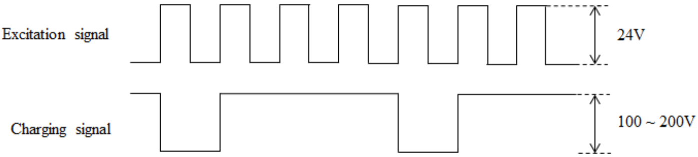

Figure 5.17.: Synchronization of the charging signal with the excitation signal.

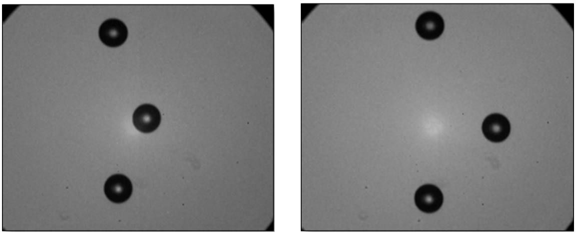

Figure 5.18.: Influence of the "low time" on the amplitude of the deflection. The "low time" were respectively 30% (left) and 80% (right) of the period of the excitation signal. The drops were $\phi 200\,\mu$m in diameter.

out by trial and error for each application. More comprehensive information on the selective deflection can be found in the report of C. Guichet for this IREP summer exchange program [44].

By keeping the charging voltage high for 10 s to 20 s, and thus deflecting all the drops, the deposited water on the impact surface could be removed by centrifugal force and aerodynamic shear stress effectively. The time for drying was tested out by trial and error for each rotational frequency.

The deflected drops were forbidden to enter the cabin of the rotating target, because the wind made them in a cloud form which continuously wetted the impact surface. Therefore a piece of napkin paper was laid on the shield aluminum plate as in Figure 5.21. The napkin paper served as a capillary pump, which drained the water continuously away.

The drop deflection was imperfectly under control on account of the following factors. The first was the undesired charge of the drop train. Frequently and irregularly, the "uncharged" drop stream was deflected by the electrode. In fact drop charging is a phenomenon that can not be safely avoided, as commented by Lee, who proposed 5 different charging mechanisms that could happen in drop and spray generation [75]. It was unknown which causes were responsible for the awkward charging in our experiment, but evidently it was helpful to keep the device dry. The second was the wind induced by the rotating target. The wind

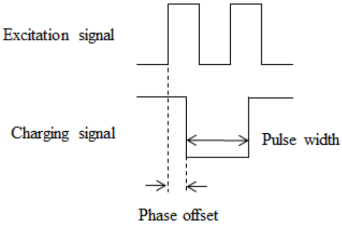

Figure 5.19.: Phase shift and pulse width of the charging signal.

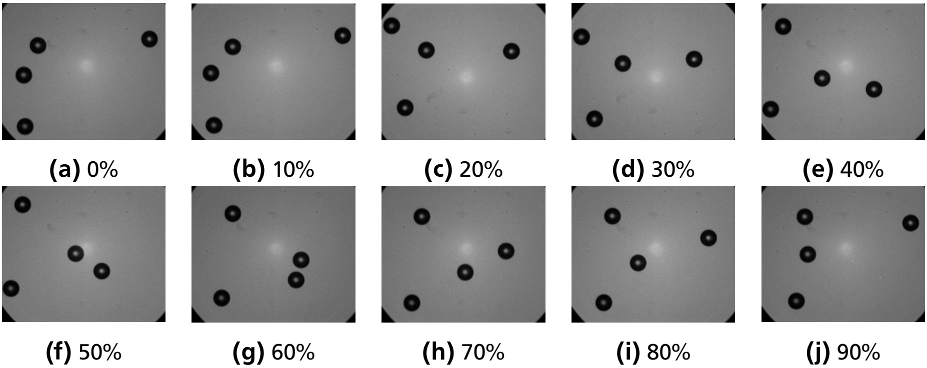
(a) 0% **(b)** 10% **(c)** 20% **(d)** 30% **(e)** 40%

(f) 50% **(g)** 60% **(h)** 70% **(i)** 80% **(j)** 90%

Figure 5.20.: Deflection of $\phi 200\,\mu$m drop with different phase offsets.

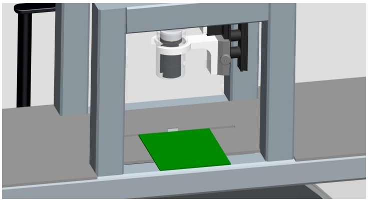

Figure 5.21.: The deflected water was removed by a napkin paper.

assisted the deflection by pushing the drop train further apart from the target, but meanwhile the drops might impact on the electrodes, which increased the chance of breakdown.

The third factor was brought by the trigger system. Since the position of the target must be detected before the drop impact, the trigger system must be renewed each time. This led to renewal of the excitation signal, which directly resulted in a different phase offset. The phase offset could not be tested out by trial and error because each drop train was used only once. Furthermore, only the pulse width (i.e. the "low time") was adjusted while the phase offset was kept at 0 invariantly because the 8 digital counters on the NI 6602 module were all occupied by necessary trigger signals (more description about the trigger system is in Section 5.6). The limitation on the control side severely harmed the probability of successful operation of the drop deflection. The imperfect drop deflection was recognized as the second reason for the low probability of successful capturing of the drop impact, beside the wind induced by the moving target.

To sum up, a drop train of arbitrary frequency was achieved by the electrostatic deflection of charged drops. The charge quantity was sufficient for 3 mm horizontal deflection. In-situ optimization of the deflection could be achieved by manual adjustment of the charging voltage from 100 V to 300 V, the electrodes' voltage from 1 kV to 5 kV, the gap width between the drop generator and the charging ring, the pulse width of the charging signal, and the velocity of the drop train. Because of the length of the stable drop train, the electrodes was chosen to be 40 mm long. Although successful operation was limited by a number of factors, this device was functional.

5.4 Imaging System

The high-speed impact of small drops demands high frame rate of recording. The duration of the impact process can be estimated by the time constant $\tau = d_0/v_0$, where d_0 and v_0 are the drop diameter and the impact velocity. Taking the drop diameter as 200 μm, and the impact speed as 50m/s for an example, τ is calculated as 4 μs. In order to capture as much details as possible, 1 million frame rate of recording was applied with the Shimadzu HPV-2 high-speed camera.

In contrast to many high-speed cameras which reduce the pixel resolution to achieve a higher frame rate, the Shimadzu camera operates with a constant pixel resolution of 312 × 260 at all frame rates from 30 fps to 1 Mfps. This unique functioning mode results from the structure of the IS-CCD (in situ storage CCD) image sensor. In a typical CCD chip, each pixel has a single shift register, where the charge induced by irradiance is saved. After one exposure time passes, the charge in the shift register is transferred from the chip through an AD (analog-to-digital) converter to a memory. The low sampling rate of the AD converter is a primary limitation of high frame rate recording. To solve this problem, IS-CCD chip embeds 102 shift registers for each pixel. Charge can be quickly transferred from an individual pixel into its registers in the microsecond time scale, enabling a frame rate of 1 Mfps. After all the registers are consumed, the charges are read out and saved in memory at a time. The advantage of the IS-CCD is the high frame rate, while the disadvantage is that the number of images is limited to 102 for each video recording. At the maximum frame rate, the recording has a duration of only $100\,\mu$s. Therefore the precise timing is indispensable in the application of this camera.

The size of the field of view (FOV) conflicted with the spatial resolution on account of the limited pixel resolution. On the one hand, fine spatial resolution was desired to resolve the secondary droplets generated by drop splash. Although dependent on the impact angle, the diameter of the secondary droplets was most likely of the order of $10\,\mu$m, or smaller. On the other hand, a complete view of the drop splash must be achieved, including the spreading lamella and the ejected secondary droplets. In general, larger drops and higher impact velocities required larger FOV due to wider spreading of the lamella and stronger splash. Furthermore, the movement of the target demanded a sufficient width of the FOV, so that the lamella could achieve the maximum spreading before the impact surface traveled out of the FOV. For each impact condition, the spatial resolution was experimentally optimized. Finally, spatial resolutions between 3.07μm/pixel and 8.35μm/pixel were chosen for image data acquisition. The FOV was hence between 0.958 mm × 0.798 mm and 2.605 mm × 2.171 mm.

To achieve such fine resolutions with the Shimadzu camera is a particularly challenging task because of large magnification. The IS-CCD is about 21 mm × 19 mm in size. Although detailed structure of the chip, especially the pixel pitch is not released by the camera provider, the size of one pixel can be estimated by assuming a uniform distribution of photoactive elements, which yields $67\,\mu$m × $73\,\mu$m. The magnification were thus as large as over 20. Conventional objectives are impractical in this magnification range. For example, a 50 mm objective would require an image-to-objective distance greater than 1 m. After comparison with various microscopes, the Questar QM100 long-distance microscope was chosen. This Maksutov-Cassegrain catadioptric telescope has a convenient working distance between 150 mm and 350 mm, and the corresponding aperture ranges from 3.5 to 6.0, specified by the f number. Additionally, three zoom lenses, ×1.5, ×2.0 and ×3, can further increase the magnification. Combination of the camera and the objective reaches a spatial resolution as fine as 1.9μm/pixel.

Large magnification is generally accompanied with small depth of field (DOF) as Eq. 5.10 calculates [116],

$$DOF = 2f_{aper}\, d_{CoC}\, \frac{mag+1}{mag^2}, \tag{5.9}$$

where f_{aper} is the f number of aperture, d_{CoC} is the acceptable circle of confusion, mag is the magnification. The circle of confusion is the diameter of the blur spot that a point object produces, when the object is defocused. Since the secondary droplets had a velocity component along the optical axis, narrow DOF led to disappearance of these droplets within a couple of frames. Although the velocity component perpendicular to the focal plane is unaccessible by shadowgraph imaging, greater DOF was desired to enhance the visibility of these droplets.

Quantitative calculation of the DOF according to Eq. 5.10 was impossible on account of the unknown f number of the complex combination of QM100 and the zoom lens. Nevertheless this equation says that decreasing f number expands the DOF. The most simply way to decrease the aperture is to use larger working distance. The same magnification can be achieved by either shorter working distance with a weaker zoom lens, or a longer working distance with a more powerful zoom lens. As long as the illumination permitted, the latter was always chosen.

Furthermore, one manually adjustable aperture (SM3 Lever-Actuated Iris Diaphragm, $\phi 2$ to $\phi 50$mm, Thorlabs GmbH, Munich, Germany) was mounted in front of the QM100 in order to reduce the aperture further in a more convenient way. The maximum DOF obtained by these efforts was measured by imaging. The acceptable circle of confusion was defined as no significant defocus blur occurred. Figure 5.22 pictured the tolerance. Table 5.1 contains the the DOF and the spatial resolution of this optical system with corresponding configurations. Reduction of the aperture was effective on the DOF enhancement.

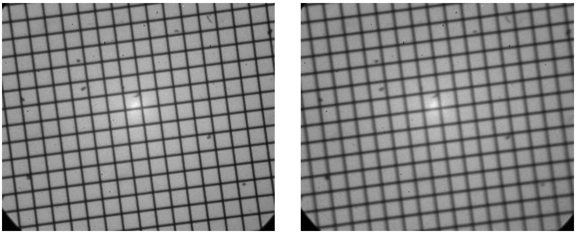

Figure 5.22.: Image in focus (left) and at the border of the DOF (right).

The aperture can not decrease infinitely close to 0 due to the diffraction blur. A point light source projects on the image plane a diffraction pattern composed of concentric circles. The bright center is known as the Airy disc. The radius of the Airy disc is approximated by the product of the distance l between the aperture

Zoom Lens	Working Distance	Spatial Resolution	DOF_1	DOF_2
3×	285 mm	3.07μm/pixel	250 μm	350 μm
2×	285 mm	5.18μm/pixel	300 μm	400 μm
1.5×	250 mm	6.34μm/pixel	350 μm	450 μm
1.5×	285 mm	7.07μm/pixel	400 μm	500 μm
1.5×	320 mm	7.80μm/pixel	450 μm	750 μm
1.5×	350 mm	8.35μm/pixel	500 μm	800 μm

Table 5.1.: Spatial resolutions and DOFs of the optical system. DOF_1 had an aperture of 65 mm, while DOF_2 had a 35 mm aperture.

and the image plane, and the angle at which the first minimum intensity of light occurs [3],

$$\sin\theta \approx 1.22\frac{\lambda}{d}, \tag{5.10}$$

where λ is wavelength of the light, d is the diameter of the aperture. This approximation is valid because the angle is in general very small. Taking a typical wavelength for visible light as λ =550 nm for a quick estimation, θ yields 0.000 61° with the diameter of the aperture of QM100 being 63 mm. The distance l is roughly 1 m, so that the diameter of the Airy disc is 21 μm. Diffraction blur occurs when the diameter of the Airy disc exceeds one pixel pitch. Apparently, bigger pixels are less vulnerable to the diffraction blur.

In shadowgraph imaging, the diffraction pattern appears differently from the typical Airy disk pattern. Firstly, the illumination is usually inherent, therefore the diffraction pattern is a superposition of Airy patterns corresponding to various wavelengths. Secondly, the object casts a shadow in the image, instead of a bright spot. The final compound effect was that both the bright background and the dark interior of the object was invisibly influenced, but the edges appeared blurred. The minimum aperture was experimentally found out for each magnification, and was avoided.

The maximum applicable DOF listed in Table 5.1 was still narrower than the half width of the impact surface. Consequently, simultaneous focus of the drop and a flat impact surface is impossible, because the drop impacts at the center line of the impact surface, while the shadow in the image is casted by one edge of the impact surface, which is outside the DOF. In order to bring both the drop and the impact surface inside the DOF, a curvature with a radius of 5 mm was applied to the impact surface, so that the most front outline of the impact surface was the center line, where the drop landed. The curvature should be as small as possible, but smaller values were impossible because of difficulties in manufacture. The caused deviation from a flat surface could be evaluated by the sagitta of the wetted arc. Estimating the spread factor as 5, the wetted arc is then 1 mm for a $\phi 200\,\mu$m drop. A simple plane geometry calculation shows that the corresponding sagitta was $25\,\mu$m, negligible compared to the maximum spreading diameter.

The sizes of the FOV and the DOF give the dimensions of the measurement volume, in which the drop could appear in the image, ranging from 0.958 mm × 0.798 mm × 0.2 mm to 2.605 mm × 2.171 mm × 0.8 mm. In practice, the drop must appear in a portion of the measurement volume. Firstly, the impact must take place at the lower right corner of the FOV, because the target moved from the right to the left gradually out of the FOV. Secondly, the valid impact region had a narrower depth than the DOF. At smaller magnifications, the DOF was so large that the impinging drop was in focus, but the impact point offset from the center line. Therefore the measurement volume was very small.

The probability of single $\phi 200\,\mu$m drop fell into the limited measurement volume was of low probability on account of the incompletely controllable drop deflection as well as the unsteady strong wind caused by the rotating target. Although the drop deflection was always optimized before running the target, continual in situ adjustment of the charging signal, the electrode voltage and the position of the drop generator was nearly inevitable in order to achieve the highest probability of capturing the drop impact. As the rotational frequency increased, the probability dropped gradually.

Precise positioning of the optical system was realized by a three dimensional motor driven traversing stage (“x.act LT 100-1 ST” for vertical positioning, “x.act XY 50-1 ST” for horizontal positioning, “Stepping Motor Controller PC Card M50.PCI” for computer controlling, LINOS Photonics GmbH, Göttingen, Germany). The resolution of the traversing stage is $2\,\mu$m, sufficient for positioning. The load capacity 30 kg exceeded the 10 kg total weight of the camera, objective and aluminum holding structure. The traversing table was fixed on an optical table (LW3036B-OPT, Newport Spectra-physics GmbH, Darmstadt).

The temporal resolution of the imaging is quantified by two parameters: the exposure time and the repetition rate. The sufficiency of the exposure time can be expressed by the motion blur, which is the displacement of object in the exposure time of one frame. The exposure time is sufficiently short, if the displacement is shorter than one pixel. The most rapid motion of the target was at 63m/s, and the minimum applicable exposure time of the HPV-2 camera is 250 ns. The two values make a motion blur of $15\,\mu$m, well beyond the spatial resolution. Consequently, the impact surface was not a sharp line but a gray belt region of several pixels. Although the exposure time was too long, the visibility of the spreading lamella and the secondary droplets was insignificantly influenced, because these objects appreciably darkened the gray pixels of the impact surface.

If a process is perfectly repeatable, there lies a possibility to record a single shot with sufficiently short exposure time and of high resolution for each experiment. A "video" is then reconstructed by the images acquired in multiple experiments with a sequence of delay times. Because of the imperfect reproducibility of the drop generation and the strong wind, the drop diameter and the impact velocity differed from one impact incident to another. Therefore sufficiently high frame rate was desired to achieve a time-resolved recording of the transient process of drop impact.

The IS-CCD chip has high sensitivity as the huge pixels indicate. Bigger pixels receives more irradiance in the same exposure time, and thus have higher sensitivity. Additionally, the sensitivity is variable by setting the Gain number. Gain is a measure of the ability of an amplifier to increase the power or amplitude of a signal from the input to the output. It is usually defined as the mean ratio of the signal output to the signal input of a system. Subjected to the same illumination, higher Gains leads to higher readings of the gray value, but meanwhile increases the random noise. Gain ×2 to Gain ×10 of the Shimadzu camera are advisable on account of insignificant noise.

The sensitivity of the IS-CCD is wavelength dependent, as shown in Figure 5.23. The peak is at 500 nm, corresponding to blue (450 nm to 495 nm) and green (495 nm to 570 nm) light. An optimum illumination should have wavelength of the same range.

No constant light source could provide sufficient illumination intensity for such high frame rate recording. A flash light, Esprit1500 (Bowens, Clacton-on-Sea, Essex, UK), was employed to supply the bright background in the shadowgraph imaging. The intensity was sufficient for the highest frame rate with the reduced aperture. In fact the flash was so strong that the flash and the camera was covered by a black weave (Blackout Fabric, Thorlabs GmbH, Dachau, Germany) during operation, in order to protect the operators from the exposure to the continual flashes.

The intensity of the flash light is neither spatially nor temporally constant. The spatial uniformity of the illumination was satisfactory at large magnifications. At small magnifications, a frosted plastic binding cover was fixed between the object and the flash lamp as a diffusor and a uniformly illuminated background was adequately guaranteed. Temporally, the intensity of the flash illumination rises rapidly

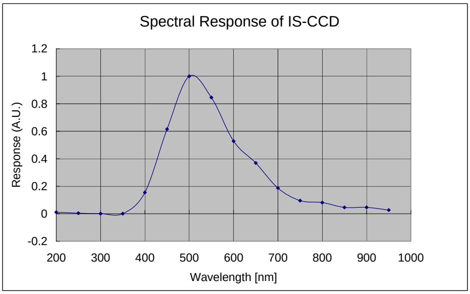

Figure 5.23.: Spectral sensitivity of the image sensor of the Shimadzu HPV-2 camera, provided by the manufacturer.

to the maximum and decays with a slower rate. Figure 5.24 provides an example of the lifetime of the illumination. Since the recording time was limited to 102 frames, 816 μs at the longest, temporally constant illumination was adequately achieved.

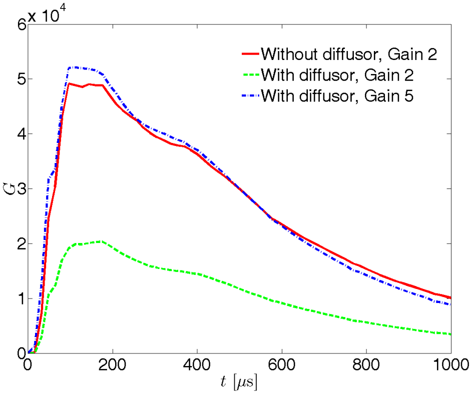

Figure 5.24.: Temporal variation of the illumination of the flash lamp Esprit 1500. This test was conducted with the Shimadzu camera. The intensity is the average gray value of a uniformly illuminated image of 16 bits. The diffusor reduced the intensity by a factor of 2.5. Increase of the Gain compensated this reduction with the same denominator.

5.5 Synchronization

Both single pulses and pulse trains were required in the experimental setup for various equipments. NI 6602 digital counter module played a central role in the pulse generation.

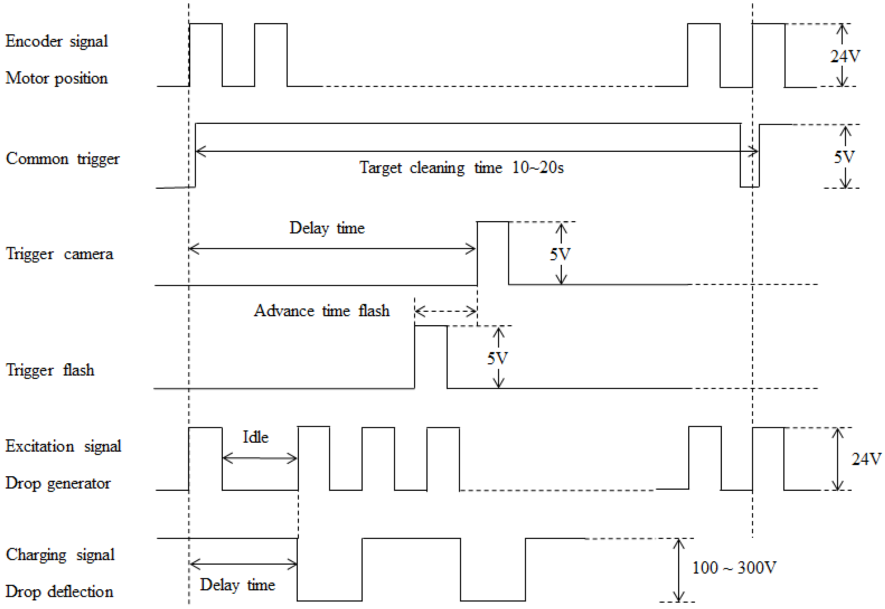

Figure 5.25.: Trigger signals for the synchronization.

The position of the target was given by an encoder which was mounted on the axis of the motor. The absolute 0 angular position of the motor is an invariant factory-set. In each rotation the encoder gives out a pulse signal when the rotor passes this position. The absolute position was experimentally found out by trial and error as 48.6° prior to the highest point of the rotation. This pulse train from the encoder had a voltage of 24 V. It was transformed to 5 V TTL signal with a minimal delay by a solid-state relay (SSR) (100 kHz, MOS 12-28 VDC/5V TTL, Weidmüller GmbH, Detmold, Germany) before it entered the NI 6602 module as an input trigger signal. The delay was at the maximum one period of the sampling frequency of the SSR, 10 μs, plus 2 ticks of the 20 M Hz internal clock of the NI 6602 module, 0.1 μs, thus in total 10.1 μs.

The position signal was received by the master counter which provided the common trigger input for the other slave counters. The common trigger had a “high time” of 10 s to 20 s, during which all the input trigger pulses from the encoder were rejected during this time. Meanwhile, all the droplets were deflected, which allowed the target to get completely dried. Before the common trigger, the slave counters must be set “armed”, i.e. ready to respond on the input trigger signal.

The trigger signal for the camera was a 5 V single pulse directly from the NI 6602 module. The delay time corresponded to the absolute 0 position plus one rotational period. The additional one period delay time was for proper operation of the drop deflection. Another 5 V single pulse was sent to the flash with an advance time of $50\,\mu$s to $100\,\mu$s. The flash must be triggered ahead of the recording, because the intensity of the illumination takes a certain time to reach the optimum level. The advance time was found out by trial and error for each flash setting.

The excitation signal and the charging signal shared the same start, namely the same delay time. The idle state of the charging signal was “high”, so that all the drops were charged and deflected by default. The delay time must be shorter than the one for the camera, so that there would be drops waiting in the observation region when the target passed by. On the other hand the difference of the two delay times must be sufficient, because the uncharged drops needed some time to arrive at the FOV. In order to guarantee this time difference, one additional period of rotation was added to the delay time of the camera. As a result, the charging ring was activated shortly after the target passed by the FOV for the first time, and the drops met the target when it traveled through the FOV for the second time.

The excitation signal and the charging signal did not share the same end, as manifested in the Figure 5.25. It was desired that during the delay time of the charging signal, the excitation signal could be still on, in order to make the drop train under control. However the counter for the excitation signal must be armed before the common start trigger signal came. Therefore there was always a short idle state when no signal was provided to the vibrating orifice drop generator. During this short time of roughly 1 ms, the drop train was out of control and frequently wetted the electrodes.

Figure 5.25 confirmed the difficulty in the controlling of the drop deflection. Since all the save counters must be reset for the master counter before each recording, the drop generation was also renewed each time, and each drop train was used only once. It was impossible to examine by trial and error whether the phase offset or the pulse width was correct. The hints on the operation of the vibrating orifice drop generator in Section 5.2 and the drop deflection in Section 5.3 helped to produce a reproducible performance of the sparse drop train generation.

The last note on these two pulse trains is the amplitude. The NI 6602 module offers only 5 V square wave signal, while the drop generator required 24 V pulse train and the charging voltage was as high as 300 V. The NI 6602 module supplied only the control signal, and the final signal was acquired with a commercial SSR (100 kHz, MOS 5V TTL/24VDC 0.1 A, Weidmüller) for the drop generation and a custom made module which took advantage of a high voltage transistor for the charging ring. The quality of the signal were adequately good as read from an oscilloscope.

The Labview program is shown in Figure 5.26 by the front panel. Beside the parameters described above, the drop isolate rate means one out of which number of drops was uncharged. Switches for flash and the charging ring were offered for the purpose of adjustment.

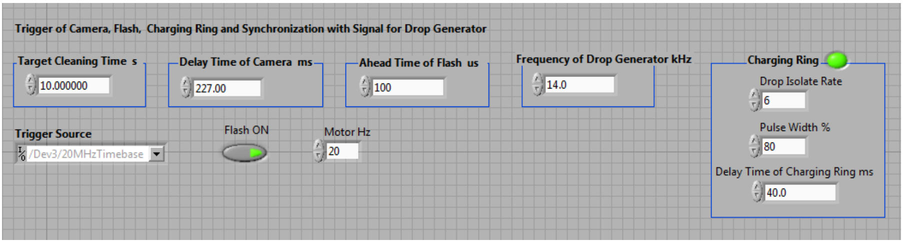

Target Cleaning Time s: 10.000000
Delay Time of Camera ms: 227.00
Ahead Time of Flash us: 100
Frequency of Drop Generator kHz: 14.0
Trigger Source: /Dev3/20MHzTimebase
Motor Hz: 20
Drop Isolate Rate: 6
Pulse Width %: 80
Delay Time of Charging Ring ms: 40.0

Figure 5.26.: The front panel of the Labview program for the synchronization.

5.6 Performance of the Experimental Setup

Figure 5.27 sums up the construction of the experimental setup with a visual picture of the experimental setup. High impact velocities of 10m/s to 63m/s were achieved by a rotating target which was driven by a AC motor. The targets were manufactured with different slopes to facilitate inclined impact. Monodisperse drop train was generated by a vibrating orifice drop generator with desired diameter range of 50 μm to 200 μm. The frequency of drops was reduced effectively by electrostatic deflection, in order to achieve single drop impact. High-speed imaging up to 1 Mfps was undertaken with the Shimadzu HPV-2 camera with a constant pixel resolution of 312 × 260. The spatial resolution ranged from 3.07μm/pixel to 8.35μm/pixel. The depth of field was increased by reducing the aperture. Synchronization was accomplished by Labview programming and NI 6602 digital counter module together with multiple solid-state relays.

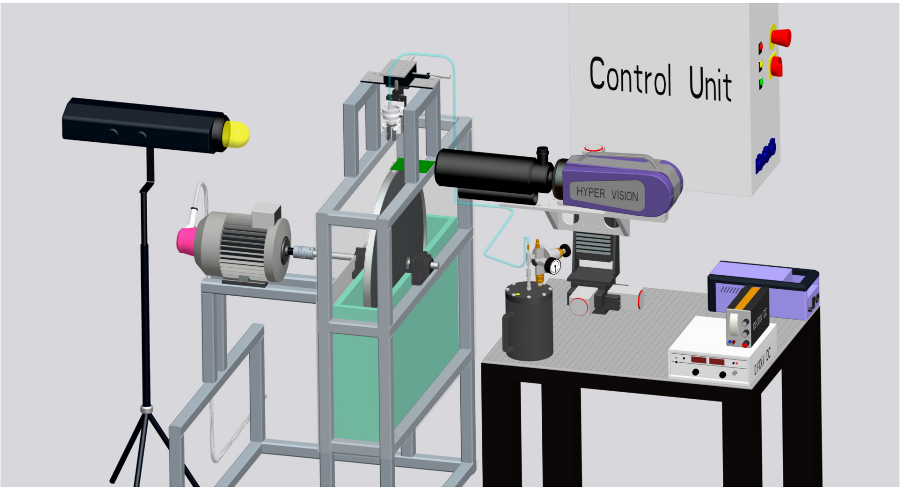

Figure 5.27.: Experimental setup for high speed impact of single drops on dry surfaces. From the left to the right are the flash illumination, the motor-wheel system, the drop generator connected to the water container, the imaging system, the control unit, and three DC power units respectively for the camera, electrostatic deflection and the charging ring. The drop generator was mounted on a 2D traversing table, so that the drop train could be located right in the middle of the impact surface. All the hardware of the trigger system were in the control unit, which was a metal container to further minimize the electromagnetic interference.

The capability of the experimental setup is quantitatively expressed by the realized impact condition, i.e. the drop diameter and the impact velocity, which were measured from the videos as Figure 5.28 sketches.

Most of the drop impacts had an angle between 0° and 90°. Occasionally at large target angles and low speeds, the impact angle exceeded 90°, which means the drop impacted from the other side. The splash, or the lamella, in the direction of the tangent velocity is designated as forward, and the one in the opposite direction is designated as backward.

The absolute velocity of the drop was calculated by dividing the distance between the centroid of the same drop in two images with the corresponding temporal interval. The time was taken as long as possible, namely from the first complete appearance of the drop in the image to the time point right before impact. The

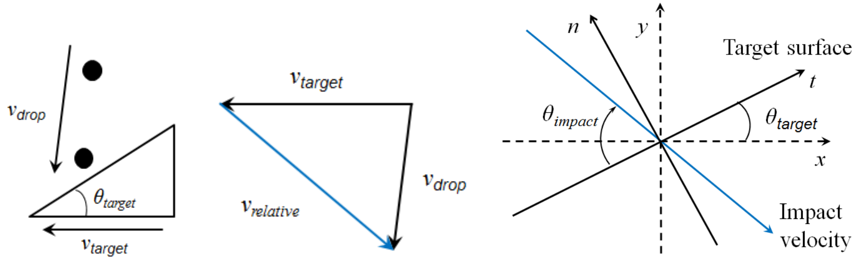

Figure 5.28.: Calculation of the impact conditions. The impact velocity was the relative velocity between the target and the drop. The impact angle was defined from lower side of the impact surface expanding to the upper side. The definition yields that the impact angle was 0° for horizontal impacts and 90° for normal impacts.

choice of this average velocity was validated by the standard derivation of the frame-wise velocities of the drop, which was less than 5% for most cases. Furthermore the drop velocity, ranging from 0.7m/s to 7m/s, was small compared to the target velocity, which were from 10m/s to 63m/s. Therefore such slight temporal variations of the drop velocity were negligible.

The common convention to express the precision by means of significant figures is taken that the margin of error is one-half the value of the last significant place, thus half of a pixel. For the diameter measurement the error comes from both sides of the drop, so that the error is in total 1 pixel. Since the diameter of the drop mostly covered more than 30 pixels, and the displacement of the drop for the velocity measurement was much larger than one drop diameter, the precision is sufficiently high, and therefore the error bar is neglected.

The measurement of the impact condition was conducted by O. Bartella [11] in the scope of his Bachelor thesis with the software ImageJ. The realized impact speed was from 12m/s to 63m/s, and the impact angle was from 5° to 106°. Figure 5.29 exposes the achieved *Re* and *We*, both of which were of large values.

Both Pan et al. [103] and Faßmann et al. [140] reached high *We* over 10 000. In the former experiment, the impact speed was estimated instead of measured [68], thus the accuracy is questionable. In the latter experiment the drop size was more than ten times greater than in our experiment (2.7 mm), while the impact speed was limited to 13m/s. Mehdizadeh et al. [83] reached higher *We* up to 50 000, and higher *Re* up to 23 000, because larger drops ($\approx 550\,\mu$m) was applied, and the velocities were of a similar range. In these experiments, only normal impact was

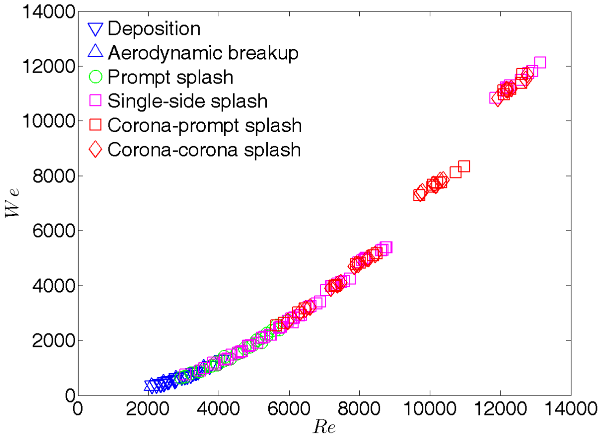

Figure 5.29.: The Re and We numbers realized in the experiment. The drop diameter was of a narrow range between $180\,\mu\mathrm{m}$ and $205\,\mu\mathrm{m}$, and distilled water was the only applied liquid. Therefore the velocity was the only effective variable, and We was thus proportional to the Re^2.

investigated. In our experiment, most of the impacts were oblique. The outcomes of the high-speed inclined impact are introduced in the next chapter.

6 Results and Discussion

This chapter is dedicated to the experimental results on the drop splash phenomena. Section 6.1 introduces graphically the four types of splash as well as the aerodynamic breakup observed in the experiment. Section 6.2 discusses on the modeling of the splash threshold after examining the previous models with our experimental results. Section 6.3 comprises the measurement of the velocity of the uprising jet. It is found out that the velocity of the uprising jet was multiple times higher than the impact velocity, and it had a strong dependency on the impact angle. Section 6.4 introduces the measurement of the spreading radii, which clearly exhibits the discrepancy from the normal impact. Drop impact on the 0° target layer led to generation of singular secondary droplets. Mass-loss was hence measurable in this special case. Section 6.5 introduces the mass-loss coefficient of this special case. This chapter emphasizes the reliability of the measurements, and therefore only representative graphic data are exhibited. Comprehensive graphic data and diagrams are listed in the appendixes.

6.1 Outcomes of the Oblique Drop Impact

Single drop impact on dry surfaces were conducted under various conditions. The impact surface was always dry. The drop diameter was of a narrow range from 181 μm to 204 μm. Variation of the impact speed and the impact angle were accomplished by incrementing the rotational frequency of the target and the target angle, respectively. The target angles included 0°, 5°, 10°, 15°, 30°, 45°, 60° and 75°. The rotational frequency of the target was from 5 Hz to 30 Hz, corresponding to 10m/s to 63m/s. Both the deposition and the splash were observed. Aerodynamic breakup of the spreading lamella was discovered.

6.1.1 Morphologies of the Drop Splash

Four types of drop splash were identified in the oblique impact as Figure 6.1 to Figure 6.4 represent. With larger impact angles, prompt splash emerged ahead of the corona splash as the impact velocity incremented. Secondary droplets emerged spontaneously upon impact, and flew away from the spreading lamella quickly. This observation provides a side-view of the prompt splash observed by

Mehdizadeh et al. [83] and Pan et al. [103], which is shown in Figure 2.14 in Chapter 2.

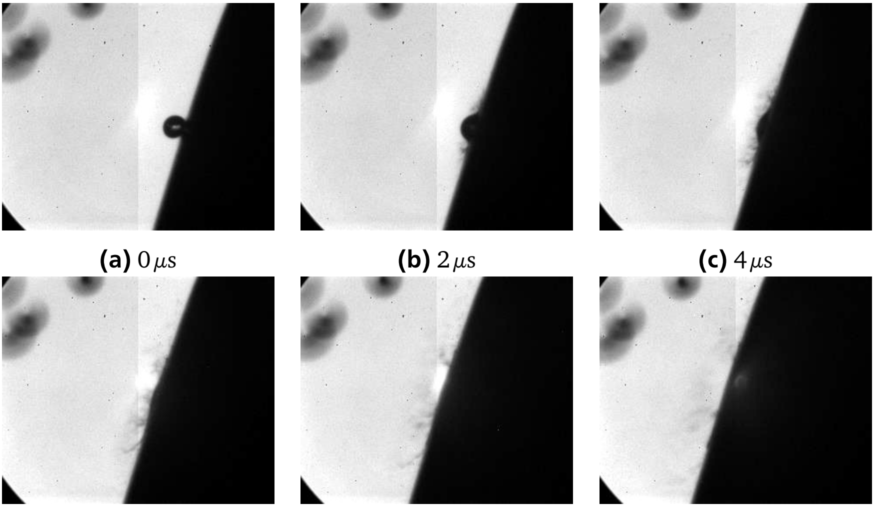
(a) 0 μs (b) 2 μs (c) 4 μs (d) 7 μs (e) 10 μs (f) 14 μs

Figure 6.1.: Prompt splash. Target angle: 75°, drop diameter: 188 μm, impact velocity: 34m/s, impact angle: 82°. Spatial resolution: 7.07μm/pixel, field of view: 2.21 mm × 1.84 mm, fps: 1 MHz.

With sufficiently high velocities, a thin uprising jet emerged at the edge of the spreading lamella, and the secondary droplets formed at the tip of the uprising jet. This is a typical corona splash, although one side was significantly weaker than the other side because of the oblique impact, as shown in Figure 6.2. A pixel-wise scrutiny of these images reveals that no single drops were visible in the cloud composed of liquid jets and secondary droplets. The reason lies at their rapid motion. The secondary droplets had a larger velocity than the rotating target, as they flew away from the impact surface. Motion blur happened unanimously to these secondary droplets and consequently denied the diameter measurement. At lower impact angles the uprising jet was formed only on one side as shown by Figure 6.3, while the other side was in the regime of the prompt splash. The two types of splash are named as corona-corona splash and corona-prompt splash, respectively.

At sufficiently small impact angles, one side of the asymmetric spreading lamella ended up in deposition, while the other side rose up, forming an uprising jet, which

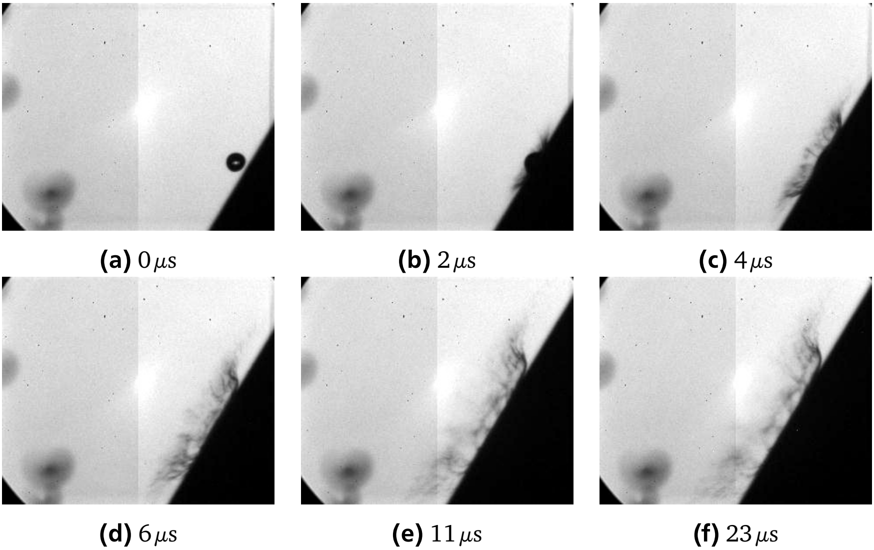

(a) $0\,\mu s$ **(b)** $2\,\mu s$ **(c)** $4\,\mu s$

(d) $6\,\mu s$ **(e)** $11\,\mu s$ **(f)** $23\,\mu s$

Figure 6.2.: Corona-corona splash. Target angle: $60°$, drop diameter: $194\,\mu\mathrm{m}$, impact velocity: $64\mathrm{m/s}$, impact angle: $63°$. Spatial resolution: $8.35\mu\mathrm{m/pixel}$, field of view: $2.61\,\mathrm{mm} \times 2.17\,\mathrm{mm}$, fps: $1\,\mathrm{MHz}$.

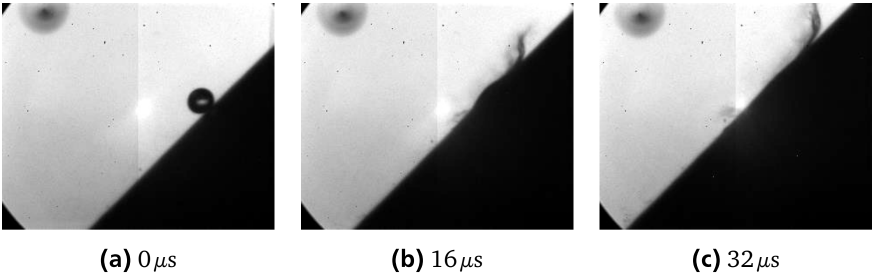

(a) $0\,\mu s$ **(b)** $16\,\mu s$ **(c)** $32\,\mu s$

Figure 6.3.: Corona-prompt splash. Target angle: $45°$, drop diameter: $191\,\mu\mathrm{m}$, impact velocity: $64\mathrm{m/s}$, impact angle: $48°$. Spatial resolution: $6.34\mu\mathrm{m/pixel}$, field of view: $1.98\,\mathrm{mm} \times 1.65\,\mathrm{mm}$, fps: $1\,\mathrm{MHz}$.

eventually disintegrated from the residual lamella in a form of a liquid ligament. Secondary droplets were formed by the secondary breakup of the liquid ligament. This type of splash is named as "single-side splash", as pictured in Figure 6.4. The secondary breakup took place mostly beyond the limited FOV because of its longer duration.

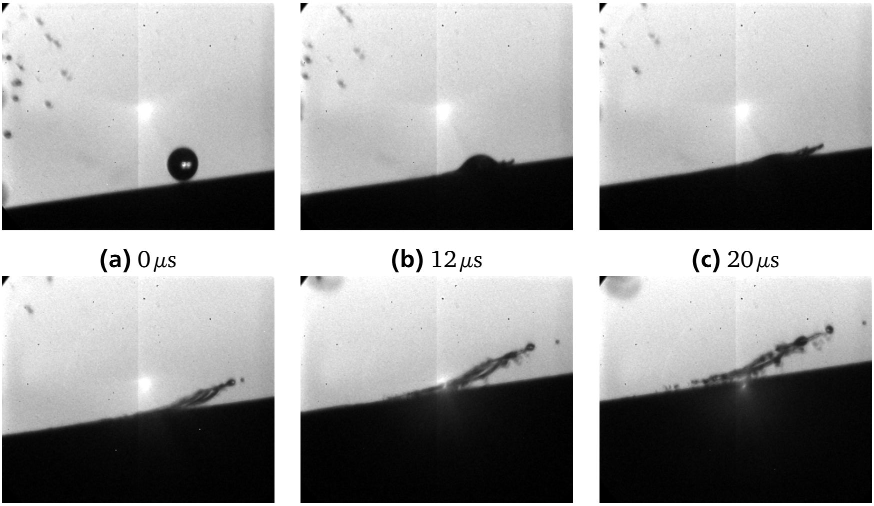

(a) $0\,\mu s$ **(b)** $12\,\mu s$ **(c)** $20\,\mu s$

(d) $40\,\mu s$ **(e)** $60\,\mu s$ **(f)** $70\,\mu s$

Figure 6.4.: Single-side splash. Target angle: 10°, drop diameter: $191\,\mu\mathrm{m}$, impact velocity: $43\mathrm{m/s}$, impact angle: 13°. Spatial resolution: $5.18\mu\mathrm{m/pixel}$, field of view: $1.62\,\mathrm{mm} \times 1.35\,\mathrm{mm}$, fps: $500\,\mathrm{kHz}$.

The drop splash is of course three dimensional. In the case of single-side splash, the liquid lamella obtained occasionally a velocity component perpendicular to the focal plane, and eventually flew out of the DOF. In the case of the corona-corona splash, the secondary droplets formed in the middle of the spreading lamella moved perpendicular to the focal plane, and vanished quickly from the image on account of the narrow DOF. This velocity information perpendicular to the focal plane is inaccessible in shadowgraph imaging. Therefore the classification of the drop splash is in a two dimensional manner, as the names of the splash imply.

Although accurate measurement was impossible, the diameter of the secondary droplets exhibited a clear dependency on the impact angle. Lower impact angle favored larger secondary droplets. In the extreme cases with the 0° target, the secondary droplet was singular and could be as large as the impinging drop at high impact velocities approaching 40m/s. In the opposite case of nearly normal drop impact, invisibly tiny droplets were generated. In the cases of the corona-corona splash and the corona-prompt splash, the secondary droplets formed in the direction of the tangent velocity possessed larger diameters than those in the other direction.

6.1.2 Aerodynamic Breakup of the Spreading Lamella

Splash was not the only mechanism to generate secondary droplets. Figure 6.5 pictured an exception. The drop impacted on a 0° target, and spread in the opposite direction of the target motion. The drop did not move initially except deformation until the 64 μs, when the liquid boundary layer reached the top of the lamella. The lamella began to move toward left, and simultaneously the tip began to deform, and eventually rose above the impact surface at 160 μs. One secondary droplet pinched off from the tip of the liquid ligament. Notably, the absolute velocity of the lamella, increasing from 0m/s to 7m/s toward left, was significantly lower than the target velocity of 15m/s. Therefore the lamella continued to wet the solid surface, although with a decreasing relative velocity.

The length of the impact surface, 14 mm, was 70 times larger than the diameter of the impinging drop, which was typically 200 μm. Therefore the flow field above the impact surface can be simplified as on a semi-infinite plate. At presence of the gas viscosity, the velocity of air at the wall was equal to the velocity of the target. The thickness of the air boundary layer is estimated by [138]

$$\delta = 1.7208\sqrt{\frac{\nu x}{v_\infty}}, \tag{6.1}$$

where δ is thickness of the displacement boundary layer, $\nu = 15.7 \times 10^{-6}\mathrm{m}^2/\mathrm{s}$ is the kinematic viscosity of air at 20 °C, and x is the distance from the leading edge of the target to the location of observation, v_∞ is the target velocity. In Figure 6.5, $x = 4\,\mathrm{mm}$, and $v_\infty = 15\mathrm{m/s}$. Hence this equation yields 111 μm, approximately three times of the lamella thickness at the 64 μs.

Consequently, the spreading lamella was subjected to an airflow with decreasing velocity from the wall upwards. The strongest aerodynamic total pressure adjacent to the wall raised the lamella up, forming a liquid ligament. The rest process is similar to the jet breakup in the vibrating orifice drop generator: the Rayleigh instability came into effect and a secondary droplet disintegrated from the liquid jet. The secondary droplet was further accelerated toward left by the airflow in

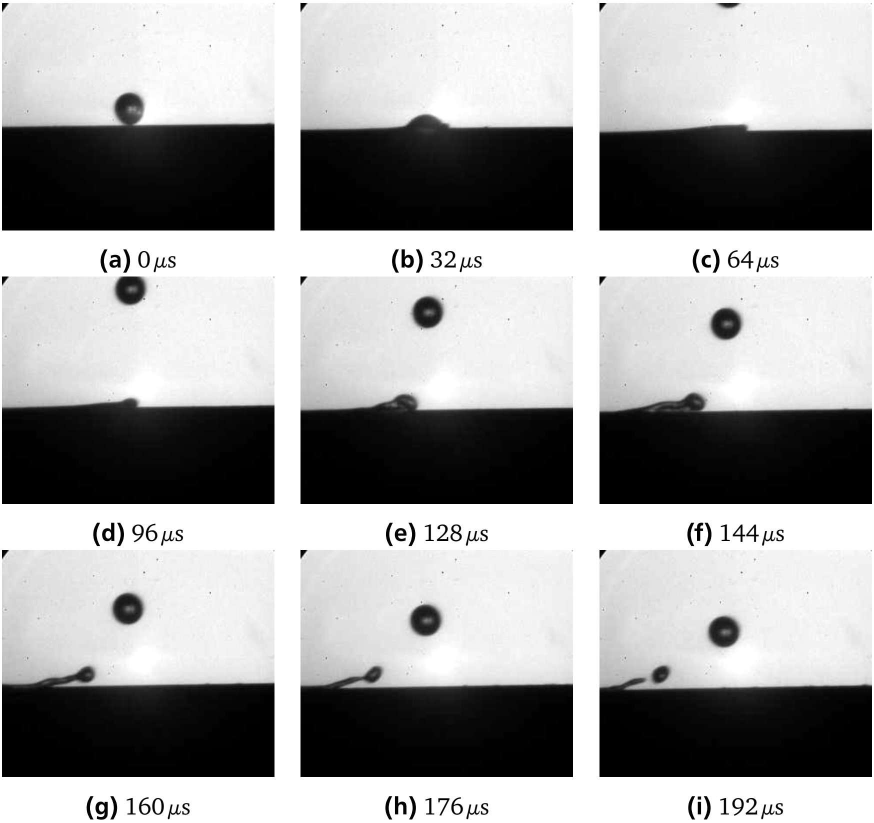
(a) 0μs (b) 32μs (c) 64μs (d) 96μs (e) 128μs (f) 144μs (g) 160μs (h) 176μs (i) 192μs

Figure 6.5.: Aerodynamic breakup on a 0° target at 15.12m/s. Drop diameter: 181μm, impact velocity: 15m/s, impact angle: 16°. Spatial resolution: 5.18μm/pixel, field of view: 1.62 mm × 1.35 mm, fps: 125 kHz.

the boundary layer. This phenomenon is essentially deposition in the topic of drop splash.

At presence of insufficient aerodynamic pressure, the lamella was not lifted completely from the solid surface, rather a capillary wave was created, and it propagated in the direction of the viscous airflow, as Figure 6.6 pictured.

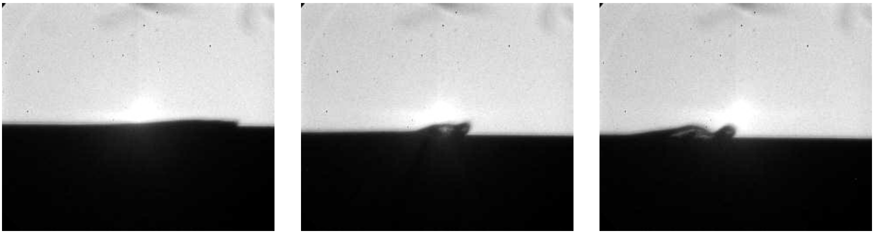

(a) $32\mu s$ **(b)** $84\mu s$ **(c)** $100\mu s$

Figure 6.6.: Capillary wave created by the aerodynamic pressure on a 0° target at $15.12 \mathrm{m/s}$. Drop diameter: $136\mu\mathrm{m}$, impact velocity: $16\mathrm{m/s}$, impact angle: 23°. Spatial resolution: $3.07\mu\mathrm{m/pixel}$, field of view: $0.96\,\mathrm{mm} \times 0.80\,\mathrm{mm}$, fps: $250\,\mathrm{kHz}$.

6.2 Splash Threshold

Figure 6.7 expresses the outcomes of drop impact with impact angle and impact speed. The aerodynamic breakup resulted from the interaction between the air boundary layer and the residual liquid film, thus belongs to the deposition regime. Each chain of the symbols was acquired from one target. Since the drop had a considerable velocity before impact, the impact angle was larger than the target angle at lower target speeds. As the velocity increased, the discrepancy between the target angle and the impact angle shrank. Since the drop diameter was of a narrow range, a primitive conclusion could be made that the impact angle dominated the type of the splash, while the velocity governed the splash threshold. Noticeably, there is a sharp jump of the corona splash threshold at the impact angle of 40°.

The semi-empirical splash threshold models introduced in Chapter 2 are compared with our experimental data as shown in Figure 6.8. Only the data points on the borders of the splash regimes for each target inclination are plotted for the sake of clarity.

The one from Vander Wal et al. [156] is developed for normal impact, therefore only the red diamond points with large impact angles of 67° and 82° are appropriate for examination. Clearly, the experimental data are well beyond the critical capillary number $Ca_{crit} = 0.1225$. The splash threshold from Bird et al. [18], which takes the tangent velocity into consideration, exhibits similar results. Figure 6.8 (c) shows that there was no universal value for the parameter $\sum_G / \sum_L$ for the oblique impact, and the experimental values were lower than the observation of Xu et al. [168].

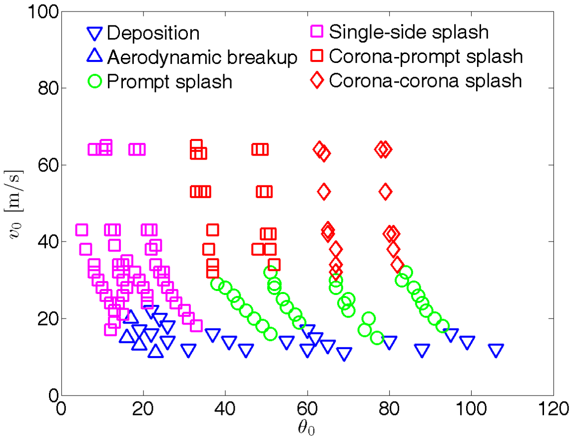

Figure 6.7.: Outcome of oblique impact on dry surfaces. The drop diameter was in a narrow range between $180\,\mu\mathrm{m}$ and $205\,\mu\mathrm{m}$, thus is not expressed explicitly.

In order to develop accurate splash threshold models, it is necessary to examine the mechanism of the prompt splash and the corona splash. The prompt splash was observed at lower speeds on rough surfaces, or at high speeds on smooth surfaces as summarized in Table 6.1. An appropriate threshold model for the prompt splash should include the drop diameter, impact velocity, liquid property, and the roughness characteristics. In general, higher roughnesses [171] and higher impact speeds enhance the prompt splash, and the viscosity seems to be insignificant [103] since the characteristic time scale is short. However the development of a general model is complicated by the finding that both the roughness height and the spacing of the roughness element have a non-monotonic effect on the occurrence of the prompt splash, as discovered by Xu [166]. The state-of-art experimental data are insufficient for a reliable modeling of the prompt splash threshold. Concerning the SLD impact, the prompt splash is an insignificant effect, because the total mass of the secondary droplets is minimal, and the tiny secondary droplets are more likely to follow the airstream without re-impingement on the aft wing surfaces.

In the corona splash regime, the outward spreading lamella was bent upwards by the pressure exerted by the surrounding gas, forming the uprising jet as shown in Figure 6.2, 6.3 and 6.4. The secondary droplets were emitted from the rim of the liquid sheet, or formed by the secondary breakup of the disintegrated liquid ligament. The force field analysis of the spreading lamella is proposed in Figure 6.9.

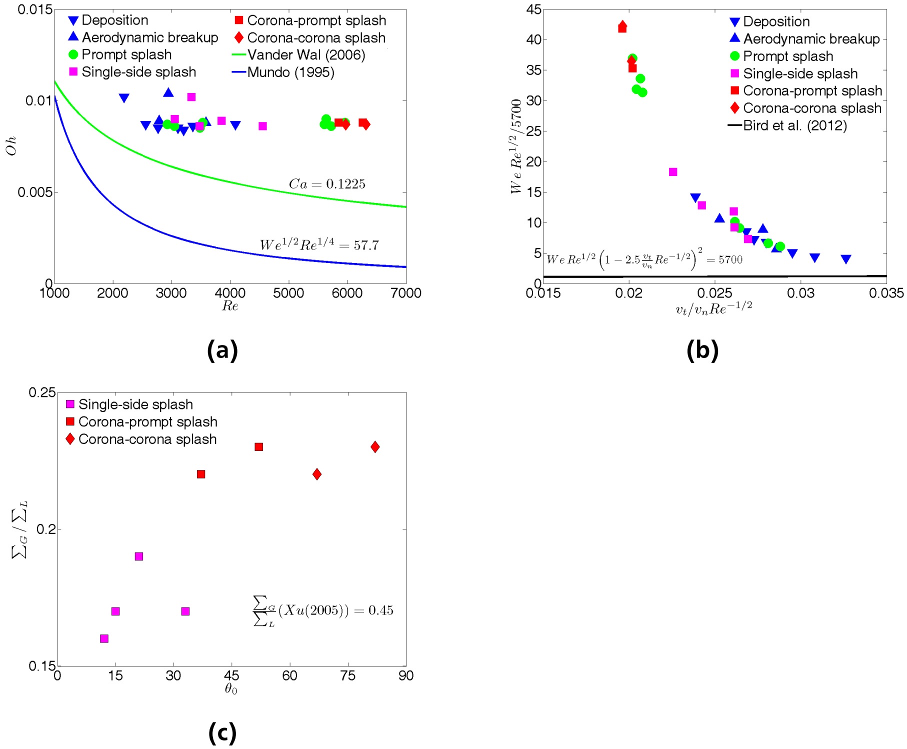

Figure 6.8.: Examination of splash threshold models from Vander Wal et al. [156] (a), Mundo et al. [99] (a), Bird et al. [18] (b) and Xu et al. [168] (c). The Re and We are calculated with the total impact velocity.

The lamella has a certain thickness, $H_{lamella}$, and a spreading velocity, $v_{lamella}$. The impinging drop pushes the lamella out, thus exerts an inertial force on the lamella, scaled as $\rho_{water} v_{lamella}^2/2$. The no-slip boundary condition on the solid wall states a shear stress scaled as $\eta(dv_{lamella}/dy)$. The height of the lamella is small, therefore the surface tension plays a notable role. The laplace pressure is scaled as $\sigma/H_{lamella}$. The aerodynamic pressure is simplified with the Bernoulli's equation as $\rho_{air} v_{lamella}^2/2 + p_0$, where p_0 is the pressure of the surrounding gas.

The lamella is lifted, when the inertial force and the aerodynamic force are strong enough to squeeze the lamella upwards by overcoming the laplace pressure. This hypothesis suggests one stabilizing factor, the Laplace pressure, and two destabilizing factors, inertial force and aerodynamic force. Both of the inertial force and

Experiment of	drop diameter mm	impact velocity m/s	roughness μm
Stow and Hadfield [142]	1.65	3.62 to 3.82	3 to 12
Range and Feuillebois [115]	1.94	2.16	12 to 23
Xu et al. [166, 167]	3.4	4.3	5 to 78
Pan et al. [103]	0.5	29.6 to 32.5	0.003 to 0.2
Mehdizadeh et al. [83]	0.55	30	0.03
our experiment	0.2	11 to 18	0.75 to 1.25

Table 6.1.: Summary of the conditions of the prompt splash.

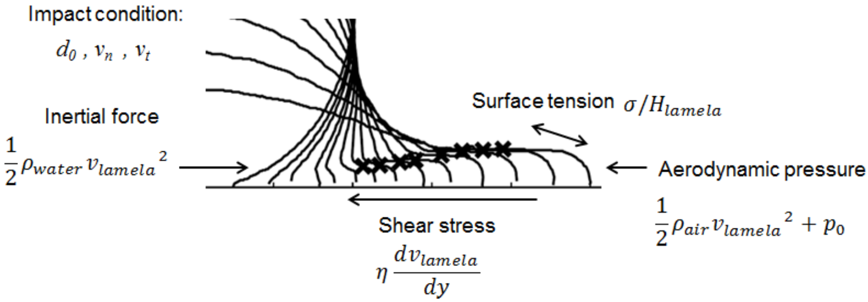

Figure 6.9.: Force field analysis on the spreading lamella.

the aerodynamic force are dependent on the lamella thickness and the spreading velocity. Beside the necessity of sufficiency, the lamella thickness and the spreading velocity correlate to each other in a complementary manner that a thicker lamella requires a lower spreading velocity to create the uprising liquid film. For a certain lamella thickness, there exists a minimum spreading velocity, above which the liquid corona forms. This velocity is named as the critical spreading velocity. The viscosity does not enter this hypothesis explicitly, however it influences both the lamella thickness and the spreading velocity.

Two submodels are desired for the thickness of the lamella, and the corresponding critical spreading velocity. Ruiter et al. [124] shows that the thickness of the lamella for the normal impact is multiple times thicker than the boundary layer which grows proportional to $\sqrt{\nu_{water} t}$, where ν is the kinematic viscosity. Furthermore, the lamella thickness is dependent on the impact velocity. Far away from splash threshold, the lamella thickness decreased with the increasing impact velocity. While approaching the splash threshold, the lamella thickness increased, probably due to the aerodynamic pressure which stalls the spreading of the lamella.

Our observations show that the lamella is also dependent on the impact angle. Lower impact angle led to thicker forward lamella. For example in Figure 6.2 the upper corona formed with an impact angle of 63° had a thickness of approximately $16\,\mu$m, while in Figure 6.4 it was $37\,\mu$m with an impact angle of 13°. An accurate theoretical prediction of the lamella thickness remains a missing prerequisite of the corona splash threshold.

The critical spreading velocity is known to be dependent on the gas properties (i.e. density and pressure), but quantitative measurement on the critical spreading velocity remained unreported in the literature. For the normal impact, this critical velocity is not directly measurable because splash happens at very early times, shorter than $1\,\mu$s after impact [18, 109]. This time scale is confirmed by our observation at higher impact angles. For example in Figure 6.2, the secondary droplets appeared in the first image after impact, thus shorter than $1\,\mu$s. However, because of this short time, it is reasonable to assume that the viscous forces in both the gas and liquid phase, as well as the friction at the liquid/gas interface, do not decelerate the lamella during this short time. Consequently the critical velocity of the spreading lamella is equal to the velocity of the uprising jet, i.e. the initial velocity of the secondary droplets. It must be noted that the secondary droplets were emitted from the tip of the liquid corona continually, and the velocity decreased as the expansion of the lamella proceeded. Restricted to the topic of the splash threshold, only the first generation of the secondary droplets was interested. The next section introduces the measurement of the velocity of the uprising liquid jets.

The above hypotheses for prompt splash and corona splash implicate that the two phenomena occur independently from each other. On rough surfaces as the experiments listed in Table 6.1, the prompt splash was triggered by a lower velocity than the corona splash. On smooth surfaces, the corona splash could occur at a lower speed than the prompt splash, for example in the experiment of Xu et al. with $\phi 3.4$ mm ethanol drop [168], Bird et al. with $\phi 2.5$ mm ethanol drop [18], and Vander Wal et al. with 2 mm drops of similar surface tension as ethanol, 23.1mN/m [156]. In these experiments the drop is large and the surface tension is low. Therefore the threshold impact velocity was relatively low.

The experiments of Pan et al. [103] and Mehdizadeh et al. [83], as well as our experiments evidenced that with small drops of high surface tension, 72mN/m for water, the prompt splash could occur at a lower speed than the corona splash on smooth surfaces. A smaller drop diameter leads to thinner lamella, and higher surface tension requires larger destabilizing forces. Both of the two factors require high impact velocities. Meanwhile, at higher impact velocities the spreading lamella became sensitive to smaller roughnesses. The impact conditions of the three experiment accidently lay at such a range, where the prompt splash was firstly triggered, while the condition of the corona splash was not yet fulfilled. The oblique impact further suggests that only the normal velocity accounts for the prompt splash, since this type of splash vanished at sufficiently low impact angles, for instance in the case of the single-side splash.

In the case of oblique impacts, the tangent velocity leads to asymmetric distribution of the liquid. On the 0° target, the forward lamella was the thickest with other conditions equal. Additionally, the gas flow of the viscous boundary layer contributed to the aerodynamic pressure: $\rho_{air} v_{air}^2/2 + p_0$, where $v_{air} = v_{lamella} + v_{target}$ is the relative velocity between the spreading lamella and the viscous airflow. This peculiarity leads to the lowest threshold velocity of the corona splash as shown in Figure 6.7. This effect shrank rapidly as the target angle increased, not only because the direction of the air velocity deviated from the direction of the spreading lamella, but also because the boundary layer became thinner. Therefore the threshold velocity rose sharply to the 10° target, where the effect of the gas boundary layer was no longer recognizable.

Further increase of the impact angle had two conflicting effects. On the one hand, higher normal velocity raised the spreading velocity, promoting the corona splash. On the other hand, the mass distribution became more even on account of the lower tangent velocity, leading to thinner forward lamella. From 20° to 35° of the impact angle, the forward lamella was still sufficiently thick, therefore the threshold velocity dropped rapidly as the impact angle increased. When the impact angle exceeded 35°, the lamella became so thin that the increase of the spreading velocity could not complement the reduction of the lamella thickness. Therefore a sharp increase of the threshold velocity was encountered. At larger impact angles, the threshold velocity appeared to be constant, indicating that the reduction of the lamella thickness complemented exactly the increase of the spreading velocity. These observations support the hypothesis with the force field analysis.

The splash threshold in our experiments were significantly higher than the earlier semi-empirical models as Figure 6.8 demonstrates. The reason lay at the thinner lamella caused by the small drop diameters. The necessity of the high impact velocity raised the threshold values of Re and We. The scaling parameter $\sum_G / \sum_L$ had lower values than in the original experiment because of the greater contribution of the dynamic pressure, $\rho v_{lamella}^2/2$, in the total aerodynamic pressure.

6.3 Velocity of the Uprising Jet

In the case of the single-side splash, the formation, deformation, and separation of the uprising jet was recorded with sufficient temporal resolution as shown in Figure 6.4. The velocity of the uprising jet was designated by its upper-right tip as shown in Figure 6.10. Beside the drop spreading, the strong airflow created by the fast rotating target influenced the motion of the ligament. In order to minimize this undesired aerodynamic effect, the measurement was taken from the formation of the uprising jet to one of the earlier events: the drop became flat, or the tip disintegrated from the ligament. The flattened drop was an indicator that the ligament began to separate from the lamella. After separation the influence of the airflow on the motion of the ligament, or the secondary droplets, was considerable.

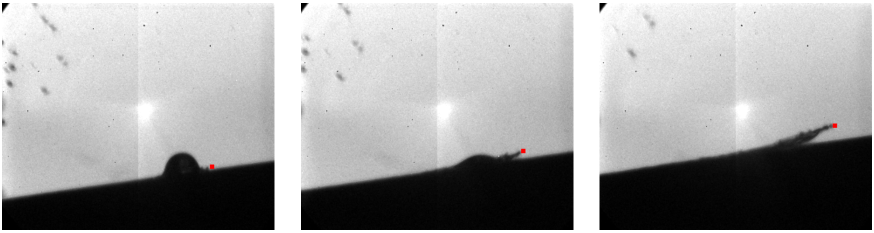

(a) 28 μs **(b)** 36 μs **(c)** 50 μs

Figure 6.10.: Measurement of the velocity of the uprising jet in the case of the single-side splash. The impact event is introduced in Figure 6.4.

Limited to this temporal range, the velocity of the jet tip was measured framewise for three cases of the single-side splash, including the one shown earlier in Figure 6.4. The results are shown in Figure 6.11. Despite the irregular variations caused by the strong deformation of the uprising jet, the velocity did not exhibit a considerable tendency of variation. This suggests that the assumption of zero loss of the kinetic energy by friction is valid. Therefore the average velocity of the tip was taken as the indicative velocity of the ligament.

As the impact angle increased, the forward corona splash became weaker, and the backward splash emerged firstly as prompt splash, further as corona splash. Secondary droplets were emitted continuously from the tip of the uprising jet with smaller sizes. In order to acquire the critical spreading velocity, which is the largest velocity of the secondary droplets, the measurement was conducted from the formation of the uprising jet, to the time instant right before the first generation of the secondary droplets disappeared into the background. Typically 2 to 4 frames

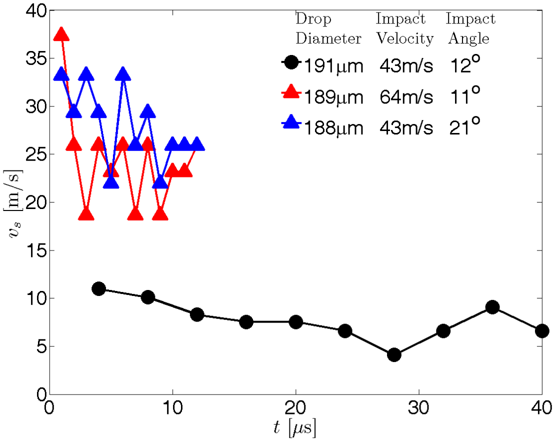

Figure 6.11.: Temporal variation of the absolute velocity of the jet tip in the laboratory coordinate system. The time 0 is taken as the instant of impact. The large variation was caused by strong deformation of the uprising jet.

were used for the velocity measurement. Drop impact with the largest target angle and the highest target velocity is taken as an example to demonstrate the choice of the frames, as shown in Figure 6.12. Only the liquid jets on the upper and lower side of the splash cloud were measurable because their movement were in the focal plane.

After measurement of the absolute velocity of the secondary droplets in the laboratory coordinate system, the relative velocities between the liquid jets and the target were acquired by subtracting the target velocity, and further transformed to the target coordinate system by a rotation of the target angle by a rotation of the target angle, expressed as

$$\begin{bmatrix} v_t \\ v_n \end{bmatrix} = \begin{bmatrix} \cos\theta & \sin\theta \\ -\sin\theta & \cos\theta \end{bmatrix} \begin{bmatrix} v_x \\ v_y \end{bmatrix}, \tag{6.2}$$

where θ is the target angle, v_x and v_y are respectively horizontal and vertical components of the relative velocity in the laboratory coordinate system, and v_t and v_n are tangent component and normal component of the relative velocity in the target coordinate system.

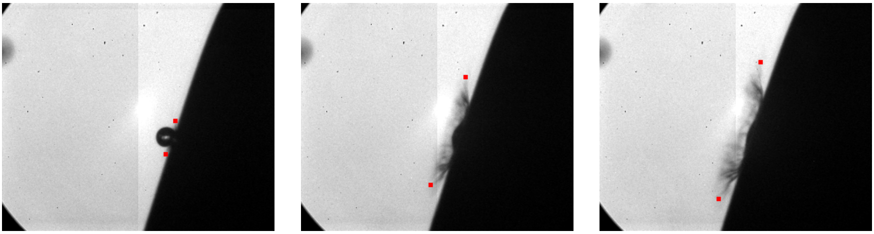

(a) $1\,\mu s$ **(b)** $3\,\mu s$ **(c)** $4\,\mu s$

Figure 6.12.: Measurement of the velocities of the uprising jets in the corona-corona splash mode. Image (a) and (b) were taken for the velocity measurement, because the tip of the thin liquid jets had sharp contrast with the background. In the next frame, the tip of the jets disintegrated into secondary droplets, and faded into the background. The measurement in this case is no longer reliable. Drop diameter: $191\,\mu\mathrm{m}$, impact velocity: $64\mathrm{m/s}$, impact angle: $78°$. Spatial resolution: $8.35\mu\mathrm{m/pixel}$, field of view: $2.61\,\mathrm{mm} \times 2.17\,\mathrm{mm}$, fps: $1\,\mathrm{MHz}$.

The magnitude of the velocity is shown in Figure 6.13. The velocity of the liquid jets had a magnitude of multiple times higher than the impact velocity, and larger impact angles led to larger velocities of the liquid jets. The backward splash had lower velocities than the forward ones, because the tangent component of the impact velocity contributed to the spreading.

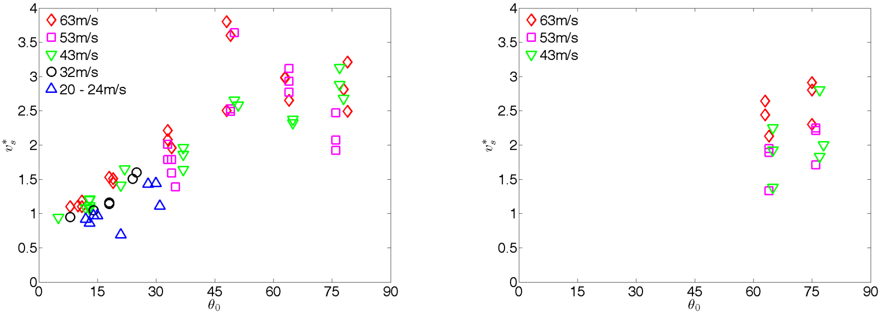

Figure 6.13.: Magnitudes of the velocity of the liquid jets in the target coordinate system. The dimensionless velocity is defined with the reference of the impact velocity as $v_{sec}^* = v_{sec}/v_0$. θ_0 is the impact angle. The left graph is for the forward corona splash, and the right one is for the backward corona splash. The data points are clustered by the magnitude of the impact velocity, as denoted by the symbols.

6.4 Dynamic Spreading Radius

The early stages of the dynamic spreading diameter obeys a square root law for normal impact of a single drop on an unyielding dry surface [121]. It is of interest to examine how the spreading characteristics changes while subjected to a tangent impact velocity. It is anticipated that the tangent velocity pushes the lamella in the forward direction, and creates a larger radius than the backward side. The radii on the both sides of the spreading lamella were defined with the reference of the location of the impact on the target, named as the impact point. The impact point moved horizontally with the target.

Figure 6.14 illustrates an example of the radii measurement. It is noticeable that the forward splash was on the downward side of the lamella, because the impact angle was larger than 90°. The margin of error in the measurement is as conventionally one half pixel. Since the radii were from 10 to more than 100 pixels, the precision of the measurement is sufficiently high, and the error bar is thus omitted.

Strong splash took place when the rotational frequency reached 20 Hz. The presence of secondary droplets harmed the accuracy of the diameter measurement by overlapping with the edge of the lamella, for instance in the case of Figure 6.15. The optical access to the leading edge of the lamella was hindered in these cases. It

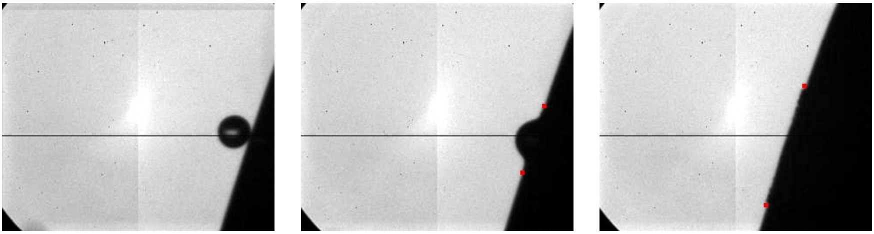

(a) $0\,\mu s$ **(b)** $8\,\mu s$ **(c)** $32\,\mu s$

Figure 6.14.: Measurement of the spreading radii at a low impact speed. The borders of each radius are marked by red squares. The position of the impact point is indicated by the horizontal dark line. Drop diameter: $200\,\mu\mathrm{m}$, impact velocity: $12\mathrm{m/s}$, impact angle: 106°. Spatial resolution: $5.18\mu\mathrm{m/pixel}$, field of view: $1.62\,\mathrm{mm} \times 1.35\,\mathrm{mm}$, fps: $500\,\mathrm{kHz}$.

is postulated that the spreading lamella is a continuous liquid film until the drop is flattened, because the lamella acquires continuous feed of liquid from the impinging drop. Therefore the edge of the lamella coincide with feet of the uprising jet at this early stages.

After all the secondary droplets left from the impact surface, the residual liquid film emerged as shown in the last image of Figure 6.15. The final diameter was larger than the last measured spreading diameter when the drop became flat. This implies that the lamella continued to expand after it became flat. Visibility of the residual liquid film at high impact speeds was limited to the 75° target. At lower impact angles, the liquid film was thinner because of longer stretching of the lamella by the tangent velocity.

In most cases, the instant of impact was well time-resolved, such as in Figure 6.14. In several cases with high impact speeds such as in Figure 6.15, the first contact of the drop with the substrate was not captured. A temporal offset was calculated by dividing the closest distance between the drop and the target surface with the normal component of the impact velocity. The impact point was taken from the first image after impact. There was a slight error on account of the asymmetric spreading, but it was negligible, because the temporal offset was very short, always smaller than one frame, thus $1\,\mu s$.

Typical measurement results are shown in Figure 6.16. As expected, the presence of the tangent velocity led to asymmetric spreading as manifested by the comparison of Figure 6.16 (a) with Figure 6.16 (b). Lower impact angle led to larger discrepancy between the two radii. The forward spreading lasted always longer

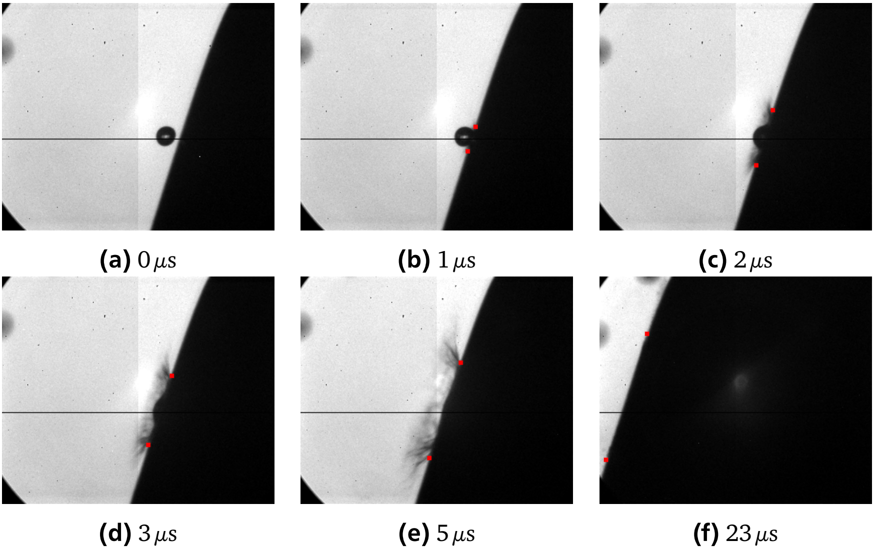

(a) $0\,\mu s$ (b) $1\,\mu s$ (c) $2\,\mu s$ (d) $3\,\mu s$ (e) $5\,\mu s$ (f) $23\,\mu s$

Figure 6.15.: Measurement of the spreading radii at a high impact speed. The borders of each radius are marked by red squares. The position of the impact point is indicated by the horizontal dark line. The measurement was conducted until the impinging drop became flat at the $5\,\mu s$. Drop diameter: $191\,\mu m$, impact velocity: $64 m/s$, impact angle: 78°. Spatial resolution: $8.35 \mu m/pixel$, field of view: $2.61\,mm \times 2.17\,mm$, fps: $1\,MHz$.

than the backward one, and had longer dimensionless duration at higher impact velocities. Noticeably, the forward spreading lamella in Figure 6.16 (b) and Figure 6.16 (c) had a final radius larger than the one at the instant when the drop became flat, quantitatively confirming the observation in Figure 6.15. Appendix B contains more comprehensive results of the radius measurement.

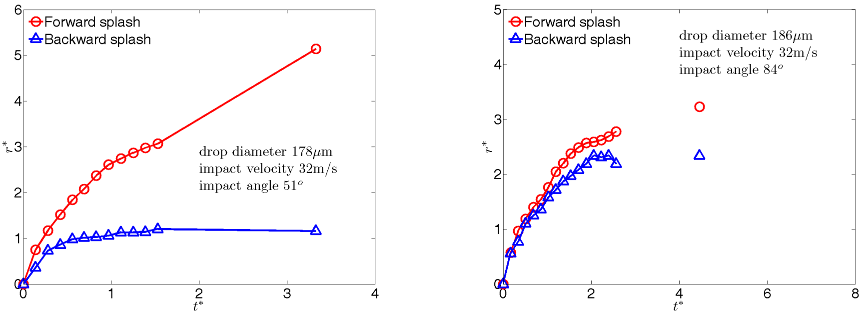

(a) 45° target

(b) 75° target

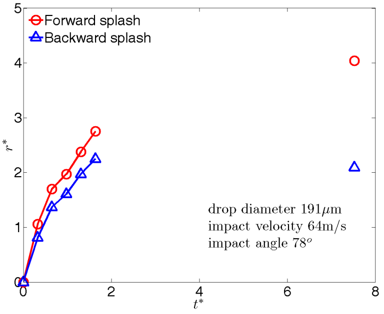

(c) 75° target

Figure 6.16.: The dynamic spreading radii of the spreading lamella. Forward is defined as in the direction of the tangent velocity. The dimensionless radius is scaled by the diameter of the impinging drop as $r^* = r/d_0$. The dimensionless time is as conventionally defined as $t^* = t/(d_0/v_0)$. In Plot (a) the final data point is connected with the second last one, because the radius was clearly recognizable during the entire spreading process. In Plot (b) and (c) the assumption made in Figure 6.15 took effect, and the missing radii were unrecognizable. Therefore there is no line between the last two data points.

6.5 Mass-loss of Drop Impact on the 0° Target

Drop impact on the 0° target distinguished from the other cases with the generation of singular secondary droplets, whose volume could be estimated. As illustrated in Figure 6.17, the impinging drop "rebounded" partially from the impact surface upon impact.

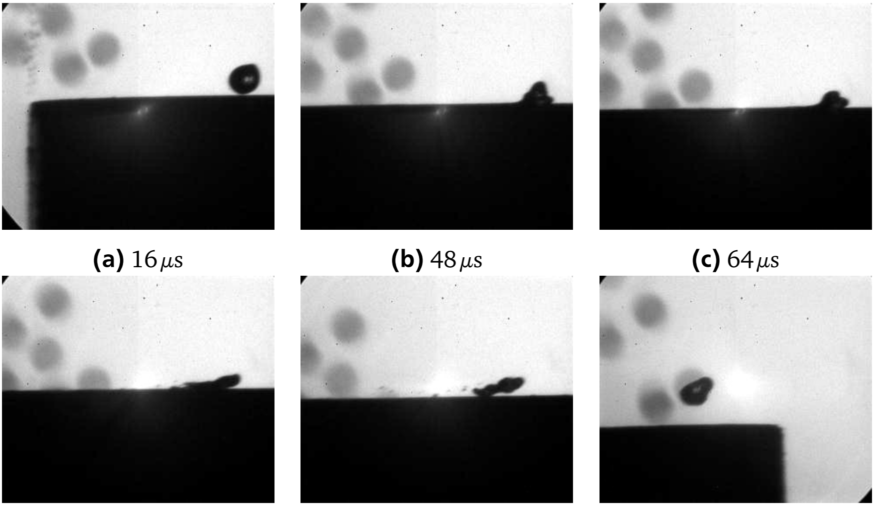
(a) $16\mu s$ (b) $48\mu s$ (c) $64\mu s$ (d) $96\mu s$ (e) $126\mu s$ (f) $320\mu s$

Figure 6.17.: Generation of a singular secondary droplet of drop impact on a 0° target. Drop diameter: $191\,\mu$m, impact velocity: 43m/s, impact angle: 5°. Spatial resolution: 5.18μm/pixel, field of view: 1.62 mm × 1.35 mm, frame rate: 250 kfps.

This observation is reminiscence of the partial rebounding on a Teflon surface observed by Chen et al. [28] and the total rebounding on a steep slope reported by Šikalo et al. [153] as shown in Figure 2.11 in Chapter 2. However, our observation is essentially the single-side splash, except that the uprising jet formed only one drop, while the ones from the two authors mentioned above were similar to drops rebounding on hydrophobic surfaces.

The secondary droplet deformed strongly, both during the disintegration from the residual lamella and in flight while being exposed to the strong airflow. Therefore precise measurement of the volume of the secondary droplet was impossible.

Nevertheless, the drop volume was estimated while the drop appeared relatively cylindrical as at the $126\mu s$, and roughly spherical as at the $320\mu s$ in Figure 6.17. An indicative value was achieved by averaging several such estimations.

In order to identify an appropriate scaling parameter, it was necessary to vary the impact Re and We. Smaller water drops of $130\mu m$ and the aqueous solution of methanol were applied for drop impact on the 0° target. The aqueous solution of methanol with 80% volume concentration has similar density and viscosity as water, but a significantly lower surface tension. The properties of the liquids are listed in Table 6.2. The test was conducted with target speeds ranging from 10m/s to 43m/s. As expected, higher Re and We promoted splash, led to higher mass-loss coefficient. Detailed graphic data are documented in Appendix A.

Substance	Density kg m^{-3}	Dynamic viscosity mPa s	surface tension mN /m
water	1000	1	70
80% Methanol	855 [86]	1.11 [86]	26.95 [152]

Table 6.2.: Properties of applied liquids, percentage in volume fraction.

The mass-loss coefficient, Ψ, is defined as the ratio of the mass of the secondary droplet to the mass of the impinging drop, in accordance with the definition in Chapter 2. In Figure 6.18 the estimated mass-loss coefficient is scaled with the K number. This interpretation is empirical, because the role of the air is missing. Accurate prediction of the corona splash threshold is prerequisite of the mass-loss modeling. Nonetheless the data collapse roughly on one curve, suggesting the parameter be partially meaningful.

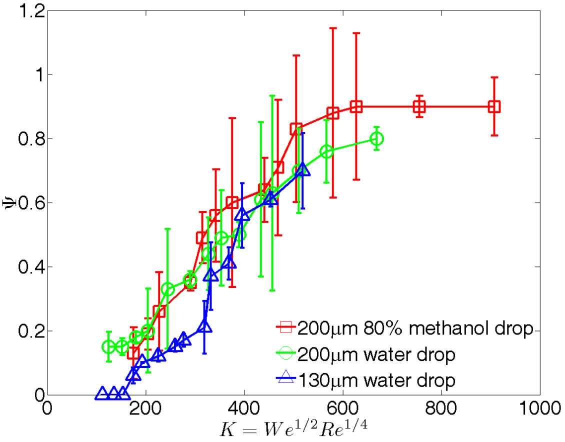

Figure 6.18.: Mass-loss coefficient of drop impact on the 0° targets. The error bar results from strong deformation of the secondary drop.

6.6 Conclusion

In this experiment, high impact speeds ranging from 10m/s to 63m/s were achieved by the impact of a slowly falling drop on a target of rapid motion. 130 μm to 200 μm drops were obtained with a vibrating orifice drop generator. Together with a custom made electrostatic drop deflector, single drop impact on dry surfaces was achieved. The target had inclinations from 0° to 75° in order to observe oblique impacts. High We up to 12 000 and high Re up to 13 000 were achieved, calculated by the total velocity.

The impact process was captured by shadowgraph imaging with a frame rate up to 1 MHz. Six outcomes of the drop impact was discovered: deposition, prompt splash, corona-corona splash, corona-prompt splash, single-side splash, as well as the aerodynamic breakup on the 0° target. The aerodynamic breakup was an interaction of the gas boundary layer with the spreading lamella, which was essentially deposition instead of splash. The semi-empirical correlations for the splash threshold in the literature were compared with our experimental data, and no agreement was found.

A hypothesis on the corona splash threshold was proposed by a force field analysis on the three phase contact line. It was proposed that the destabilizing factor in a corona splash was inertial force and aerodynamic force, and the stabilizing factor was surface tension. These factors were related to the lamella thickness and the critical spreading velocity, which complemented each other. The non-monotonic threshold velocity for various impact angles supported this hypothesis. On the 0° target, the forward lamella was thickest, and the gas boundary layer contributed additionally to the aerodynamic force, therefore the threshold velocity was the lowest. As this effect vanished with the increasing target angle, the threshold velocity rose sharply. Further increase of the impact angle enhanced the spreading velocity, but meanwhile reduced the lamella thickness, leading to firstly a decrease of the threshold velocity from 20° to 35° of the impact angle, and a subsequent steep increase. With impact angles greater than 35°, the threshold velocity became almost constant indicating that the increase of the spreading velocity and the reduction of the lamella thickness complemented each other exactly.

The velocity of the liquid jets of asymmetric splash was for the first time reported. It was found out that the velocity of the liquid jets had higher magnitudes than the impact velocity, and it increased as the impact angle increased, i.e. while approaching the normal impact. Neglecting the kinetic losses because of the short time scale, the velocity of the liquid jets was the velocity of the secondary droplets.

The dynamic spreading radii were measured for the oblique impact, highlighting the asymmetric spreading of the lamella in the presence of a tangent velocity.

The mass-loss was measured for the drop impact on the 0° target, in which case the secondary droplet was singular. It was found out that higher Re and We promoted mass-loss. The scaling parameter, $K = We^{1/2}Re^{1/4}$, collapsed the data on one curve. Although empirical, this parameter reflected the physics partially.

7 Summary and Outlook

7.1 Summary

The goal of this thesis is to improve the understanding of the impact of supercooled drops. Two separate experiments were conducted to this purpose. The first experiment was on the impact of supercooled drops on both aluminum and superhydrophobic surfaces. The intention was to examine the influence of phase change on the hydrodynamics of the drop impact. The second experiment was the high-speed impact of single drops on dry surfaces, in order to observe the drop splash phenomenon at high impact velocities and various impact angles.

In the first experiment, a supercooled drop was created by a 1.5 mm drop falling through a cold passage at −196 °C. Such a low temperature was provided by circulating liquid nitrogen. The drop acquired approximately −5 °C after a falling distance of 600 mm. The impact surfaces included aluminum surfaces and superhydrophobic surfaces. The substrate was dry and its temperature was well controlled.

The dynamic spreading diameter was measured for the drop impact on aluminum surfaces. The influence of supercooling on the drop spreading was unrecognizable. Together with another analytical approach, it was found out that the phase change was negligible for typical drop impacts in the in-flight icing conditions.

Receding and rebounding of drops on superhydrophobic surfaces offered better observations of the differences brought by the supercooling. Both shadowgraph imaging and infrared imaging were taken for observation. Nucleation occurred mostly during drop receding. Occasionally nucleation occurred right upon impact. At low contact temperatures, nucleation frequently occurred during spreading . The duration of the first stage of solidification in the drop impact was significantly shorter than in a sessile liquid, because numerous nucleation sites formed simultaneously during drop deformation. Ice crystals formed in the supercooled water had a similar morphology to a snowflake.

The drop receding on SHS was determined by the contact temperature, which was measured by the bottom-view infrared imaging. The contact temperature was uninfluenced by the presence of supercooling.

Supercooling was found to be a prerequisite of the formation for the formation of rime ice. The ice/water mixture formed in the first stage of solidification hinders the motion of the impinging water, leading to a regular ice shape to the profile of the airfoil.

Since at low supercooling and relatively high substrate temperatures, the drop spreading remained uninfluenced by the phase change, it is permissable to conduct the drop splash experiment at room temperatures.

In the second experiment high impact speeds ranging from 10m/s to 63m/s were achieved by the impact of slowly falling drops onto a target of rapid motion. $100\,\mu$m to $200\,\mu$m drops were obtained with a vibrating orifice drop generator. Together with a custom made electrostatic drop deflector, single drop impact on dry surfaces was achieved. The target had inclinations from 0° to 75° in order to observe oblique impacts. High We up to 12 000 and high Re up to 13 000 were achieved, calculated using the total velocity.

Six outcomes of drop impact were identified: deposition, prompt splash, corona-corona splash, corona-prompt splash, single-side splash and the aerodynamic breakup. The aerodynamic breakup on a horizontal target was an interaction between the spreading lamella and the gas boundary layer. A qualitative force field analysis made on the spreading lamella pointed out that in a corona splash, the stabilizing factor is surface tension, and the destabilizing factors are aerodynamic force and inertial force. The lamella thickness and critical spreading velocity correlate with each other in a complementary manner, leading to non-monotonic threshold impact velocities at different impact angles. The hypothesis and the experimental results were in good agreement with each other. The velocity of the uprising jet and the asymmetric spreading radii were measured from videos. The mass-loss coefficient was measured for the drop impact on horizontal targets. The scaling parameter for the mass-loss, $K = We^{1/2}Re^{1/4}$, collapsed the data on one curve. Although empirical, this parameter reflected the physics partially.

7.2 Outlook

When, where and how many nucleation sites are formed upon drop impact are critical questions concerning the influence of supercooling on the outcome of drop impact. Only low supercooling was acquired in the experiment. It is desirable to achieve higher supercooling and conduct drop impact on structured surfaces in order to further examine the influence of nucleation in a quantitative manner. Furthermore supercooled drop impact on ice surfaces, as well as ice/water mushy layers are interesting investigations for more accurate prediction of the ice accretion.

The corona splash threshold requires two submodels for the lamella thickness and the critical spreading velocity respectively. Both of them remain as open questions in the scope of this doctoral study.

The lamella thickness at various impact speeds was reported by Ruiter at al. [124], who conducted the measurement close to the inception of splash. The lamella thickness was unmeasurable once splash occurred, because of the overlapping of secondary droplets with the lamella edges. In our experiment, this incapability was confirmed by drop impacts with large impact angles. However, in the cases of the single-side splash, the forward spreading lamella had a clear shape, and was of a significant thickness. In this case, the thickness could be measured. However, the limited spatial resolution induced very large error in the measurement. The thickness was merely 2 to 4 pixels. With larger drops and lower impact speeds, as well as a camera of lower frame rate but higher pixel resolution, the measurement of the lamella thickness could be conducted reliably. We expect a scaling parameter to describe the lamella thickness for the oblique impact. This information, although limited to highly oblique impacts, would be a significant contribution to the modeling of the splash threshold.

The critical spreading velocity (i.e. the velocity of the uprising jets) exhibited an apparent dependency on the impact angle. The same dependency, but in the opposite direction, was observed for the size of the disintegrating liquid ligaments, or the secondary droplets. Since the lamella thickness determines the thickness of the liquid ligament and the diameter of the secondary droplets, it can be concluded that the lower the impact angle is, the thicker the spreading lamella is, and the slower the critical spreading velocity is.

Notably, the critical spreading velocity and the lamella thickness are linked to each other by the critical time at which corona splash occurs. This time is not measurable for normal drop impact because of its small value. However in the cases of the single-side splash, this time, from the formation of the uprising jet to the disintegration of the liquid ligament, was well resolved in time. Observations show that higher impact angles led to longer critical times.

Recalling the Newton's second law: $F_{net} t_{crit} = m_s v_s$, where F_{net} is the net force caused by the inertial force, aerodynamic force, and the surface tension, t_{crit} is the critical time, m_s is the mass of a liquid ligament, or a secondary droplet, v_s is the velocity magnitude of the uprising jet, the observations show that the liquid ligament needs the critical time to acquire sufficient momentum to stretch out from the rest part of liquid.

Successful modeling of the F_{net}, t_{crit} and the v_s would lead to the modeling of the mass-loss, which is the most critical part of the SLD splash model. In the cases of the single-side splash, the latter two parameters are measurable. Although the F_{net} is not directly accessible, it could be derived by measuring the m_s.

A 2.5 mm drop has a weight of 8 mg, while a precise balance has a resolution of $100\,\mu g$. 1.25% precision could be achieved. It should be noted that the force model is linked to the lamella thickness, the critical spreading velocity, and the critical time, because all these models share the same assumption of the force analysis made for the corona splash.

Modeling of the mass-loss becomes significantly more difficult for drop impacts of large impact angles, because the lamella thickness, the critical time are not directly measurable. For a normal impact, the dynamic spreading diameter obeys a square root law at early stages. If this law preserves when splash emerges, the critical time, t_{crit}, can be derived with the measurable velocity of the liquid jet by finding the corresponding value on the diameter curve. At the presence of the tangent velocity, the spreading radius becomes an unknown function, as measured in our experiment. If this function could be modeled, the critical time could be known. Consequently the F_{net} could be modeled.

These preliminary ideas suggest continual employment of the current experimental setup with large drops, and a separate experiment on the mass-loss. Analytical study on the modeling of the lamella thickness, the critical spreading velocity, the critical time, the net force and the mass-loss are recommended.

A Image Collection of High-speed Oblique Impacts

High-speed impact of single drops on dry surfaces are illustrated by sequential images in this appendix. The images are clustered by the target angle. Image sequences which appear in Chapter 6 are not listed in the appendix.

A.1 75° target

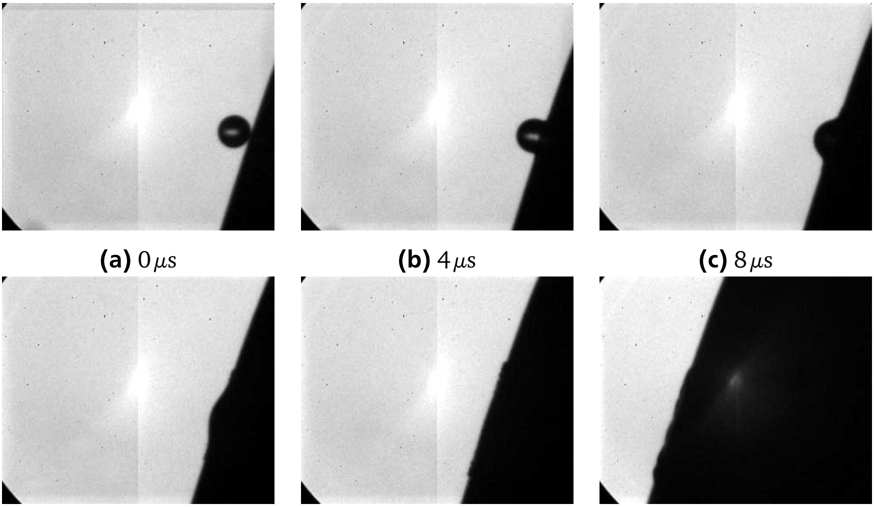

(a) $0\,\mu$s **(b)** $4\,\mu$s **(c)** $8\,\mu$s

(d) $16\,\mu$s **(e)** $32\,\mu$s **(f)** $94\,\mu$s

Figure A.1.: Drop diameter: $200\,\mu$m, impact velocity: 12m/s, impact angle: 106°. Spatial resolution: 5.18μm/pixel, field of view: $1.62\,$mm × $1.35\,$mm, fps: $500\,$kHz.

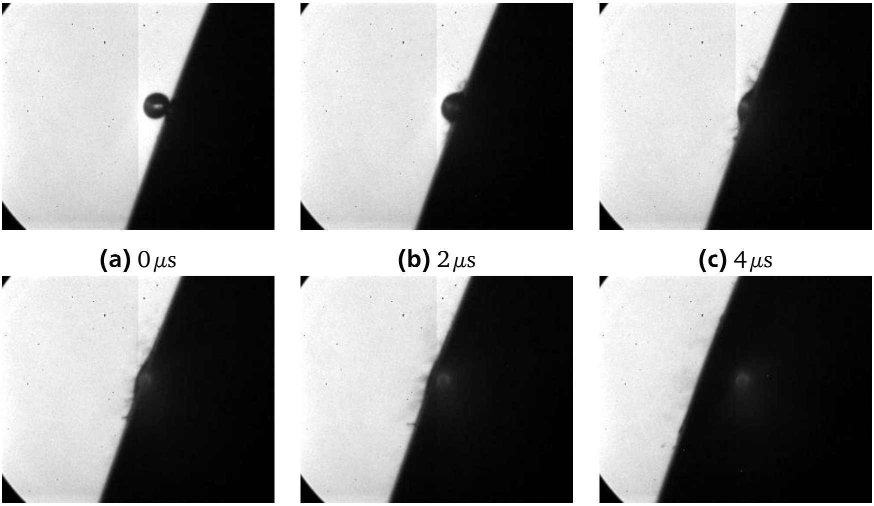

(a) $0\,\mu s$ **(b)** $2\,\mu s$ **(c)** $4\,\mu s$

(d) $6\,\mu s$ **(e)** $8\,\mu s$ **(f)** $15\,\mu s$

Figure A.2.: Drop diameter: $186\,\mu\mathrm{m}$, impact velocity: $32\mathrm{m/s}$, impact angle: $84°$. Spatial resolution: $6.34\mu\mathrm{m/pixel}$, field of view: $1.98\,\mathrm{mm} \times 1.65\,\mathrm{mm}$, frame rate: $1\,\mathrm{Mfps}$.

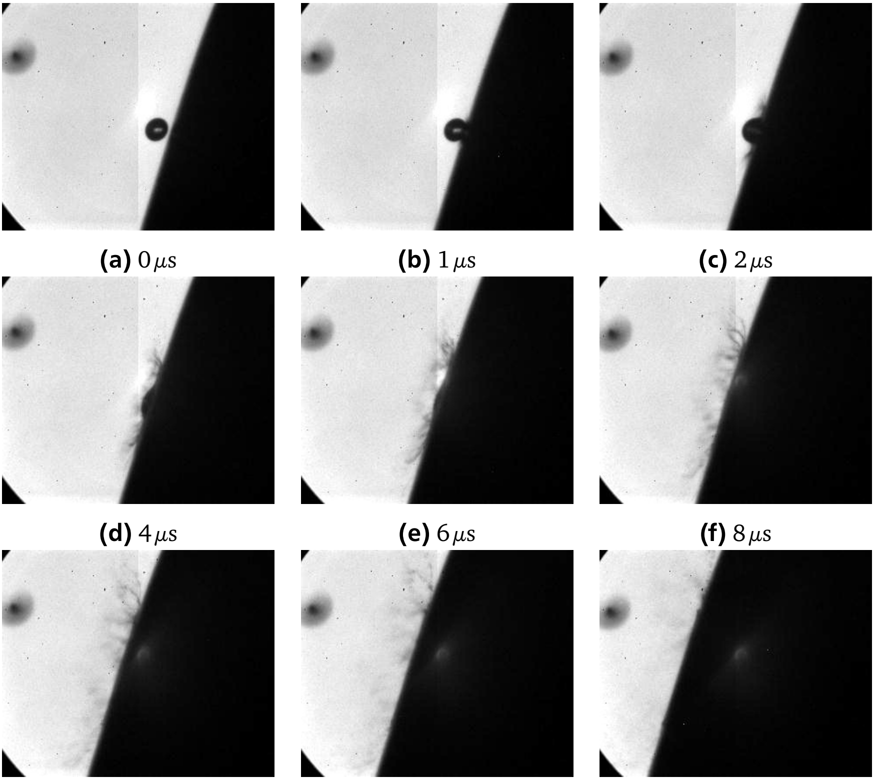

(a) $0\,\mu s$ **(b)** $1\,\mu s$ **(c)** $2\,\mu s$

(d) $4\,\mu s$ **(e)** $6\,\mu s$ **(f)** $8\,\mu s$

(g) $10\,\mu s$ **(h)** $12\,\mu s$ **(i)** $17\,\mu s$

Figure A.3.: Drop diameter: $190\,\mu\mathrm{m}$, impact velocity: $42\mathrm{m/s}$, impact angle: $80°$. Spatial resolution: $7.07\mu\mathrm{m/pixel}$, field of view: $2.21\,\mathrm{mm} \times 1.84\,\mathrm{mm}$, frame rate: $1\,\mathrm{Mfps}$.

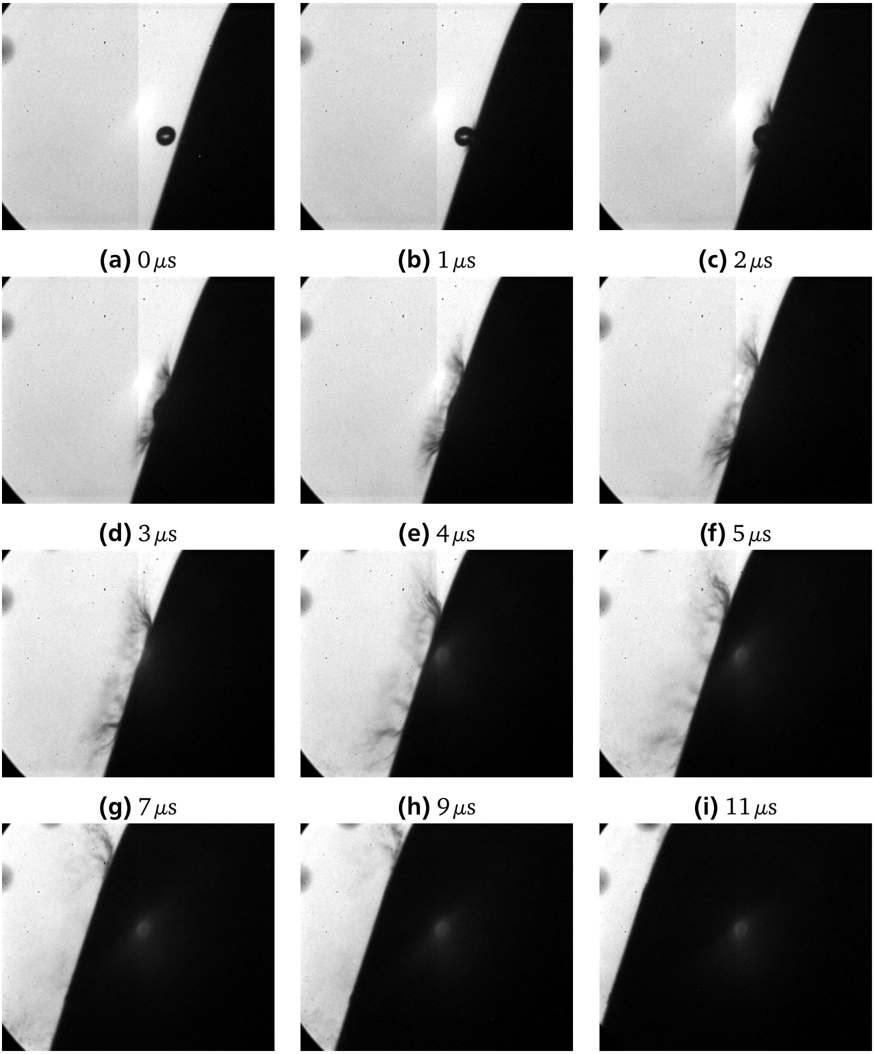
(a) $0\,\mu s$ **(b)** $1\,\mu s$ **(c)** $2\,\mu s$

(d) $3\,\mu s$ **(e)** $4\,\mu s$ **(f)** $5\,\mu s$

(g) $7\,\mu s$ **(h)** $9\,\mu s$ **(i)** $11\,\mu s$

(j) $15\,\mu s$ **(k)** $17\,\mu s$ **(l)** $23\,\mu s$

Figure A.4.: Drop diameter: $199\,\mu\mathrm{m}$, impact velocity: $64\mathrm{m/s}$, impact angle: $79°$. Spatial resolution: $8.35\mu\mathrm{m/pixel}$, field of view: $2.61\,\mathrm{mm} \times 2.17\,\mathrm{mm}$, fps: $1\,\mathrm{M\,Hz}$.

A.2 60° target

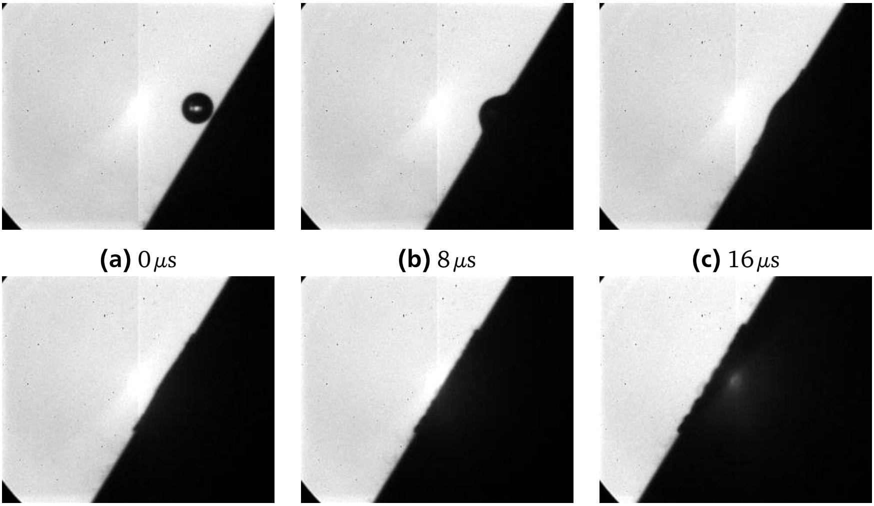

(a) 0 μs **(b)** 8 μs **(c)** 16 μs

(d) 24 μs **(e)** 32 μs **(f)** 48 μs

Figure A.5.: Drop diameter: 189 μm, impact velocity: 14m/s, impact angle: 80°. Spatial resolution: 5.18μm/pixel, field of view: 1.62 mm × 1.35 mm, frame rate: 500 kfps.

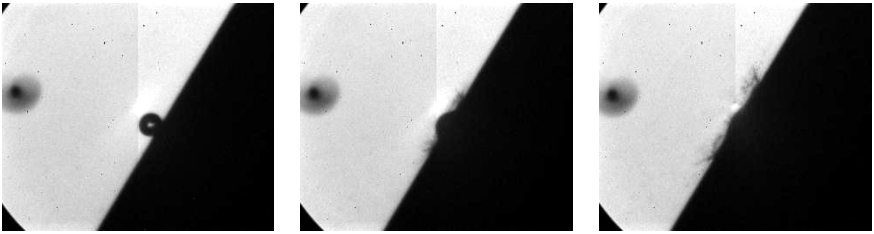

(a) $0\,\mu s$ **(b)** $3\,\mu s$ **(c)** $6\,\mu s$

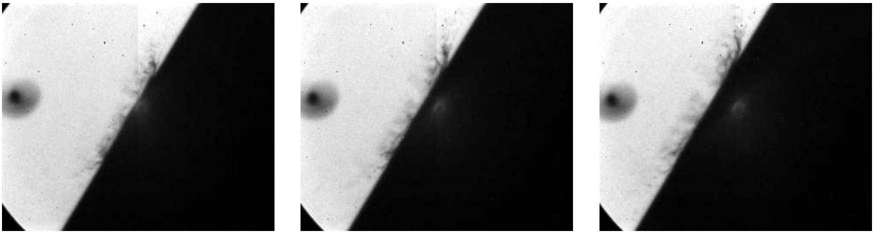

(d) $9\,\mu s$ **(e)** $12\,\mu s$ **(f)** $15\,\mu s$

(g) $20\,\mu s$ **(h)** $25\,\mu s$ **(i)** $28\,\mu s$

Figure A.6.: Drop diameter: $189\,\mu\mathrm{m}$, impact velocity: $32\mathrm{m/s}$, impact angle: $67°$. Spatial resolution: $7.07\mu\mathrm{m/pixel}$, field of view: $2.21\,\mathrm{mm} \times 1.84\,\mathrm{mm}$, frame rate: $1\,\mathrm{Mfps}$.

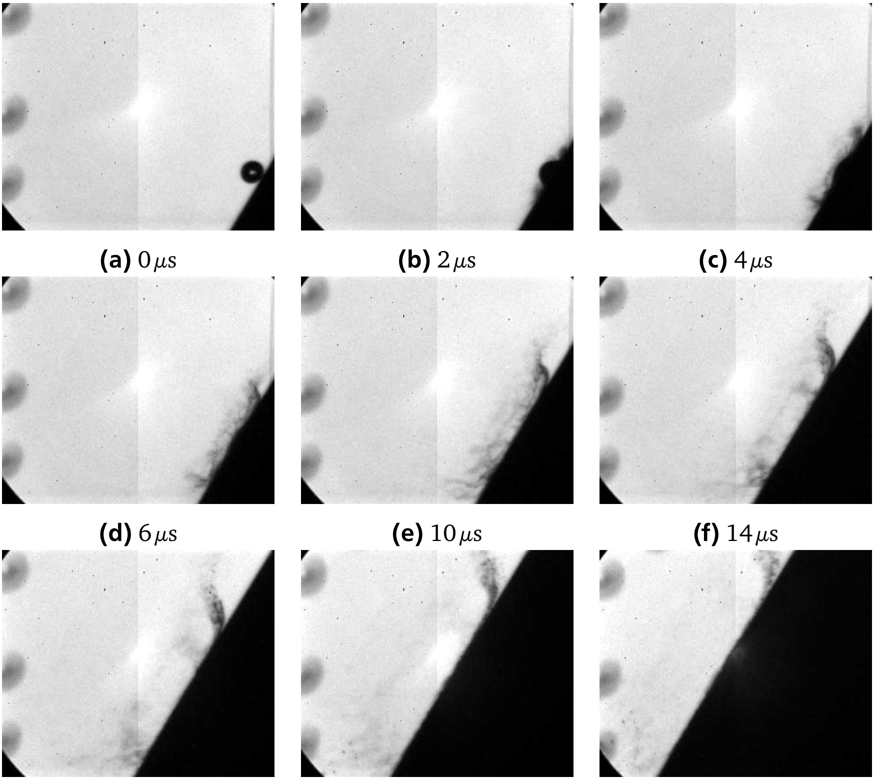

(a) $0\,\mu s$ **(b)** $2\,\mu s$ **(c)** $4\,\mu s$

(d) $6\,\mu s$ **(e)** $10\,\mu s$ **(f)** $14\,\mu s$

(g) $18\,\mu s$ **(h)** $26\,\mu s$ **(i)** $32\,\mu s$

Figure A.7.: Drop diameter: $190\,\mu\mathrm{m}$, impact velocity: $42\mathrm{m/s}$, impact angle: $80°$. Spatial resolution: $7.07\mu\mathrm{m/pixel}$, field of view: $2.21\,\mathrm{mm} \times 1.84\,\mathrm{mm}$, frame rate: $1\,\mathrm{Mfps}$.

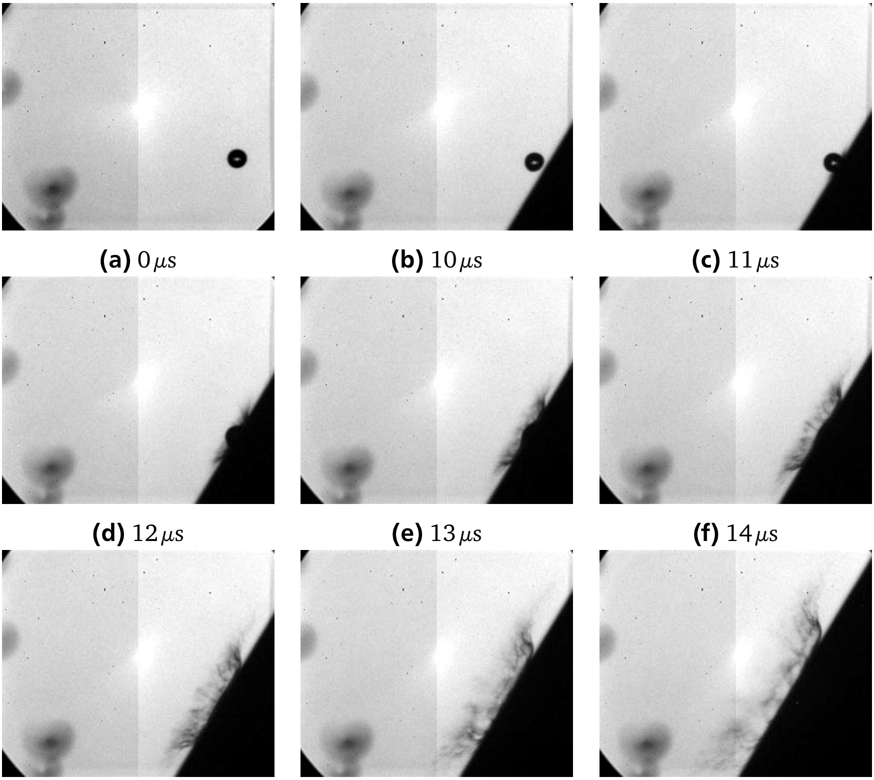

(a) 0 μs **(b)** 10 μs **(c)** 11 μs

(d) 12 μs **(e)** 13 μs **(f)** 14 μs

(g) 15 μs **(h)** 17 μs **(i)** 33 μs

Figure A.8.: Target angle: 60°, drop diameter: $194\,\mu\mathrm{m}$, impact velocity: $64\mathrm{m/s}$, impact angle: 63°. Spatial resolution: $8.35\mu\mathrm{m/pixel}$, field of view: $2.61\,\mathrm{mm} \times 2.17\,\mathrm{mm}$, fps: $1\,\mathrm{M\,Hz}$.

A.3 45° target

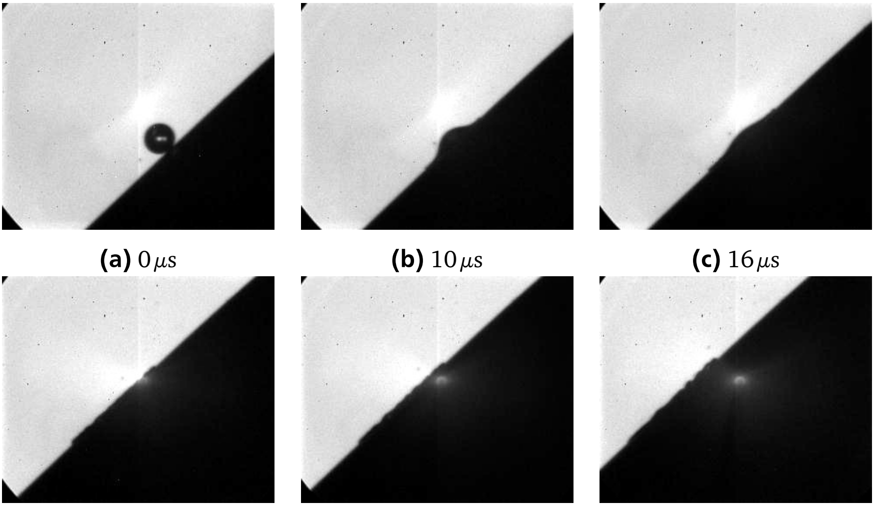

(a) $0\,\mu s$ **(b)** $10\,\mu s$ **(c)** $16\,\mu s$

(d) $34\,\mu s$ **(e)** $40\,\mu s$ **(f)** $54\,\mu s$

Figure A.9.: Drop diameter: $187\,\mu\text{m}$, impact velocity: 13m/s, impact angle: $65°$. Spatial resolution: $5.18\mu\text{m/pixel}$, field of view: $1.62\,\text{mm} \times 1.35\,\text{mm}$, frame rate: $500\,\text{kfps}$.

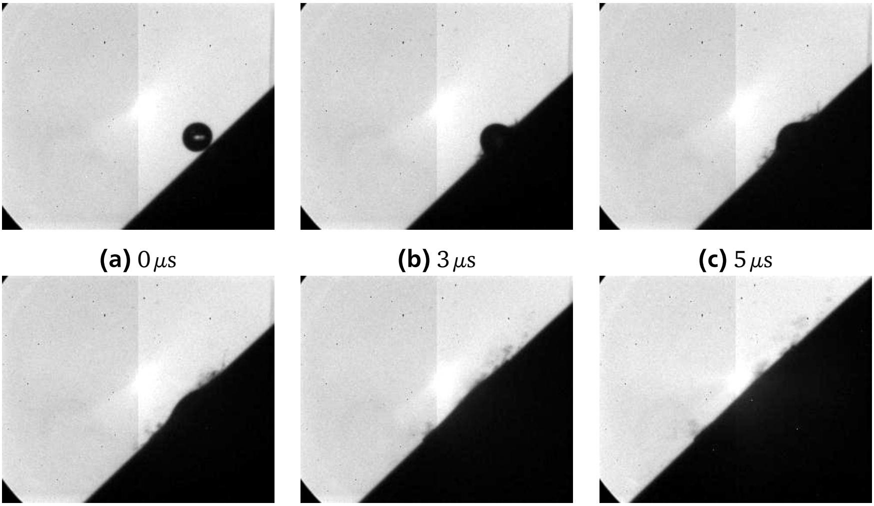

(a) $0\,\mu s$ **(b)** $3\,\mu s$ **(c)** $5\,\mu s$

(d) $8\,\mu s$ **(e)** $13\,\mu s$ **(f)** $19\,\mu s$

Figure A.10.: Drop diameter: $184\,\mu\mathrm{m}$, impact velocity: $28\mathrm{m/s}$, impact angle: $52°$. Spatial resolution: $5.18\mu\mathrm{m/pixel}$, field of view: $1.62\,\mathrm{mm} \times 1.35\,\mathrm{mm}$, frame rate: $1\,\mathrm{Mfps}$.

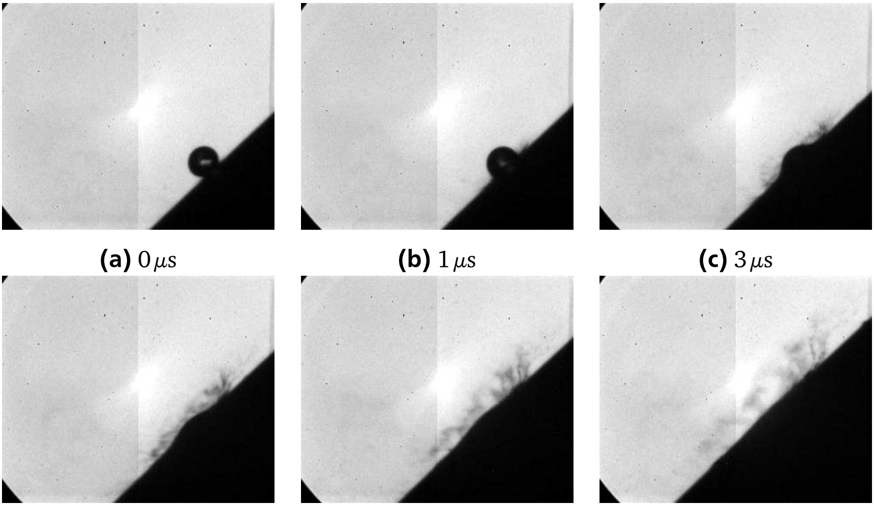

(a) $0\,\mu s$ **(b)** $1\,\mu s$ **(c)** $3\,\mu s$

(d) $5\,\mu s$ **(e)** $7\,\mu s$ **(f)** $10\,\mu s$

Figure A.11.: Drop diameter: $191\,\mu\mathrm{m}$, impact velocity: $38\mathrm{m/s}$, impact angle: $48°$. Spatial resolution: $5.18\mu\mathrm{m/pixel}$, field of view: $1.62\,\mathrm{mm} \times 1.35\,\mathrm{mm}$, frame rate: $1\,\mathrm{Mfps}$.

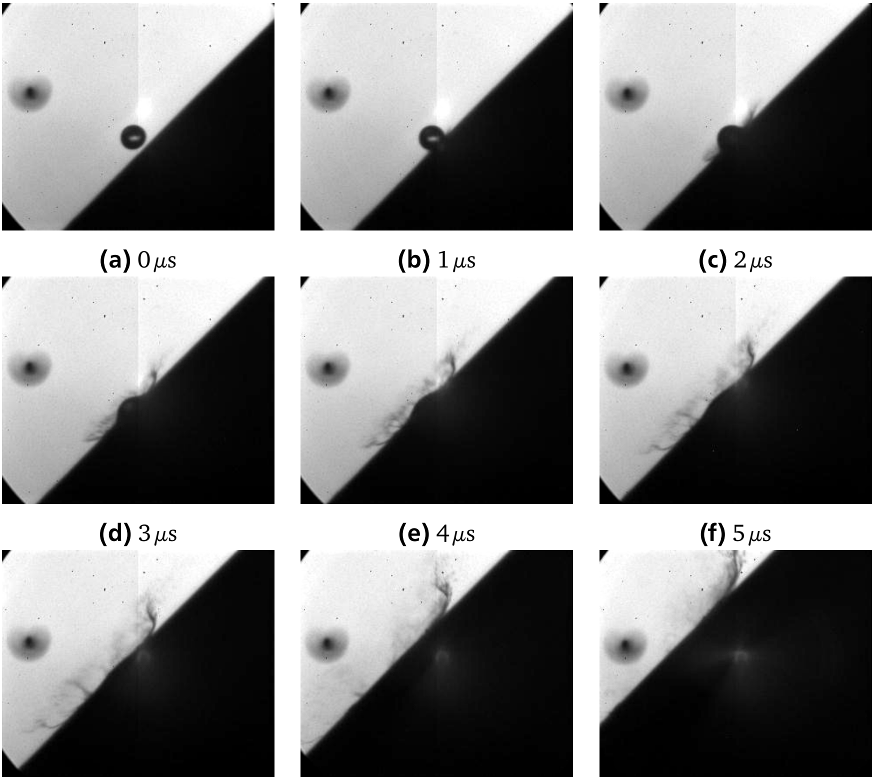
(a) $0\,\mu s$ **(b)** $1\,\mu s$ **(c)** $2\,\mu s$

(d) $3\,\mu s$ **(e)** $4\,\mu s$ **(f)** $5\,\mu s$

(g) $6\,\mu s$ **(h)** $9\,\mu s$ **(i)** $13\,\mu s$

Figure A.12.: Drop diameter: $193\,\mu\mathrm{m}$, impact velocity: $64\mathrm{m/s}$, impact angle: $48°$. Spatial resolution: $6.34\mu\mathrm{m/pixel}$, field of view: $1.98\,\mathrm{mm} \times 1.65\,\mathrm{mm}$, frame rate: $1\,\mathrm{Mfps}$.

A.4 30° target

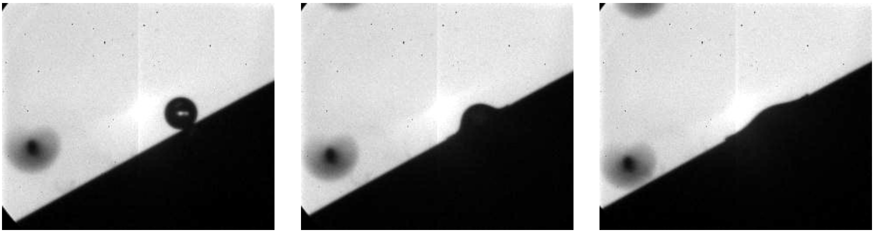

(a) $0\,\mu s$ **(b)** $8\,\mu s$ **(c)** $16\,\mu s$

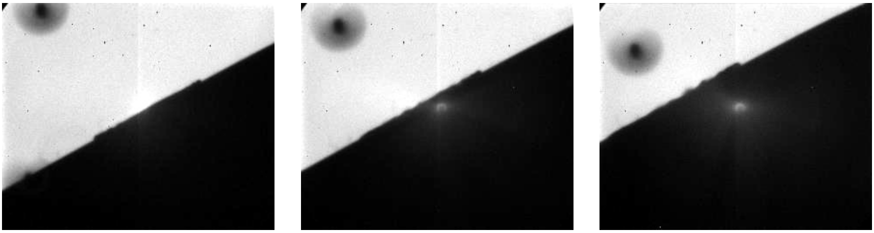

(d) $32\,\mu s$ **(e)** $48\,\mu s$ **(f)** $72\,\mu s$

Figure A.13.: Drop diameter: $199\,\mu\mathrm{m}$, impact velocity: $14\mathrm{m/s}$, impact angle: 55°. Spatial resolution: $5.18\mu\mathrm{m/pixel}$, field of view: $1.62\,\mathrm{mm} \times 1.35\,\mathrm{mm}$, frame rate: $500\,\mathrm{kfps}$.

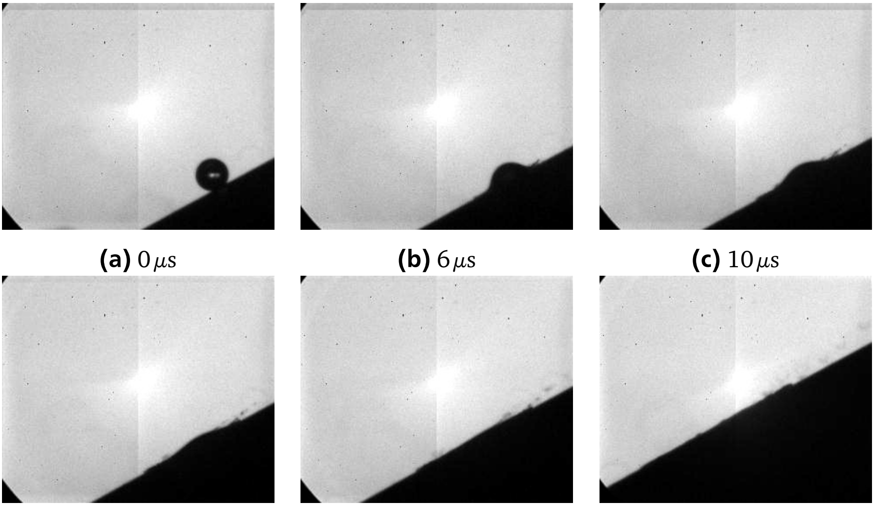

(a) $0\,\mu s$ **(b)** $6\,\mu s$ **(c)** $10\,\mu s$

(d) $14\,\mu s$ **(e)** $22\,\mu s$ **(f)** $44\,\mu s$

Figure A.14.: Drop diameter: $195\,\mu\mathrm{m}$, impact velocity: $22\mathrm{m/s}$, impact angle: $45°$. Spatial resolution: $5.18\mu\mathrm{m/pixel}$, field of view: $1.62\,\mathrm{mm} \times 1.35\,\mathrm{mm}$, frame rate: $500\,\mathrm{kfps}$.

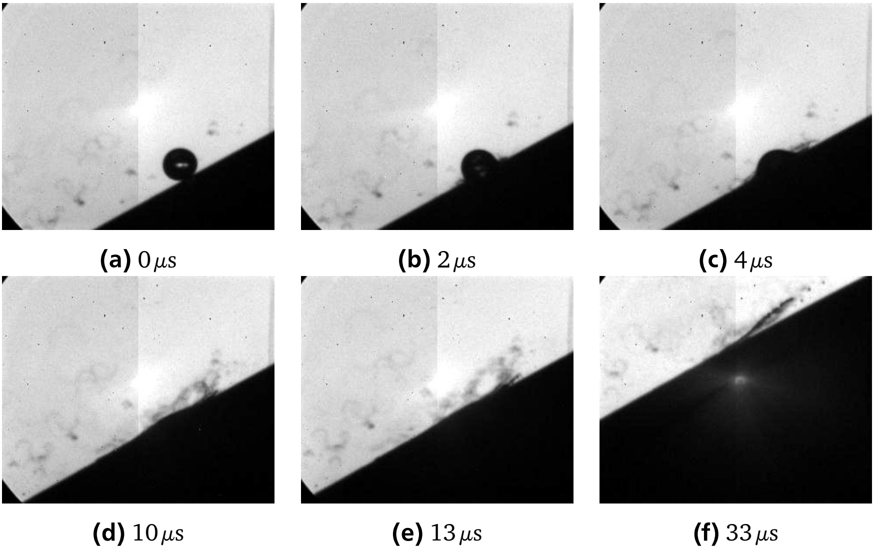

(a) $0\,\mu s$ **(b)** $2\,\mu s$ **(c)** $4\,\mu s$

(d) $10\,\mu s$ **(e)** $13\,\mu s$ **(f)** $33\,\mu s$

Figure A.15.: Drop diameter: $197\,\mu\text{m}$, impact velocity: 43m/s, impact angle: $37°$. Spatial resolution: $5.18\mu\text{m/pixel}$, field of view: $1.62\,\text{mm} \times 1.35\,\text{mm}$, frame rate: $1\,\text{Mfps}$.

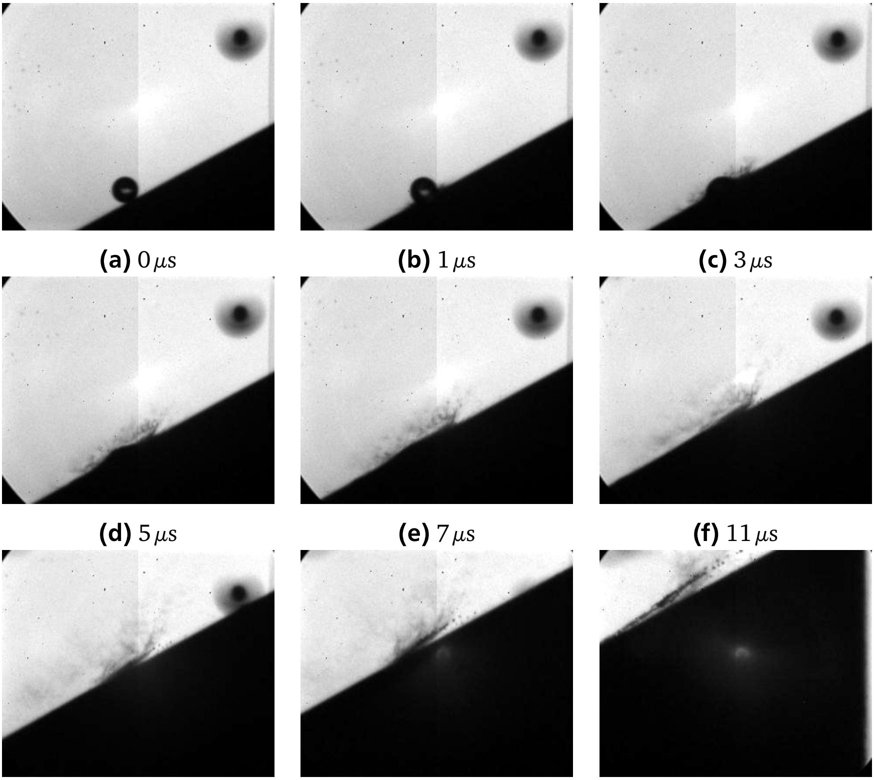

(a) 0 μs **(b)** 1 μs **(c)** 3 μs

(d) 5 μs **(e)** 7 μs **(f)** 11 μs

(g) 16 μs **(h)** 21 μs **(i)** 35 μs

Figure A.16.: Drop diameter: $199\,\mu\mathrm{m}$, impact velocity: $63\mathrm{m/s}$, impact angle: $33°$. Spatial resolution: $6.34\mu\mathrm{m/pixel}$, field of view: $1.98\,\mathrm{mm} \times 1.65\,\mathrm{mm}$, frame rate: $1\,\mathrm{Mfps}$.

A.5 15° target

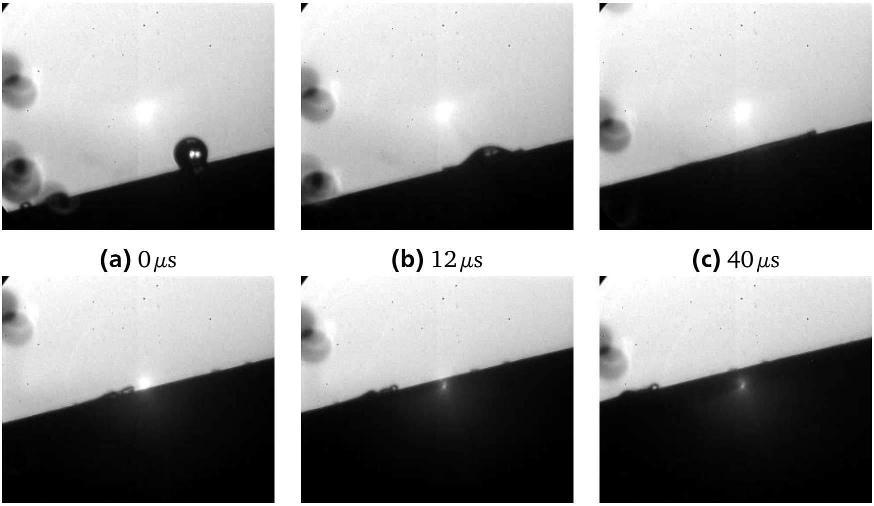
(a) $0\,\mu s$ **(b)** $12\,\mu s$ **(c)** $40\,\mu s$ **(d)** $96\,\mu s$ **(e)** $112\,\mu s$ **(f)** $128\,\mu s$

Figure A.17.: Drop diameter: $201\,\mu\mathrm{m}$, impact velocity: $16\mathrm{m/s}$, impact angle: 37°. Spatial resolution: $5.18\mu\mathrm{m/pixel}$, field of view: $1.62\,\mathrm{mm} \times 1.35\,\mathrm{mm}$, frame rate: $250\,\mathrm{kfps}$.

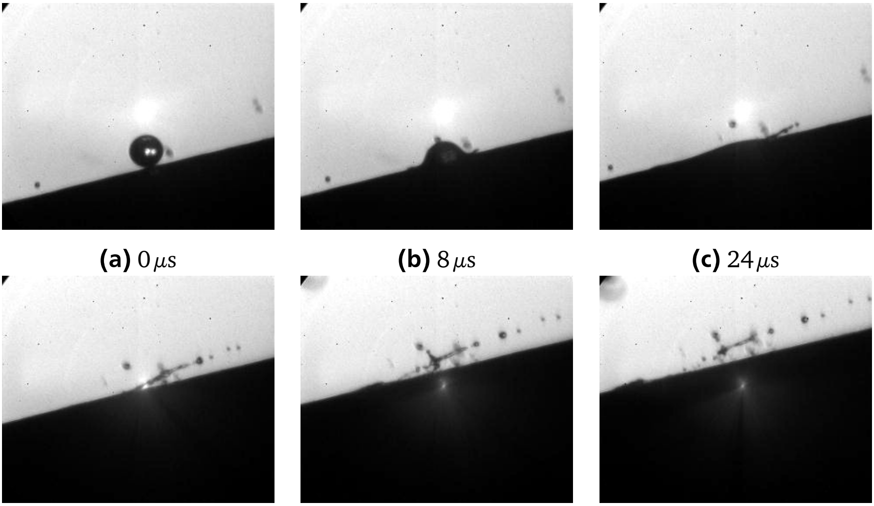

(a) $0\,\mu s$ **(b)** $8\,\mu s$ **(c)** $24\,\mu s$

(d) $56\,\mu s$ **(e)** $76\,\mu s$ **(f)** $88\,\mu s$

Figure A.18.: Drop diameter: $195\,\mu\mathrm{m}$, impact velocity: $22\mathrm{m/s}$, impact angle: 30°. Spatial resolution: $5.18\mu\mathrm{m/pixel}$, field of view: $1.62\,\mathrm{mm} \times 1.35\,\mathrm{mm}$, frame rate: $250\,\mathrm{kfps}$.

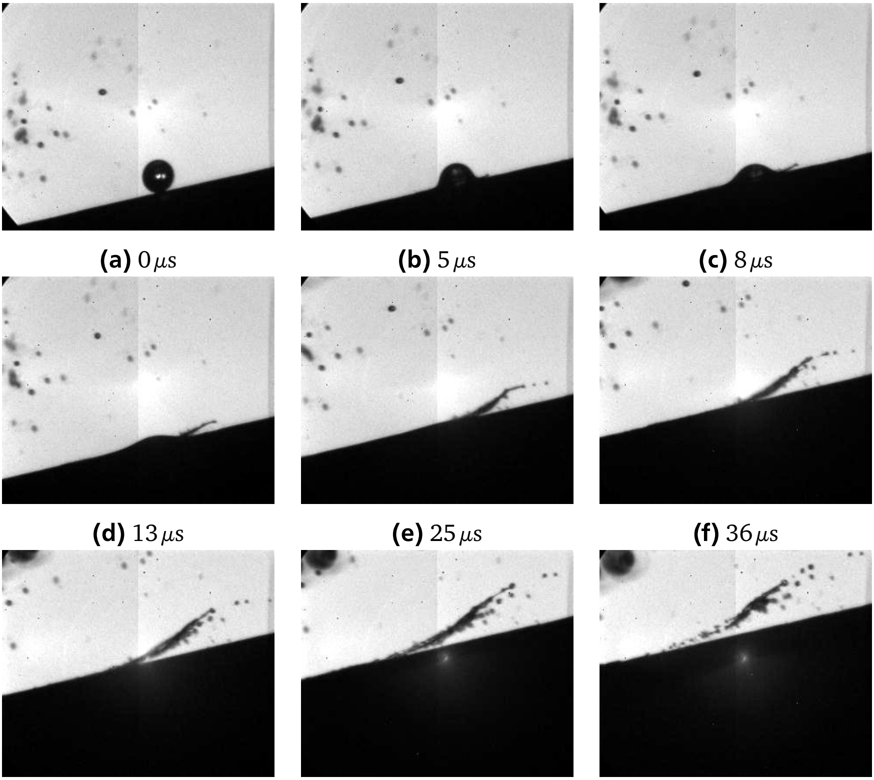

(a) $0\,\mu s$ **(b)** $5\,\mu s$ **(c)** $8\,\mu s$

(d) $13\,\mu s$ **(e)** $25\,\mu s$ **(f)** $36\,\mu s$

(g) $44\,\mu s$ **(h)** $53\,\mu s$ **(i)** $60\,\mu s$

Figure A.19.: Drop diameter: $191\,\mu\mathrm{m}$, impact velocity: $43\mathrm{m/s}$, impact angle: $21°$. Spatial resolution: $5.18\mu\mathrm{m/pixel}$, field of view: $1.62\,\mathrm{mm} \times 1.35\,\mathrm{mm}$, frame rate: $1\,\mathrm{Mfps}$.

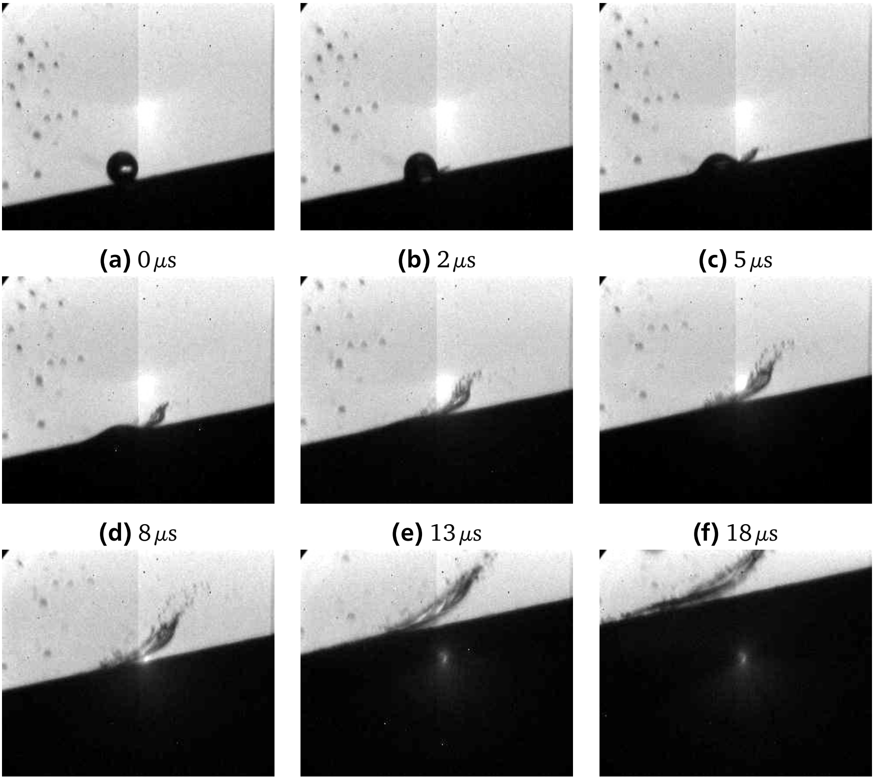

(a) $0\,\mu s$ (b) $2\,\mu s$ (c) $5\,\mu s$ (d) $8\,\mu s$ (e) $13\,\mu s$ (f) $18\,\mu s$ (g) $23\,\mu s$ (h) $36\,\mu s$ (i) $47\,\mu s$

Figure A.20.: Drop diameter: $197\,\mu\mathrm{m}$, impact velocity: $64\mathrm{m/s}$, impact angle: $19°$. Spatial resolution: $5.18\mu\mathrm{m/pixel}$, field of view: $1.62\,\mathrm{mm} \times 1.35\,\mathrm{mm}$, frame rate: $1\,\mathrm{Mfps}$.

A.6 10° target

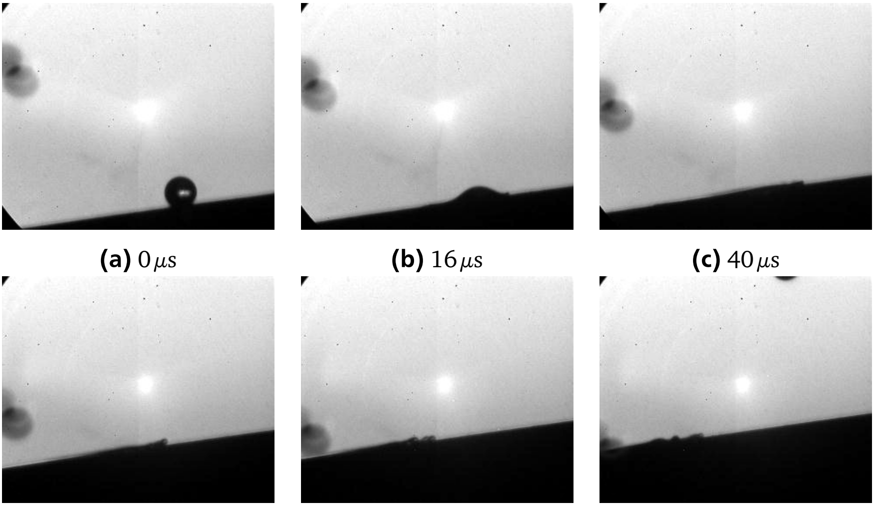

(a) $0\,\mu s$ **(b)** $16\,\mu s$ **(c)** $40\,\mu s$

(d) $80\,\mu s$ **(e)** $100\,\mu s$ **(f)** $116\,\mu s$

Figure A.21.: Drop diameter: $200\,\mu\mathrm{m}$, impact velocity: $18\mathrm{m/s}$, impact angle: 50°. Spatial resolution: $5.18\mu\mathrm{m/pixel}$, field of view: $1.62\,\mathrm{mm} \times 1.35\,\mathrm{mm}$, frame rate: $250\,\mathrm{kfps}$.

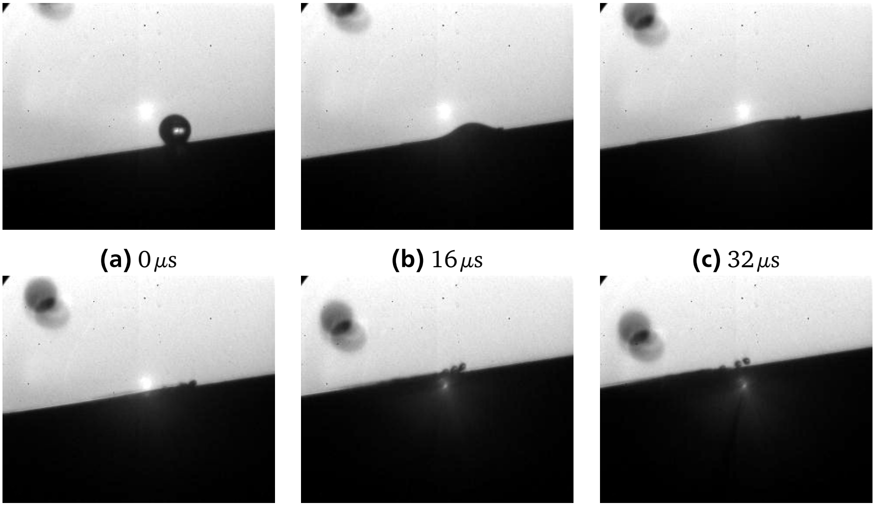

(a) $0\,\mu s$ **(b)** $16\,\mu s$ **(c)** $32\,\mu s$

(d) $44\,\mu s$ **(e)** $72\,\mu s$ **(f)** $84\,\mu s$

Figure A.22.: Drop diameter: $192\,\mu\mathrm{m}$, impact velocity: $24\mathrm{m/s}$, impact angle: $21°$. Spatial resolution: $5.18\mu\mathrm{m/pixel}$, field of view: $1.62\,\mathrm{mm} \times 1.35\,\mathrm{mm}$, frame rate: $250\,\mathrm{kfps}$.

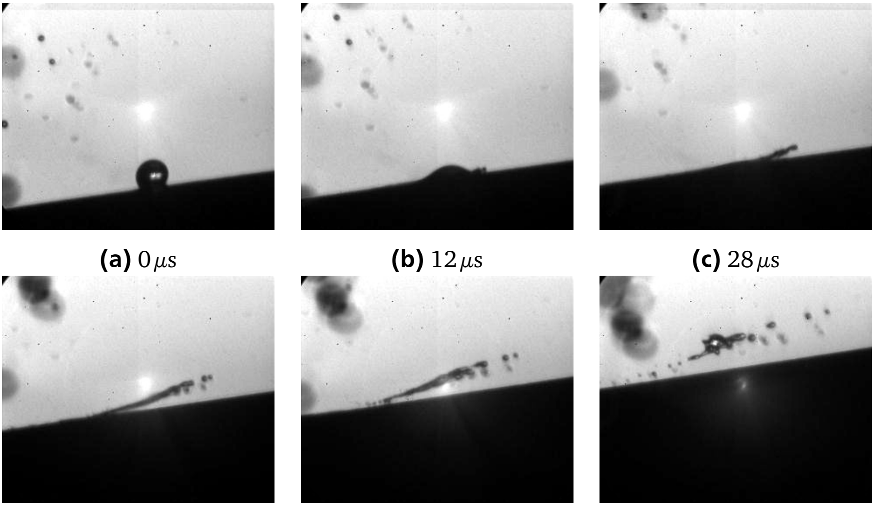

(a) $0\,\mu s$ **(b)** $12\,\mu s$ **(c)** $28\,\mu s$

(d) $60\,\mu s$ **(e)** $76\,\mu s$ **(f)** $108\,\mu s$

Figure A.23.: Drop diameter: $191\,\mu\mathrm{m}$, impact velocity: $32\mathrm{m/s}$, impact angle: $18°$. Spatial resolution: $5.18\mu\mathrm{m/pixel}$, field of view: $1.62\,\mathrm{mm} \times 1.35\,\mathrm{mm}$, frame rate: $250\,\mathrm{kfps}$.

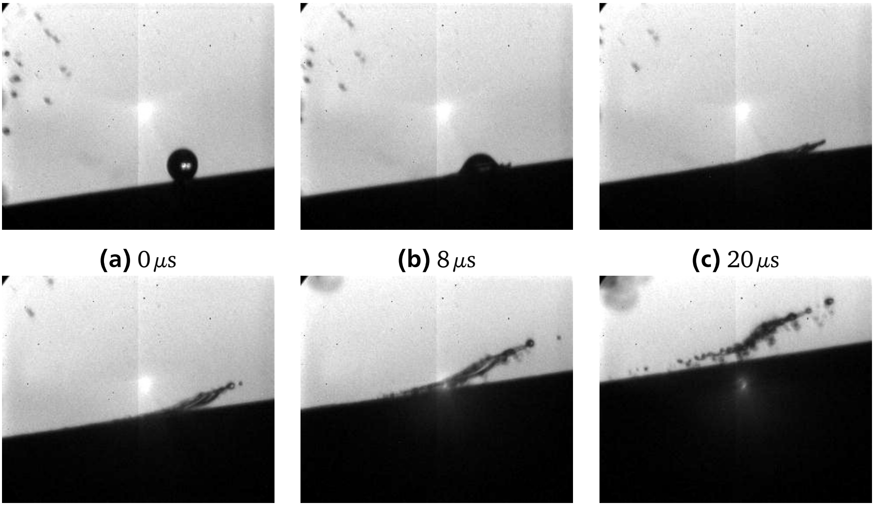

(a) $0\,\mu s$ **(b)** $8\,\mu s$ **(c)** $20\,\mu s$

(d) $36\,\mu s$ **(e)** $60\,\mu s$ **(f)** $84\,\mu s$

Figure A.24.: Drop diameter: $191\,\mu\text{m}$, impact velocity: 43m/s, impact angle: $13°$. Spatial resolution: $5.18\mu\text{m/pixel}$, field of view: $1.62\,\text{mm} \times 1.35\,\text{mm}$, frame rate: $500\,\text{kfps}$.

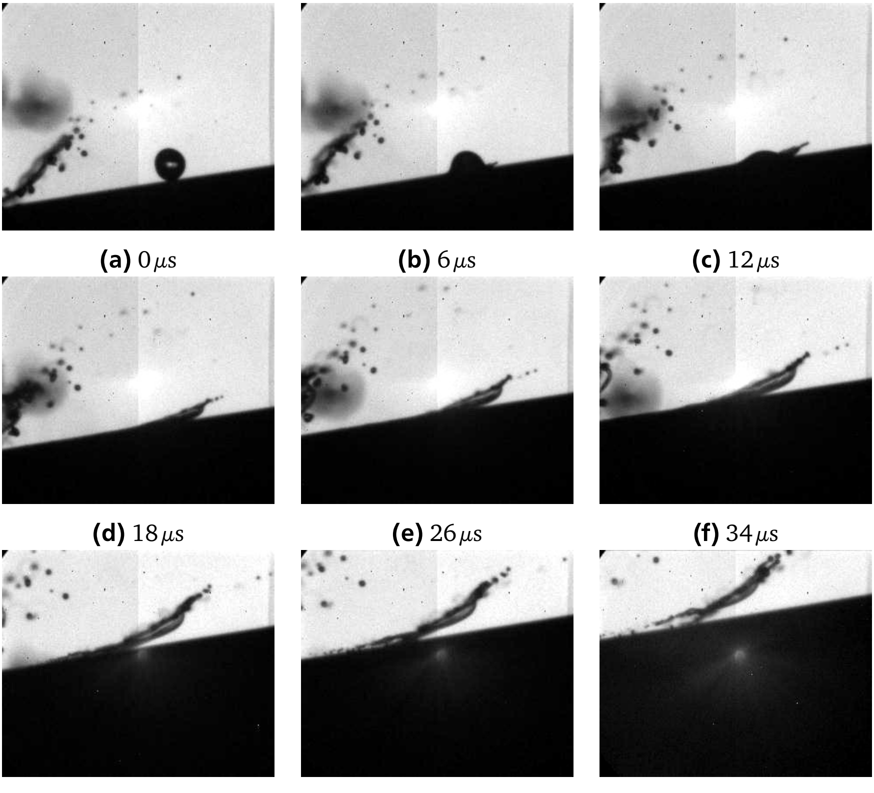

(a) $0\,\mu s$ **(b)** $6\,\mu s$ **(c)** $12\,\mu s$

(d) $18\,\mu s$ **(e)** $26\,\mu s$ **(f)** $34\,\mu s$

(g) $48\,\mu s$ **(h)** $54\,\mu s$ **(i)** $65\,\mu s$

Figure A.25.: Drop diameter: $191\,\mu\mathrm{m}$, impact velocity: $64\mathrm{m/s}$, impact angle: $11°$. Spatial resolution: $5.18\mu\mathrm{m/pixel}$, field of view: $1.62\,\mathrm{mm} \times 1.35\,\mathrm{mm}$, frame rate: $1\,\mathrm{Mfps}$.

A.7 5° target

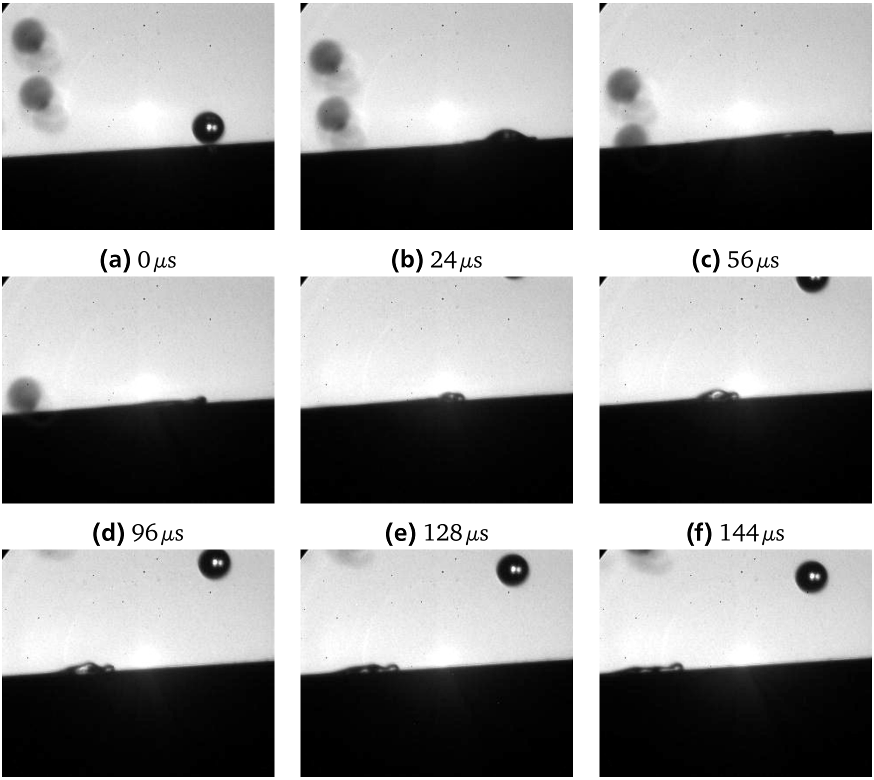

(a) 0 μs **(b)** 24 μs **(c)** 56 μs

(d) 96 μs **(e)** 128 μs **(f)** 144 μs

(g) 160 μs **(h)** 168 μs **(i)** 172 μs

Figure A.26.: Drop diameter: 188 μm, impact velocity: 14m/s, impact angle: 26°. Spatial resolution: 5.18μm/pixel, field of view: 1.62 mm × 1.35 mm, frame rate: 125 kfps.

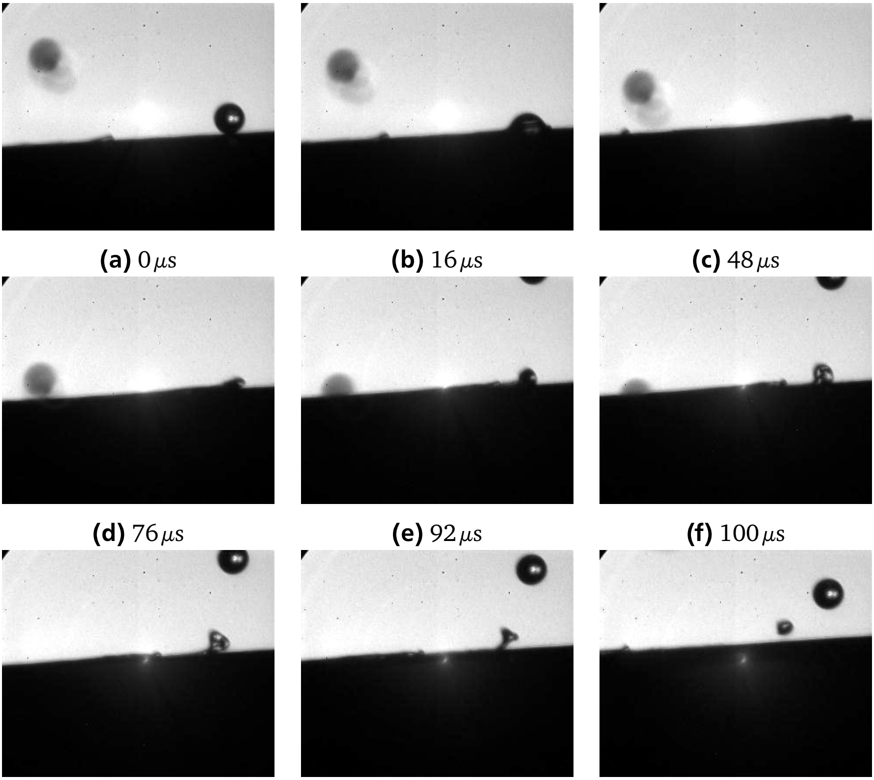

(a) $0\,\mu s$ (b) $16\,\mu s$ (c) $48\,\mu s$ (d) $76\,\mu s$ (e) $92\,\mu s$ (f) $100\,\mu s$ (g) $116\,\mu s$ (h) $132\,\mu s$ (i) $168\,\mu s$

Figure A.27.: Drop diameter: $183\,\mu\mathrm{m}$, impact velocity: $20\mathrm{m/s}$, impact angle: $17°$. Spatial resolution: $5.18\mu\mathrm{m/pixel}$, field of view: $1.62\,\mathrm{mm} \times 1.35\,\mathrm{mm}$, frame rate: $250\,\mathrm{kfps}$.

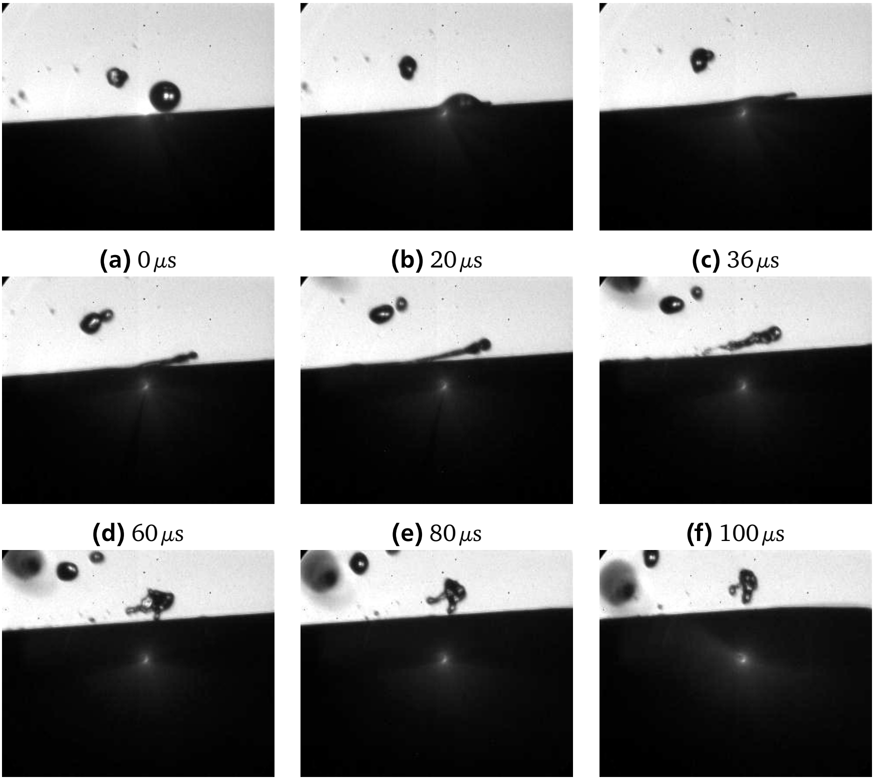

(a) $0\,\mu s$ **(b)** $20\,\mu s$ **(c)** $36\,\mu s$

(d) $60\,\mu s$ **(e)** $80\,\mu s$ **(f)** $100\,\mu s$

(g) $116\,\mu s$ **(h)** $132\,\mu s$ **(i)** $148\,\mu s$

Figure A.28.: Drop diameter: $188\,\mu\text{m}$, impact velocity: 26m/s, impact angle: $15°$. Spatial resolution: $5.18\mu\text{m/pixel}$, field of view: $1.62\,\text{mm} \times 1.35\,\text{mm}$, frame rate: $250\,\text{kfps}$.

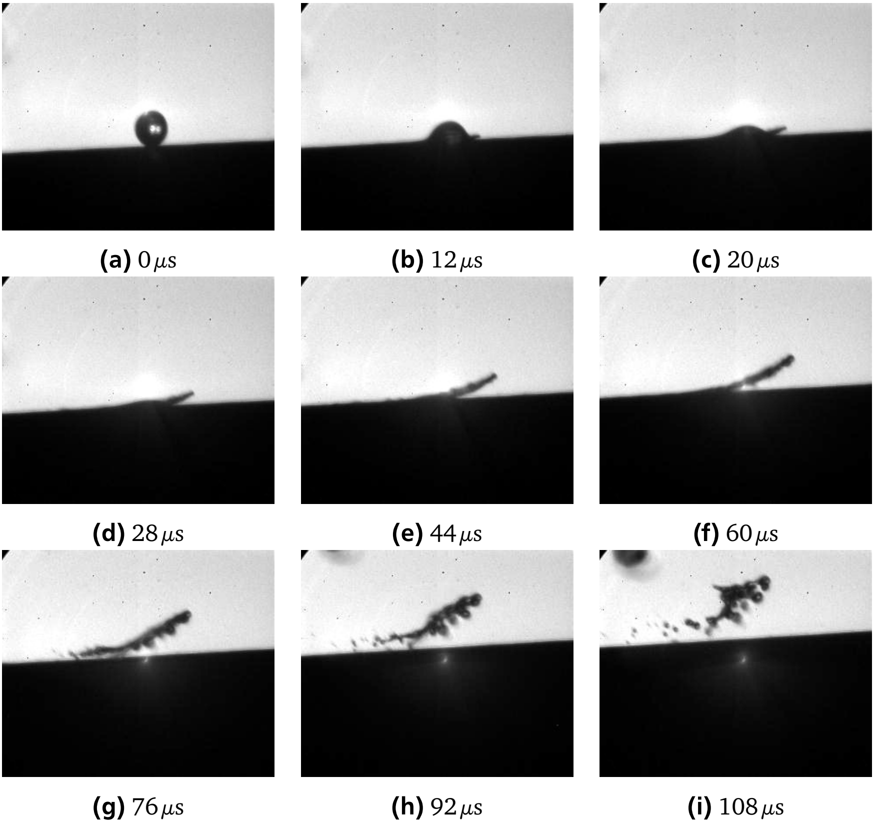

(a) 0 μs **(b)** 12 μs **(c)** 20 μs

(d) 28 μs **(e)** 44 μs **(f)** 60 μs

(g) 76 μs **(h)** 92 μs **(i)** 108 μs

Figure A.29.: Drop diameter: 203 μm, impact velocity: 43m/s, impact angle: 13°. Spatial resolution: 5.18μm/pixel, field of view: 1.62 mm × 1.35 mm, frame rate: 250 kfps.

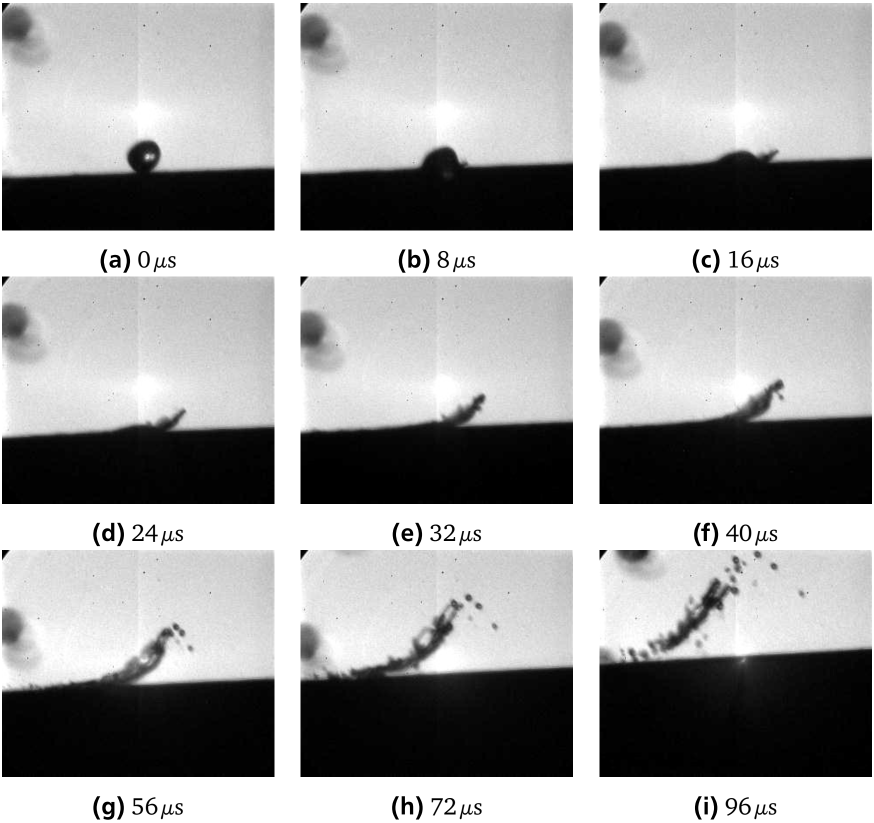

(a) $0\,\mu s$ **(b)** $8\,\mu s$ **(c)** $16\,\mu s$

(d) $24\,\mu s$ **(e)** $32\,\mu s$ **(f)** $40\,\mu s$

(g) $56\,\mu s$ **(h)** $72\,\mu s$ **(i)** $96\,\mu s$

Figure A.30.: Drop diameter: $201\,\mu\mathrm{m}$, impact velocity: $64\mathrm{m/s}$, impact angle: $10°$. Spatial resolution: $5.18\mu\mathrm{m/pixel}$, field of view: $1.62\,\mathrm{mm} \times 1.35\,\mathrm{mm}$, frame rate: $500\,\mathrm{kfps}$.

A.8 0° target, water, bigger drop

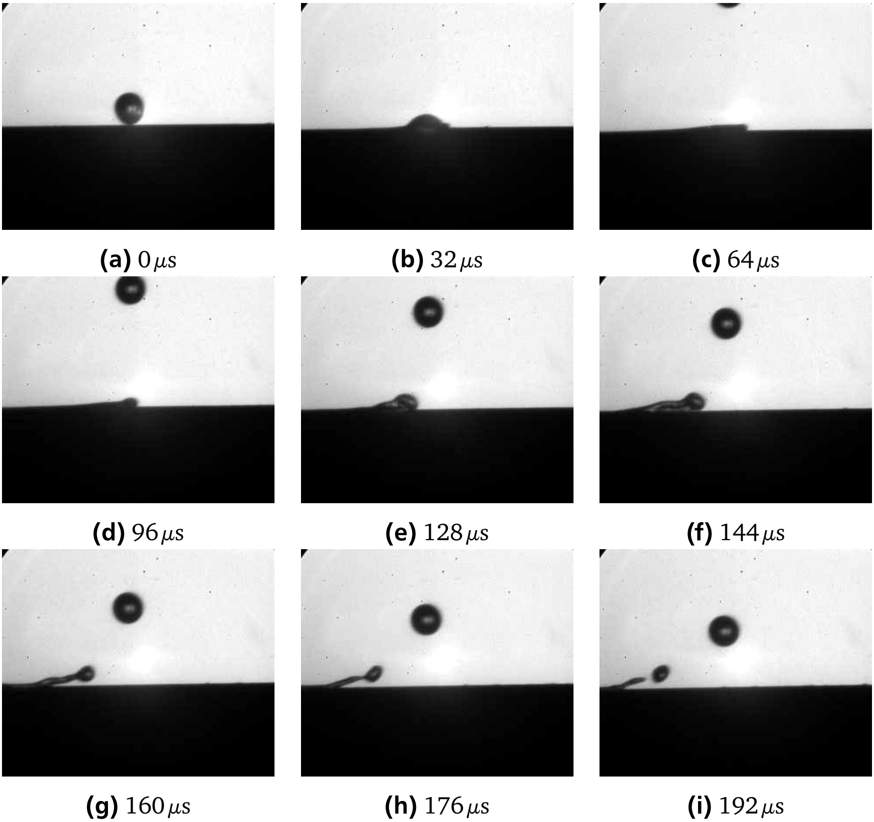

(a) $0\,\mu s$ (b) $32\,\mu s$ (c) $64\,\mu s$

(d) $96\,\mu s$ (e) $128\,\mu s$ (f) $144\,\mu s$

(g) $160\,\mu s$ (h) $176\,\mu s$ (i) $192\,\mu s$

Figure A.31.: Drop diameter: $181\,\mu\mathrm{m}$, impact velocity: $15\mathrm{m/s}$, impact angle: $16°$. Spatial resolution: $5.18\mu\mathrm{m/pixel}$, field of view: $1.62\,\mathrm{mm} \times 1.35\,\mathrm{mm}$, frame rate: $125\,\mathrm{kfps}$.

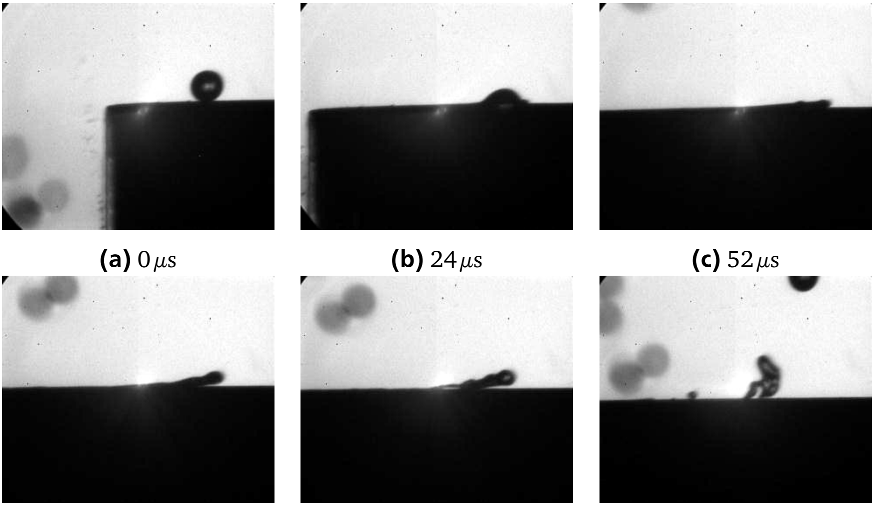

(a) 0 μs **(b)** 24 μs **(c)** 52 μs

(d) 92 μs **(e)** 108 μs **(f)** 176 μs

Figure A.32.: Drop diameter: 193 μm, impact velocity: 24m/s, impact angle: 12°. Spatial resolution: 5.18μm/pixel, field of view: 1.62 mm × 1.35 mm, frame rate: 250 kfps.

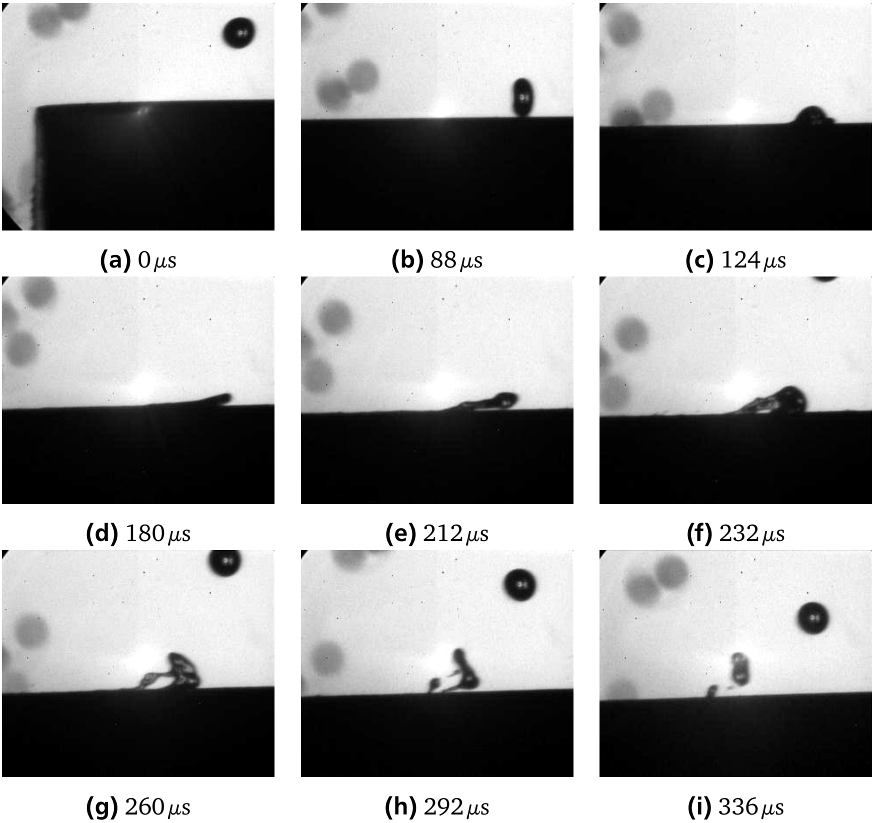

(a) $0\,\mu s$ **(b)** $88\,\mu s$ **(c)** $124\,\mu s$

(d) $180\,\mu s$ **(e)** $212\,\mu s$ **(f)** $232\,\mu s$

(g) $260\,\mu s$ **(h)** $292\,\mu s$ **(i)** $336\,\mu s$

Figure A.33.: Drop diameter: $188\,\mu\mathrm{m}$, impact velocity: $32\mathrm{m/s}$, impact angle: $8°$. Spatial resolution: $5.18\mu\mathrm{m/pixel}$, field of view: $1.62\,\mathrm{mm} \times 1.35\,\mathrm{mm}$, frame rate: $250\,\mathrm{kfps}$.

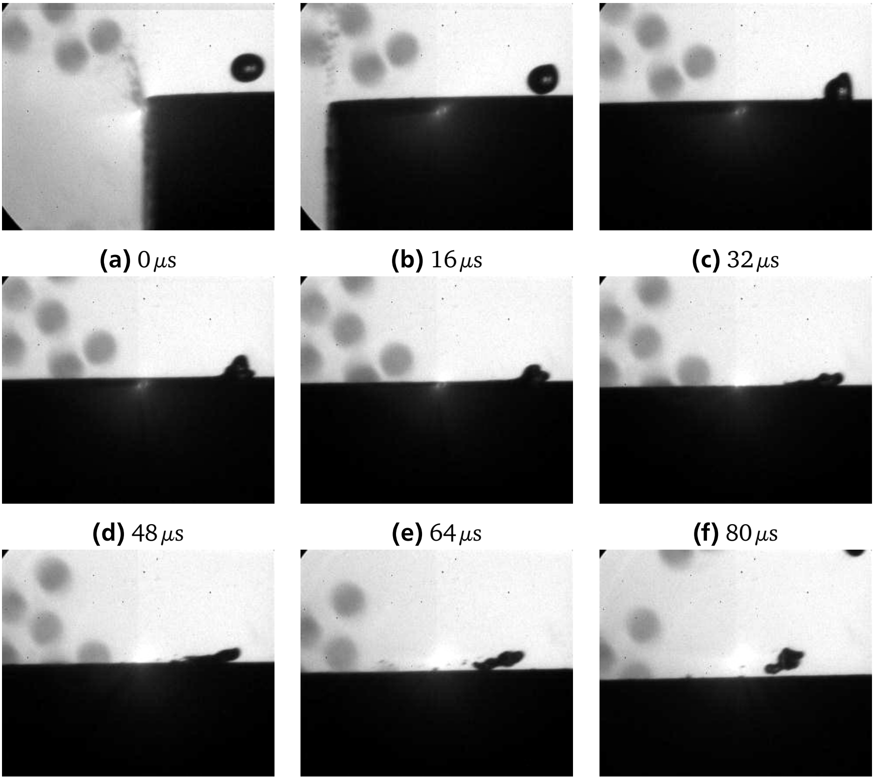

(a) $0\,\mu s$ **(b)** $16\,\mu s$ **(c)** $32\,\mu s$

(d) $48\,\mu s$ **(e)** $64\,\mu s$ **(f)** $80\,\mu s$

(g) $96\,\mu s$ **(h)** $128\,\mu s$ **(i)** $160\,\mu s$

Figure A.34.: Drop diameter: $191\,\mu\mathrm{m}$, impact velocity: $43\mathrm{m/s}$, impact angle: $5°$. Spatial resolution: $5.18\mu\mathrm{m/pixel}$, field of view: $1.62\,\mathrm{mm} \times 1.35\,\mathrm{mm}$, frame rate: $250\,\mathrm{kfps}$.

A.9 0° target, water, smaller drop

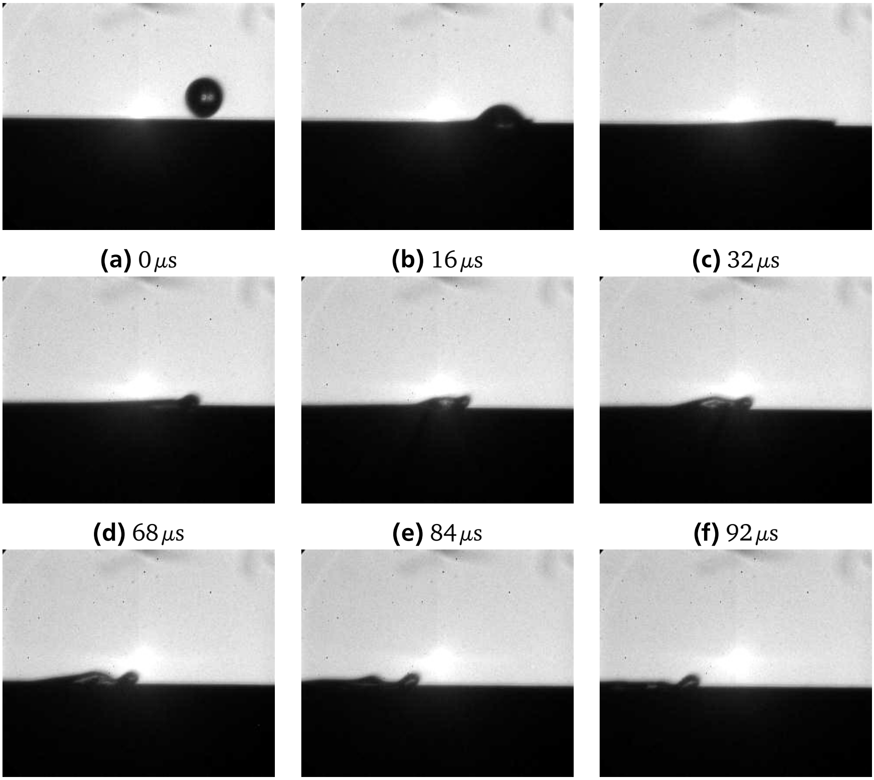

(a) $0\,\mu s$ **(b)** $16\,\mu s$ **(c)** $32\,\mu s$

(d) $68\,\mu s$ **(e)** $84\,\mu s$ **(f)** $92\,\mu s$

(g) $100\,\mu s$ **(h)** $108\,\mu s$ **(i)** $116\,\mu s$

Figure A.35.: Drop diameter: $136\,\mu\mathrm{m}$, impact velocity: $16\mathrm{m/s}$, impact angle: 23°. Spatial resolution: $3.07\mu\mathrm{m/pixel}$, field of view: $0.96\,\mathrm{mm} \times 0.80\,\mathrm{mm}$, frame rate: $250\,\mathrm{kfps}$.

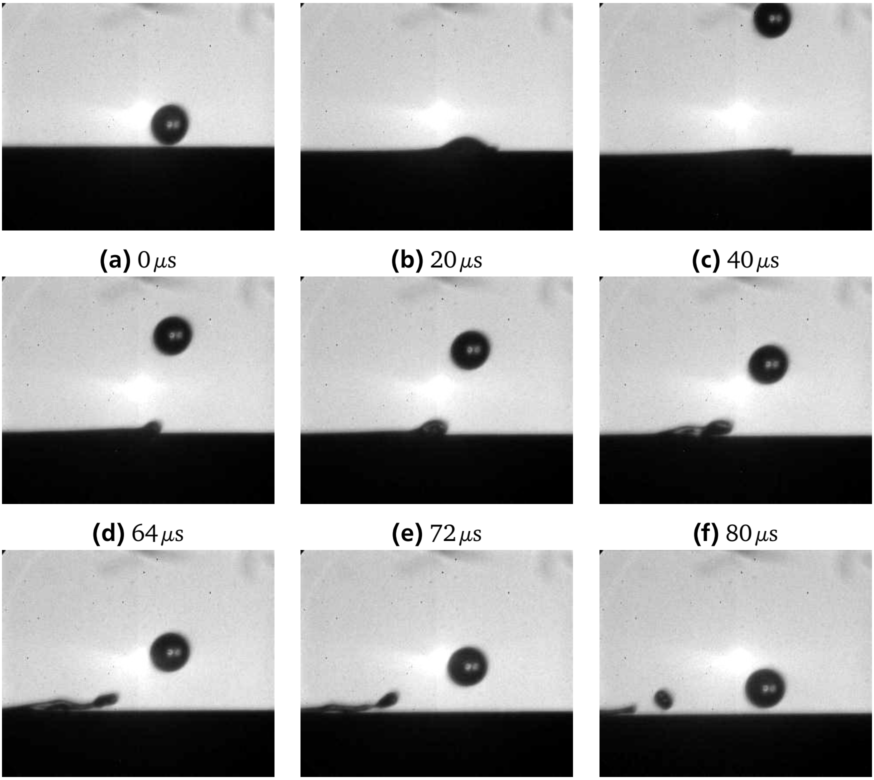

(a) 0μs **(b)** 20μs **(c)** 40μs

(d) 64μs **(e)** 72μs **(f)** 80μs

(g) 88μs **(h)** 96μs **(i)** 108μs

Figure A.36.: Drop diameter: $133\,\mu\mathrm{m}$, impact velocity: $22\mathrm{m/s}$, impact angle: $16°$. Spatial resolution: $3.07\mu\mathrm{m/pixel}$, field of view: $0.96\,\mathrm{mm} \times 0.80\,\mathrm{mm}$, frame rate: $250\,\mathrm{kfps}$.

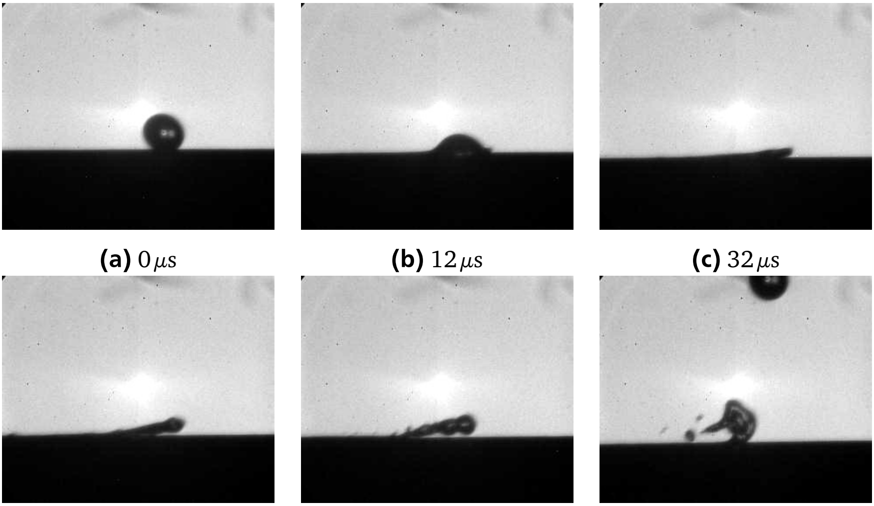

(a) $0\,\mu s$ **(b)** $12\,\mu s$ **(c)** $32\,\mu s$

(d) $52\,\mu s$ **(e)** $60\,\mu s$ **(f)** $84\,\mu s$

Figure A.37.: Drop diameter: $135\,\mu m$, impact velocity: $33 m/s$, impact angle: $12°$. Spatial resolution: $3.07 \mu m/pixel$, field of view: $0.96\,mm \times 0.80\,mm$, frame rate: $250\,kfps$.

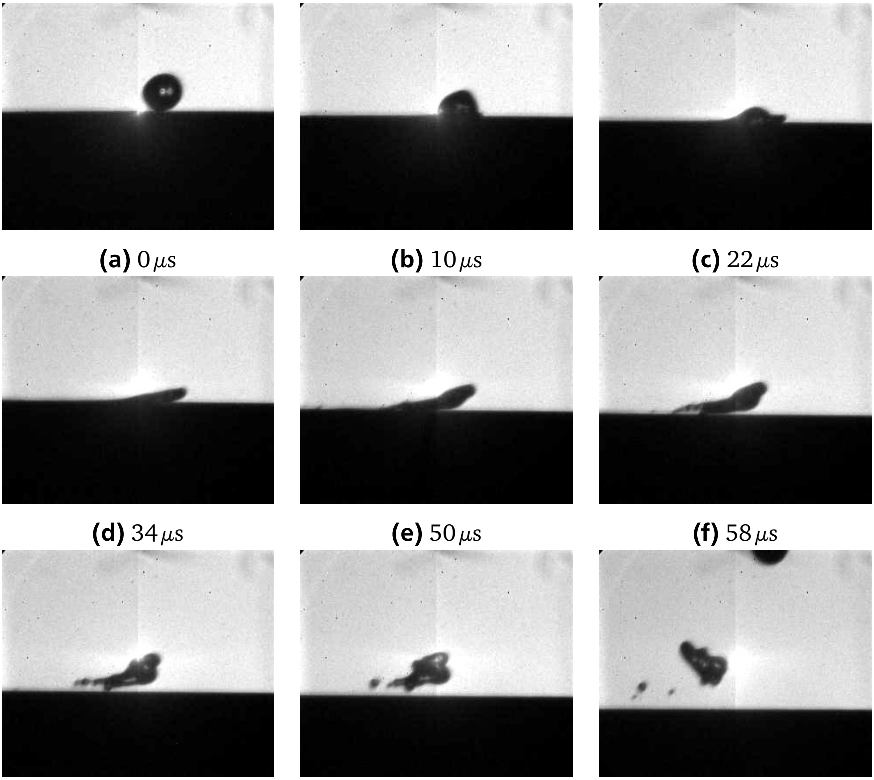

(a) $0\,\mu s$ **(b)** $10\,\mu s$ **(c)** $22\,\mu s$

(d) $34\,\mu s$ **(e)** $50\,\mu s$ **(f)** $58\,\mu s$

(g) $66\,\mu s$ **(h)** $74\,\mu s$ **(i)** $102\,\mu s$

Figure A.38.: Drop diameter: $134\,\mu\mathrm{m}$, impact velocity: $43\mathrm{m/s}$, impact angle: $9°$. Spatial resolution: $3.07\mu\mathrm{m/pixel}$, field of view: $0.96\,\mathrm{mm} \times 0.80\,\mathrm{mm}$, frame rate: $500\,\mathrm{kfps}$.

A.10 0° target, 80% methanol

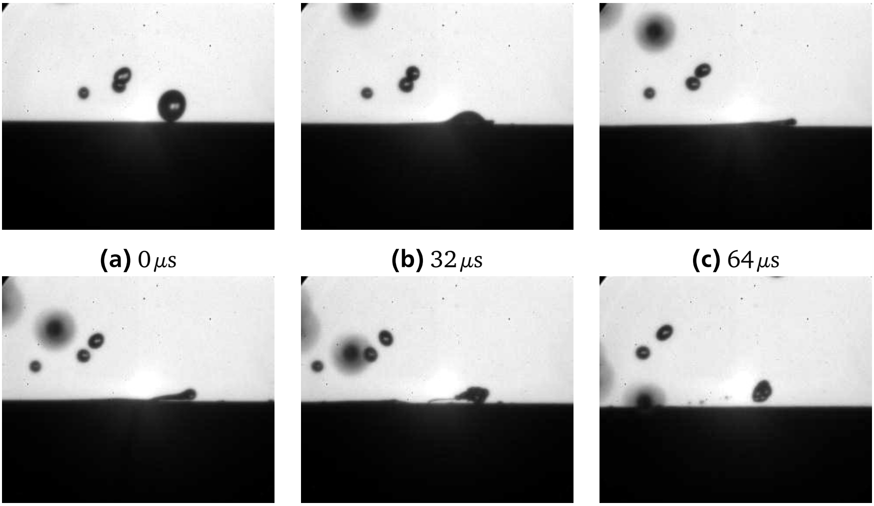

(a) 0 μs **(b)** 32 μs **(c)** 64 μs

(d) 96 μs **(e)** 128 μs **(f)** 192 μs

Figure A.39.: Drop diameter: 177 μm, impact velocity: 13m/s, impact angle: 19°. Spatial resolution: 5.18μm/pixel, field of view: 1.62 mm × 1.35 mm, frame rate: 125 kfps.

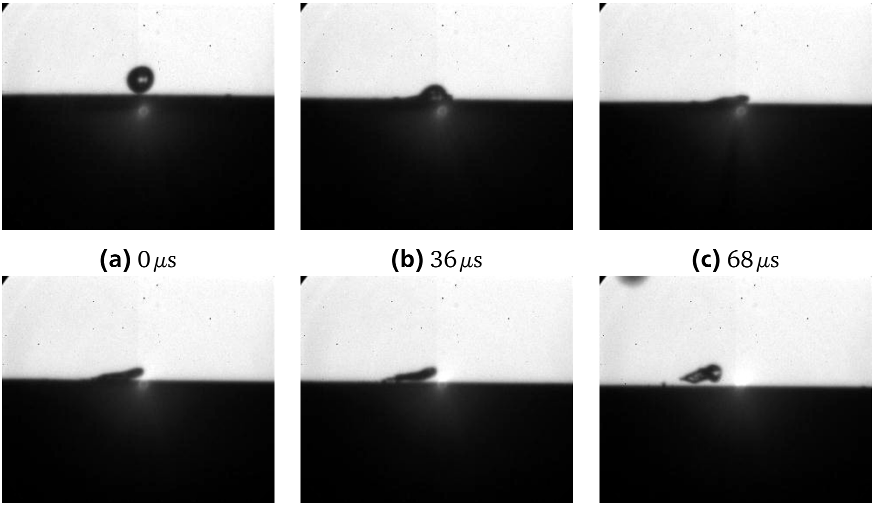

(a) $0\,\mu s$ **(b)** $36\,\mu s$ **(c)** $68\,\mu s$

(d) $100\,\mu s$ **(e)** $116\,\mu s$ **(f)** $148\,\mu s$

Figure A.40.: Drop diameter: $162\mu\text{m}$, impact velocity: 21m/s, impact angle: 9°. Spatial resolution: $5.18\mu\text{m/pixel}$, field of view: $1.62\,\text{mm} \times 1.35\,\text{mm}$, frame rate: $250\,\text{kfps}$.

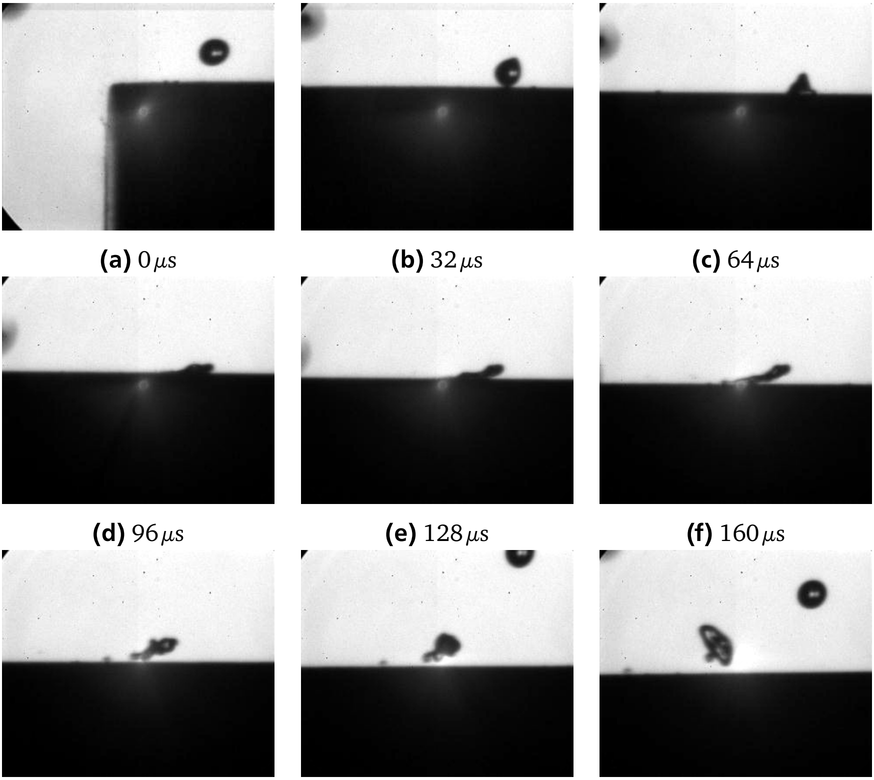

(a) 0 μs **(b)** 32 μs **(c)** 64 μs

(d) 96 μs **(e)** 128 μs **(f)** 160 μs

(g) 192 μs **(h)** 224 μs **(i)** 288 μs

Figure A.41.: Drop diameter: $165\,\mu\mathrm{m}$, impact velocity: $32\mathrm{m/s}$, impact angle: $7°$. Spatial resolution: $5.18\mu\mathrm{m/pixel}$, field of view: $1.62\,\mathrm{mm} \times 1.35\,\mathrm{mm}$, frame rate: $250\,\mathrm{kfps}$.

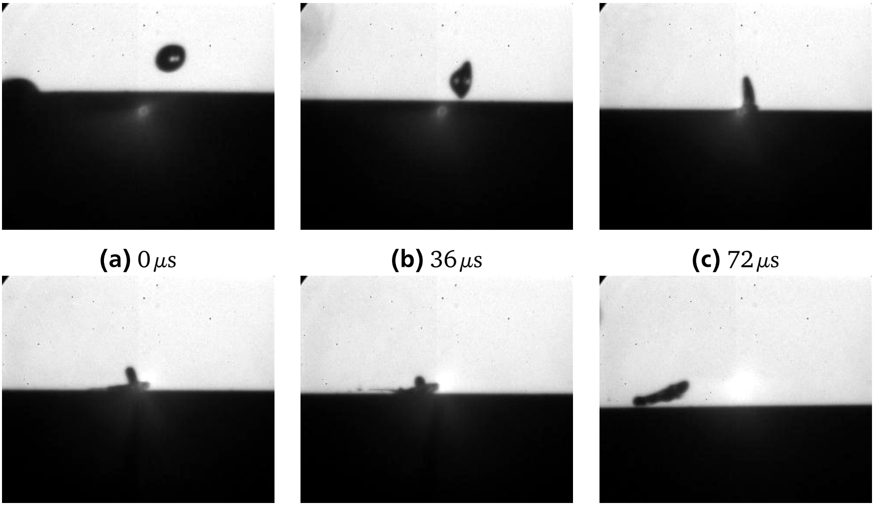

(a) $0\,\mu s$ **(b)** $36\,\mu s$ **(c)** $72\,\mu s$

(d) $104\,\mu s$ **(e)** $120\,\mu s$ **(f)** $200\,\mu s$

Figure A.42.: Drop diameter: $185\,\mu\mathrm{m}$, impact velocity: $42\mathrm{m/s}$, impact angle: $5°$. Spatial resolution: $5.18\mu\mathrm{m/pixel}$, field of view: $1.62\,\mathrm{mm} \times 1.35\,\mathrm{mm}$, frame rate: $250\,\mathrm{kfps}$.

B Dynamic Spreading Radius

The dynamic spreading radius of the high-speed impact of single drops on dry surfaces are shown in this appendix. The graphs are clustered by the target angle.

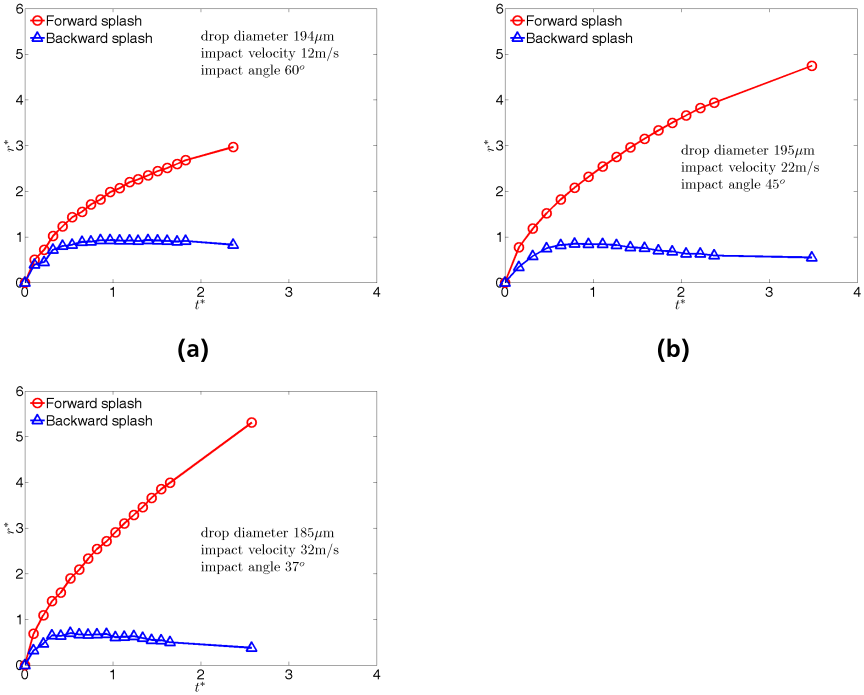

(a)

(b)

(c)

Figure B.1.: 30° target. Dimensionless spreading radius $r^* = r/d_0$, where r is the dynamic spreading radius, and d_0 is the diameter of the impinging drop.

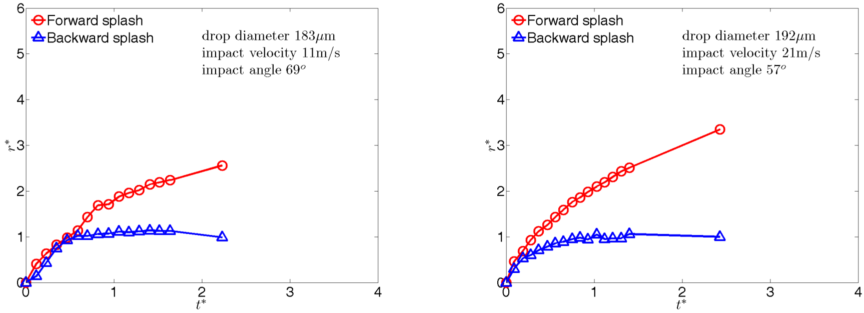

(a) 0 μs **(b)** 8 μs

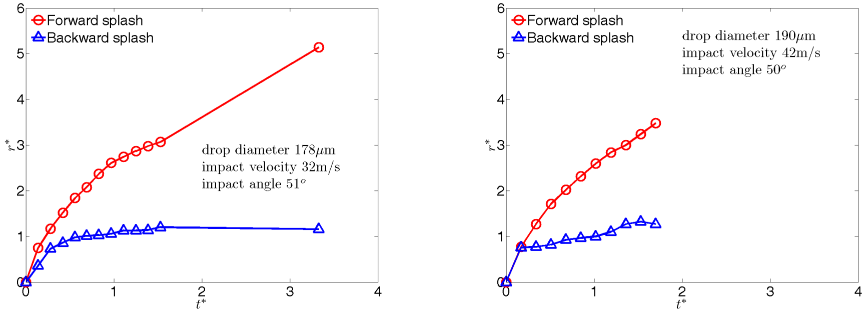

(c) 16 μs **(d)** 24 μs

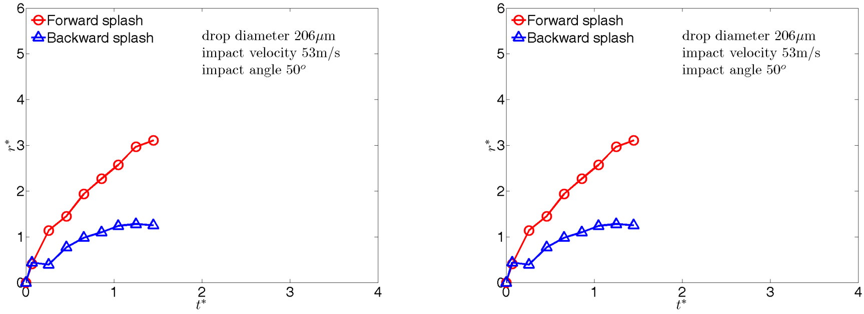

(e) 48 μs **(f)** 48 μs

Figure B.2.: 45° target. Dimensionless spreading radius $r^* = r/d_0$, where r is the dynamic spreading radius, and d_0 is the diameter of the impinging drop.

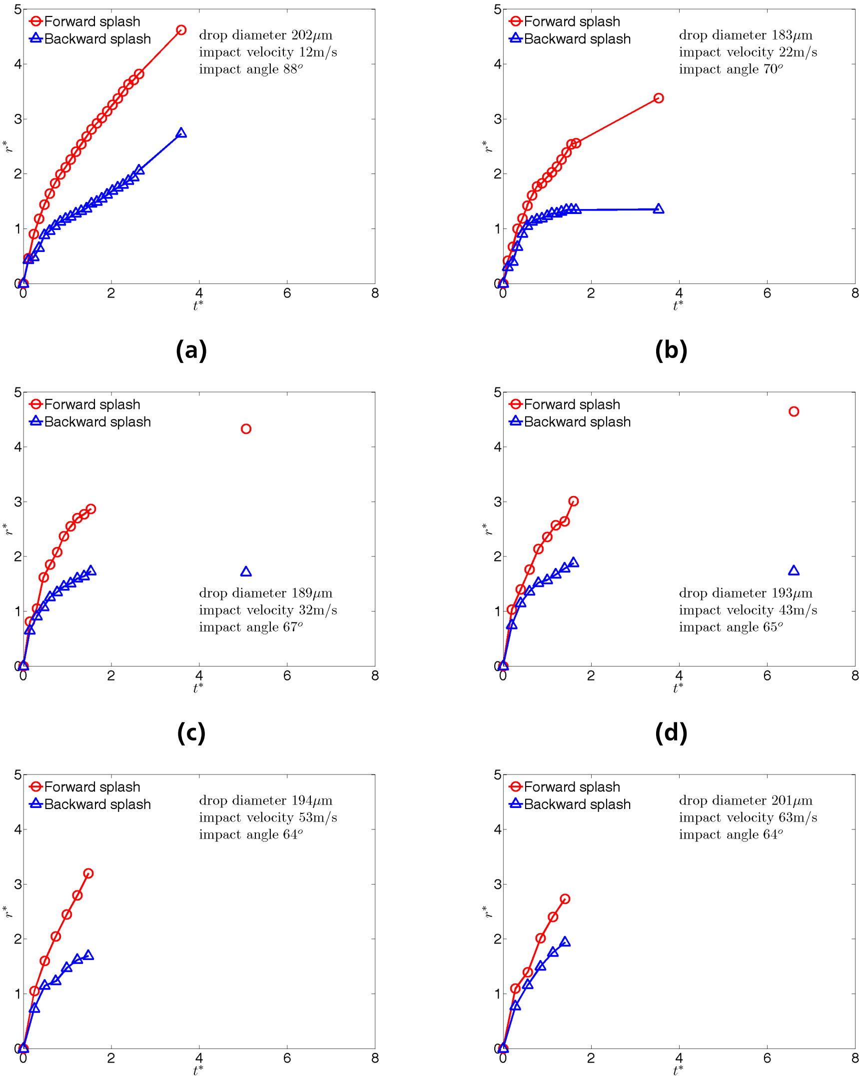

(a) (b)

(c) (d)

(e) (f)

Figure B.3.: 60° target. Dimensionless spreading radius $r^* = r/d_0$, where r is the dynamic spreading radius, and d_0 is the diameter of the impinging drop.

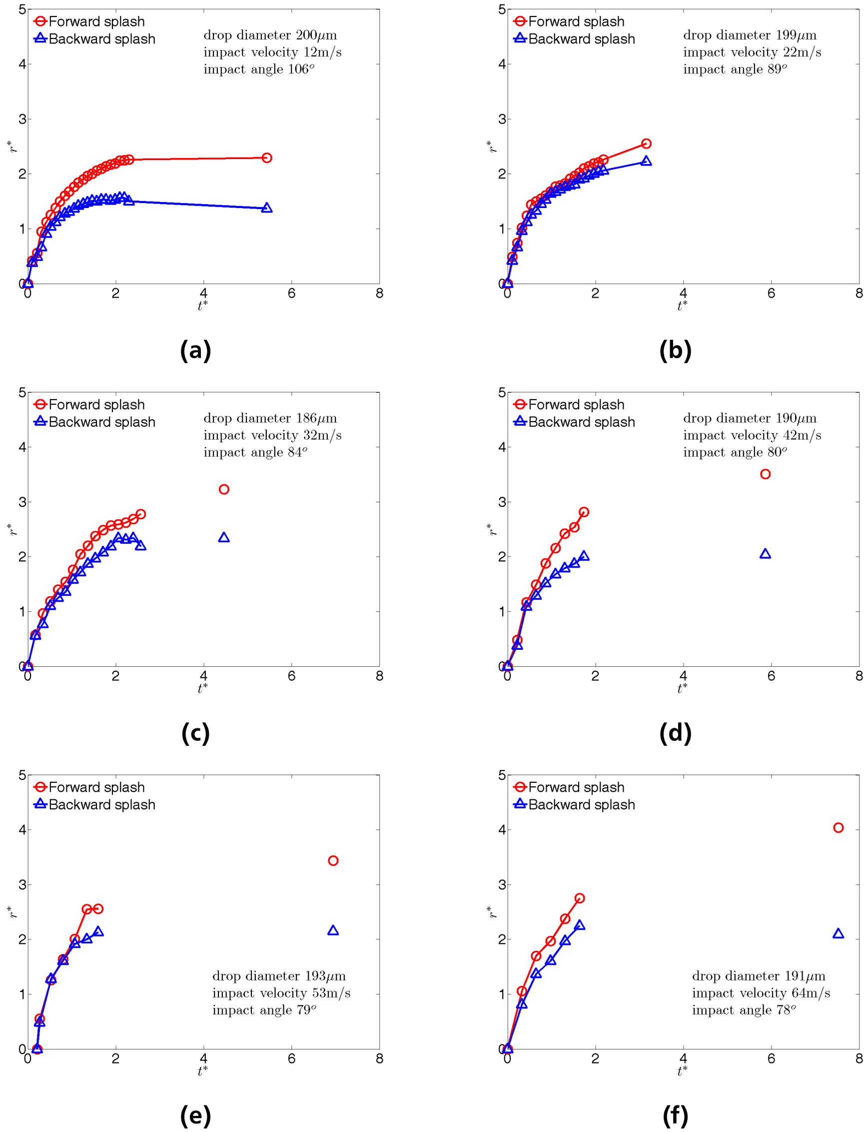

Figure B.4.: 75° target. Dimensionless spreading radius $r^* = r/d_0$, where r is the dynamic spreading radius, and d_0 is the diameter of the impinging drop.

C Supercooled Drop Impact on Super Hydrophobic Surfaces

High-speed shadowgraph imaging of supercooled drop impact on SHS at temperatures below 0 °C are illustrated by sequential images in this appendix.

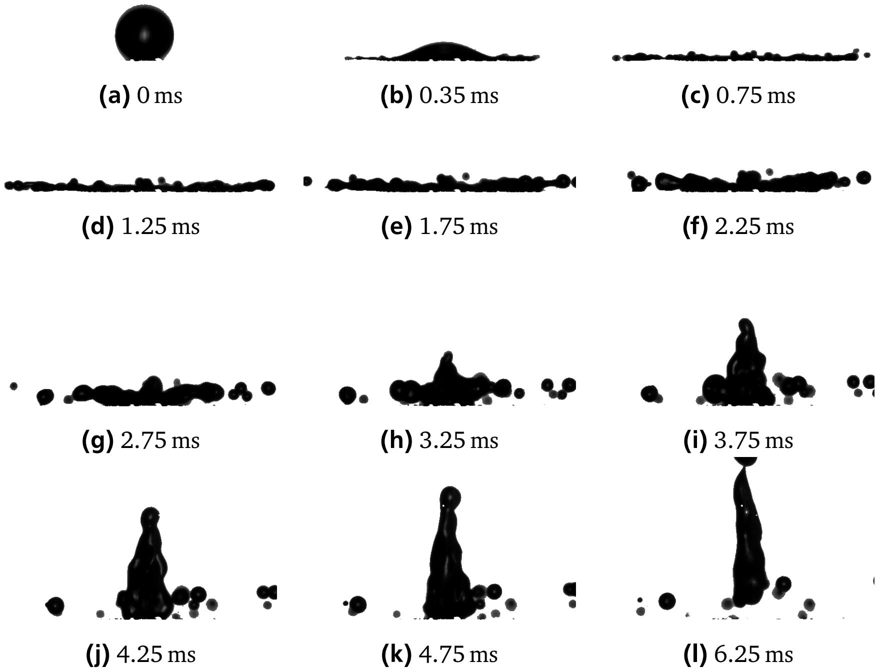

(a) 0 ms **(b)** 0.35 ms **(c)** 0.75 ms

(d) 1.25 ms **(e)** 1.75 ms **(f)** 2.25 ms

(g) 2.75 ms **(h)** 3.25 ms **(i)** 3.75 ms

(j) 4.25 ms **(k)** 4.75 ms **(l)** 6.25 ms

Figure C.1.: Supercooled drop impact on the SHS at −2 °C. Drop diameter: 1.586 mm, impact velocity: 3.52m/s.

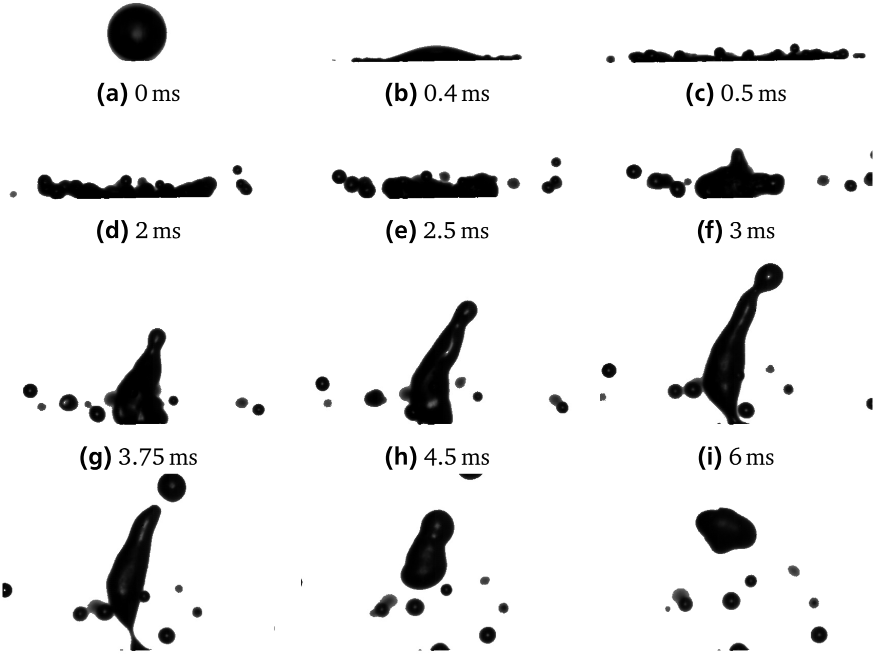

(a) 0 ms **(b)** 0.4 ms **(c)** 0.5 ms

(d) 2 ms **(e)** 2.5 ms **(f)** 3 ms

(g) 3.75 ms **(h)** 4.5 ms **(i)** 6 ms

(j) 6.8 ms **(k)** 7.8 ms **(l)** 9.25 ms

Figure C.2.: Supercooled drop impact on the SHS at −4 °C. Drop diameter: 1.50 mm, impact velocity: 3.44m/s.

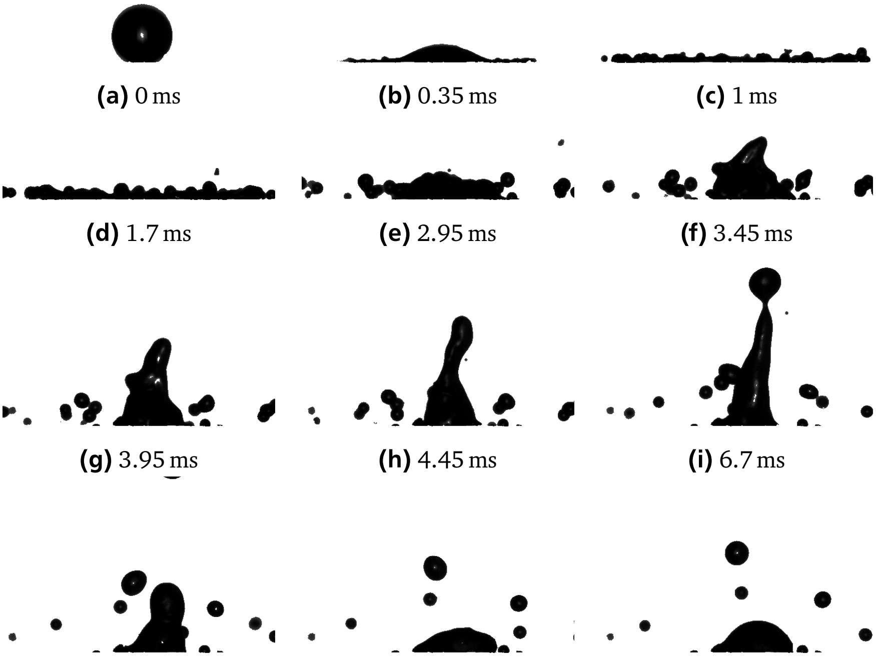

(a) 0 ms **(b)** 0.35 ms **(c)** 1 ms

(d) 1.7 ms **(e)** 2.95 ms **(f)** 3.45 ms

(g) 3.95 ms **(h)** 4.45 ms **(i)** 6.7 ms

(j) 9.45 ms **(k)** 11.8 ms **(l)** 14.7 ms

Figure C.3.: Supercooled drop impact on the SHS at $-10\,^{\circ}\mathrm{C}$. Drop diameter: $1.55\,\mathrm{mm}$, impact velocity: $3.40\mathrm{m/s}$.

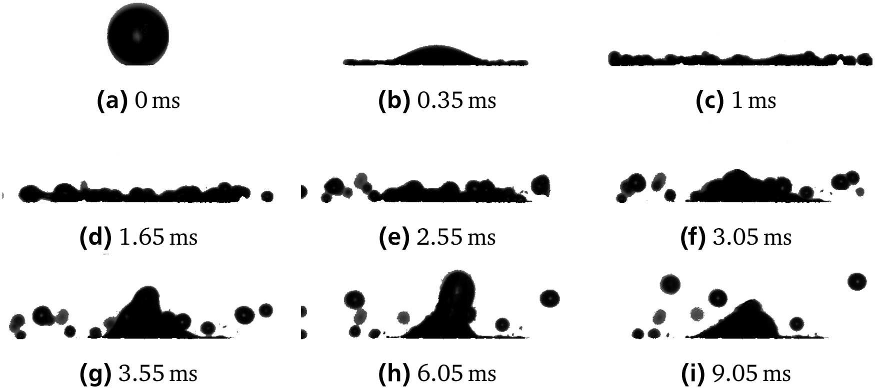
(a) 0 ms (b) 0.35 ms (c) 1 ms

(d) 1.65 ms (e) 2.55 ms (f) 3.05 ms

(g) 3.55 ms (h) 6.05 ms (i) 9.05 ms

Figure C.4.: Supercooled drop impact on the SHS at $-20\,^{\circ}\mathrm{C}$. Drop diameter: $1.47\,\mathrm{mm}$, impact velocity: $3.41\mathrm{m/s}$.

List of Figures

List of Tables

Bibliography

[1] *Fed. Aviat. Regul. Parts 25, 27, 29. 1914. Airworthiness Standards: Transportation Category Airplanes, Normal Category Rotorcraft, and Transport Category Rotorcraft, Appendix C. Washington, DC: Dep. Transp. Fed. Aviat. Admin.*, 1914.

[2] *API RP 2003: Protection Against Ignitions Arising out of Static, Lightning, and Stray Currents*, 2008.

[3] AIRY, G. B.: *On the Diffraction of an Object-glass with Circular Aperture*. Transactions of the Cambridge Philosophical Society, 5:283–291, 1835.

[4] ALEXIADES, VASILIOS and ALAN D. SOLOMON: *Mathematical Modelling of Melting and Freezing Processes*. Hemisphere Publishing Corporation, Washington DC, 1993.

[5] AMENDOLA, A., G. MINGIONE, D. CAILHOL and T. HAUF: *EURICE - An European effort for the improvement of in-flight aircraft icing safety*. AIAA-98-0092, 1998.

[6] ANTONINI, CARLO, ALIDAD AMIRFAZLI and MARCO MARENGO: *Drop impact and wettability: From hydrophilic to superhydrophobic surfaces*. Physics of Fluids, 24(102104), 2012.

[7] ARCHER, DONALD G. and RICHARD W. CARTER: *Thermodynamic Properties of the NaCl + H2O System. 4. Heat Capacities of H2O and NaCl(aq) in Cold-Stable and Supercooled States*. The Journal of Physical Chemistry B, 104(35), 2000.

[8] ASCHER, CHRIS, SEBSTIAN GATZKA, CARINA KLOSTERMANN and PATRICK STEGMANN: *Development of a test section for the investigation of droplet icing*. ADP Report, TU Darmstadt, 2011. Supervisor: Hai Li.

[9] BAI, C. and A. D. GOSMAN: *Development of Methodology for Spray Impingement Simulation*. In *SAE, TR 950283*, 1995.

[10] BAKSHI, SHAMIT, ILIA V. ROISMAN and CAM TROPEA: *Investigations on the impact of a drop onto a small spherical target*. Physics of Fluids, 19(032012), 2007.

[11] BARTELLA, OLIVER: *Splash Phänomen beim Tropfenaufprall auf trockene Oberflächen: Auswertungen von Hochgeschwindigkeitsaufnahmen*. Bachelor thesis, TU Darmstadt, 2013. Supervisor: Hai Li.

[12] BAUERECKER, SIGURD, PETER ULBIG, VICTORIA BUCH, LUBOŠ VRBKA and PAVEL JUNGWIRTH: *Monitoring Ice Nucleation in Pure and Salty Water via High-Speed*

Imaging and Computer Simulations. The Journal of Physical Chemistry C, 112(20), 2008.

[13] Berglund, R. N. and B. Y. H. Liu: *Generation of monodisperse aerosol standards,*. Environ. Sci. Technol., 7:147, 1973.

[14] Bernstein, Ben C.: *Evaluation of NCAR Icing/SLD Forecasts, Tools and Techniques Used During the 1998 NASA SLD Flight Season*. NASA/CR-2001-210954, 2001.

[15] Bernstein, Ben C., Frank McDonough and Randy Bullock: *An Inferred Climatology of Supercooled Large Droplet Icing Conditions for North America*. AIAA 2003-563, 2003.

[16] Bernstein, Ben C., Thomas P. Ratvasky, Dean R. Miller and Frank McDonough: *Freezing Rain as an In-Flight Icing Hazard*. NASA/TM-2000-210058, 2000.

[17] Bidone, G.: *Experiences sur la forme et sur la direction des veines et des courants d'eau lances par diverses ouvertures*, pages 1–136. Imprimerie Royale, Turin, 1829.

[18] Bird, James C, Scott S H Tsai and Howard A Stone: *Inclined to splash: triggering and inhibiting a splash with tangential velocity*. New Journal of Physics, 11(063017), 2009.

[19] Bond, Thomas H., Dean R. Miller and Mark G. Potapczuk: *Overview of SLD engineering tools development*. AIAA 2003-386, 2003.

[20] BOULANGé-PETERMANN, LAURENCE, CHRISTELLE GABET and BERNARD BAROUX: *Relation between the cleanability of bare or polysiloxane-coated stainless steels and their water contact angle hysteresis*. Journal of Adhesion Science and Technology, 20(13):1463–1474, 2006.

[21] Boussinesq, J., 1877.

[22] Brenn, G. and U. Lackermeier: *Drop formation from a vibrating orifice generator driven by modulated electrical signals*. Physics of Fluids, 9(12):3658–3669, 1997.

[23] Broeren, Andy P., Christopher M. LaMarre, Michael B. Bragg and Sam Lee: *Characteristics of SLD Ice Accretions on Airfoils and Their Aerodynamic Effect*. AIAA 2005-75, 2005.

[24] Brüggeller, P. and E Mayer: *Complete vitrification in pure liquid water and dilute aqueous solutions*. Nature, 288:569–571, 1980.

[25] Buchenhorst, Christoph, Jan Breitenbach, Samim Doost and Hannah Kittel: *Experimentelle Untersuchung vom Aufprall unterkühlter Tropfen*. ADP report, TU Darmstadt, 2012. Supervisor: Hai Li.

[26] Carslaw, H. S. and J. C. Jaeger: *Conduction of Heat in Solids*. Clarendon Press, Oxford, U.K., Second edition, 1959.

[27] Cebeci, Tuncer and Fassi Kafyeke: *AIRCRAFT ICING*. Annual Review of Fluid Mechanics, 35:11–21, 2003.

[28] Chen, R. H. and H. W. Wang: *Effects of tangential speed on low-normal-speed liquid drop impact on a non-wettable solid surface*. Experiments in Fluids, 39:754–760, 2005.

[29] Cheng, S. and S. Chandra: *A pneumatic droplet-on-demand generator*. Experiments in Fluids, 34:755–762, 2003.

[30] Cober, Stewart G. and George A. Isaac: *Estimating Maximum Aircraft Icing Environments Using a Large Data Base of In-Situ Observations*. AIAA 2006-266, 2006.

[31] Cober, Stewart G., George A. Isaac and Thomas P. Ratvasky: *Assessment of Aircraft Icing Conditions Observed During AIRS*. AIAA 2002-0674, 2002.

[32] Cober, Stewart G., George A. Isaac, Anil D. Shah and Richard Jeck: *Defining Characteristic Cloud Drop Spectra from In-Situ Measurements*. AIAA 2003-0561, 2003.

[33] Cober, Stewart G., George A. Isaac and J. Walter Strapp: *Characterizations of Aircraft Icing Environments that Include Supercooled Large drops*. Journal of Applied Meteorology, 40:1984–2002, 2001.

[34] Cossali, G. E., A. Coghe and M. Marengo: *The impact of a single drop on a wetted solid surface*. Experiments in Fluids, 22:463–472, 1997.

[35] Czichos, Horst: *Hütte: Die Grundlagen der Ingenieurwissenschaften*, chapter E Technische Mechanik, pages E148–E149.

[36] Dabora, E. K.: *Production of monodisperse sprays*. THE REVIEW OF SCIENTIFIC INSTRUMENTS, 38:502, 1967.

[37] Dhiman, Rajeev and Sanjeev Chandra: *Rupture of thin films formed during droplet impact*. Proceedings of the Royal Society A, 466:1229–1245, 2010.

[38] Downing, Harry D. and Dudley Williams: *Optical constants of water in the infrared*. JOURNAL OF GEOPHYSICAL RESEARCH, 80(12):1656–1975, 1975.

[39] Eggers, J. and E. Villermaux: *Physics of liquid jets*. REPORTS ON PROGRESS IN PHYSICS, 71(036601), 2008.

[40] Eichhorn, Helge: *Image Post-Processing of the Impact of Super-Cooled Drops*. Bachelor thesis, TU Darmstadt, 2011. Supervisor: Hai Li.

[41] Fahrenheit, D. G.: *german translation in: Ostwald's Klassiker der exakten Wissenschaften, 57, Abhandlungen über Thermometrie von Fahrenheit, R´eaumur, Celsius (1724, 1730-1733, 1742)*. Philosophical Transactions of the Royal Society London, 1724. A. J. Von Oettigen (Ed.), Engelmann, Leipzig (1894).

[42] GENT, R. W., N. P. DART and J. T. CANSDALE: *Aircraft icing*. Philosophical Transactions of the Royal Society London, 358:2873–2911, 2000.

[43] GOGHARI, A. AMIRZADEH and S. CHANDRA: *Producing droplets smaller than the nozzle diameter by using a pneumatic drop-on-demand droplet generator*. Experiments in Fluids, 44:105–114, 2008.

[44] GUICHET, CHRISTOPHER: *Further Design of Drop Deflection Device and Imaging of High Speed Drop Impact*. IREP report, TU Darmstadt, UC Bekerley, 2011. Supervisor: Hai Li.

[45] HALLETT, J.: *The Temperature Dependence of the Viscosity of Supercooled Water*. Proceedings of the Physical Society, 82, 1963.

[46] HALLETT, J.: *Experimental Studies of the Crystallization of Supercooled Water*. Jounal of the Atmospheric Sciences, 21:671–682, 1964.

[47] HARDALUPAS, Y., A.M.K.P. TAYLOR and J.H. WILKINS: *Experimental investigation of sub-millimetre droplet impingement on to spherical surfaces*. International Journal of Heat and Fluid Flow, 20:477–485, 1999.

[48] HARE, D. E. and C. M. SORENSEN: *The density of supercooled water. II. Bulk samples cooled to the homogeneous nucleation limit*. The Journal of Chemical Physics, 87(8), 1987.

[49] HAUF, T. and F. SCHRÖDER: *Aircraft icing research flights in embedded convection*. Meteorology and Atmospheric Physics, 91:247–265, 2006.

[50] HAUSSECKER, HORST: *Messung und Simulation von kleinskaligen Austauschvorgängen an der Ozeanoberfläche mittels Thermographie*. PhD thesis, Ruprecht - Karls - Universität Heidelberg, 1996.

[51] HEINBÜCHER, KATRIN: *Hochgeschwindigkeitsauf-nahme des Aufpralls unterkühlter Tropfen*. Bachelor thesis, TU Darmstadt, 2011. Supervisor: Hai Li.

[52] HOBBS, PETER V.: *Ice Physics*, chapter 7 Nucleation of Ice, pages 461–472. Oxford University Press, Great Britain, 1974.

[53] HOBBS, PETER V.: *Ice Physics*, chapter 9 Growth of Ice from the Liquid Phase, pages 615–619. Oxford University Press, Great Britain, 1974.

[54] HOLTEN, V., C. E. BERTRAND, M. A. ANISIMOV and J. V. SENGERS: *Thermodynamics of supercooled water*. The Journal of Chemical Physics, 136, 2012.

[55] HONSEK, RAIMUND and WAGDI G. HABASHI: *FENSAP-ICE Eulerian Modeling of Droplet Impingement in the SLD Regime of Aircraft Icing*. AIAA 2006-465, 2006.

[56] HONSEK, RAIMUND, WAGDI G. HABASHI and MARTIN S. AUBÉ: *Eulerian Modeling of In-Flight Icing Due to Supercooled Large Droplets*. Jounal of Aircraft, 45(4), 2008.

[57] INGENIEURE, VEREIN DEUTSCHER, VDI-GESELLSCHAFT VERFAHRENSTECHNIK and CHEMIEINGENIEURWESEN: *VDI-Wärmeatlas Auflage 9*, chapter Dba 2 Stoffwerte von Wasser. Springer, Heidelgerg, Germany, 2002.

[58] INGENIEURE, VEREIN DEUTSCHER, VDI-GESELLSCHAFT VERFAHRENSTECHNIK and CHEMIEINGENIEURWESEN: *VDI-Wärmeatlas Auflage 9*, chapter Ka 2 Stoffwerte von Wasser. Springer, Heidelgerg, Germany, 2002.

[59] INGENIEURE, VEREIN DEUTSCHER, VDI-GESELLSCHAFT VERFAHRENSTECHNIK and CHEMIEINGENIEURWESEN: *VDI-Wärmeatlas Auflage 9*, chapter Ec 11 Instationäre Wärmeleitung in ruhenden Körpern. Springer, Heidelgerg, Germany, 2002.

[60] ISAAC, G.A., S.G. COBER, A.V. KOROLEV, J.W. STRAPP, A. TREMBLAY and D.L. MARCOTTE: *Canadian Freezing Drizzle Experiment*. AIAA-99-0492, 1999.

[61] ISAAC, G.A., S.G. COBER, J.W. STRAPP, D. HUDAK, T.P. RATVASKY, D.L. MARCOTTE and F. FABRY: *Preliminary Results from the Alliance Icing Research Study (AIRS)*. AIAA 2001-0393, 2001.

[62] IVANTSOV, G.P. Dokl. Akad. Nauk SSSR 58, 567, 1947.

[63] JACOBS, SANDER J., JACCO M. HOSPERS and HARRY W.M. HOEIJMAKERS: *NUMERICAL SIMULATION OF ICE ACCRETION ON MULTIPLE-ELEMENT AIRFOIL SECTIONS*. In *26TH INTERNATIONAL CONGRESS OF THE AERONAUTICAL SCIENCES*, 2008.

[64] JUNG, STEFAN, MANISH K. TIWARI, N. VUONG DOAN and DIMOS POULIKAKOS: *Mechanism of supercooled droplet freezing on surfaces*. nature communications, 2012.

[65] KELVIN), SIR WILLIAM THOMSON (LORD: *On a self-acting apparatus for multiplying and maintaining electric charges, with applications to illustrate the voltaic theory*. Proceedings of the Royal Society of London, 16:67–72, 1867. Reprinted in: Philosophical Magazine, series 4, vol. 34, no. 231, pages 391-396,1867.

[66] KEPLER, J.: *The Six-Cornered Snowflake*. translated by C. Hardie, originally published as De Nive Sexangula, Godfrey Tamnpach, Frankfur am Main, 1611. Clarendon Press, Oxford, 1966.

[67] KIDAMBI, NARAYANAN: *Infrared Imaging of Drop Impact on Cold Surfaces*. IREP Report, TU Darmstadt, UC Berkeley, 2011. Supervisor: Hai Li.

[68] KL, PAN, CHENG KR, CHOU PC and WANG CH: *Collision dynamics of high-speed droplets upon layers of variable thickness*. Experiments in Fluids, 45:435–446, 2008.

[69] KOOP, THOMAS: *Homogeneous Ice Nucleation in Water and Aqueous Solutions*. Zeitschrift für Physikalische Chemie, 218:1231–1258, 2004.

[70] Korolev, Alexei V., George A. Isaac, J.Walter Strapp and Stewart G. Cober: *Observation of Drizzle at Temperatures below - 20°C.* AIAA-2002-0678, 2002.

[71] Kumar, Pradeep and H. Eugene Stanley: *Thermal Conductivity Minimum: A New Water Anomaly*. The Journal of Physical Chemistry B, 115:14269–14273, 2011.

[72] Langer, J. S.: *Instabilities and pattern formation in crystal growth*. Reviews of Morden Physics, 52(1), 1980.

[73] Langer, J.S.: *Dentrites, Viscous Fingers, and the Theory of Pattern Formation*. Science, 243:1150–1156, 1989.

[74] Langer, J.S., R.F. Sekerka and T. Fujioka: *Evidence for a Universal Law of Dentritic Growth Rates*. Jounal of Crystal Growth, 44:414–418, 1978.

[75] Lee, Eric R.: *Microdrop generation,* chapter 4 Electric Charging of Microdrops. CRC PRESS LLC, Boca Raton, U.S.A., 2003.

[76] LINDBLAD, N. R. and J. M. SCHNEIDER: *production of uniform-sized liquid droplets*. Journal OF SCIENTIFIC INSTRUMENTS, 42:635, 1965.

[77] Liu, Qingbin, Changzheng Huang and Melissa Orme: *Mutual electrostatic interactions between closely spaced charged solder droplets*. Atomization and Sprays, 10(6):565–586, 2000.

[78] M., Schneider J., N. R. Lindblad, C. D. Hendricks and J. M. Crowley: *Stability of an Electrified Liquid Jet*. Journal of Applied Physics, 38(6):2599, 1967.

[79] M. Wolde, D. Marcotte, G. A. Isaac J. Jordan and S. Haimov S.G. Cober: *Airborne radar observations of icing in winter clouds during AIRS II*. AIAA 2005-254, 2005.

[80] Macklin, W. C. and B. F. Ryan: *Habits of ice grown in supercooled water and aqueous solutions*. Philosophical Magazine, 14(130), 1966.

[81] Magnus, G.: *Hydraulische Untersuchungen*. Anne. Phys. Chem, 95:1–59, 1855.

[82] Marwitz, J. D., M.K. Politovich, B.C. Bernstein, F.M. Ralph, P.J. Neiman, R. Ashenden and J. Bresch: *Meteorological conditions associated with the ATR-72 aircraft accident near Roselawn, Indiana on 31 October 1994*. American Meteorological Society, 78(1):41–52, 1997.

[83] MEHDIZADEH, NAVID Z., SANJEEV CHANDRA and JAVAD MOSTAGHIMI: *Formation of fingers around the edges of a drop hitting a metal plate with high velocity*. Journal of Fluid Mechanics, 510:353–373, 2004.

[84] members, EXTICE: *EXTICE Annex I Description of Work*. 2008.

[85] Messinger, B. L.: *Equilibrium temperature of an unheated icing surface as a function of air speed*. Journal of the Aeronautical Sciences, 20:29–42, 1953.

[86] Mikhail, S. Z. and W. R. Kimel: *Densities and Viscosities of Methanol-Water Mixtures*. Journal of Chemical and Engineering Data, 6(4), 1961.

[87] Miller, Dean, Thomas Ratvasky, Ben Bernstein, Frank McDonough and J. Walter Strapp: *NASA/FAA/NCAR supercooled large droplet icing flight research - Summary of winter 96-97 flight operations*. AIAA-98-0577, 1998.

[88] Miller, Dean R., Mark G. Potapczuk and Thomas H. Bond: *Update on SLD Engineering Tools Development*. NASA/TM-2004-213072, 2004.

[89] Miller, Mackenzie: *Investigation of Supercooled Large Droplets as Encountered in Aircraft Icing*. IREP report, TU Darmstadt, University of Colorado at Boulder, 2012. Supervisor: Hai Li.

[90] Milón G., J.J. and S.L. Braga: *Supercooling Water in Cylindrical Capsules*. In *the Fifteenth Symposium on Thermophysical Properties*, Boulder, Colorado, U.S.A., June 2003.

[91] Mingione, G., E. Iuliano, D. Guffond and C. Tropea: *EXTICE: EXTreme Icing Environement*. SAE Technical Paper 2011-38-0063, 2011.

[92] Mishchenko, Lidiya, Benjamin Hatton, Vaibhav Bahadur, J. Ashley Taylor, Tom Krupenkin and Joanna Aizenberg: *Design of Ice-free Nanostructured Surfaces Based on Repulsion of Impacting Water Droplets*. ACS Nano, 4:7699–7707, 2010.

[93] Mishima, Osamu and H. Eugene Stanley: *The relationship between liquid, supercooled and glassy water*. Nature, 396:329–335, 1998.

[94] Mishra, Neeraj Kumar, Yan Zhang and Albert Ratner: *Effect of chamber pressure on spreading and splashing of liquid drops upon impact on a dry smooth stationary surface*. Experiments in Fluids, 51:483–491, 2011.

[95] Morrison, Faith A.: *Data Correlation for Drag Coefficient for Sphere*. www.chem.mtu.edu/ fmorriso/DataCorrelationForSphereDrag2010.pdf, Department of Chemical Engineering, Michigan Technological University, Houghton, MI, 2012. Clarendon Press, Oxford, 1966.

[96] Müller-Krumbhaar, Heiner: *Phase Transformations in Materials*, chapter 2 Solidification, pages 82–119. WILEY-VCH Verlag GmbH, Federal Republic of Germany, 2001.

[97] Mullins, W.W. and R.F. Sekerka: *Morphological Stability of a Particle Growing by Diffusion or Heat Flow*. Journal of Applied Physics, 34(2):323–329, 1963.

[98] Mullins, W.W. and R.F. Sekerka: *Stability of a Planar Interface During Solidification of a Dilute Binary Alloy*. Journal of Applied Physics, 35(2):444–451, 1964.

[99] MUNDO, CHR., M. SOMMERFELD and C. TROPEA: *Droplet-Wall collisions: Experimental Studies of the Deformation and Breakup Process*. International Journal of Multiphase Flow, 21(2):151–173, 1995.

[100] OHSAKA, K. and E.H. TRINH: *Apparatus for measuring the growth velocity of dentritic ice in undercooled water*. Journal of Crystal Growth, 194:138–142, 1998.

[101] ORME, M.: *On the genesis of droplet stream microspeed dispersions*. Physics of Fluids A, 3:2936, 1991.

[102] ORME, M. and E. P. MUNTZ: *The manipulation of capillary stream breakup using amplitude-modulated disturbances: A pictorial and quantitative representation*. Physics of Fluids A, 2:1124, 1990.

[103] PAN, KUO-LONG, KUN-CHENG TSENG and CHING-HUA WANG: *Breakup of a droplet at high velocity impacting a solid surface*. Experiments in Fluids, 48:143–156, 2010.

[104] PAPADAKIS, MICHAEL, KUOHSING E. HUNG, GIAO T. VU, HSIUNG WEI YEONG, COLIN S. BIDWELL, MARLIN D. BREER and TIMOTHY J. BENCIC: *Experimental Investigaion of Water Droplet Impingement on Airfoils, Finite Wings, and an S-Duct Engine Inlet*. NASA/TM-2002-211700, 2002.

[105] PAPADAKIS, MICHAEL, KUOHSING E. HUNG, HSIUNG-WEI YEONG, COLIN S. BIDWELL and MARLIN D. BREER: *Experimental investigation of water impingement on single and multi-element airfoils*. AIAA 2000-0100, 2000.

[106] PAPADAKIS, MICHAEL, ARIEF RACHMAN, SEE-CHEUK WONG, HSIUNG-WEI YEONG, KUOHSING E. HUNG, GIAO T. VU and COLIN S. BIDWELL: *Water Droplet Impingement on Simulated Glaze, Mixed, and Rime Ice Accretions*. NASA/TM-2007-213961, 2007.

[107] PAPADAKIS, MICHAEL, SEE-CHEUK WONG, HSIUNG-WEI YEONG, KUOHSING E. HUNG and COLIN S. BIDWELL: *Water Impingement Experiments on a NACA 23012 Airfoil with Simulated Glaze Ice Shapes*. AIAA 2004-0565, 2004.

[108] PASANDIDEH-FARD, M., Y. M. QIAO, S. CHANDRA and J. MOSTAGHIMI: *Capillary effects during droplet impact on a solid surface*. Physics of Fluids, 8:650–659, 1996.

[109] PEPPER, RACHEL E., LAURENT COURBIN and HOWARD A. STONE: *Splashing on elastic membranes: The importance of early-time dynamics*. PHYSICS OF FLUIDS, 20(082103), 2008.

[110] PLATEAU, J.: *Statique experimentale et theorique des liquids soumis aux seules forces moleculaires*. Cited by Lord Rayleigh, Theory of sound, 1945, 1873.

[111] POLITOVICH, M. K., G. ZHANG, J. VIVEKANANDAN and J. K. WILLIAMS: *Characteristics of Clouds Containing SLD Relevant to Icing Remote Sensing*. AIAA 2003-562, 2003.

[112] POTAPCZUK, MARK G.: *Ice Mass Measurements Implications for the Ice Accretion Process*. AIAA 2003-387, 2003.

[113] POVAROV, O. A., O. I. NAZAROV, L. A. IGNAT'EVSKAYA and A. I. NIKOL'SKII: *Interaction of Drops with Boundary Layer on Rotating Surface*. Inzhenerno-Fizicheskii Zhurnal, 31(6):1068–1073, 1976.

[114] R., RIOBOO, C. TROPEA and MARENGO M.: *Outcomes from a drop impact on solid surfaces*. Atomization and Sprays, 11:155–165, 2001.

[115] RANGE, KAI and FRANÇOIS FEUILLEBOIS: *Influence of Surface Roughness on Liquid Drop Impact*. JOURNAL OF COLLOID AND INTERFACE SCIENCE, 203:16–30, 1998.

[116] RAY, SIDNEY F.: *The Manual of Photography: Photographic and Digital Imaging*, chapter The geometry of image formation, pages 50–56. Focal Press, Great Britain, 2000.

[117] RAYLEIGH, LORD: *On the equilibrium of liquid conducting masses charged with electricity*. Philosophical Magazine Series 5, 14(87):184–186, 1882.

[118] RAYLEIGH, W. S.: *On the instability of jets*. Proc. Lond. math. Soc., 10:4–13, 1878.

[119] REIN, MARTIN and JEAN-PIERRE DELPLANQUE: *The role of air entrainment on the outcome of drop impact on a solid surface*. Acta Mechanica, 201:105–118, 2008.

[120] REPORT, NATIONAL TRANSPORTATION SAFETY BOARD AVIATION ACCIDENT: *In-flight icing encounter and uncontrolled collision with terrain, Comair Flight 3272, Embraer EMB-120T, N265CA, Monroe, Michigan. NTSB Accid. No. DCA97MA017*, 1997.

[121] RIOBOO, R., M. MARENGO and C. TROPEA: *Time Evolution of Liquid Drop Impact onto Solid, Dry Surfaces*. Experiments in Fluids, 33:112–124, 2002.

[122] ROBINSON, P.J. and J.A. DAVIES: *Laboratory Determinations of Water Surface Emissivity*. Journal of Applied Meteorology, 11:1391–1393, 1972.

[123] ROISMAN, ILIA V.: *Inertia dominated drop collisions. II. An analytical solution of the Navier-Stokes equations for a spreading viscous film*. Physics of Fluids, 21(052104), 2009.

[124] RUITER, JOLET DE, RACHEL E. PEPPER and HOWARD A. STONE: *Thickness of the rim of an expanding lamella near the splash threshold*. PHYSICS OF FLUIDS, 22(022104), 2010.

[125] RYERSON, CHARLES C., GEORGE G. KOENIG and FORREST R. SCOTT: *Analysis of Summit Icing Cloud Microphysical Poperties During MWISP*. AIAA-2002-0680, 2002.

[126] SABRI, FARHAD, OCTAVIAN TRIFU and ION PARASCHIVOIU: *In-Flight Ice Accretion Simulation in SLD Conditions*. AIAA 2007-4282, 2007.

[127] SAVART, F.: *Memoire sur la constitution des veines liquides lancees par des orifices circulaires en mince paroi*. Ann. Chim, 53(337), 1833.

[128] SCHNEIDER, J. M. and C. D. HENDRICKS: *Source of uniform-sized liquid droplets*. THE REVIEW OF SCIENTIFIC INSTRUMENTS, 35(10):1349, 1964.

[129] SCHNEIDER, TIMOTHY, BEN C. BERNSTEIN and ROGER REINKING: *Forecasting and Ground-based Remote Icing Detection System (Grids) Documentation of the Transition From a Glaciated Environment to an SLD Icing Enviroment*. AIAA 2005-257, 2005.

[130] S.C.TAN and M.PAPADAKIS: *Droplet Breakup, Splashing and Re-Impingement on An Iced Airfoil*. AIAA 2005-5185, 2005.

[131] S.C.TAN and M.PAPADAKIS: *Simulation of SLD Impingement on a High-Lift Airfoil*. AIAA 2006-463, 2006.

[132] SEKERKA, R.F.: *Application of the Time-Dependent Theroy of Interface Stability to an Isothermal Phase Thansformation*. Journal of Physics and Chemistry of Solids, 28:983–994, 1967.

[133] SEKERKA, R.F.: *Morphological Stability*. Journal of Crystal Growth, 3,4:71–81, 1968.

[134] SEKERKA, R.F.: *Crystal Growth: An Introduction*, chapter 15, pages 403–443. North-Holland, Amsterdam-London, 1973.

[135] SHIBKOV, A. A., YU. I. GOLOVIN, M. A. ZHELTOV, A. A. KOROLEV and A. A. VLASOV: *Kinetics and Morphology of Nonequilibrium Growth of Ice in Supercooled Water*. Crystallography Reports, 46(3):549–555, 2001.

[136] SHIBKOV, A.A., YU.I. GOLOVIN, M.A. ZHELTOV, A.A. KOROLEV and A.A. LEONOV: *In situ monitoring of growth of ice from supercooled water by a new electromagnetic method*. Journal of Crystal Growth, 236:434–440, 2002.

[137] SHIBKOV, A.A., YU.I. GOLOVIN, M.A. ZHELTOV, A.A. KOROLEV and A.A. LEONOV: *Morphology diagram of nonequilibrium patterns of ice crystals growing in supercooled water*. Physica A, 319:65–79, 2003.

[138] SPURK, SPURK H. and NURI AKSEL: *Fluid Mechaniscs*, chapter 12 Boundary Layer Theory, pages 417–450. Springer, Heidelberg, Germany, 2008.

[139] STEPHAN, PETER. Lecture notes: Heat and Mass Transfer, 2012.

[140] Stephan E. Bansmer, Benjamin W. Fassmann abd, Thorsten J. Möller, Rolf Radespiel and Michael Hartmann: *High velocity impingement of single droplets on a dry smooth surface*. Experiments in Fluids, 54(1516), 2013.

[141] Steuernagle, John, Kathleen Roy and David Wright: *Safty Advisor - Aircraft Icing*. Internet: www.asf.org.

[142] Stow, C. D. and M. G. Hadfield: *An Experimental Investigation of Fluid Flow Resulting from the Impact of a Water Drop with an Unyielding Dry Surface*. Proceedings of the Royal Society of London. Series A, Mathematical and PhysicalSciences, 373(1755):419–441, 1981.

[143] Strapp, J.W., R.A. Stuart and G.A. Isaac: *A Canadian climatology of freezing precipitation and a detailed study using data from St. John's, Newfoundland*. In *Proceedings FAA Intl. Conf. on Aircraft Inflight Icing*, pages 45–66, Springfield, Virginia, May 1996. DOT/FAA/AR-96/81,II.

[144] Tan, S.C.: *A Tentative Mass Loss Model for Simulating Water Droplet Splash*. AIAA 2004-410, 2004.

[145] Tan, S.C., M. Papadakis, D. Miller, T. Bencic, P. Tate and M.C. Laun: *Experimental Study of Large Droplet Splashing and Breakup*. AIAA 2007-904, 2007.

[146] Trujillo, M F, W S Mathews, C F Lee and J E Peters: *Modeling and Experiment of Impingement and Atomization of a Liquid Spray on a Wall*. International Journal of Engine Research, 283:141–173, 2000.

[147] Tsao, Jen-Ching and David N. Anderson: *ADDITIONAL STUDY OF MVD EFFECTS ON ICE SHAPES*. AIAA 2004-413, 2004.

[148] Uhara, I., S. Doi, M. Makino and S. Teratani: *Crystal nucleation given rise by fracturing or by mechanical shock*. Kolloid-Zeitschrift und Zeitschrift für Polymere, 244:218–222, 1971.

[149] Valarezo, W. O.: *Maximum lift degradation due to wing upper surface contamination*. In *Proceedings of the 1st Bombardier International Workshop, Aircraft Icing/Boundary-Layer Stability and Transition*, Montreal, Canada, September 1993.

[150] Vargas, Mario and Jen-Ching Tsao: *Observations on the Growth of Roughness Elements into Icing Feathers*. AIAA-2007-0900, 2007.

[151] Vassallo, P. and N. Ashgriz: *Satellite formation and merging in liquid jet breakup*. Proc. R. Soc. London, Ser. A, 433:269, 1991.

[152] Vázquez, Gonzalo, Estrella Alvarez and José M. Navaza: *Surface Tension of Alcohol + Water from 20 to 50* °C. Journal of Chemical and Engineering Data, 40(3):611–614, 1995.

[153] Šikalo Š., C. Tropea and E.N. Ganić: *Impact of droplets onto inclined surfaces*. Journal of Colloid and Interface Science, 286:661–669, 2005.

[154] Vukits, Thomas J. and Raytheon: *Overview and Risk Assessment of Icing for Transport Category Aircraft and Components*. AIAA-2002-0811, 2002.

[155] Wagenknecht, Erik: *Aufbau eines pneumatischen Tropfengenerators*. Bachelor thesis, TU Darmstadt, 2012. Supervisor: Hai Li.

[156] Wal, Randy L. Vander, Gordon M. Berger and Steven D. Mozes: *The combined influence of a rough surface and thin fluid film upon the splashing threshold and splash dynamics of a droplet impacting onto them*. Experiments in Fluids, 40:23–32, 2006.

[157] Waller, R.: *(trans.) Essays of Natural Experiments*. (original in Italian by the Secretary of the Academie del Cimento); facsimile of the 1684 English translation, New York, 1964. Johnson Reprint.

[158] Weber, C.: *On the breakdown of a fluid jet*. ZAMM, 1:136, 1931.

[159] Weigand, B., N. Roth, S. Jakirlic and C. Tropea: *Sonderforschungsbereich Transregio 75 Jahresbericht 2012*. Technical Report, 2012.

[160] Worthington, A. M.: *on the form assumed by drops of liquid falling vertically on a horizontal plate*. Proceedings of the Royal Society of London, 25:261–272, 1876.

[161] Worthington, A. M.: *A Second Paper on the form assumed by drops of liquid falling vertically on a horizontal plate*. Proceedings of the Royal Society of London, 25:498–503, 1876.

[162] Wright, William B.: *Validation Results for LEWICE 3.0*. AIAA-2005-1243, 2005.

[163] Wright, William B.: *Further Refinement of the LEWICE SLD Model*. AIAA-2006-464, 2006.

[164] Wright, William B. and Mark G. Potapczuk: *Semi-Empirical Modeling of SLD Physics*. AIAA 2004-412, 2004.

[165] Wright, William B. and Adam Rutkowski: *Validation Results for LEWICE 2.0*. NASA/CR-1999-208690, 1999.

[166] Xu, Lei: *Liquid Drop Splashing on Smooth, Rough, and Textured Surfaces*. PHYSICAL REVIEW E, 75(056316), 2007.

[167] Xu, Lei, Loreto Barcos and Sidney R. Nagel: *Splashing of Liquids: Interplay of Surface Roughness with Surrounding Gas*. PHYSICAL REVIEW E, 76(066311), 2007.

[168] Xu, Lei, Wendy W. Zhang and Sidney R. Nagel: *Drop Splashing on a Dry Smooth Surface*. PHYSICAL REVIEW LETTERS, 94(184505), 2005.

[169] YANG, J. C., W. CHIEN, M. KING and W. L. GROSSHANDLER: *A Simple Piezoelectric Droplet Generator*. Experiments in Fluids, 23:445–447, 1997.

[170] YARIN, A. L. and D. A. WEISS: *impact of drops on solid surfaces self-similar capillary waves, and splashing as a new type of kenimatic discontinuity*. Journal of Fluid Mechanics, 1(1), 1995.

[171] YARIN, A.L.: *Drop Impact Dynamics: Splashing, Spreading, Receding, Bouncing. . .* Annual Review of Fluid Mechanics, 38:159–192, 2006.

[172] YOKOYAMA, ETSURO, IZUMI YOSHIZAKI, TARO SHIMAOKA, TAKEHIKO SONE, TATSUO KIYOTA and YOSHINORI FURUKAWA: *Measurements of Growth Rates of an Ice Crystal from Supercooled Heavy Water under Microgravity Conditions Basal Face Growth Rate and Tip Velocity of a Dendrite*. The Journal of Physical Chemistry B, 115:8739–8745, 2011.

[173] YOUNG, S. W.: *MECHANICAL STIMULUS TO CRYSTALLIZATION IN SUPER-COOLED LIQUIDS*. Journal of the American Chemical Society, 33:148–162, 1911.

[174] ZASETSKY, A. Y., A. F. KHALIZOV, M. E. EARLE and J. J. SLOAN: *Frequency Dependent Complex Refractive Indices of Supercooled Liquid Water and Ice Determined from Aerosol Extinction Spectra*. The Journal of Physical Chemistry A, 2005(109):2760–2764, 2005.

[175] ZEN, TAIN-SHI, FU-CHU CHOU and JU-LUNG MA: *Ethanol drop impact on an inclined moving surface*. International Communications in Heat and Mass Transfer, 37:1025–1030, 2010.

Curriculum Vitae

Personal Information:

Name: Hai Li
Date of Birth: 13. Nov. 1983
Place of Birth: Shanxi, China
Nationality: China

Education:

2008.09 - 2013.07: Doctoral study at Chair of Fluid Mechanics and Aerodynamics, Technische Universität Darmstadt.

2006.09 - 2008.06: Master study at School of Aeronautical Science and Engineering, Beijing University of Aeronautics and Astronautics, Beijing, China.

2002.09 - 2006.07: Bachelor Study at School of Aeronautical Science and Engineering, Beijing University of Aeronautics and Astronautics, Beijing China.